# THE ELECTROCHEMISTRY OF METALLOENZYMES CONFINED IN IONIC LIQUIDS




Yiduo Wang

St Cross College

Trinity Term 2016

A thesis submitted to the Board of the Faculty of Physical Sciences, for the degree of Doctor of Philosophy, University of Oxford

# The Electrochemistry of Metalloenzymes Confined in Ionic Liquids

Yiduo Wang, St Cross College, University of Oxford

A thesis submitted for the degree of DPhil, Trinity Term 2016

Enzymes are superb catalysts with high selectivity and catalytic efficiency. Ionic liquids have negligible volatility, good electric conductivity, and high thermal and chemical stability, which are powerful electrolytes for electrochemical processes. To understand how to apply enzymatic catalysis in ionic liquids to carbon-neutral technologies, this thesis investigates the electrochemical properties of three metalloenzymes that are inspirational catalysts for fuel cells and $CO_2$ reduction in an almost dry condition in ionic liquids, by protein film electrochemistry (PFE).

Hydrogenase-1 from *Escherichia coli* (Hyd-1) catalyses $H_2$ oxidation at turnover frequencies ca. 100 $s^{-1}$. Bilirubin oxidase (BOD) is commercially available and catalyses the four-electron $O_2$ reduction at a lower overpotential than Pt and at turnover frequencies ca. 100 $s^{-1}$. Each enzyme was immobilized on a carbon electrode that contacts an aqueous microvolume (1–2 μL) surrounded by a hydrophobic ionic liquid. Separately, the enzymes display excellent electrocatalytic activity: brought together at a synaptic junction, an anode and cathode modified with each enzyme constitute a membrane-less fuel that produces over 0.8 V when equilibrated with 96 % $H_2$–4 % $O_2$.

Carbon monoxide dehydrogenase from *Carboxydothermus hydrogenoformans* I (CODH $I_{Ch}$) shows considerable electrocatalytic activity in tiny aqueous shell confined by EMIMTFSI saturated with $CO_2$. $CO_2$ is exceptionally soluble in ionic liquids, which are practical for $CO_2$ uptake, capture and storage. $CO_2$ reduction and CO oxidation electrocatalysed by CODH $I_{Ch}$ occurred at the same time in the tiny aqueous shell, according to cyclic voltammetry. Finally, a steady state was achieved.

# Acknowledgements

My foremost thanks go to Professor Fraser Armstrong. I thank Fraser for the backbone idea of this thesis, patient guidance, constructive criticism and encouragement.

I also thank the whole Armstrong group, who are friendly and pleasant to work with. Thank Elena for the preparation of hydrogenases used in the thesis. Thank Thomas for his help at the start of my DPhil. Thank Vincent group for being a good neighbour.

I thank the ICL staff: thank you Terri for the intricate glass wares, Ashleigh and Jonathan for efficient management of the building, Tom for fixing the IT problems.

My sincere thanks go to my parentsfor their love and support. Thank my friends: Zhe, Yunqi, Helen, Yujia, Luna, Dan, Ella, Julia, Eugina, Richard,John, Temple, Minwen in Oxford for their encouragement and friendship.

# Collaborations

Carbon monoxide dehydrogease I from *Carboxydothermus hydrogenoformans* in this thesis has been generously provided from the research group of Prof. Stephen W. Ragsdale in the University of Michigan, Ann Arbor, Michigan. Samples were purified by Dr Mehmet Can and Dr Elizabeth Pierce.

# Publication

**Wang, Y., Esterle, T.F., Armstrong, F.A.** Electrocatalysis by $H_2$-$O_2$ Membrane-free Fuel Cell Enzymes in Aqueous Microenvironments Confined by an Ionic Liquid.*RSC Advances*,**6** (50) pp. 44129 - 44134.

# Major Symbols

## Roman Symbols

| | |
|---|---|
| $A$ | electrode surface area |
| $C$ | the concentration of the substrate |
| $D$ | diffusion coefficient of the substrate |
| $E_a$ | activation energy |
| $E_f$ | formal potential |
| $F$ | Faraday constant; charge on one mole of electrons |
| $k_{cat}$ | turnover frequency of the enzyme |
| $K_m$ | Michaelis constant |
| $i_{lim(\omega)}$ | the limiting (plateau) current at rotation rate ω |
| $i_{lim}$ | the maximum limiting current |
| $R$ | gas constant |
| $T$ | temperature |

## Greek Symbols

| | |
|---|---|
| $v$ | the viscosity of the solvent |
| $\omega$ | the electrode rotation rate |
| $\Gamma$ | coverage of the enzyme |
| $\eta$ | kinematic viscosity |

## Standard Abbreviations

| | |
|---|---|
| ACS | acetyl-CoA synthase |
| AuNP | gold nanoparticle |
| $BMIMPF_6$ | 1-Butyl-3-methylimidazolium hexafluorophosphate |
| $BMIMBF_4$ | 1-Butyl-3-methylimidazolium tetrafluoroborate |
| DFT | Density Functional Theory |
| EFC | enzymatic fuel cell |
| EPR | Electron Paramagnetic Resonance |
| EMIMTFSI | 1-Ethyl-3-methylimidazolium bis(trifluoromethylsulfonyl)imide |
| GOx | Glucose Oxidase |
| LED | Light Emitting Diode |
| MBH | membrane-bound hydrogenases |
| MWNT | multiwall carbon nanotubes |

| | |
|---|---|
| *Mv*-BOD | bilirubin oxidase from *Myrothecium verrucaria* |
| OCV | open circuit voltage |
| PFE | protein film electrochemistry |
| PGE | pyrolytic graphite edge |
| PMPyrTFSI | 1-methyl-1-propyl pyrrolidinium bis(trifluoromethylsulfonyl)imide |
| PQQ | pyrroloquinoline quinone |
| RPM | revolutions per minute |
| SCE | Saturated Calomel Electrode |
| SHE | Standard Hydrogen Electrode |

# List of Figures

Figure 1.1 General scheme of a fuel cell.

Figure 1.2 Structure of the copper binding sites of bilirubin oxidase from *Myrothecium verrucaria.*

Figure 1.3 Mechanism of $O_2$ reduction to water by bilirubin oxidase (BOD).

Figure 1.4 Crystal structure of hydrogenase 1 from *Escherichia coli*

Figure 1.5 A representation of the [NiFe]-hydrogenase active site.

Figure 1.6A proposed mechanism for $H_2$ cycling by [NiFe]-hydrogenases.

Figure 1.7 Different states of [NiFe]-hydrogenases.

Figure 1.8 Structure of CODH II showing the two subunits

Figure 1.9 Crystal structure of the C-cluster of CODH $II_{Ch}$ at – 600 mV ($C_{red2}$ state).

Figure 1.10 Crystal structure of the C-cluster of CODH $II_{Ch}$ at – 320 mV ($C_{red1}$ state).

Figure 1.11 Crystal structure of the C-cluster of CODH $II_{Ch}$ at – 600 mV +$CO_2$ (-600 mV+$CO_2$ state).

Figure 1.12 Structure-based mechanism of $CO_2$/CO interconversion at C-cluster of Ni-CODH.

Figure 3.1 Model of protein film electrochemistry.

Figure 3.2 A schematic circuit diagram of the three-electrode system.

Figure 3.3 Schematic diagram of the glass electrochemical cell used for protein film electrochemistry in aqueous buffers.

Figure 3.4 Photo of the all-glass electrochemical cell used for protein film electrochemistry in aqueous buffers.

Figure 3.5 Schematic diagram of the glass electrochemical cell used for protein film electrochemistry in ionic liquids.

Figure 3.6 Photo of the all-glass electrochemical cell used for protein film electrochemistry in ionic liquids.

Figure 3.7 A typical calibration line in a Bradford assay.

Figure 4.1 Cyclic voltammetry of Hyd1 (2 µL) at graphene film (10 mg/mL) electrode (solid line) and bare PGE (dotted line) electrodes.

Figure 4.2 Cyclic voltammetry of BOD (2 µL) at graphene film (10 mg/mL) electrode

(solid line) and bare PGE (dotted line) electrodes.

Figure 4.3 Cyclic voltammograms (current density) of Hyd1 (2 μL) at PGE electrodes modified with graphene suspensions of different concentrations

Figure 4.4 Infrared Spectroscopy of graphene suspensions.

Figure 4.5 Cyclic voltammetry of Hyd1 (2 μL) at MWNT film electrode (solid line) and bare PGE (dotted line) electrodes.

Figure 4.6 Cyclic voltammetry of BOD (2 μL) at MWNT film electrode (solid line) and bare PGE (dotted line) electrodes.

Figure 4.7 Cyclic voltammograms (current density) of Hyd1 (20 μL) at MWNT pellet electrode (solid line) and blank MWNT pellet electrode (dotted line).

Figure 4.8 Chronoamperometry of Hyd-1 (20 μL) at the MWNT pellet electrode over 130 h.

Figure 4.9 Cyclic voltammograms (current density) of BOD (20 μL) at MWNT pellet electrode (solid line) and blank MWNT pellet electrode (dotted line).

Figure 4.10 BOD (20 μL) protein film stability on MWNT pellet electrode over 100 h.

Figure 4.11 Rotation rate dependence of the current density of $H_2$ oxidation electrocatalysed by Hyd1 (20 μL) at MWNT pellet electrode.

Figure 4.12 Rotation rate dependence of the current density of $O_2$ reduction electrocatalysed by BOD (20 μL) at MWNT pellet electrode.

Figure 5.1 Cyclic voltammetry of DmFc (2 mM) at a bare PGE electrode (surface area 0.03 $cm^2$) in EMIMTFSI at 10 mV/s.

Figure 5.2 Dependence of oxidative peak current for the process of $DmFc^{+/0}$ on the square root of the scan rate in EMIMTFSI.

Figure 5.3 Cyclic voltammetry of DmFc (2 mM) at a bare PGE electrode (surface area 0.03 $cm^2$) in PMPyrTFSI at 10 mV/s.

Figure 5.4 Dependence of oxidative peak current for the process of $DmFc^{+/0}$ on the square root of the scan rate in PMPyrTFSI.

Figure 5.5 Cyclic voltammetric scans (current density) of Hyd1 (2 μL) at MWNT/PGE electrode surrounded by EMIMTFSI bubbling with 100 % $H_2$.

Figure 5.6 Cyclic voltammetry (current density) of Hyd1 at the same electrode as Figure 5.5 transferred into mixed hydrogenase buffer (pH 6.0, 100 mM) right after the electrocatalytic activity vanished through continuous voltammetric scans in EMIMTFSI.

Figure 5.7 Cyclic voltammetric scans (current density) of Hyd1 (2 μL) at MWNT/PGE electrode surrounded by PMPyrTFSI bubbling with 100 % $H_2$.

Figure 5.8 Cyclic voltammetry (current density) of Hyd1 at the same electrode as Figure 5.7 transferred into mixed hydrogenase buffer (pH 6.0, 100 mM) right after the

electrocatalytic activity vanished through continuous voltammetric scans in PMPyrTFSI.

Figure 5.9 Continuous cyclic voltammetric scans (current density) of 1 µL of Hyd1 suspended in 100 mM phosphate buffer (pH 6.2), adsorbed at an MWNT/PGE electrode surrounded by EMIMTFSI (~1 mL) dissolved with 2 mM DmFc and saturated with $H_2$.

Figure 5.10 A schematic representation of a MWNT/PGE electrode modified with enzyme film and immersed in water-immiscible ionic liquid.

Figure 5.11 Cyclic voltammetric scans (current density) of Hyd1 modified MWNT/PGE electrode in pH 6mixed buffer (100 mM) under 100 % $H_2$.

Figure 5.12 Cyclic voltammetry of 2 µL of ferricyanide (5 mM, aq.) at PGE electrode surrounded by EMIMTFSI.

Figure 6.1 Cyclic voltammetric scans (current density) in 1 µL of BOD (suspended in pH 6.2 phosphate buffer, 100 mM) at MWNT/PGE electrode surrounded byEMIMTFSI bubbling with 100 % $O_2$.

Figure 6.2 Cyclic voltammetric scans (current density) of BOD in phosphate buffer (pH 6.2, 100 mM) after the electrocatalytic activity vanished through continuous voltammetric scans in EMIMTFSI at the same electrode.

Figure 6.3 Cyclic voltammetric scans (current density) of 1 µL of BOD (suspended in pH 5 phosphate buffer, 100 mM) at MWNT/PGE electrode surrounded by EMIMTFSI bubbling with 100 % $O_2$.

Figure 6.4 Cyclic voltammetric scans (current density) of 1 µL of BOD (suspended in pH 7 phosphate buffer, 50 mM) at MWNT/PGE electrode surrounded by EMIMTFSI bubbling with 100 % $O_2$.

Figure 6.5Cyclic voltammetric scans (current density) of 1 µL of BOD (suspended in pH 6.2 phosphate buffer, 1 mM) at MWNT/PGE electrode surrounded by EMIMTFSI (~1 mL) bubbling with 100 % $O_2$.

Figure 6.6Cyclic voltammetric scans (current density) of 2 µL of BOD (suspended in pH 7 phosphate buffer, 50 mM) at MWNT/PGE electrode surrounded by PMPyrTFSI bubbling with 100 % $O_2$.

Figure 6.7Cyclic voltammetric scans (current density) of BOD in phosphate buffer (pH 6.2, 100 mM) after the electrocatalytic activity vanished through continuous voltammetric scans in PMPyrTFSI at the same electrode.

Figure 6.8Cyclic voltammetry (current density) of BOD modified MWNT/PGE electrode in pH 6.2 phosphate buffer (100 mM) under 100 % $O_2$.

Figure 6.9 Cyclic voltammetric scans (current density) of 1 µL of BOD suspended in 100 mM phosphate buffer (pH 6.2), at an MWNT/PGE electrode in EMIMTFSI (~1 mL) dissolved with 2 mM DmFc and saturated with $O_2$.

Figure 7.1 (Panel A) Vertical view diagram of the synaptic fuel cell. (Panel B) Side

view diagram of the synaptic fuel cell.

Figure 7.2 (Panel A) Photo of the synaptic fuel cell. (Panel B) Photo of the whole setup of SFC in a sandwich box.

Figure 7.3 Cyclic voltammograms (current density, first scans) of Hyd1 (black solid line) and BOD (red solid line) modified MWNT/PGE electrodes and blank MWNT/PGE electrodes (dotted lines) in $H_2$-$O_2$ fuel cell conditions.

Figure 7.4 Dependence of power density (P, per total electrode area) on fuel cell voltage for the buffer-SFC before (black) and after (red) 9 h's operation at 0.75 V with a humidified gas mixture of 96 % $H_2$–4 % $O_2$.

Figure 7.5 Dependence of power density (P, per total electrode area) on fuel cell voltage for the buffer-SFC before (black) and after (red) 9 h's operation at 0.75 V with a gas mixture of 96 % $H_2$–4 % $O_2$.

Figure 7.6 (A) The synaptic fuel cell assembly. Black areas correspond to aqueous zones where enzymes have been spotted on the electrodes and the pale grey area indicates the protective coverage of EMIMTFSI over the two electrodes. (B and C) Performances of the fuel cells, 26 ± 2 ˚C, box atmosphere 96 % $H_2$–4 % $O_2$. Solid lines show initial polarisation curve (black) and power curve (blue).

Figure 7.7 Open circuit voltage of the tiny enzymatic fuel cell using phosphate buffer (100 mM, pH 5) as electrolyte under 96 % $H_2$–4 % $O_2$ (black line) and 100 % $H_2$ (red line).

Figure 7.8 Open circuit voltage of the tiny enzymatic $H_2$-$O_2$ fuel cell using EMIMTFSI as electrolyte under 96 % $H_2$–4 % $O_2$ (black line) and 100 % $H_2$ (red line).

Figure 7.9 Time dependence of cell voltage of buffer-SFC (Panel A), EMIMTFSI-SFC (Panel B) and that of current density (cathode area 0.00785 $cm^2$) of buffer-SFC (Panel C), EMIMTFSI-SFC (Panel D) over the course of 3 steps

Figure 8.1 Scheme showing an electrode modified with CODH $I_{Ch}$ film (hydrated with approx. 1 µL of buffer) and immersed in water-immiscible ionic liquid.

Figure 8.2 Continuous cyclic voltammetric scans (current density) of 1 µL of CODH $I_{Ch}$ (suspended in the buffer containing 50 mM Tris/HCI, initially pH 7.5 at 30 ˚C, 1 mM Dithiothreitol and 1 mM sodium dithionite) adsorbed at an MWNT/PGE electrode surrounded by EMIMTFSI (~1 mL) dissolved with 2 mM DmFc and saturated with 1 bar $CO_2$.

Figure 8.3 Cyclic voltammetric scans (current density) of 1 µL of CODH $I_{Ch}$ (suspended in the buffer containing 50 mM Tris/HCI, initially pH 7.5 at 30 ˚C, 1 mM Dithiothreitol and 1 mM sodium dithionite) adsorbed at an MWNT/PGE electrode surrounded by EMIMTFSI (~1 mL) dissolved with 2 mM DmFc and saturated with 1 bar $CO_2$.

Figure 8.4 Continuous cyclic voltammetric scans (current density) of 1 µL of CODH $I_{Ch}$ (suspended in the buffer containing 50 mM Tris/HCI, initially pH 7.5 at 30 ˚C, 1 mM Dithiothreitol and 1 mM sodium dithionite) adsorbed at an MWNT/PGE electrode surrounded by EMIMTFSI (~1 mL) dissolved with 2 mM DmFc and saturated with 1

bar $CO_2$.

Figure 8.5 Chronoamperometry of (A) 1 μL of CODH $I_{Ch}$ (suspended in the buffer containing 50 mM Tris/HCI, initially pH 7.5 at 30 ˚C, 1 mM Dithiothreitol and 1 mM sodium dithionite) adsorbed at an MWNT/PGE electrode; (B) a blank MWNT/PGE electrode surrounded by EMIMTFSI (~1 mL) dissolved with 2 mM DmFc and saturated with 1 bar $CO_2$.

Figure 8.6 Chronoamperometry of (A) 1 μL of CODH $I_{Ch}$ (suspended in the buffer containing 50 mM Tris/HCI, initially pH 7.5 at 30 ˚C, 1 mM Dithiothreitol and 1 mM sodium dithionite) adsorbed at an MWNT/PGE electrode; (B) a blank MWNT/PGE electrode surrounded by EMIMTFSI (~1 mL) dissolved with 2 mM DmFc and saturated with 1 bar $CO_2$.

# List of Schemes

Scheme 1.1 Interconversion between bilirubin and biliverdin.

Scheme 1.2 Structures of cofactors and their redox reactions.

Scheme 1.3 Oxidation of D-Glucose

Scheme 2.1 Proposed Electrochemical Reduction of Imidazolium Cation

# List of Tables

Table 2.1 Physical properties and structures of ionic liquids

Table 3.1 Calibration with BSA protein standard.

Table 5.1 Cyclic Voltammetric Data for $DmFc^{+/0}$ at a PGE (0.03 $cm^2$) Electrode in EMIMTFSI and PMPyrTFSI.

Table 6.1 Cyclic voltammetric data for $O_2$ reduction ($1^{st}$ Scan) catalysed by BOD at MWNT/PGE electrode in EIMIMTFSI bubbling with 100 $O_2$ at 30 ˚C

Table 8.1 Solubility (mole fraction) of CO and $CO_2$ in water and EMIMTFSI at 1 bar.

Table 8.2 Summary of data obtained by chronoamperometry at –0.45 and –0.65 V vs $DmFc^{+/0}$.

# Contents


**1. Introduction ..... 1**

**1.1. The Earth is Getting Warmer ..... 2**

**1.2. Hydrogen as an Energy Store ..... 2**

**1.3. Enzymatic Fuel Cells ..... 4**

1.3.1. Characterisation of Enzymatic Fuel Cells ..... 6

1.3.2. The History of Enzymatic Fuel Cells ..... 8

1.3.3. Enzymes for Cathodes ..... 11

1.3.3.1. Reduction of Dioxygen ..... 11

1.3.3.1.1. Mechanism of the Oxygen Reduction Reaction Catalysed by Bilirubin Oxidase. 14

1.3.3.1.2. Catalytic Activity Comparison of Bilirubin Oxidase with Pt ..... 16

1.3.3.2. Reduction of Hydrogen Peroxide ..... 18

1.3.4. Enzymes for Anodes ..... 19

1.3.4.1. Oxidation of Sugars and Alcohols ..... 19

1.3.4.2. Oxidation of $H_2$ ..... 22

1.3.4.3. Electron Relay Centers of Hydrogenases ..... 23

1.3.4.4. Gas Channels of Hydrogenases ..... 24

1.3.4.5. Hydrogenase 1 from *Escherichia coli* (Hyd1) ..... 25

1.3.4.6. Reaction Mechanism of [NiFe]-Hydrogenases ..... 28

1.3.4.7. Complexity of [NiFe]-Hyrogenase States ..... 30

1.3.4.8. Activity Comparison of Hydrogenases with Precious Metals ..... 32

**1.4. Nickel Carbon Monoxide Dehydrogenase ..... 35**

**2. Electrochemical Reactivity in Ionic Liquids ..... 44**

**2.1. The Definition and History of Ionic Liquids ..... 45**

**2.2. Properties of Ionic Liquids ..... 46**

2.2.1. Viscosity ..... 48

2.2.2. Conductivity ..... 51

2.2.3. Electrochemical Window ..... 53

2.2.4. Impurities and Their Effects ..... 55

**2.3. Electrochemical Methods in Ionic Liquids ..... 56**

2.3.1. Reference Electrodes ..... 56

2.3.2. Ionic Liquid/Electrode Interface ..... 58

2.3.3. Voltammetry in Ionic Liquids ..... 59

**2.4. Electrochemical Applications of Ionic Liquids ..... 60**

2.4.1. Lithium Batteries ..... 60

2.4.2. Inorganic Fuel Cells ..... 61

2.4.3. Supercapacitors ..... 62

**2.5. Bioelectrochemistry in Ionic Liquids ..... 62**

2.5.1. Ionic Liquids as Components of Electrodes ..... 63

2.5.2. Ionic Liquids as Electrolytes ..... 65

**3. Experimental Theory and Methods ..... 67**

**3.1. Protein Film Electrochemistry ..... 68**

**3.2. Cyclic Voltammetry ..... 71**

3.2.1. Non-Faradaic Current ..... 71

3.2.2. Faradaic Current ..... 72

**3.3. Chronoamperometry ..... 74**

**3.4. The Three-Electrode System ..... 74**

3.4.1. Experimental Procedures of Protein Film Electrochemistry in Aqueous Phases .. 79

3.4.2. Experimental Procedures of Protein Film Electrochemistry in Ionic Liquids ..... 80

**3.5. Materials ..... 83**

**3.6. Enzymes ..... 84**

3.6.1. Hydrogenase 1 from *E.coli* (Hyd1) ..... 84

3.6.2. Bilirubin Oxidase ..... 84

3.6.3. Concentration of Protein ..... 86

**3.7. Buffers ..... 89**

3.7.1. Mixed Hydrogenase Buffer ..... 89

3.7.2. Phosphate Buffer ..... 90

3.7.3. Borate Buffer ..... 90

**4. Electrodes of Carbon Nanomaterials ..... 91**

**4.1. Abstract ..... 92**

**4.2. Introduction ..... 93**

**4.3. Experimental ..... 97**

4.3.1. Preparation of Graphene Film Electrodes ..... 97

4.3.2. Preparation of MWNT Film Electrodes ..... 98

4.3.3. Preparation of MWNT Pellet Electrodes ..... 98

4.3.4. IR Spectroscopy ..... 99

**4.4. Results and Discussion ..... 99**

4.4.1. Graphene Film Electrode ..... 99

4.4.2. MWNT Film Electrode ..... 104

4.4.3. MWNT Pellet Electrode ..... 106

**4.5. Conclusions and Perspectives ..... 115**

**5. Oxidation of $H_2$ Electrocatalysed by Hydrogenase Confined in Ionic Liquids ..... 117**

**5.1. Abstract ..... 118**

**5.2. Introduction ..... 119**

**5.3. Experimental ..... 120**

**5.4. Results and Discussion ..... 120**

5.4.1. Potential Calibration with DmFc as Internal Reference in Ionic Liquids ..... 120

5.4.1.1. EMIMTFSI ..... 121

5.4.1.2. PMPyrTFSI ..... 124

5.4.2. Enzyme Film Electrochemistry of Hyd1 Confined in EMIMTFSI and PMPyrTFSI 127

5.4.3. Cyclic Voltammetry of Ferricyanide (aq.) at PGE in EMIMTFSI ..... 138

**5.5. Conclusions and Perspectives ..... 140**

**6. Reduction of $O_2$ Electrocatalysed by Bilirubin Oxidase Confined in Ionic Liquids 142**

**6.1. Abstract ..... 143**

**6.2. Introduction ..... 144**

**6.3. Experimental ..... 145**

**6.4. Results and discussion ..... 146**

6.4.1. Potential Calibration with DmFc as Internal Reference in Ionic Liquids ..... 146

6.4.2. Enzyme Film Electrochemistry of BOD Confined in EMIMTFSI and PMPyrTFSI .. 146

**6.5. Conclusions and Perspectives ..... 164**

**7. Synaptic Enzymatic $H_2$-$O_2$ Fuel Cell Using an Ionic Liquid ..... 166**

**7.1. Abstract ..... 167**

**7.2. Introduction ..... 168**

**7.3. Experimental ..... 169**

7.3.1. Characterisation of anode and cathode in EMIMTFSI ..... 169

7.3.2. The Synaptic Fuel Cell (SFC) ..... 169

**7.4. Results ..... 173**

7.4.1. Characterisation of Cathode and Anode in EMIMTFSI ..... 174

7.4.2. Synaptic Fuel Cell Performance ..... 176

**7.5. Discussion ..... 187**

**7.6. Conclusions ..... 192**

**8. Reduction of $CO_2$ Electrocatalysed by Carbon Monoxide Dehydrogenase Confined in an Ionic Liquid ..... 193**

**8.1. Abstract ..... 194**

**8.2. Introduction ..... 195**

**8.3. Experimental ..... 197**

**8.4. Results and Discussion ..... 198**

**8.5. Conclusions ..... 206**

**9. Conclusions and Perspectives ..... 207**

**10. Appendices ..... 212**

**10.1. The Nernst Equation ..... 213**

**10.2. The Arrhenius Equation ..... 215**

# 1 Introduction

## 1.1 The Earth is Getting Warmer

One of the greatest challenges currently facing humanity is the increasing demand for energy, because of rapidly growing human population and rising economic expectations. Fossil fuels including coal, oil and natural gas are finite, it is clear that we must eventually have technologies to harness alternative sources of energy that are plentiful and, ideally, inexhaustible. The drive for research in this field has been boosted by the trend of global warming. The earth has risen between 0.4 and 0.8 ˚C over last century. This trend of global warming is primarily caused by increased volumes of carbon dioxide and other greenhouse gases released by the burning of fossil fuels [1]. In May 2016, at Mauna Loa Observatory, the atmospheric $CO_2$ levels reached 407 ppm, which is the highest value since record began, and the levels are increasing at a rate exceeding 2 ppm per year [2]. So exploiting carbon-neutral technologies is important for the wellbeing of the human society. This thesis is focusing on the application of enzymes that are inspirational and working catalysts for fuel cells and fixation of $CO_2$ in new electrolyte media, i.e. ionic liquids.

## 1.2 Hydrogen as an Energy Store

Hydrogen is widely recognized as a "fuel of the future", but more accurately, it is a form of stored energy and a transportable fuel. Hydrogen is the most abundant element in the universe and the tenth abundant element on earth. In both biology and technology, $H_2$ is a fuel[3]. Reaction of $H_2$ with $O_2$ (1.1) releases a large amount of energy, and most mixtures explode upon ignition.

$$2H_2(g) + O_2(g) \rightarrow 2H_2O(l) \qquad \Delta H^{o} = -286 \text{ kJ mol}^{-1} \quad (1.1)$$

In technology, one important advantage of $H_2$is its high specific enthalpy of reaction with $O_2$ ($\Delta H^o$ per gram), which makes it useful where weight is important, e.g. rocket propulsion. In both biology and technology, $H_2$ is the strongest reducing agent to be thermodynamically stable in aqueous solution, because its reduction product is water. But $H_2$ also has remarkable disadvantages. $H_2$ has low solubility in water, which limits its availability as an energy source in aqueous medium, although it can move rapidly to replenish areas where it has been depleted as a result of its large diffusion coefficient. Most importantly, $H_2$ is difficult to store due to its high volatility, which is a thorny issue to be solved before $H_2$ become a truly reliable source of energy.

Although reaction 1.1 occurs extremely rapidly by a radical chain mechanism, $H_2$ is quite inert and need a catalyst to be oxidized rapidly. To convert chemical energy of hydrogen into electric energy, we need a fuel cell (Figure 1.1).A fuel cell is an electrochemical device that converts chemical energy from fuels and oxidants into electric energy. The fuels that accept electrons at anodes can be $H_2$, methanol, ethanol, glucose etc. The oxidants such as $O_2$accept electrons at cathodes. The first hydrogen fuel cell was demonstrated by a lawyer and scientist William Grove in 1839 [4]. It was not until 1960s that NASA first used fuel cells commercially. There are environmental advantages of fuel cells making them competitive candidates for power sources for portable gadgets and local power generating systems needed for combined heat and power systems. First, unlike combustion engines that produce $NO_x$ at high temperatures, fuel cells avoid such emission because they can generate electricity at low temperatures through electrochemical processes. Second, fuel cells have higher efficiency (typically 50– 60 %) than internal combustion engines (20 – 25%) [5]. Third, fuel cells are quiet. Fourth, fuel cells are of simple design, which ensures the reliability and stability of the systems.

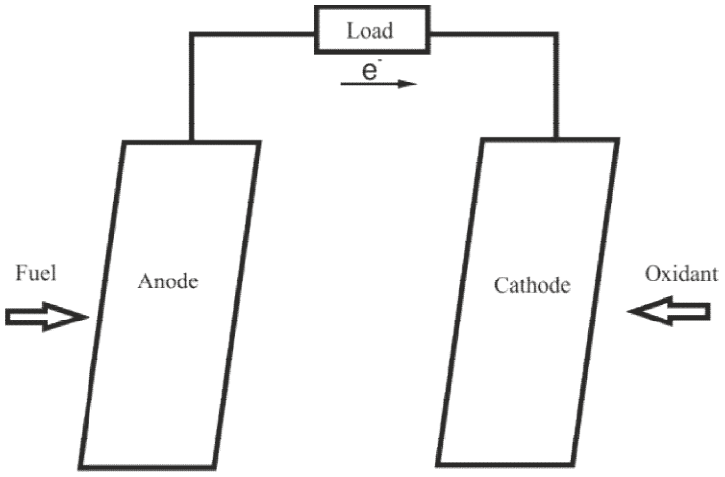



Figure 1.1 General scheme of a fuel cell. The fuel is oxidized at anode while the oxidant is reduced at cathode. The electrons are flowing from anode to cathode through the load.

Fuel cells vary greatly in their power output, ranging from large-scale (kW- MW) building-integrated systems, known as "combined heat and power" systems [4], to those that just provide enough power to operate electronics for special applications, e.g. an implantable glucose sensor for sensing and controlling glucose levels in the body [6]. Vehicles using fuel cells as power source were sold commercially recently. For example, the power of the fuel cell stack of Toyata FCV Mirai is 114 kW, and its power density is as high as 3.1 kW/L (2.2 times higher than that of the previous Toyota FCHV-adv limited-lease model), or 2.0 kW/kg [7].

.

## 1.3 Enzymatic Fuel Cells

To increase the power outputs of fuel cells, we have three main methods: to use electrocatalysts, to increase temperature, and to increase electrode area. Conventional fuel cells such as the polymer-electrolyte, direct methanol and solid-oxide systems

depend on noble metals such as Pt as electrocatalysts [4]. On the other hand, enzymatic fuel cells (EFC) use enzymes as electrocatalysts, either at both anode and cathode or just one of the electrodes. For conventional fuel cells using noble metal as electrocatalyst, ionic conductive membranes separating the fuel from oxidant are necessary. Otherwise, the net current will be zero because both the oxidizing and reducing reactions take place at the same electrode site. On the contrary, because enzymes are highly substrate-selective, EFCs can operate on a mixture of fuel and oxidant without costly membranes, which not only lower the cost but also make it possible to miniaturize the fuel cells to power up portable gadgets. Enzymes are highly active on a per mole basis. For example, blue copper oxidases have turnover frequency ($k_{cat}$) as high as 100 $s^{-1}$, and some hydrogenases have $k_{cat}$ values exceeding $10^4$ $s^{-1}$ [5].On the other hand, the equivalent turnover frequency of Pt is approximately 15 $s^{-1}$. Quite a few enzymes work very close to the thermodynamic potential of their substrate/product couple, i.e. catalysis is achieved at minimal overpotential. Examples include $H_2$ production and oxidation by many hydrogenases[5], $CO_2$/CO interconversion by carbon monoxide dehydrogenase [8]. In addition, enzymes are available from abundant raw materials and renewable. These advantages of enzymes as electrocatalysts attract intensive research on EFCs.

EFC research is currently at a “proof of concept” stage [5]. Their power densities reported of EFC are far from the target figures of ~ 100 mW $cm^{-2}$ [9]. Their stability is still too low for practical applications. These drawbacks of low power density and stability of EFCs are due to the following three disadvantages of enzymes as electrocatalyst. First, enzymes have bulky proteins surrounding their active sites(e.g. hydrogenases typically have molecular weights of around 50–100 kDa), and so whereas the activity of each molecule may be very high, their turnover per unit volume/footprint

on a surface may not be so remarkable[10]. As a result, considerable efforts are made to incorporate enzymes into three dimensional electrode structures in order to maximise current densities, which is crucial in enzymatic fuel cells. Second,enzymes havepoor and restricted temperature range. Once isolated, there is no mechanism for repairing enzymes, whereas in the living cell they may be continuously replaced according to needs. Short lifetime (a few hours) is an inherent characteristic of enzymes even in their natural environment,but lifetime may be increased to a few days by immobilization [11]. For certain classes of enzymes such as hydrogenases oxygen tolerance is sometimes very low. Laccases are inhibited by halide ions.Third, it's difficult to achieve good electronic coupling to the electrode in some situations. Moreover, time and cost of isolation and purification of enzymes are usually too high for them to be commercially competitive.

### 1.3.1 Characterisation of Enzymatic Fuel Cells

In this thesis, I characterised the performance of fuel cells by open circuit voltage and power curve in Chapter 7.

Open circuit voltage (OCV) is the voltage between the cathode and anode of a fuel cell at zero current, i.e. when the fuel cell is disconnected from any circuit. In an ideal situation, the OCV is determined by the difference between the thermodynamic potentials of the fuel/oxidized product redox couple and the oxidant/reduced product redox couple, adjusted for all the nonstandard conditions of fuel cell operation[4].

The measured OCV for a given fuel cell assembly is determined by the difference between the onset potential for catalysis at the respective electrodes [5].The OCV may

be decreased further by slow interfacial electron transfer as a result of poor electronic coupling of enzymes to the electrode or by use of electron-transfer mediators with potentials that are significantly more negative than the oxidant couple or more positive than the fuel couple. The OCV is measured by chronopotentiometry at zero current using a potentiostat in Chapter 7. The OCV of $H_2$-$O_2$ fuel cell in reversible condition is 1.23 V at 25 ˚C.

The power curve illustrates the relationship between power density and voltage of a fuel cell. Typical power curves of fuel cells are bell-shaped. Power curves can be measured by three methods when fuels and oxidants are supplied [12]:

a) Connect a series of resistors to the fuel cell and record the corresponding currents.

b) Apply chronoamperometry at various potentials and record the corresponding currents. Chronoamperometry rather than chronopotentiometry is chosen for EFC because enzymes such as hydrogenases can be switched off at certain potentials.

c) Apply linear scan voltammetry to the whole SFC starting from its OCV to 0 V at a low scan rate (≤1 mV/s).The low scan rate ensures that the fuel cell is at steady state. The third method was used in Chapter 7.

The highest fuel cell currents are usually attained at low cell voltages; however, an interesting exception was reported for fuel cells using hydrogenases that are reversibly inactivated at high potential. In detail, the fuel cell used [NiFe]-hydrogenases at anode and operated on a mixture of 3% $H_2$ in air. Its power drops sharply at cell voltages below about 500 mV, which is consistent with inactivation of [NiFe]-hydrogenases at high electrode potential in electrochemical experiments[13].

EFCs are generally aimed at the relatively low power outputs, i.e. in the range of micro to milliwatts. Although conventional fuel cells generally give kilowatt outputs, they operate at high temperatures and pressures, unlike EFCs, which operate close to ambient temperature and pressure. “Stacking” the individual cells, for both enzymatic and conventional fuel cells, can increase the power output.

The maximum (short-circuit)current attainable at either electrode of the EFC depends on the density of catalytic active sites (i.e. the electroactive coverage, which for bulky enzymes tends to be low) and rate of catalysis per active site, which is conversely high for enzymes. A monolayer of enzyme usually only contains a few picomoles of catalyst per square centimetre at most, which is too low for application target [6]. To improve the cell current, multilayers of enzyme can be applied to an electrode. The resulting “three-dimensional” electrode must ensure that mass transport of reactants and products is not impeded and all enzyme molecules are electronically well coupled to the electrode. Even so, the catalytic current of an EFC may still be not high enough for practical application.

### 1.3.2 The History of Enzymatic Fuel Cells

To the best of my knowledge, the first enzyme fuel cell dates back to 1964, when Yahiro et al. designed the cell featuring Pt foil electrodes immersed in phosphate buffer solutions in both anode and cathode compartments, which were separated by a membrane [14]. Glucose and glucose oxidase were placed in the anode solution and the cathode solution was either open to air or bubbled with $O_2$. The OCV of the fuel cell was in the range of 625 – 750 mV. The current density was 30 nA $cm^{-2}$ at 330 mV (in this thesis, all current densities refer to electrode area). The poor current and power

output may be caused by the absence of any mediator to transfer electron between glucose and the electrode, and that glucose oxidase may not function, as glucose is oxidized at Pt at high potential. In 1981, a methanol oxidizing fuel cell that used a bacterial methanol dehydrogenase in solution as the anode catalyst that catalyses the two-electron oxidation of methanol to formate and further to formaldehyde. Phenazine ethosulfate was mediating electron transfer from the enzyme to a Pt electrode. The fuel cell gave an OCV of 0.3 V, and a maximum current density of ~ 0.5 mA $cm^{-2}$ (based on anode surface area) [15]. Throughout the 1980s and 1990s, enzyme-based biosensors were simultaneously under intense investigation. Remarkably, a very successful amperometric glucose sensor using glucose oxidase with functionalized ferrocene as electron mediator was developed[16].

In 1999, a novel membranless fuel cell with immobilized enzymes as catalysts at both anode and cathode was reported [17, 18]. The cell incorporated flavin-containing glucose oxidase that catalysed the oxidation of glucose at the anode, and microperoxidase or cytochrome *c* oxidase that catalysed reduction ofperoxide or $O_2$, respectively. Since then, it was more widely recognized that enzymes allow a simple design of tiny fuel cell, without the necessity of expensive membranes separating the anode chamber from cathode chamber. With such designation, enzymatic fuel cells could cover a technological niche, e.g. as implantable power sources (operating in biological fluids) or ambient, self-powered sensors [5].

As mentioned above, major problems in enzymatic fuel cells include the short lifetime of the enzyme caused by a reduction in its stability when functioning in a foreign environment, and the low power densities caused by a low electron transfer rate from the enzyme active site to the electrode [11]. So the bulk of research in enzymatic

fuel cells has been focused on enzyme/electrode integration methods that alleviate theses problem since 2000. Remarkably, in 2003 Heller and co-workers reported a fuel cell using enzymes embedded into a conducting hydrogel polymer to which Os-complexes are attached as electron mediators. The membrane-less miniature glucose-$O_2$ biofuel cell comprised only of two enzyme-coated carbon fibers, each of 7 μm diameter and 2 cm length. The anodic enzymeis glucose oxidase electrically "wired" by the Os-polymer having a redox potential of –0.19 V vs Ag/AgCl. The cathodic enzyme is bilirubin oxidase "wired" by the Os-polymerhaving a redox potential of +0.36 V vs Ag/AgCl. Implantation of the fibers in the grape leads to an operating biofuel cell producing 2.4 μW at 0.52 V[19]. In 2005, using covalent attachment of the cofactor that reinserts into the apoenzyme, PQQ-dependent enzymes were electronically coupled to electrodes[20]. A similar concept was demonstrated for laccase successfully[21]. In the study, laccase was electronically coupled to the PGE electrode by substrate-like anthracene based units, providing a stable cathode that catalyses the four-electron reduction of $O_2$ to water for at least 30 min.

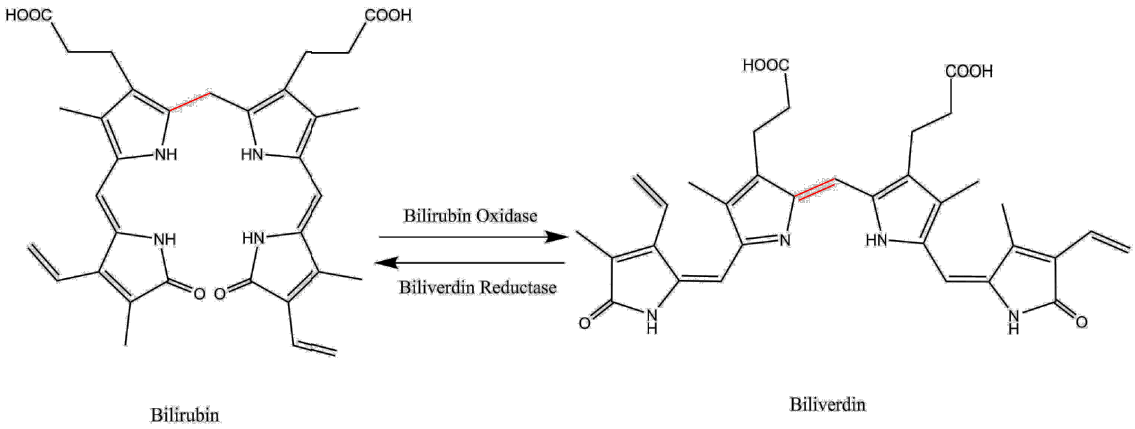
Further recent developments in EFCs have been highlighted by the application of high-surface area electrode materials such as carbon cloth, carbon fiber paper[22], carbon papers modified with Ketjen black carbon particles [23], carbon felt [24], carbon cloth [25, 26], mesoporous carbon[27], nanotubes [28-30]and graphene [31-33]. Moreover, enzymes have inspired development of new synthetic electrocatalysts for $O_2$ reduction [34, 35], and $H_2$ oxidation[5, 36].

### 1.3.3 Enzymes for Cathodes

#### 1.3.3.1 Reduction of Dioxygen

$O_2$ is the oxidant of choice for most EFCs, because it is freely available and has a high reduction potential (the standard electrode potential for four-electron reduction of $O_2$ at 25 °C is +1.23 V [37]), hence resulting in a high voltage output of the cell. Catalysis of the four-electron reduction of $O_2$ to $H_2O$ is sluggish at mild overpotentials, and the overpotential for this reaction determines the cell voltage of fuel cells [5]. For EFCs, the enzymes are typically multi-copper oxidases that catalyse the four-electron reduction of $O_2$ to $H_2O$ and have a high specificity towards this reaction [38]. Recent examples include laccases [21, 39] and bilirubin oxidase (BOD) [40]. Laccases are generally used in slightly acidic conditions without the presence of chlorides, while BOD functions from neutral to alkaline pH ranges. Cytochrome oxidase and cytochrome c have also been used. In this case, the potential of electrocatalysis of $O_2$ reduction is only 0.1 V, which is a serious disadvantage for fuel cells.

Bilirubin oxidase (BOD, EC 1.3.3.5—bilirubin: oxygen oxidoreductase) is a sub class of multicopper oxidase. BOD was first discovered in 1981 by Tanaka and Murao [41]. BOD is produced by a variety of organisms including fungi, bacteria and animals. BOD not only catalyses the oxidation of tetrapyrroles (e.g. bilirubin), diphenols and aryl amines, with $O_2$ as electron acceptor, but also catalyses the four-electron reduction of $O_2$ without producing any intermediates [38]. BOD was first used for detecting bilirubin in 1988, because it efficiently catalyses the oxidation of bilirubin to biliverdin [42]. The reaction is shown in Scheme 1.1.




Scheme 1.1 Interconversion between bilirubin and biliverdin. The red bond undergoes redox reaction.

In 2001, BOD was used for bioelectrocatalytic reduction of $O_2$ to water at neutral pH with 2,2′-azinobis (3-ethylbenzothiazolin-6-sulfonate) as an electron transfer mediator [43]. BOD is an efficient catalyst of 4-electron $O_2$ reduction at neutral pH with the presence of chloride. Hence BOD is an ideal candidate for catalysing reduction of $O_2$ at cathodes of enzymatic fuel cells in physiological conditions(20 mM phosphate buffer, pH 7.4, 0.14 M NaCl, 37˚C)[44, 45].

The complete structure of BOD from *Myrothecium verrucaria* has been solved [46]. BOD, as well as other multicopper oxidases including Spore Coat Protein A (CotA), ascorbate oxidase, CueO, laccase, ceruloplasmin, Fet3p and PcoA [47], are single-subunit proteins incorporating four Cu atoms in their active sites [46]. In the active site, there is a trinuclear Cu cluster formed by an apical Type 2 Cu and two Cu atoms that are known as Type 3 Cu pair, 1.2-1.3 nm from which lies the Type 1 Cu site (brown spheres in Figure 1.2). The Type 1 and Type 3 Cu atoms are linked by a short histidine-cysteine-histidine sequence that is conserved in multicopper oxidases and may

provide a fast electron-transfer pathway [48]. In more detail, the Type 1 Cu is coordinated by two histidines (H398 and H462 in Figure 1.2) and a cysteine (C457) that is adjacent to another histidine ligating one of the Type 3 Cu atoms. In addition, the Type 1 Cu has a weakly coordinated methionine (M467), which determines the reduction potential of the site [49]. Cu atoms of Type 2/Type 3 trinuclear cluster are coordinated by histidines and small O-ligands (red sphere in Figure 1.2) deriving from reduction of $O_2$ or exchange with solvent. In more detail, three histidines bound to each Type 3 Cu and two histidines bound to Type 2 Cu.

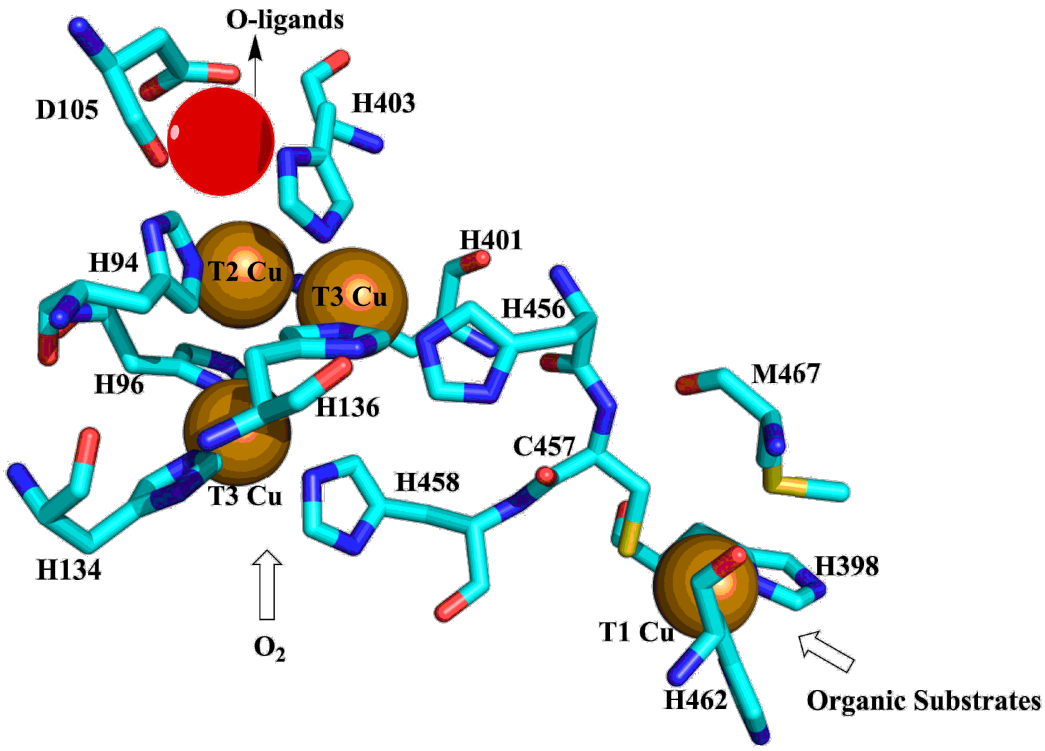



Figure 1.2 Structure of the copper binding sites of bilirubin oxidase from *Myrothecium verrucaria* (Protein Data Bank code: 2XLL, constructed using Pymol[50]).Brown spheres: Cu atoms.Red sphere: an oxygen species bound to the Type 2/Type 3 trinuclear

cluster. An aspartate (D105) is proposed to be the proton donor during the oxygen reduction reaction. All the amino acids shown are conserved identically in BOD, CotA, Fet3p, CueO, ceruloplasmin, ascorbate oxidase, tree laccase and PcoA. Adapted from reference[47].

#### 1.3.3.1.1 Mechanism of the Oxygen Reduction Reaction Catalysed by Bilirubin Oxidase

The four-electron electroreduction of oxygen to water has been studied extensively (eq. 1.2):

$$O_2 + 4\,H^+ + 4\,e^- \rightarrow 2H_2O \qquad (1.2)$$

This is the fundamental reaction of most fuel cell cathodes and of electrochemical oxygen sensors.

In $O_2$ reduction catalysed by BOD, the Type 1 Cu binds the organic substrates of BOD. The Type 2/Type 3 trinuclear cluster binds $O_2$ [51-53]. The Type 1 Cu first accepts electrons. Type 1 Cu is also proposed to be the entry site for electrons from electrodes in enzyme film electrochemistry [18]. Then the electrons transferred, one at a time, to Type2/Type 3 trinuclear cluster, where $O_2$ is reduced to $H_2O$. The first step is rate-determining and driven by the presence of an anionic Asp residue near the Type 2 Cu. The second step has a low energy barrier, reflecting the large driving force for two electron reduction of peroxidecombined with the triangular topology of the Type 2/Type 3 trinuclear cluster[54].Thereductionpotential$E°'_{T1}$of the Type 1 Cu of BOD from *M. verrucaria* is +670 mV vs. the standard hydrogen electrode (SHE) at pH 7.0, according to the most recent report by Christenson et al.[55].Experiments in which

the reduction potential of the Type 1 Cu centre was made more negative by altering the coordination site using site-directed mutagenesis indicate that $E^{\circ\prime}_{T1}$ is highly influential in determining the potential at which electrocatalysis commences[52, 56]. Detailed spectroscopic studies of the catalytic mechanism by Solomon and co-workers have identified two highly active intermediates that are produced as follows: (a) $O_2$ reacts with the fully-reduced enzyme with a rate constant about $2 \times 10\ \ M^{-1}\ \ s^{-1}$ to produce a 'peroxy-intermediate' (PI), in which the $O_2$ molecule has been reduced by two electrons and an O–O bond remains; (b) PI reacts rapidly to generate the 'native intermediate' (NI) in which all four Cu atoms are in the 2+ state and the elements of the original $O_2$ remain in the Type 2/Type 3 site as bridging oxo and hydroxo ligands; (c) NI reacts rapidly to produce the fully reduced state by fast transfer of four electrons and four protons, releasing two $H_2O$. Since both the oxygenated states PI and NI are highly reactive and probably strongly oxidizing, it is difficult for them to be 'titrated' in an equilibrium reaction. On the contrary, a resting, fully oxidized state was also reported, which has a hydroxide bridging the Type 3 Cu pair. The resting state is produced from NI slowly, with a rate constant of 0.034 $s^{-1}$. This state accepts four electrons slowly to give the fully reduced enzyme (Figure 1.3) [54].

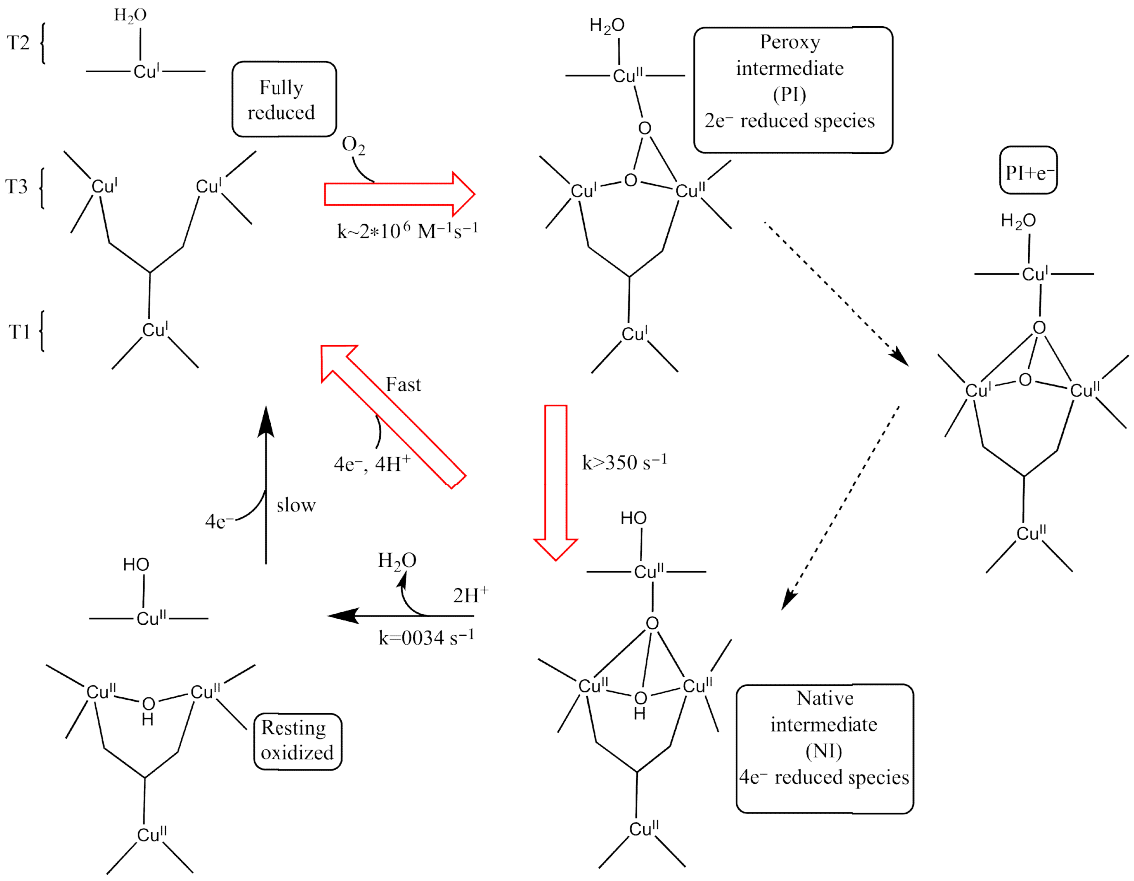



Figure 1.3 Mechanism of $O_2$ reduction to water by bilirubin oxidase (BOD). Red arrows indicate the steps of the catalytic cycle of BOD. Black arrows indicate steps that can be experimentally observed but are not part of the catalytic cycle. The dashed arrows at the right indicate the transfer of an electron from the T1 Cu to the T2 Cu to create PI + $e^-$, that occurs in going from PI to NI but is not experimentally observed in the wild type enzyme. Adapted from reference[54].

#### 1.3.3.1.2 Catalytic Activity Comparison of Bilirubin Oxidase with Pt

The oxygen reduction reaction (ORR) shown in eq. 1.2 requires addition of catalysts, such as platinum, to increase electrode kinetics in traditional fuel cell cathodes. For

more than a century, the reference catalyst of the reaction has been Pt in 0.5 M $H_2SO_4$. Such catalysts are, however, non-selective, and reportedly less efficient, compared to enzyme catalysts [40,47].

Mano et al. established that a film of BOD that was electrically connected ("wired") to the vitreous carbon electrode by a redox polymer is superior to Pt [40]. Comparison of the overpotential of the polished platinum cathode in 0.5 M $H_2SO_4$ with that of a polished vitreous carbon cathode modified with a film of bilirubin oxidase (BOD), which was electrically connected ("wired") to the electrode by a redox polymer, showed that the overpotential of the "wired" BOD cathode was much lower than that of the Pt cathode. The "wired" BOD cathode operated in a physiological pH 7.2 (20 mM phosphate,0.15 M NaCl) buffer solution (PBS), where the Pt cathode would have rapidly corroded. Because the solubility and diffusivity of $O_2$in PBS at 37 °C are higher than in 0.5 M $H_2SO_4$, the absolute current densities of the "wired" enzyme electrode were much higher than those of platinum at any overpotential. For example, at1 atm $O_2$ pressure, $O_2$ was electroreduced to water at a current density of 9.5 mA $cm^{-2}$ at an overpotential of −0.31 V on the "wired" BOD cathode. At this overpotential, the current density of the polished platinum cathode in 0.5 M $H_2SO_4$ was 16-fold lower, only 0.6 mA $cm^{-2}$.Current density as high as 50 mA $cm^{-2}$ can be attained by the application of rotating porous "wired" BOD cathodes, whose area could be at least 5-fold larger than that of smooth electrodes. Even higher current densities are likely to be achieved with air-diffusing cathodes of the type applied in fuel cells, in which Pt-loaded carbon particle cathodes reach 1 A $cm^{-2}$ at the highest. The authors also suggested that these BOD cathodes should be made at a cost low enough to be discarded after their shorter functional life (ca. a few weeks).

A more recent study comparing the activity of BOD to that of Pt was reported by Armstrong and co-workers [47]. The experiment involved a BOD film adsorbed on Pt (111) that showed an important pre-wave to electrocatalysis by Pt surface atom. This substantiates that the minimum overpotential required for ORR electrocatalysed by BOD is appreciably smaller than required for Pt, in a single experiment. The potential of ORR electrocatalysed by BOD was only 0.14 V more negative than the reversible value of 1.23 V at pH 8, 25 ˚C.

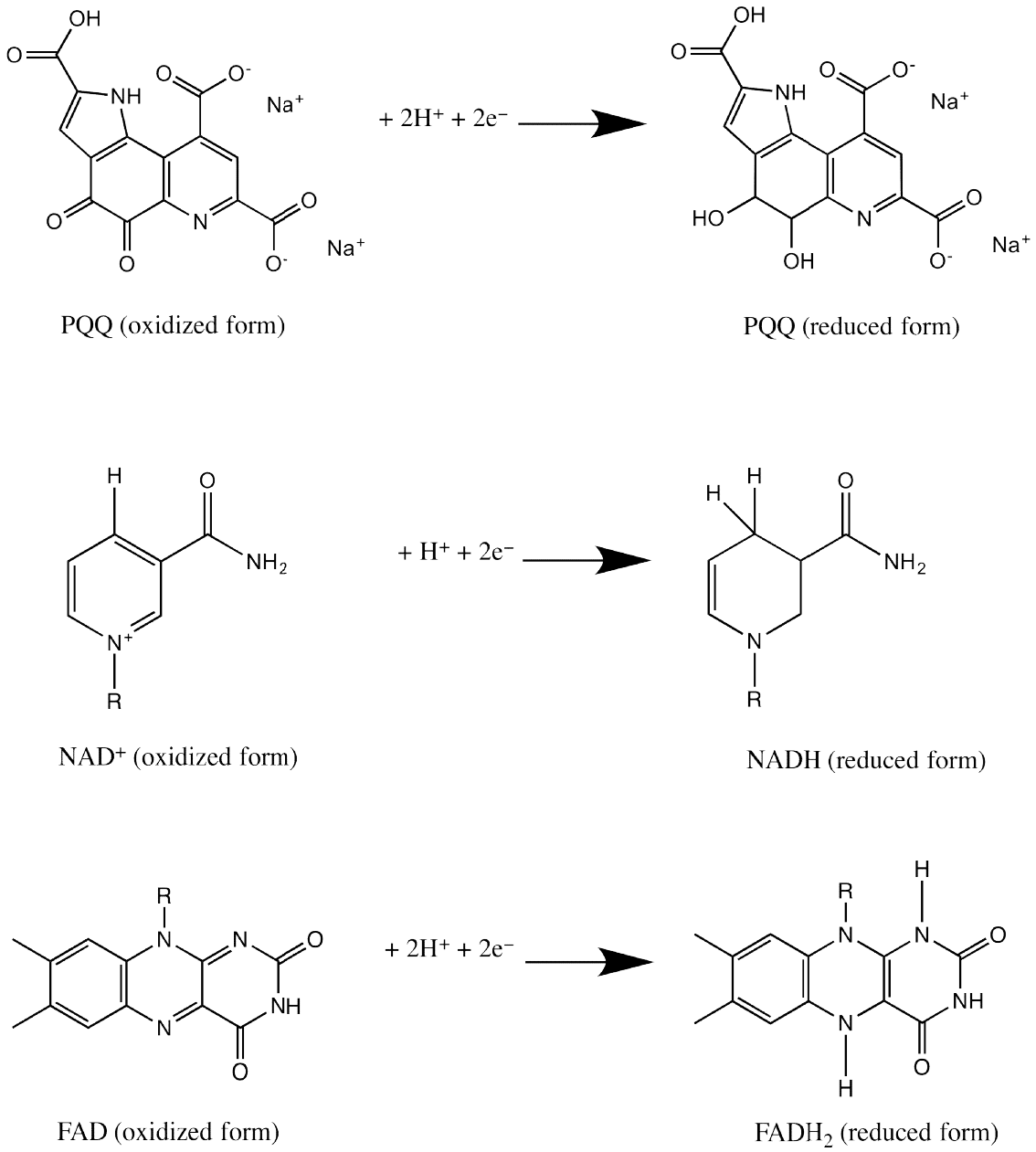
#### 1.3.3.2 Reduction of Hydrogen Peroxide

Hydrogen peroxide is a stronger oxidant than $O_2$. The standard electrode potential for the one-electron reduction of hydrogen peroxide is as high as + 1.76 V at 25 °C [37], hence maximising the fuel cell voltage. Microperoxidase, a highly truncated form of mitochondrial cytochrome c which retain the heme group and some surrounding amino acids [18], horseradish peroxidase which is commercially available [57], and cytochrome *c* peroxidase [58] are commonly used for EFCs. However, cytochrome *c* peroxidase has not achieved a stable electrochemistry, meaning that this enzyme is a poor electrocatalyst for EFCs. The fuel cell using microperoxidase-11 and glucose oxidase as cathode and anode electrocatalyst respectively produced an OCV of ca. 1 V and a short-circuit current density of ca. 830 μA $cm^{-2}$. The maximum electrical power, extracted from the cell is 520 μW at an external optimal load of 0.4 kΩ [18].The OCV of the cell using glucose oxidase and horseradish peroxidase was 0.22 V, which is too low to be useful, and the power output of the cell was 0.15 μW $cm^{-2}$at 0.021 V. The biofuel cell proved to be stable for an extended period of continuous work (30 days)[57].

## 1.3.4 Enzymes for Anodes

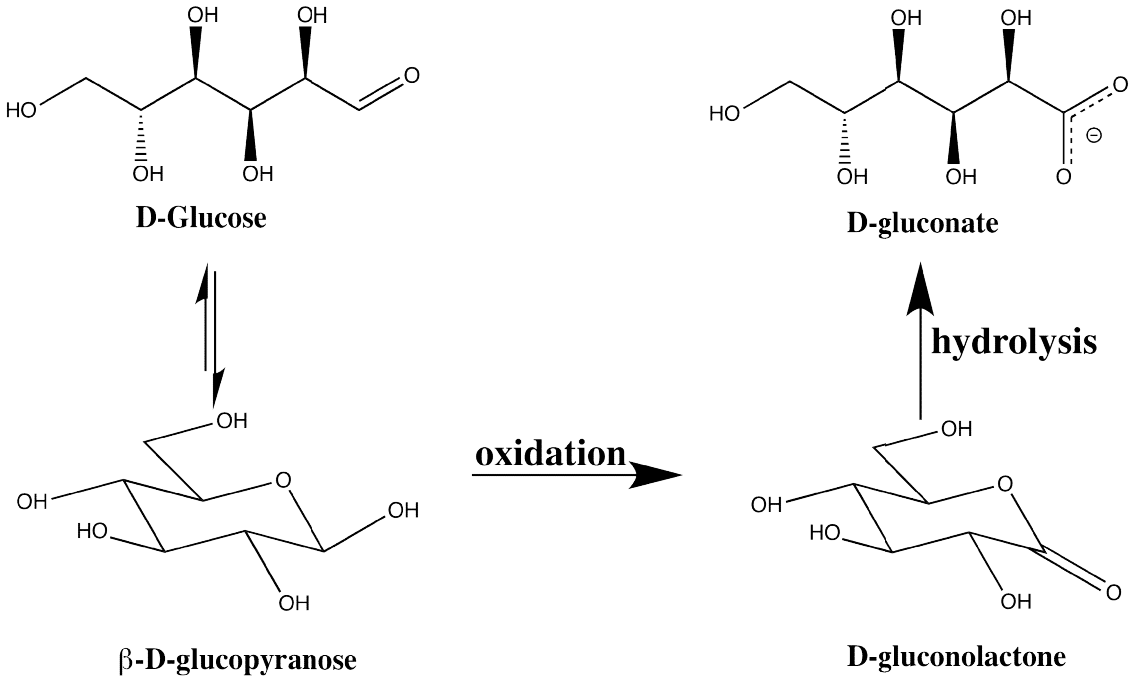
### 1.3.4.1 Oxidation of Sugars and Alcohols

Most fuels in EFCs are either saccharides, e.g. glucose, lactose, fructose and cellobiose, or alcohols such as ethanol and glycerol. Enzymes used as anode electrocatalysts in theses fuel cells can be categorised into three groups by the type of electrical communication or their associated redox cofactors [45, 59]. The first class includes pyrroloquinoline quinone (PQQ)-dependent dehyrogenases, e.g. alcohol dehydrogenase (AlcDH), glucose dehydrogenase and glycerol dehydrogenase, most of which have multiple metal centers and coenzyme PQQ is bound to the enzymes. The second class consists of enzymes with a nicotinamide adenine dinucleotide ($NADH/NAD^+$) or nicotinamide adenine dinucleotide phosphate ($NADPH/NADP^+$) cofactor, e.g. AlcDH and glucose dehydrogenase. These cofactors are redox centers that bound loosely to the enzymes and can act as diffusing charge carriers of electrons, shuttling between different oxidoreductases (able to catalyse oxidation and reduction reactions) in biology, e.g. between different dehydrogenases and reductases. To apply the second class of enzymes in EFCs that function over extended periods, loss of $NADH/NAD^+$ or $NADPH/NADP^+$ should be prevented by covalent attachment of these cofactors to the apoenzymes via a flexible chain. This chain should be long enough for the back-and-forth movement of the cofactors from their site in the apoenzymes to the electrode surface. The third class comprises enzymes that have a tightly bound flavin adenine dinucleotide (FAD) redox cofactor. The FAD cofactor is usually buried deep inside the protein, so the extraction of electrons from this class of enzymes is often difficult. The most commonly used enzyme in the third class is glucose oxidase (GOx). The structures and redox reactions of the cofactors mentioned above are shown in Scheme 1.2.




Scheme 1.2 Structures of cofactors and their redox reactions. R links adenosine diphosphate via ribitol to the flavin (in FAD/$FADH_2$) or nicotinamide (in $NAD^+$/NADH).

Most EFCs use glucose-oxidizing enzymes that target the C1 hydroxyl group of β-D-glucopyranose (Scheme 1.3). Scheme 1 shows the oxidation reaction of glucose at fuel cell anodes.




Scheme 1.3 Oxidation of D-Glucose

Some EFCs using glucose [22, 60, 61] or glycerol [62]as fuels have achieved power densities above 1 mW $cm^{-2}$, which is sufficient to power practical electronics. In 2011, Zebda and co-workers reported a mediatorless glucose/$O_2$ enzymatic fuel cell using carbon nanotubes disks compressed with GOx and laccase as anode and cathode respectively. The EFC gave a power density up to 1.3 mW $cm^{-2}$ and an OCV of 0.95 V. Moreover, the EFC remains stable for 1 month and delivers 1 mW $cm^{-2}$power density under physiological conditions ($5\times10^{-3}$M glucose, pH 7) [61]. In 2013, a glucose/$O_2$ enzymatic fuel cell delivering an OCV of 0.76 V and a maximum power density of

maximum power output of 1.54 mW $cm^{-2}$, 1.92 mW $mL^{-1}$ and 2.67mW $g^{-1}$ was reported by the same group[60]. This is the highest power density of EFC reported to date, to my best knowledge. In detail, this EFC incorporated carbon nanotube-based 3D bioelectrodes and used naphthoquinone-mediated oxidation of glucose by GOx and direct $O_2$ reduction by laccase. The EFC constantly deliver 0.56 mWh $cm^{-2}$ under discharge at 0.5 V, showing among the best in vitro performances for a glucose/$O_2$ enzymatic fuel cells. Using a charge pump, the EFC finally powered a Light Emitting Diode (LED).

Glycerol is a fuel of choice because of its abundance and high energy density. Glycerol is a by-product of the production of biodiesel. The energy density of glycerol is 6.260 kWh $L^{-1}$(pure liquid), higher than ethanol (5.442 kWh $L^{-1}$ pure liquid), methanol (4.047 kWh $L^{-1}$ pure liquid), or glucose (4.125 kWh $L^{-1}$ saturated solution)[63]. Glycerol was first applied to EFCs by Minteer and co-workers in 2007 [63]. The Glycerol/$O_2$ fuel cell gave a power density up to 1.21 mW $cm^{-2}$. The anode catalysts of PQQ-alcohol dehydrogenase and PQQ-aldehyde dehydrogenase immobilized in a Nafion membrane modified with trimethyloctylammonium bromide at carbon paper/Pt cathode. This cell was further improved by adding a third anode enzyme, oxalate oxidase, which allowed the complete oxidation of glycerol and increased the maximum power density to 1.32 mW $cm^{-2}$ [62].

#### 1.3.4.2 Oxidation of $H_2$

Hydrogenases catalyse the fast interconversion between $H_2$ and protons [64]. Hydrogenases use metal carbonyl active sites that are unique in biology. Hydrogenases are categorized into three classes: [FeFe]-, [NiFe]- and [Fe]-hydrogenases according to

the metal composition of their active sites. [FeFe]-hydrogenases are mainly $H_2$-producers. [NiFe]-hydrogenases are mainly $H_2$-oxidizers, which are under intense investigation as anode catalyst in fuel cells. [FeFe] hydrogenases show the highest turnover rates but are notoriously oxygen sensitive, being irreversibly damaged by exposure to even traces of dissolved $O_2$ [65, 66]. In contrast, most [NiFe] hydrogenases are reversibly inactivated by exposure to $O_2$ and are usually able to be reactivated under $H_2$. So [NiFe] hydrogenases are termed as $O_2$ tolerant hydrogenases and regarded as candidates for special technological applications (e.g. fuel cells).[Fe]-hydrogenases are only found in methanogens, whose active site is a mononuclear iron-carbonyl center. At this center, $H_2$ is split to release a proton and hydride. The hydride is then transferred to the hydride carrier, $N^5$,$N^{10}$-methenyltetrahydromethanopterin [67].

#### 1.3.4.3 Electron Relay Centers of Hydrogenases

The protein environment of enzymes is more than just a protecting scaffold for the sensitive and fragile catalytic centers. In the protein environment of both [NiFe]- and [FeFe]-hydrogenases, Fe-S clusters function as electron relay centers to connect the buried active sites to the protein surface. And in both classes of hydrogenases the Fe-S clusters are typically positioned 12 – 14 Å. This type of spacing may allow electron transfer to be sufficiently fast as to not limit the catalytic rate of the enzyme [68].

Different classes of hydrogenases incorporate different combinations of Fe-S clusters. This may have important implications for catalytic activity and bias. The [FeFe]-hydrogenases have a [4Fe-4S] cluster bound directly to the [FeFe] active site via a bridging cysteine ligand. The [4Fe-4S] cluster not only shortens the path for long-range electron transfer, but also contributes to the electronic and catalytic properties of the

enzyme as an integral part of the active site. The [NiFe]-hydrogenases from *D. gigas* and *D.fructosovorans* each include two [4Fe-4S] clusters and one [3Fe-4S] cluster. The [NiFeSe]-hydrogenase from *Desulfomicrobium bactulatum* incorporates three [4Fe-4S] clusters [69]. For [NiFe]- and [NiFeSe]-hydrogenases, a histidine ligand is present at the distal [4Fe-4S] cluster, rather than a cysteine at one Fe subsite. The unusual substitution of cysteine with histidine at the distal [4Fe-4S] cluster, which is the electron entry/exit site, confers the ability for fast interfacial electron transfer in either direction. Consequently, histidine is also essential for intermolecular electron transfer in homogeneous kinetic measurements and probably in physiological function as well. This effect results from an inherent change in kinetic ability rather than any change in reduction potential. Histidine ligation was proposed to lower the reorganization energy as well as provide greater electron coupling to the protein surface [70].

#### 1.3.4.4 Gas Channelsof Hydrogenases

Hydrophobic channels large enough to allow access for gas molecules have been identified in a [NiFe]-hydrogenase from *D.fructosovorans* by the trapping of Xe atoms within the protein at high Xe pressures according to X-ray crystallography [71]. Gas channels may also exist in [FeFe]-hydrogenases based on modelling of gas access within [FeFe]-hydrogenases from *D. desulfuricans* [72] and *C. pasteurianum* [73]. Although $H_2$ easily enters the protein, certain gas channels are preferential, based on molecular dynamics simulations that show that $H_2$ accesses the active site via these gas channels to the active site on the time scale of 9 ns [74]. In [NiFe]-hydrogenase with $H_2$-sensing and gene regulation roles, it has been hypothesized that bulky isoleucine and phenylalanine residues gate the end of a channel close to the Ni atom and hinder access

of larger neutral molecules (e.g. $O_2$, CO, or $H_2S$) to the active site. This hypothesis is supported by experiments on the $O_2$-tolerant regulatory hydrogenases from *R. eutropha* H16 or *Rhodobacter capsulatus*in which substitution of these amino acids by less bulky valine and leucine residues causes $O_2$ sensitivity [75, 76].

#### 1.3.4.5 Hydrogenase 1 from *Escherichia coli* (Hyd1)

Oxygen-tolerant membrane-bound hydrogenases (MBHs) from *Ralstonia* species, *Aquifex aeolicus* and *Escherichia coli* have been extensively studied by protein film electrochemistry (PFE), crystallography and spectroscopy, which give us a considerable body of mechanistic detail. In this thesis, I used hydrogenase 1 from *Escherichia coli* (Hyd1), which is a [NiFe] membrane-bound hydrogenase that can catalyse the $H_2$ oxidation in aerobic conditions [77]. Hyd1 is an excellent subject for experiments because it is easily produced in good yield and is very amenable to engineering by site-directed mutagenesis [78]. Hence Hyd1 has been under extensive investigation for application as anodic electrocatalyst in $H_2$-$O_2$ enzymatic fuel cells since 2010 [27, 30, 79].

The crystal structure of Hyd1 was solved recently (Figure 1.4) [80]. Hyd1 is a dimer of heterodimers, like other [NiFe] membrane-bound hydrogenases. Each monomer incorporates a hydrophobic membrane-anchoring small subunit C-terminal domain and its bound His tag. The larger subunit of the heterodimer contains the [$(Cys–S)_2$–Ni–($\mu^2$-Cys–S)$_2$–Fe(CO)$(CN)_2$] core of the active site (Figure 1.5).The smaller subunit contains three Fe–S clusters for electron transport to and from the active site: the proximal [4Fe-3S], medial [3Fe-4S] and distal [4Fe-4S] clusters. The dimer of heterodimers is isostructural with that reported by Shomura et al. [81], substantiating

that this oligomeric arrangement is physiologically relevant. The proximity of the two distal clusters in these two dimeric enzymes suggests that intermonomer electron transfer could play a role in $O_2$ tolerance. This proposition was supported by two studies: (i) hydrogenase fuel cell inactivated by a low-load/short-circuit is restarted using a second anode loaded with active hydrogenase [79]; (ii) monomeric form of Hyd-1 is much more sensitive to $O_2$ than native dimer [82]. The proximal [4Fe-3S] cluster can provide two successive electrons to the active site in the attack by $O_2$.

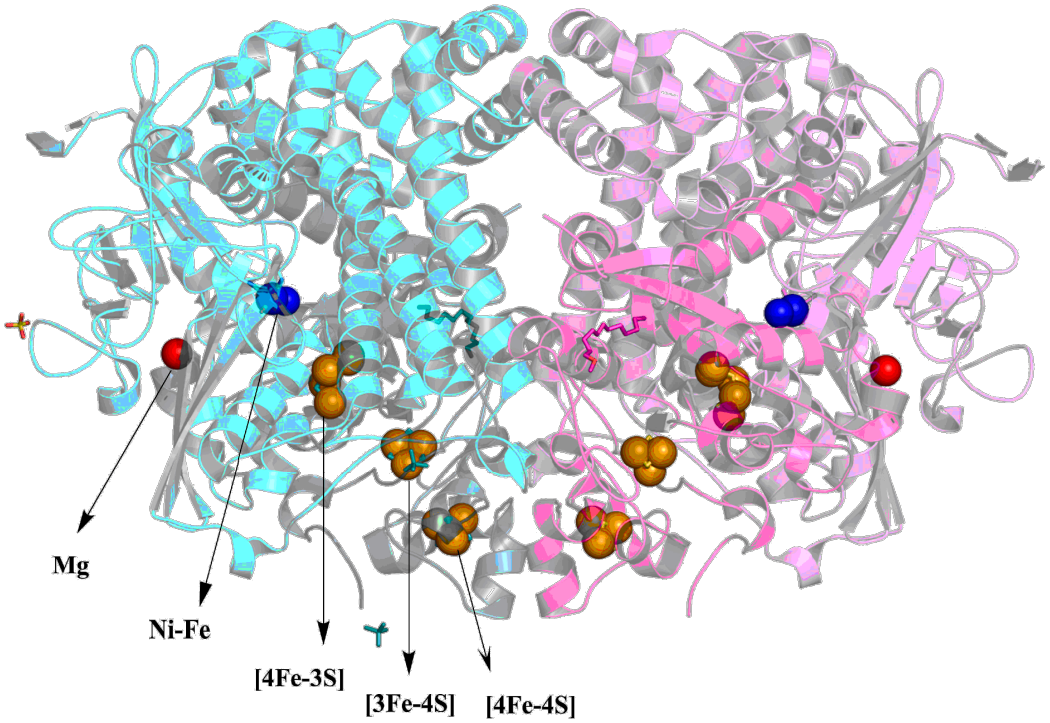



Figure 1.4 Crystal structure of hydrogenase 1 from *Escherichia coli*(PDB code 3USC[83],constructed using Pymol[50]).The redox centres in one half of the molecule (a dimer of heterodimers) are labelled. The identical subunits are in cyan and magenta.

The iron-sulfur clusters are in orange. The Ni-Fe active sites are in blue. The Mg ion is in red.

The [Ni-Fe]-hydrogenase active site includes a bimetallic center in which the Fe appears to remain as +2 while the Ni accesses oxidation states +1, +2 and +3 (Figure 1.5). The metal atoms are anchored by four cysteines, two bridging the Fe and Ni and two bound terminally to the Ni. The Fe is further coordinated by one CO and two $CN^-$. The canopy above the space contains a strictly conserved pendant arginine, and two strictly/highly conserved aspartates. Recent studies on the protein environment surrounding the active site have led to a new proposal for the $H_2$ activation mechanism involving arginine as catalytic base [84]. Combined with the [NiFe] bridging hydride (X in Figure 1.5), expected to be present in reduced states of the enzyme [85], Hyd-1 can provide four electrons to reduce molecular oxygen to $H_2O$ and $OH^-$. This process bypasses the formation of either a stable (hydro) peroxide ligand or reactive oxygen species, or both, that may inflict serious or even irreversible damage to the active site of $O_2$-sensitive [NiFe]-hydrogenase.

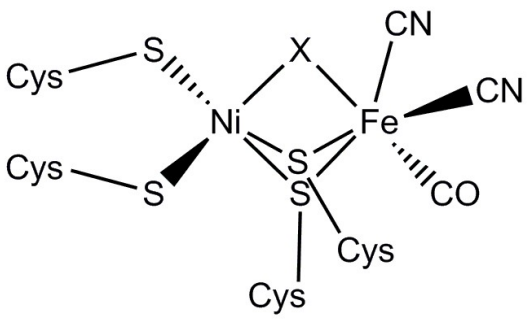



Figure 1.5 A representation of the [NiFe]-hydrogenase active site. The bridging ligand `X' can have a number of identities.

### 1.3.4.6 Reaction Mechanism of [NiFe]-Hydrogenases

The exact mechanism for the interconversion of $H_2$ and H by [NiFe]-hydrogenases has been debated, but it is widely agreed that Ni-SIa, Ni-C and Ni-R are all involved in $H_2$cycling. One possible mechanism proposed by Siegbahn et al. is represented in Figure 1.6[86]. This mechanism proceeds via $H_2$ binding to the Fe atom whilst the active site is in the Ni and Ni-SIa state. Prior to the binding of $H_2$, this state does not contain a ligand in the bridging position between Ni and Fe (Figure 1.5), so it is believed that it is this state that binds $H_2$ during $H_2$ oxidation. However, it is not yet confirmed whether $H_2$ binds to the Ni or the Fe atom. Density Functional Theory (DFT) studies have suggested that $H_2$ may bind to both metal atoms [87]. Some data indicate that the $H_2$ binding site may be at the Ni atom: (i) Hydrophobic gas channel that links the active site to the protein surface ends at the Ni atom[74, 88]; (ii) CO, which acts as a competitive inhibitor to $H_2$ oxidation, binds at the Ni [89]. However, the small distance between the Ni and Fe atoms means that the position of the gas channel may not accurately predict the binding position of $H_2$. The vacant binding site and the unusual choice of ligands at the Fe, which maintains a low spin electron configuration ideal for binding $H_2$, [86] may suggest that it is the Fe atom at which $H_2$ binds.

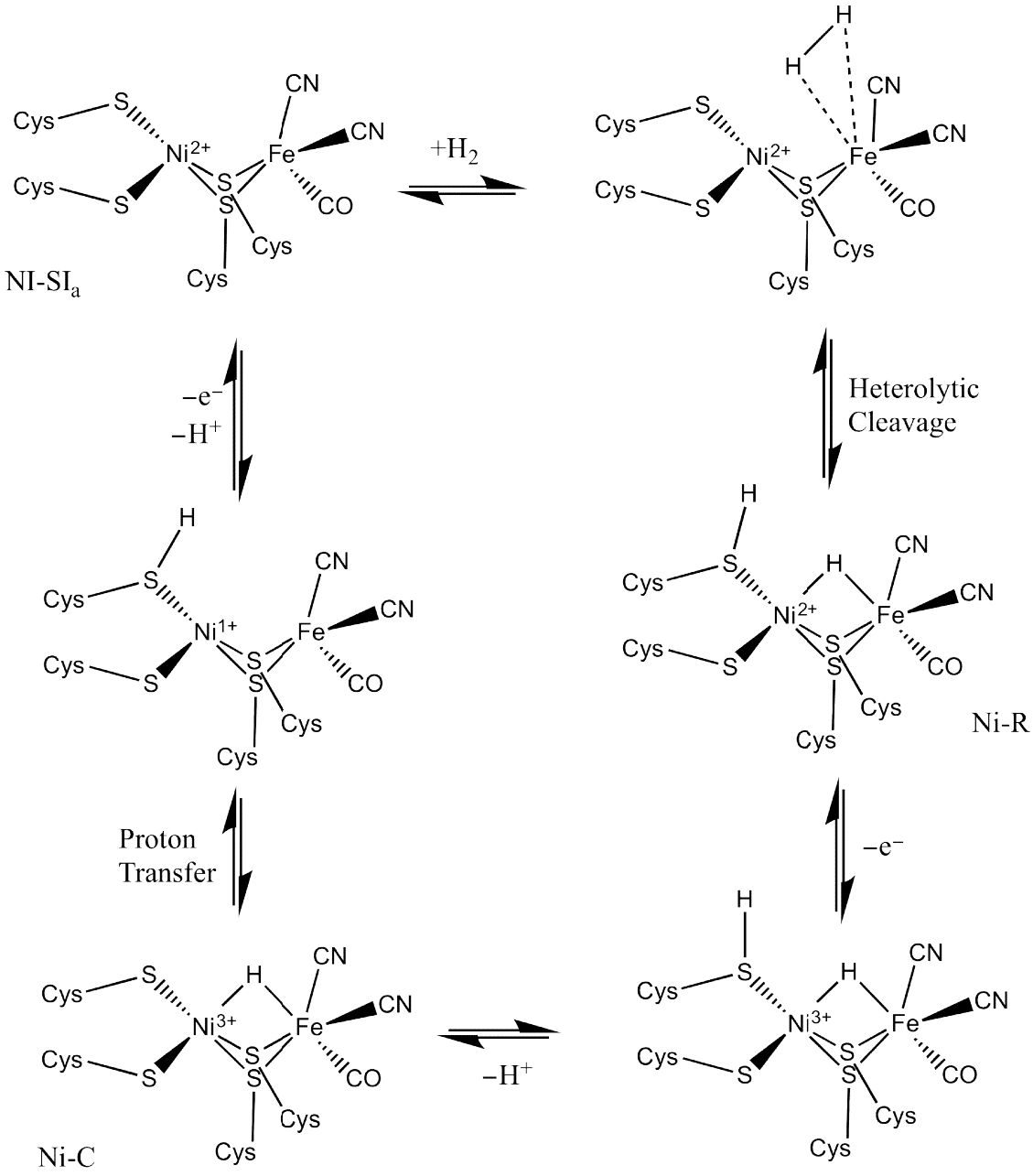



Figure 1.6 A proposed mechanism for $H_2$ cycling by [NiFe]-hydrogenases, adapted from reference [86]. Previously characterised catalytic intermediates are labelled with their EPR spectroscopic signatures.

Whether $H_2$ binds to the Fe or the Ni atom, the next step most likely involves heterolytic cleavage of the $H_2$ resulting in a hydride which bridges the Ni and the Fe atoms (in position `X' in Figure 1.5) [86]. A nearby basic residue, such as one of the

terminal or bridging cysteine residues, or another nearby residue, may assist the cleavage of $H_2$ resulting in the protonation of the residue. This results in the formation of the $Ni^{2+}$ Ni-R state. Oxidation of the Ni atom, forming $Ni^{3+}$, and removal of a proton via a proton transfer pathway, then generates the Ni-C state. A redox reaction then follows in which the bridging hydride is lost resulting in the $Ni^{3+}$ being reduced to $Ni^{1+}$ and a proton being transferred to one of the cysteine ligands. The Ni-SIa state can now be regenerated via oxidation of $Ni^{1+}$ to $Ni^{2+}$ and loss of a proton.

### 1.3.4.7 Complexity of [NiFe]-Hyrogenase States

During the catalytic reaction process, the $Fe^{2+}$ in the active site does not change the oxidation state the Ni accesses oxidation states +1, +2 and +3. The most oxidized states Ni-A or "unready" and Ni-B or "Ready" (both Ni ) are paramagnetic (S=1/2) and distinguished by their g-values (EPR) and reductive re-activation kinetics. The Ni-A species is slow to activate, requiring elevated temperatures and a long reductive treatment, whereas the Ni-B state reactivates rapidly under reducing conditions. In the Ni-A state, the bridging position has been discussed to be a peroxide species. In the Ni-B state, a hydroxide ($OH^-$) is bridging the Ni and Fe atoms. One-electron reduction of the fully oxidized Ni-A and Ni-B states gives the EPR-silent Ni-SU and Ni-SIr states (both $Ni^{2+}$), respectively. The bridging ligand may be still retained. Removing the bridging ligands can reactivate the inactive states. In fact, Ni-SIr state is activated by releasing the bridging ligand as a water molecule and generating the EPR-silent active Ni-SIa state ($Ni^{2+}$). Ni-SIa state can be inhibited by CO, forming the EPR-silent Ni-SCO state. The Ni-SCO converts back to the Ni-SIa state upon illumination at cryogenic temperature. One electron reduction of the Ni-SIa state rapidly generates the paramagnetic Ni-C state ($Ni^{3+}$, S=1/2). In this state a hydride ($H^-$) forms a bridge

between Ni and Fe atoms. The Ni-C state is light sensitive and it reversibly converts to the paramagnetic Ni-L ($Ni^+$) state upon illumination with white light at cryogenic temperature. Ni-L state can be inhibited by CO, giving the EPR-detectable Ni-SCO state ($Ni^+$). Ni-R is produced by one-electron reduction of Ni-C. Three different Ni-R states have been detected by FTIR spectroscopy and are pH dependent. Figure 1.7 shows the possible structures of Ni-R state with hydrogen and hydride bound to Ni. Release of hydride and an electron from Ni-R'' produces Ni-C. A direct conversion from Ni-R'' or Ni-R' to Ni-SIa is also possible, involving another proton [88].

In protein film voltammetry, both oxidized and reduced forms of a redox couple can exist simultaneously in the cell solution. The thermodynamic bias provided by the electrode potential and the kinetic bias of the enzymes control the rate of reaction in either direction [64].

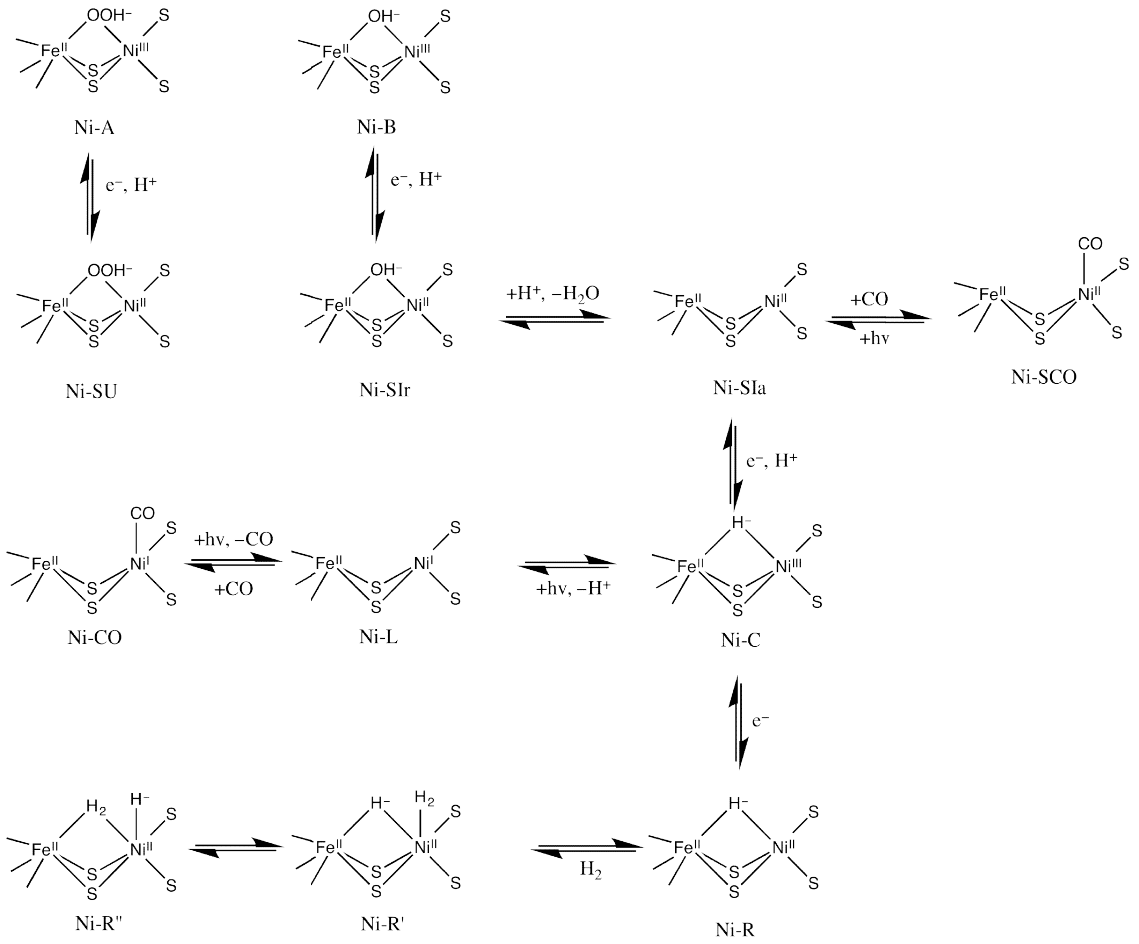



Figure 1.7 Different states of [NiFe]-hydrogenases. Adapted from ref [88].

### 1.3.4.8 Activity Comparison of Hydrogenases with Precious Metals

Hydrogen oxidation reaction (HOR) involves the activation of $H_2$ on precious metal (M) surfaces that takes place by homolytic cleavage of the H– H bond and formation of neighbouring M – H bonds [90]. Pt catalysts for both anode and cathode electrodes of proton exchange membrane (PEM) fuel cells usually function in a humidified gaseous environment rather than in aqueous solution, at ~ 100 ˚C [91]. On the contrary, hydrogenases operate in ambient aqueous solutions and are consequently limited by the solubility of $H_2$ in water (ca. 1 mM).

A study to compare the hydrogen oxidation activities of a [NiFe]-hydrogenase and a Pt electrode under ambient conditions was reported by Armstrong and co-workers in 2002 [92]. This study compares the limiting currents of a high-coverage film of *A. vinosum* [NiFe]-MBH on a pyrolytic graphite edge (PGE) electrode and a Pt electrode prepared by treating either the same PGE electrode or a gold electrode of the same size, with $H_2PtCl_6$. The limiting currents were of the same magnitude and diffusion-controlled up to 2500 RPM in all instances. For example, at 2500 RPM, the limiting catalytic current densities of $H_2$ oxidation at *A. vinosum* [NiFe]-MBH on a pyrolytic graphite edge (PGE) electrode and Pt on graphite were both ca. 3.6 mA $cm^{-2}$.The principal difference was that raising the $H_2$ level caused the hydrogenase electrode to require a larger overpotential than Pt electrode to achieve the limiting current. The reason is: the active site of the hydrogenase is very active, but its maximum turnover frequency is eventually limited by the rate of interfacial electron transfer (section 3.1). Obtaining the highest current needs contributions from enzyme molecules that not well linked to the electrode, and thus, an increasingly higher driving force is essential to engage them. A similar result agreeing with the study was reported by Karyakin and co-workers in 2005 [93]. This work compared the current density attained for [NiFeSe]-hydrogenases adsorbed on a carbon filament electrode (with $H_2$ bubbling through the solution) with the current density reported for a rotating disc Pt/vulcan electrode. The catalytic current densities of $H_2$ oxidation at [NiFeSe]-hydrogenases adsorbed on a carbon filament electrode (with $H_2$ bubbling through the solution, pH 7 phosphate buffer) and the rotating disc Pt/vulcan electrode (in 0.5 M $H_2SO_4$, rotation rate: 900 RPM) achieved ca. 1.6 and 2.3 mA $cm^{-2}$, respectively, at +150 mV vs SHE, 60 °C.

To compare the activity of hydrogenases with that of precious metal catalysts per electrode area is unreasonable, because the footprint of a hydrogenase molecule on a

surface is several orders of magnitude larger than that of a pair of precious metal atoms, and in any case, the currents are diffusion controlled. Accordingly it is more informative to compare site-for-site activities from a fundamental viewpoint. The catalytic activities of transition metals are often represented by Volcano Plots [94], in which the exchange current density of $H_2$ oxidation (the rate of flow of electrons back and forth at the reversible potential) is plotted against the energy of the M –H bond. The underlying principle is that the rate of oxidation of $H_2$ increases with the thermodynamic ease of formation of an M –H bond that is not so strong as to become a stable product rather than an intermediate. The volcano plot shows that Pt and Re give the exchange current densities of about $10^{-3}$ A $cm^{-2}$, which are the highest among all the metal catalysts reported. However, a recent appraisal has suggested that this value could be as high as about 1 A $cm^{-2}$ [95]. An economically efficient Pt electrode has a coverage of <0.1mg $cm^{-2}$ [90], equivalent to $10^{-8}$ mol atom Pt per $cm^2$. As a result, the turnover frequency of a Pt "active site" is about 0.1−100 $s^{-1}$. The equivalent quantity for the enzyme was estimated by the rate of $H_2/D^+$ exchange catalysed at the active site measured by mass spectrometry, giving values > 100 $s^{-1}$ [96].

A second way of comparing is to investigate maximum currents for Pt and hydrogenase electrodes typically measured under comparable conditions. For Pt, typical current densities are 1 – 10 A $cm^{-2}$at overpotentials of around 0.4 V. By comparison, *A. vinosum* [NiFe]-MBH adsorbed at PGE electrodes can produce about 3 – 4 mA $cm^{-2}$ at 45 °C at an overpotential ranging from 0.4 to 0.6 V. As the coverage of hydrogenase was $10^{-12}$mol $cm^{-2}$, the activity per active site of the enzyme lies in the same range as that of the equivalent PtPt site [64].

## 1.4 Nickel Carbon Monoxide Dehydrogenase

$CO_2$ is the final product of the compete oxidation of carbon. $CO_2$ is abundant in atmosphere (above 400 ppm, according to Mauna Loa Observatory[97]), stored as various forms of carbonate, and relatively inert, which attracts more research on strategies to convert $CO_2$ to useful products. The most synthetically valuable $CO_2$ reduction product is arguably CO, because it is gaseous and a raw material for two large-scale industrial processes: the water-gas shift reaction that uses CO and water to produce $H_2$ (eq. 1.3) and the Fischer-Tropsch processes that use CO and $H_2$ to produce hydrocarbons (eq. 1.4).

$$CO + H_2O \rightleftharpoons CO_2 + H_2 \quad (1.3)$$

$$(2n + 1)\ H_2 + n\ CO \rightarrow C_nH_{2n+2} + n\ H_2O \quad (1.4)$$

Carbon monoxide dehydrogenases (CODHs) catalyse the rapid and direct redox interconversion of CO and $CO_2$, with water as the oxygen source (eq. 1.5).

$$CO + H_2O \longleftrightarrow CO_2 + 2H^+ + 2e^- \quad (1.5)$$

CODHs have been categorised into two principle types that differ in their cofactorcomposition, structure, and stability in the presence of $O_2$: Aerobic, carboxydotrophic bacteria use flavoenzymes containing Cu, Mo and Fe, whereas anaerobic bacteria and archaea use oxygen-sensitive CODHs containing Ni and Fe [98].

Ni-containing CODHs found in anaerobic organisms are referred to as Ni-CODHs. Five Ni-CODHs are expressed by the thermophilic bacterium *Carboxydothermus hydrogenoformans* (Ch), which can grow chemolithoautotrophically on CO as sole carbon and energy source. In the Wood-Ljungdahl pathway (also known as reductive acetyl-CoA pathway), CODHs catalyse the reduction of $CO_2$ to CO, which is then

combined with a methyl group to give acetyl-CoA in a reaction catalysed by acetyl-CoA synthase (ACS).This pathway occurs in methanogenic and acetogenic bacteria and archaea. Two of these enzymes, CODH $I_{Ch}$ and CODH $II_{Ch}$ only catalyse the $CO/CO_2$ interconversion and have similar spectroscopic properties [8]. Both enzymes show turnover frequencies above 30 000 $s^{-1}$ at pH 8, 70 °C, according to conventional kinetic assays [99]. The crystal structures of CODHs from *Rhodospierillum rubrum* and *Carboxydothermus hydrogenoformans* show that the enzymes are homodimeric (Figure 1.8) [100, 101]. Each subunit contains a buried active site C-cluster featuring a cubane [$NiFe_3S_4$] center linked to a mononuclear "dangling" Fe atom (Fe1) via one sulfido ligand. Electron transfer between the C-cluster and the protein surface are mediated by two [4Fe-4S] clusters in each of the two subunits: a B-cluster, and the surface-exposed D cluster that bridges the two subunits and offers a route for electrons in and out of the enzyme [102]

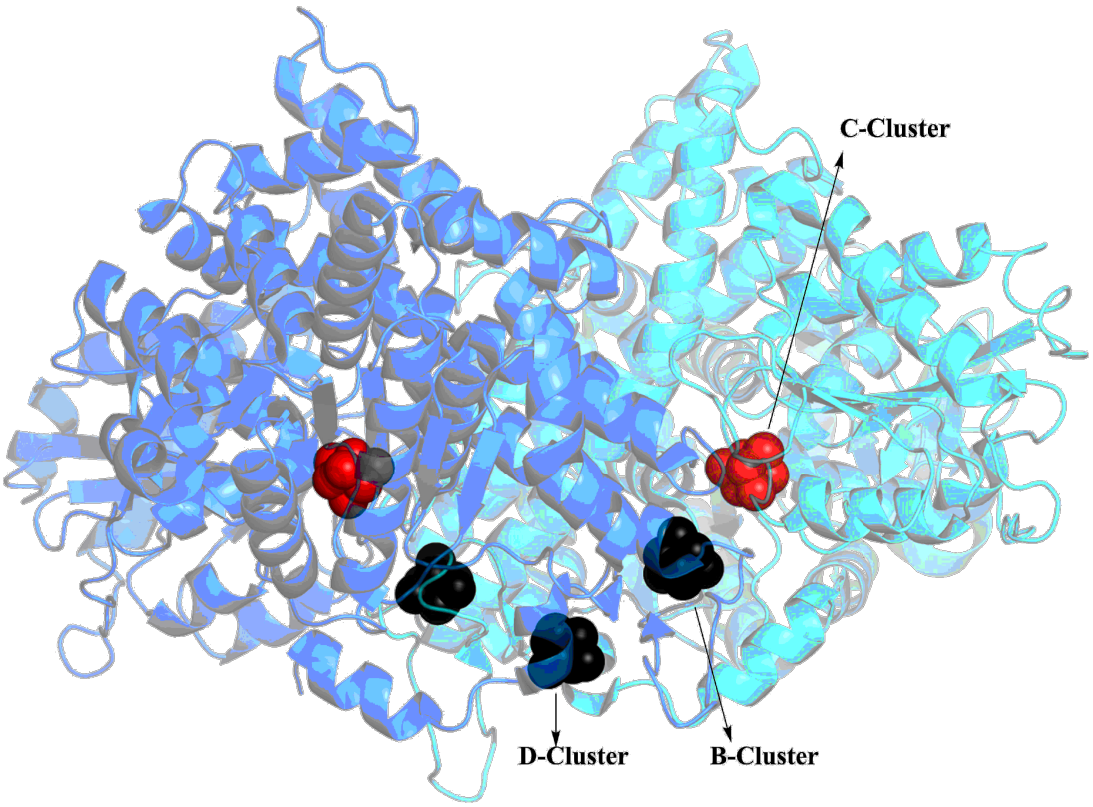



Figure 1.8 Structure of CODH II showing the two subunits (blue andcyan) and arrangement of Fe-S clusters (black) that relay electrons to andfrom the active sites C-cluster (red).The redox centers for one half of the molecule are labelled. Constructed using Pymol[50], PDB code: 1JQK [101].

The crystal structure of the C-cluster of CODH II$_{Ch}$ at – 600 mV ($C_{red2}$ state) is shown in Figure 1.9. This structure is practically identical to the C-cluster at -320 mV ($C_{red1}$ state), shown in Figure 1.10. In both structures, the Ni ion is coordinated by three sulfur ligands, in a distorted T-shape geometry. Fe1 is coordinated byHis$^{261}$ (H261), Cys$^{295}$ (C295), a $\mu_3$-sulfido ligand, and a water/hydroxo ligand [103].

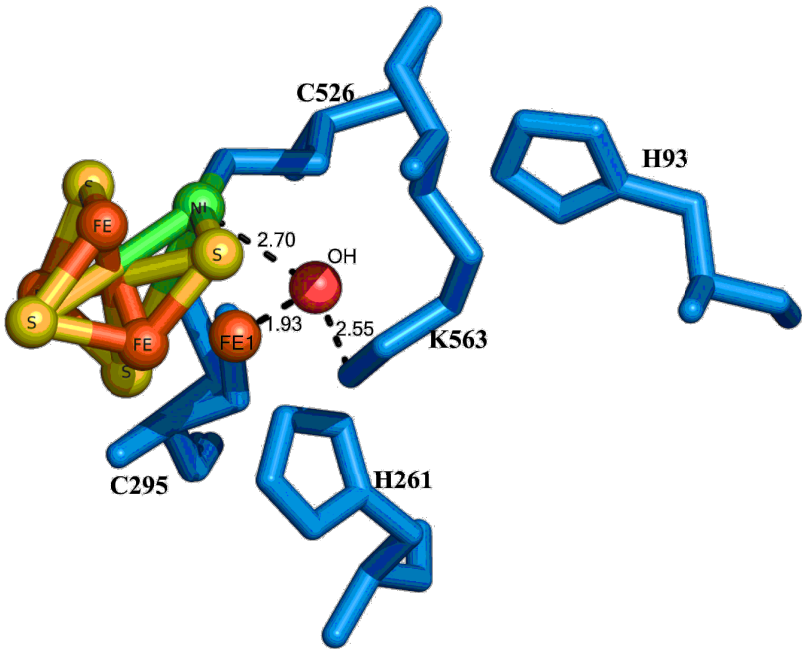



Figure 1.9 Crystal structure of the C-cluster of CODH $II_{Ch}$ at – 600 mV ($C_{red2}$state).

Selected distances are shown in Å. Constructed using Pymol[50]. PBD code 3B51 [103].

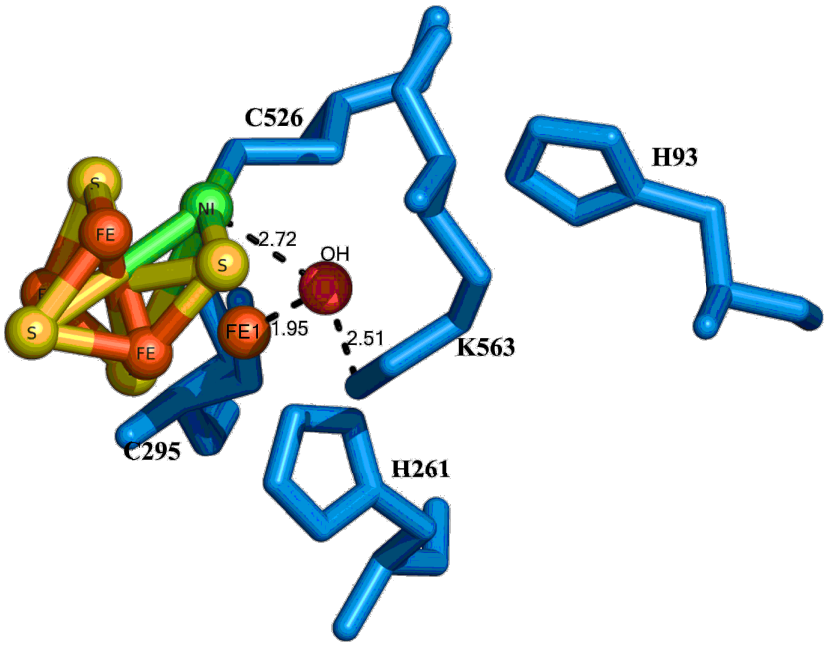



Figure 1.10 Crystal structure of the C-cluster of CODH II$_{Ch}$ at – 320 mV ($C_{red1}$state). Selected distances are shown in Å. Constructed using Pymol [50]. PBD code 3B53 [103].

When the CODHII$_{Ch}$ crystals were incubated with $NaHCO_3$ as the carbon source under reducing conditions (–600 mV), a state where a $CO_2$ ligand bridges Ni and Fe1 was formed. The $CO_2$ replaces the water/hydroxo ligand at Fe1 (Figure 1.11). $CO_2$ here is a $\eta^1$ OCO ligand at $Ni^{2+}$ with a Ni – C distance of 1.96 Å and completes the square-planar coordination geometry typically observed for $Ni^{2+}$. $CO_2$ acts as a $\eta^1$ OCO ligand at Fe1 with a Fe1-O1 distance of 2.05Å. As a result, the $CO_2$ bridges the Ni-Fe1 site in a $\mu_2$-$\eta^2$ mode. Jeffrey [104] categorizes H bonds with donor-acceptor distances of 2.2 –

2.5 Å as “strong, mostly covalent”, 2.5 – 3.2 Å as “moderate, mostly electrostatic”, and 3.2 – 4.0 Å as “weak, electrostatic”. So O1 of $CO_2$ is in hydrogen-bonding distance to $Lys^{563}$ (K563), like the $H_2O$/hydroxo ligand in the −600 mV (Figure 1.9) and −320 mV (Figure 1.10).O2 of $CO_2$ is in hydrogen-bonding distance to $His^{93}$ (H93). In the $CO_2$−cluster C complex, Ni acts as the Lewis base, and Fe1 is the Lewis acid that stabilizes the negative partial charge on O1, together with K563.

$CO_2$ binding to C-cluster causes only minor changes in the geometry of the cluster, which agrees well with the low reorganization energy expected for the interconverstion reaction between $CO/CO_2$ with turnover frequency ($k_{cat}$) of 31000 $s^{-1}$ and a ratio of $k_{cat}/K_m$ (Michaelis constant) of $1.7 \times 10^9$ $M^{-1}s^{-1}$ [99].For comparison, blue copper oxidases only have $k_{cat}$ of 100 $s^{-1}$, and the equivalent $k_{cat}$ of Pt is approximately 15 $s^{-1}$ [5].The $[Fe_3S_4]$ of C-cluster provides a solid cubane-like frame in which Ni and Fe1 are held in place. The metal-sulfur frame serves as an electronic buffer to compensate for the electronic changes at Ni and Fe1 during catalysis.

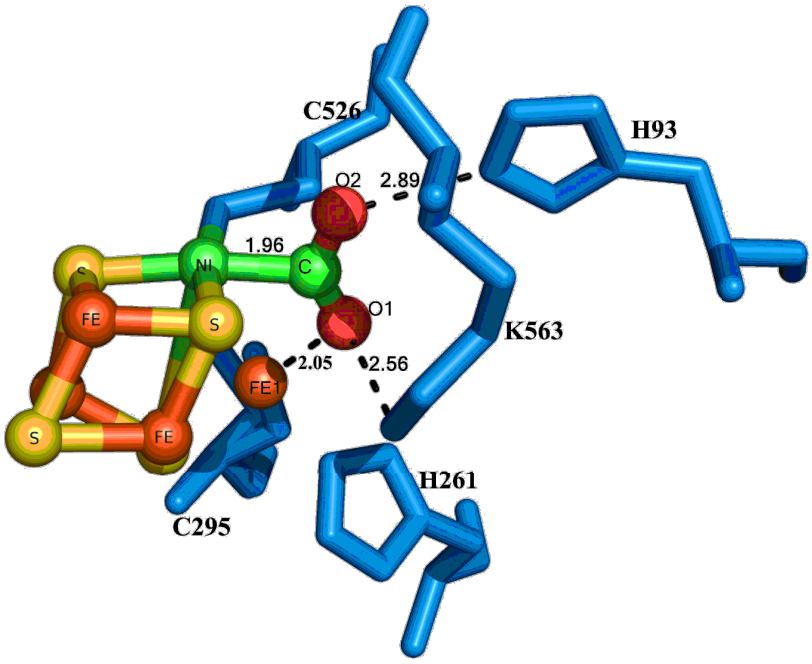



Figure 1.11 Crystal structure of the C-cluster of CODH $II_{Ch}$ at – 600 mV +$CO_2$ (–600 mV+$CO_2$ state). Selected distances are shown in Å. Constructed using Pymol [50]. PBD code 3B52 [103].

There has been controversy over whether a fifth sulfido ligand (S2) that bridges Ni and the dangling Fe is present in an active enzyme [100, 103, 105]. Because the S2 ligand is absent in some crystal structures of catalytically active CODHs, the S2 ligand is not necessary for catalysis [103]. Furthermore, the S2 ligand occupies the binding site of two substrates of C-cluster of Ni-CODH, water/hydroxo and $CO_2$ligands. So Jeoung et al. concluded that the S2 ligand is absent in active sites of catalytically competent enzymes [103].

The three structures shown in Figure 1.9– 11 lead to the mechanism of $CO/CO_2$ interconversion illustrated by Figure 1.12. All four steps are reversible in the proposed catalytic cycle. (I) In $C_{red1}$ state, C-cluster shows the structure observed at –320 mV (Figure 1.10) and activates CO. The $Ni^{2+}$ ion is at the end of the substrate channel, with three sulfido ligands as its π donors that enable CO binding to the metal ion. (II) CO binds to $Ni^{2+}$ equatorially to complete the square-planar coordination geometry, according modelling study.(III) Because $Ni^{2+}$ is weakly back donating, the binding of CO leads to an electrophilic carbon atom and facilitates its reaction with water/hydroxo ligand bound to Fe1, which facilitates the formation of $C_{red2}$ state, where C-cluster shows the structure observed in the –600 mV+ $CO_2$ state (Figure 1.11). (IV) –600 mV+ $CO_2$ state undergoes the reversible ligand exchange of $CO_2$ against water at Fe1, forming the $C_{red2}$ state that is modelled by the –600 mV state (Figure 1.9).

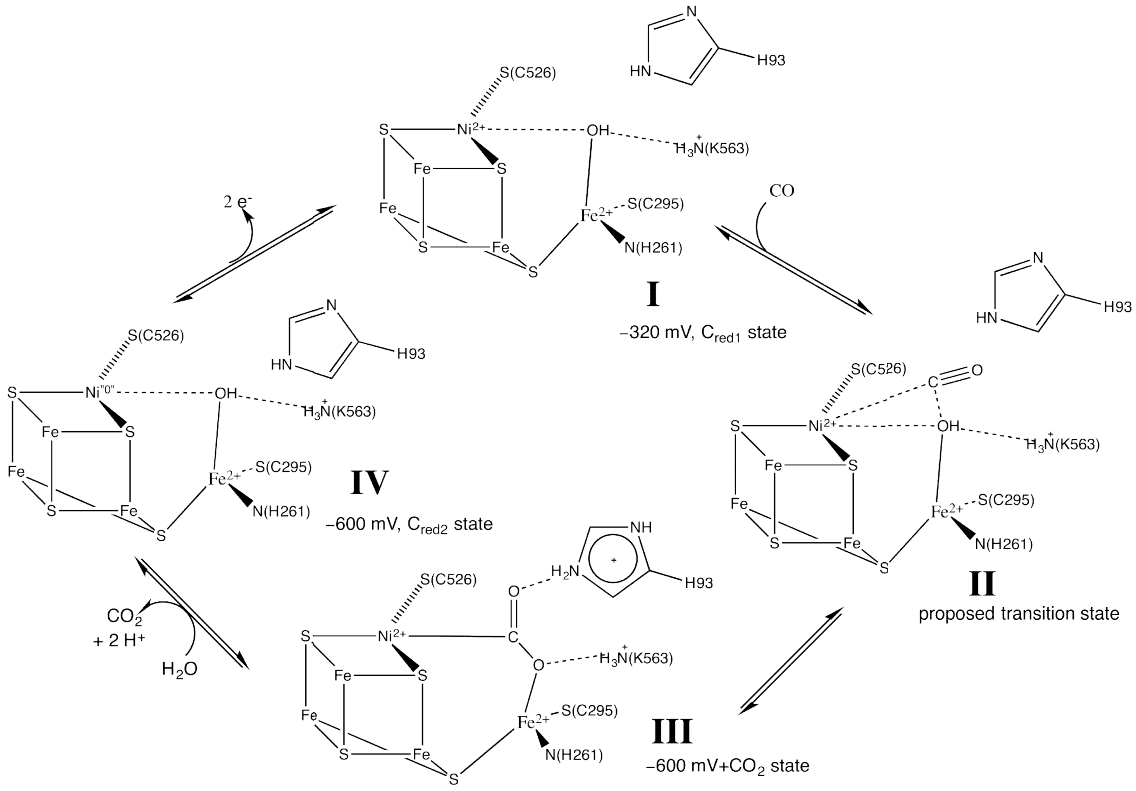



Figure 1.12 Structure-base mechanism of $CO_2$/CO interconversion at C-cluster of Ni-CODH. (I) −320 mV state is used as a model for $C_{red1}$, competent of CO oxidation. (II) A proposed transition state. The CO binds to the $Ni^{2+}$ ion and reacts with the OH group bound to Fe1. (III) −600 mV+ $CO_2$ state has been used as a model for the stabilized carboxylate state. (IV) The −600 mV state is used as a model for $C_{red2}$ state. The formal charge of Ni is denoted as zero, because this state is supposed to contain 2 more electrons than $C_{red1}$ state. Adapted from ref [103].

# 2 Electrochemical Reactivity in Ionic Liquids

## 2.1 The Definition and History of Ionic Liquids

Ionic liquids are room-temperature molten salts [106]. They are composed of organic anions and cations that undergo unlimited structural variations. So the properties of ionic liquids can be tailored for different applications, which opens up avenues for a surge of research on ionic liquids.

In 1914, Paul Walden reported the synthesis and properties of ethylammonium nitrate, the "first" ionic liquid. This ionic liquid has a low a melting temperature (12 °C) and was used for electric conductivity measurement[107]. Despite its early discovery, research activity did not renew until mid-1970s, when alkylpyridinium or 1,3-dialkylimidazoliumhaloaluminate salts were discovered. These ionic liquids were prepared by mixing aluminum halides with the corresponding imidazolium or pyridinium halides. Electrochemical studies of the new ionic liquid2:l aluminum chloride: ethylpyridinium bromide melt were first reported in 1975 [108]. The Lewis acidity of the ionic liquid was easily tuned by changing the molar ratio of the two components. Unfortunately, the new ionic liquid suffers from its high sensitivity to moisture and has to be dealt in anhydrous conditions to avoid hydrolysis.

The 1990s witnessed the significant milestone of research in the field of ionic liquids, e.g. the discovery of the imidazolium salts incorporating the tetrafluoroborate ($[BF_4]^-$) orhexafluorophosphate ($[PF_6]^-$) anions[109]. Unlike their haloaluminate analogues, the new generation of ionic liquids is much more stable with the presence of moisture, thus can be prepared, stored and handled outside a glovebox. A large variety of ionic liquids can be prepared by rational combination of these cations and anions, which raise the stakes for researchers to study the structures, properties, and application of the new

ionic liquids. Since 2000, more than 6000 papers have been dedicated to the field of ionic liquids [110].

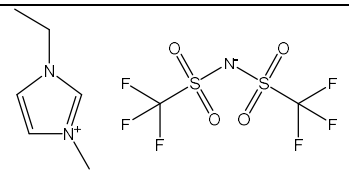
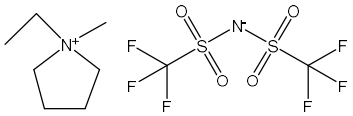
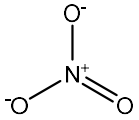
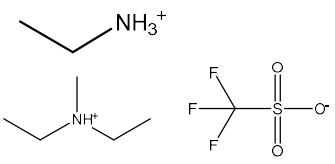
## 2.2 Properties of Ionic Liquids

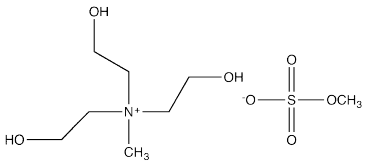
Ionic liquids have some archetypical properties including negligible volatility, high thermal, chemical stability, high viscosity, high conductivity, and large electrochemical window [106, 111, 112]. They show a high thermal stability, with decomposition temperatures around 300 – 500°C. They are able to solvate a large variety of organic and inorganic compounds, either polar or nonpolar. They are generally regarded as polar yet noncoordinating solvents. They display a good intrinsic conductivity and are extremely redox-robust. These properties of ionic liquids make them green solvents for applications in electrochemical devices, solvents for organic synthesis, $CO_2$ absorption, and so on. Because of the intense activity of research of their physicochemical properties, more data have supported that these above-mentioned properties cannot be considered as generic properties for these media. For example, many ionic liquids have shown to decompose above 80 – 90 °C and most decomposition temperatures reported in the literature are overestimates. In general, it is the anion-cation combination that determines the physicochemical properties of ionic liquids. Ionic liquids can show distinctly contrary properties. [109]

In this thesis, I used five Ionic liquids: 1-ethyl-3-methylimidazolium bis(trifluoromethylsulfonyl)imide (EMIMTFSI), 1-methyl-1-propyl pyrrolidinium bis(trifluoromethylsulfonyl)imide (PMPyrTFSI), ethylammonium nitrate (EAN), diethylmethylammonium trifluoromethanesulfonate (DEMATFO), and tris(2-hydroxyethyl)methylammonium methylsulfate (TEMAMS). Their properties and

structures are summarized in Table 2.1. These ionic liquids were used in my study because they are commercially available, chemically and electrochemically stable, have relatively low viscosity and relatively high electrical conductivities, which means they are powerful electrolytes. So in Table 2.1 and the following paragraphs, the viscosity, electric conductivity, electrochemical window, effects of impurities of ionic liquids that influence their application as electrolytes are discussed.

Table 2.1 Physical properties and structures of ionic liquids:1-ethyl-3-methylimidazolium bis(trifluoromethylsulfonyl)imide (EMIMTFSI), 1-methyl-1-propyl pyrrolidinium bis(trifluoromethylsulfonyl)imide (PMPyrTFSI), ethylammonium nitrate (EAN), diethylmethylammonium trifluoromethanesulfonate (DEMATFO), and tris(2-hydroxyethyl)methylammonium methylsulfate (TEMAMS).

| Ionic Liquid | Structure | ρ/ (g $mL^{-1}$) | η/ (mPa s) | Electrical conductivity/ (S/m) |
|---|---|---|---|---|
| EMIMTFSI |  | 1.5168[a][113] | 31.13[a][113] | 0.91[a][114] |
| PMPyrTFSI |  | 1.42786[a][115] | 49.35[a][115] | 0.16[a][116] |
| EAN |  | 0.827[a][117] | 32[b] [118] | 2.69[b][118] |
| DEMATFO |  | 1.284[a][119] | 36.9[c][119] | 0.833[c] [119] |

| | | | | |
|---|---|---|---|---|
| TEMAMS |  | 1.34087[c] [120] | 799.09[c] [120] | 3.89[c] [120] |

[a] 25 ˚C. [b] 27 ˚C. [c] 30 ˚C. All data were obtained at 101325 Pa.

### 2.2.1 Viscosity

Viscosities of ionic liquids are 1 – 3 orders of magnitude higher than those of conventional solvents [109]. The high viscosity is a major drawback of ionic liquids for application. This property is important in electrochemical studies, because the viscosity of ionic liquids may influence the rate of mass transport within solution and on the conductivity of the salts. Large viscosity of RTILs also brings practical problems to experiments and their application in electrochemical devices. The viscosities of ionic liquids I used in this thesis are shown in Table 2.1. Some preliminary studies of this thesis were carried out using TEMAMS, which has a much higher viscosity (799.09 mPa s at 30 ˚C) than the other four ionic liquids that I have used. The large viscosity of TEMAMS made this matrix difficult to handle in electrochemical experiments, because this viscous ionic liquid is easy to get stuck in electrochemical cells and pipettes.

The viscosity of ionic liquids is dependent on the ion-ion interactions, such as van der Waals interactions and hydrogen bonding. Therefore the viscosity varies significantly with chemical structure, composition, temperature and the presence of solutes of impurities.

For a given cation, the viscosity of ionic liquids is determined by the nature of the anion. Ionic liquids with large anions such asbis(trifluoromethylsulfonyl)imide, $[NTf_2]^-$,

have the lowest viscosities. Ionic liquids containing large and nonpolar anions usually have lower viscosities. The most viscous ionic liquids are those containing $[PF_6]^-$. Generally speaking, the size, shape, and molar mass of the anion contribute to the viscosity with smaller, more symmetric, and lighter anions leading to more viscous ionic liquids. However, exceptions to the rule do exist. For example, for RTILs based on imidazolium cations, bis(perfluoroethylsulfonyl)imide anion, $[BETI]^-$, caused the viscosity of its analogue with $[NTf_2]^-$ to increase by ca. 100 mPa s. So other parameters such as formation of hydrogen bonds need to be considered. Anions having greater ability to form hydrogen bonds or increase van der Waals forces lead to higher viscosity of the ionic liquids. For instance, the fluorinated anions such as $[BF_4]^-$, $[PF_6]^-$, or $[BETI]^-$ form more viscous ionic liquids due to the formation of hydrogen bonds or stronger van der Waals interactions. The relative basicity of the anion contributes to the viscosity with more basic anions leading to more viscous ionic liquids. For instance, the weakly basic $[NTf_2]^-$ anion has extensive charge delocalization within the N – S – N backbone, which decreases the interactions between ions and resulting in less viscous ionic liquids.

Cations also influence the viscosity of ionic liquids. For ionic liquids with the same anions, the viscosity increases with the alkyl chain length, due to the stronger van der Waals interactions [121]. For instance, the viscosity of a series of 3-alkyl-1-methyl-imidazolium $[NTf2]^-$ salts increase linearly with the increase of the number of $-CH_2$ groups. Branching the alkyl chains of 3-alkyl-1-methyl ionic liquids decreases the viscosity of the ionic liquids, because of the decrease of van der Waals interactions among ions. However, the introduction of a methyl group at the 2-position of the cation to form1-alkyl-2,3-dimethyl-imidazolium increases the viscosity, which appears counterintuitive. Because additional C(2) methyl group eliminates the possibility of

forming a strong hydrogen bond between the cation and the anion, the viscosity of the ionic liquid should decrease. Indeed, the anion-cation interaction decreases as a result of the additional C(2) methyl group. Computational studies demonstrated that the additional C(2) methyl group increases the viscosity, because the effects due to a loss in hydrogen bonding are outweighed by those due to a loss in entropy. The amount of disorder in the system is reduced in two ways: salts methylated at C(2) have fewer ion-pair conformers than 1-alkyl-3-methyl salts do, and an increase in the rotational barrier of the alkyl chain at C(1), which limits free rotation and facilitates alkyl chain association[122].

The viscosity of ionic liquids generally decreases as the temperature increases [109]. Two models were proposed to predict the viscosity-temperature relationship: the Arrhenius equation($\eta = Ae^{E_a/(RT)}$, where $E_a$ is the activation energy for viscous flow) and the Vogel−Tamman−Fulcher equation ($\eta = \eta_0 e^{B/(T-T_0)}$ where $\eta_0$ (mPa s), $B$(K), and$T_0$ (K) are constants). The Arrhenius equation applies to ionic liquids containing asymmetric cations without functional groups in the alkyl chains. The Vogel−Tamman−Fulcher equation applies to ionic liquids containing small, symmetrical cations with low molar mass [123]. However, the two behaviours are linked, because Arrhenius-type relationship is simply the higher temperature limit of the VTF equation.

To conclude, electrostatic interactions between anions and cations dominate the characteristic physicochemical properties of ionic liquids and distinguish them from traditional organic solvents. But, forionic liquids of similar structures, the differences in the viscosity are mainly influenced by hydrogen bonding and van der Waals interactions[109].

### 2.2.2 Conductivity

The conductivity of ionic liquids is a property of primary importance for the application of ionic liquids in electrochemical processes. The conductivities of ionic liquids I used in this thesis are shown in Table 2.1. ILs with higher electric conductivity are more desirable for application in electrochemical devices, because the internal resistance of the device can be lowered by increasing the electric conductivity of the electrolytes applied.

Because ionic liquids are composed entirely of ions, it is frequently supposed that they are the most concentrated electrolytic fluids with many charge carriers per volume. When these charge carriers are mobile, ionic liquids should have high electric conductivities. However, conductivity depends on both the number of charge carriers and their mobility. The ion mobility is reduced by high viscosity and large sizes of constitute ions of ionic liquids. Thus ionic liquids' conductivities are lower than those of aqueous electrolytes, but still comparable to organic solvents dissolved with supporting electrolyte [112]. Room-temperature ionic liquids (RTIL) have conductivity in the broad range of 0.01 – 2 S $m^{-1}$[109]. Rather high conductivities of the order of 1 S $m^{-1}$ can be found in RTILs containing imidazolium anions. Quaternary ammonium ionic liquids are always less conductive: 0.2 S $m^{-1}$is thus the highest conductivity observed for an N,N-dialkyl-pyrrolidinium [$NTf_2$] salt. RTILs containing the tricyanomethanide anion and the dicyanamide anion possess some of the highest conductivities, which are up to 3.6 S $m^{-1}$. But these values are still considerably lower than those of concentrated aqueous electrolytes. For instance, the aqueous KOH solution (29.4 wt%) serving as electrolyte for alkaline battery is 54 S $m^{-1}$.

The conductivity is inversely linked to the viscosity. The less viscous [$NTf_2$] salts usually exhibit higher conductivities. But the viscosity alone cannot account for the conductivity of RTILs. Many other factors have impact on the conductivity, i.e. ion size, anionic charge delocalization, density, aggregation and correlated ionic motions.

Conductivities and transport properties of dialkylimidazolium ionic liquids are influenced by their anion and cation structures [124, 125]. For the 1,3-methylethylimidazolium salt incoporating different anions of bromide ($Br^-$), iodide ($I^-$), trifluoromethanesulfonate ($Tf^-$) and bis(trifluoromethanesulfonyl)amide ($[NTf_2]^-$), increasing the size of the anion lowered the viscosity, whereas the measured conductivities were similar for any of the anions. However, conductivities calculated from the diffusion coefficients of the anions and the cations gave higher conductivities for the less viscous RTILs containing larger anions. The inconsistency between the calculated conductivities based on diffusion coefficient and the measured conductivities was attributed to the diffusion of neutral species that do not contribute to the conductivities and/or correlated ionic motions. More viscous RTILs exhibit stronger ion pairing. Although the diffusion coefficients of such neutral species or ion pairs can be measured, they do not contribute to conductivity as a result of lack of net ionic charge. Moreover, the random motion of one ion induces a proximal counterion to move in the same direction, which is the mechanism of correlated ionic motion without the necessity of bonded species even on a transient basis. The effect of the length of the alkyl substituent was studied for 1,3-methylalkylimidazolium iodide. Increasing the length of the alkyl chain, from methyl to a linear heptyl chain, leads to higher viscosity and lower conductivity[125].

An equivalent rationale explained the higher conductivities of [$BF_4$] salts compared with their corresponding RTILs containing [$NTf_2$]$^-$ anions. Pulsed-gradient spin-echo NMR measurements and impedance spectroscopy studies showed that stronger cation-anion association occurs in [$NTf_2$] salts. Since cation-anion association form neutral species or ion pairs that do not contribute to conductivity, [$NTf_2$] salts exhibit lower conductivities than corresponding [$BF_4$] salts [126].

The dilution of neat RTILs in molecular liquids or the addition of small cations such as $Li^+$ increases the conductivity of RTILs for applications in batteries or double-layer capacitors, which will be discussed later. But the conductivity of RTILs (0.01 – 2 S $m^{-1}$) is usually comparable to organic solvents with supporting salts and high enough for common electrochemical measurement.

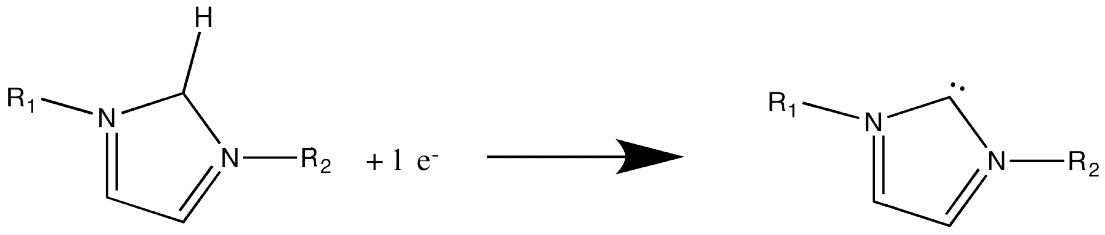
### 2.2.3 Electrochemical Window

Ionic liquids generally exhibit a wide electrochemical window, which is desirable as electrochemical solvent. The potential window is determined by the potentials at which the oxidation of cation and reduction of anion start. Typical windows are 4.5-5 V for RTILs [109]. The largest potential window was reported as 7 V for 1-Butyl-3-methylimidazolium hexafluorophosphate (BMIM$PF_6$)and 1-Butyl-3-methylimidazolium tetrafluoroborate (BMIM$BF_4$)[127]. On the whole, the potential window of RTILs largely exceeds that accessible in aqueous electrolytes and is similar to that observed in organic electrolytes. The oxidation of the anions and the reduction of the cations contribute to the anodic and cathodic limits observed in RTILs, respectively. The potentials at which these redox processes start determine the electrochemical window. However, an accurate comparison of the various potential windows is difficult

for three main reasons. First, potential windows are influenced by impurities in ionic liquids. Second, decomposition potential may change with different working electrode materials. Third, potential values are referred against quasi-references, which cannot be compared with a high level of accuracy.

However, general trends exist for the electrochemical windows of RTILs. Quaternary ammonium salts exhibit lower cathodic limit than their corresponding pyrrolidinium salts. Quaternary ammonium and pyrrolidinium salts are more stable towards reduction than the corresponding imidazolium slats. The reduction of the imidazolium cation is related to the acidic proton at C(2)[128, 129]. The reduction of 1,3-dialkyl-imidazolium cation gives a carbene [130] (Scheme 2.1). Accordingly, 1,3-dialkyl-2-methylimidazolium, without such acidic proton, shows more negative reduction potentials their analogues with 1,3-dialkyl-imidazolium cation [128]. 1,3-dialkyl-imidazolium cation was observed to form products from dimerization and dealkylation [131].

Scheme 2.1 Proposed Electrochemical Reduction of Imidazolium Cation According to ref. [130].



On the oxidative side, fluoroanions i.e. $[PF_6]^-$, $[BF_4]^-$ or $[NTf_2]^-$ are generally stable. However, $[BF_4]^-$ in $BMIMBF_4$ decomposes into $BF_3$ and fluorocarbons at the anode while the cation undergoes dimerization and dealkylation reactions at the cathode after being reduced to a carbene [131]. $[NTf_2]^-$ is usually stable towards oxidation and widely used as the anion of powerful electrolytes. But, at potentials lower than –2.0 V vs $Fc/Fc^+$, $[NTf_2]^-$ undergoes cleavage of a S–N bond [132], as indicated by the reaction below.

$$(CF_3SO_2)_2N^- + e^- \longrightarrow {}^{\cdot}NSO_2CF_3^- + SO_2CF_3^-$$

### 2.2.4 Impurities and Their Effects

One main impurity in ionic liquids is water. Even hydrophobic ionic liquids absorb water [112]. Water impurities decrease the viscosity [133], increase the conductivity [134] and shrink the electrochemical window [135, 136]. To decrease the effect of water in electrochemical experiments of ionic liquids, I heated ionic liquids under vacuum beforehand.

Halides are common impurities in ionic liquids. Halides come from starting materials for synthesis of ionic liquids. Halides are easily oxidized, so it influenced voltammetric data. Presence of chloride substantially increase viscosity of ionic liquids, even at low concentrations[137].

## 2.3 Electrochemical Methods in Ionic Liquids

The properties of ionic liquids (conductivities, viscosity, electrochemical window etc.) allow classical electrochemical principles and methods to be used as one can do in organic electrolytes. The basic use of classical electrochemical techniques has largely been reported for investigating the properties of electrode-electrolyte interfaces or molecules dissolved in the RTILs [109]. Processes in ionic liquids can be studied by traditional electrochemical methods, i.e. cyclic voltammetry, chronoamperometry and standard equipment used in electrochemistry.

### 2.3.1 Reference Electrodes

Unlike electrochemical experiments in conventional aqueous electrolytes, well-established reference electrodes are unavailable in ionic liquids at current stage. Even though attempts to build such reference electrodes for ionic liquids were made, most of them suffered from short lifetime and lack of data that support their stability and reliability [138, 139].

Quasi-reference electrodes including Ag and Pt are widely used. However, the quasi-reference does not allow accurate comparison of potentials among different electrolytes. So reversible redox systems are used to provide a known and stable reference point in non-aqueous solvents where reliable reference electrodes are difficult to be established and/or stabilized. Reversible reference systems of ferrocene/ferrocenium($Fc/Fc^+$) [140-142] and cobaltocene/colbaltoceneium ($Cc/Cc^+$) [143] have been used as internal reference in electrochemical studies of ionic liquids. The two internal reference systems

were selected arbitrarily from several published redox systems, because they fulfil the necessary requirements of a reference redox system [144];

(1) the ions or molecules forming the reference redox system should preferably be spherical with as large radius as possible,

(2) the ions should carry a low charge,

(3) the equilibrium at the electrode should be rapid and reversible,

(4) both components of the redox couple should be soluble,

(5) there should be no change in the geometry of the ligands around the metal center,

(6) the redox potential should be in a potential range that is accessible in as many solvents as possible, and

(7) both forms should be stable enough to permit potentiometric measurements.

But recently, $Fc/Fc^+$ and $Cc/Cc^+$ were found to have some drawbacks that bring systematic errors to electrochemical measurements.

$Fc/Fc^+$ was recently report to have the following drawbacks:

(1) poor solubility of Fc observed in some ionic liquids, mostly in those with high viscosity[145],

(2)moderate volatility[146, 147], and

(3)reactivity of $Fc^+$ with the ionic liquid components when the anodic potential window of the IL is close to the formal redox potential of $Fc^{0/+}$[145, 148].

$Cc/Cc^+$ reacts with $H_2$ in a range of ionic liquids[143], leading to lower $H_2$ oxidation currents in ionic liquids. These reports indicate that $Cc/Cc^+$ and $Fc/Fc^+$ can interfere with some processes in ionic liquids.

More recently, decamethylferrocene/decamethylferrocenium ($DmFc/DmFc^+$) was recommended as internal reference, because it is more stable than ferrocene and cobaltocene in different ionic liquids[144]. Such chemical stability of $DmFc/DmFc^+$ in ionic liquids is originated from the methyl-substituent groups at cyclopentadienyl rings, which hinder interaction with ionic liquids.

### 2.3.2 Ionic Liquid/Electrode Interface

Gouy−Chapman theory is canonical to describe the potential dependence of capacitance in electrochemical double layers. This theory is limited to dilute solutions, where ions are considered as point charges [37]. However, in ionic liquids, where the ion concentration is high, the size and shape of ions are of primary importance. So several anomalies were found that cannot be explained by Gouy−Chapman theory in ionic liquids [149].

Kornyshev proposed a new analytical formula to rationalize the potential dependence of double-layer capacitance at a planar metal-ionic liquid interface [149].The theory has a mean-field character, derived based on Poisson-Boltzmann lattice-gas model, and modified to account for the finite volume occupied by ions. When the volume of liquid excluded by the ions is taken to be zero (that is, if ions are extremely diluted in the ionic liquid), the formula reduces to the nonlinear Gouy-Chapman law. However, as Kornyshev notes, if there is specific adsorption of ions, the analysis will be more complicated. Another weakness of Kornyshev's model is that the simple mean-field theory may not work for highly concentrated ionic systems, where the ion-correlation effects are strong.

At present, more data are needed to establish a complete model allowing treatment of the electron transfer process at ionic liquid/electrode interface.

### 2.3.3 Voltammetry in Ionic Liquids

The most frequently used technique to study electrochemical processes in RTILs is cyclic voltammetry [109]. Two different types of processes take place at electrode surface and contribute to the total current ($I_T$) measured in voltammetry in ionic liquids: Faradaic and Non-Faradaic processes, which will be discussed in detail Chapter 3 and Appendices.

Butler-Volmer model [37] is used to study the electrode kinetics in ionic liquids. This will be discussed further in Chapter 3.The Butler-Volmer equation can be combined with mass transport equation to give a theoretical description of a cyclic voltammogram for steady-state, transient state, microelectrode or rotating disc electrode.

An electrochemically reversible system is one where the electron transfer rate is sufficiently fast that equilibrium is achieved on a short timescale and maintained as the potential is varied [112]. At another extreme, when the electrode kinetics is sufficiently slow, true equilibrium is never attained on the timescale of the experiment. Such systems are classed as irreversible. Systems displaying intermediate electrode kinetics are classed as quasi-reversible.

## 2.4 Electrochemical Applications of Ionic Liquids

### 2.4.1 Lithium Batteries

Lithium batteries seem to be the power source of choice, because they have the highest energy efficiency of all known electrochemical storage systems and have reached an advanced state of technological development [106]. However, their implementation for energy storage and in vehicle applications has been slowed by safety concerns about large-scale lithium cells. In lithium cells, unpredictable events such as short circuits or local overheating can trigger undesired reactions between the battery components and the liquid organic electrolyte. These reactions result in exothermic reaction of the electrolyte with the electrode materials, producing a rapid increase of the battery temperature and, eventually, to fire or explosion.

Ionic liquids provide a solution to this safety problem of lithium batteries, because ionic liquids are non-flammable. Ionic liquids as electrolyte in lithium batteries have been under intensive study [150-153]. Aspects need to be understood include the thermodynamic and kinetic stabilities of the ionic liquids with respect to the electrode materials. The electrode material selected for lithium batteries has been carbon. At carbon electrodes, a few ionic liquids have been reported to be stable in the potential range allowing reduction of $Li^+$ to Li [151, 154, 155]. Carbon electrodes are intercalated and exfoliated by conventional organic solvents used in lithium batteries, releasing a large amount of heat. This safety problem can be solved by the application of ionic liquids, because ionic liquids do not intercalate or exfoliate carbon.

### 2.4.2 Inorganic Fuel Cells

Ionic liquids have high ionic conductivity, which are suitable for application in fuel cells using precious metals as electrocatalysts. Conventional fuel cells use perfluorosulphonic-acid-membrane electrolyte, whose conductivity depends on humidity. This limits the operating temperature to ~ 100 ˚C. This issue can be addressed by using ionic-liquid-based polymer as electrolyte [156-159], theirhighconductivity,aswellastheirthermal,chemicalandelectrochemicalstabilityunderan hydrousconditions[160]. Such electrolyte relies on imidazole or amine as proton carrier, rather than water. Ionic-liquid-based polymer not only allows the working temperature of fuel cells to be higher, but also increases the upper pH limit from 7 to 11. Higher pH allows new catalysts to replace the conventional Pt, which is rare and expensive, and thus a bottleneck for commercialization of fuel cells.

The wide molecular designability of ILs enabled the finding of a promising candidate, diethylmethylammonium trifluoromethanesulfonate ([dema][TfO]), which exhibits favourable bulk properties and electrochemical activity. Solid thin films containing [dema][TfO] were fabricated using sulfonated polyimide as a matrix polymer. By using the composite membrane, non-humidifying fuel cell using Pt as working electrode successfully operated at 120°C. The maximum current density is 400 mA $cm^{-2}$ ,while the maximum power density is ca. 100 mW $cm^{-2}$. The fuel cell performance can be further improved by the optimization of the catalyst layer and with further research on the physiochemical properties of ILs[161].

The investigation of ionic-liquid-based polymer electrolyte for fuel cells is at its infancy [106]. But we are confident that they deserve great attention and devotion for development of zero-emission cars.

### 2.4.3 Supercapacitors

Ionic liquids are also investigated as electrolyte for supercapacitors that are electrochemical devices based on two inert electrodes separated by an electrolyte. Supercapacitors assist batteries when cars demand high power to start up or accelerate. Present supercapacitors are limited to a few watt hours per kilogram, which is well below the specific energy required to provide power assists in hybrid vehicles. One way to increase the performance of supercapacitors is to increase the voltage. So supercapacitors need ionic liquids that can tolerate high voltage as electrolyte [162, 163]. More research on the application of ionic liquids to supercapacitors is taking place.

## 2.5 Bioelectrochemistry in Ionic Liquids

A number of ionic liquids are biocompatible [164-166]. For example, using a cellulose-in-ionic-liquid dissolution and regeneration process, a new method for introducing enzymes into cellulosic matrixes which can be formed into membranes, films, or beads has been developed. Active enzyme-encapsulated films can be prepared using this methodology. Precoating the enzyme with a second hydrophobic ionic liquid prior to dispersion in the cellulose/ionic liquid solution can increase enzyme activity relative to that of untreated films, according to initial results on the formation of thin cellulose films incorporating dispersed laccase. The cellulose/ionic liquid solution may provide a stabilizing microenvironment for the enzyme [164]. Compton and co-workers studied the ability of Fe(III) protoporphyrin (IX) chloride (hemin), microperoxidase-11 (MP-11), and cytochrome c (cyt-c) to oxidize 2-methoxyphenol (guaiacol) was examined in the RTILs 1-butyl-3-methylimidazoliumbis(trifluoromethylsulfonyl)imide ([bmim][$NTf_2$]) and the hexafluorophosphates of 1-butyl- and 1-octyl-3-

methylimidazolium([bmim][$PF_6$] and [omim][$PF_6$]), respectively. All three biocatalysts displayed peroxidase activity when activated by an electron acceptor, tert-butyl hydroperoxide for hemin and hydrogen peroxide for MP-11 and cyt-c. Hemin required the addition of a coordinating base, pyridine or N-methylimidazole (NMI), to produce an active complex. Cyt-c did not require exogenous ligands for activity in ILs, although their addition increased peroxidase activity. MP-11 could not be solubilized without an exogenous ligand, therefore, whether MP-11 was active in the absence of such ligands was not determined. Hemin and MP-11 peroxidase activities were markedly higher in IL compared to molecular solvents of similar polarity, while cyt-c activity was comparable between both types of solvents. There was no consistent preference by the catalysts for a particular IL. These observations indicate that ILs are suitable media for bioelectrocatalysis.

### 2.5.1 Ionic Liquids as Components of Electrodes

Because of the widely reported biocompatibility of RTILs, effective adhering of RTILs on electrode surfaces was discovered to help to realise the direct electrochemistry of redox proteins. Even hydrophilic RTILs based on imidazolium were reported to form films that facilitate the direct electron transfer of horseradish peroxidase on glassy carbon electrodes in aqueous phosphate-buffered saline solutions [167]. The adherence of hydrophobic RTILs onto the electrode was increased by combination with Nafion or chitosan, which show good biocompatibility [109].Mixing 1-butyl-3-methyl-imidazolium hexafluorophosphate ($BMIMPF_6$) with chitosan or 1-butyl-3-methyl-imidazolium tetrafluoroborate ($BMIMBF_4$) with Nafion membranes increase the conductivity of the membranes and yielded a suitable matrix for direct

electrochemistry of horseradish peroxidase and hemoglobin. Horseradish peroxidase and hemoglobin were reported to show direct electron transfer between the protein and the supporting electrode when entrapped in these composite films. These composite films also provide a good microenvironment for horseradish peroxidase and hemoglobin to retain their catalytic activity towards $O_2$, $H_2O_2$ or trichlroacetic acid [109]. Adding a sol-gel solution, a more sophisticated composite film was formed. The resulting sol/ethyl-3-methyl-imidazolium tetrafluoroborate ($EMIMBF_4$)/Nafion/carbon electrode serves as a suitable matrix to adsorb horseradish peroxidase [168]. RTILs were used as binders for graphite powder in carbon paste electrodes, which provide a great platform for direct electrochemistry and electrocatalysis of horseradish peroxidase and hemoglobin[169]. Carbon nanotubes, carbon microbeads have been reported to mix with RTILs and produce carbon composite films that promote direct electron transfer and electrocatalytic activity of heme proteins and glucose oxidase. In particular, carbon nanotubes have been demonstrated to be physically cross-linked in RTILs, yielding gels [109].

According to the review article in 2008 [109], the redox potentials for the heme proteins including myoglobin, hemoglobin and horseradish peroxidase, whose redox sites have similar structures, were roughly identical, ca. –0.34 V vs Ag/AgCl, whatever the method of electrode modification. The authors concluded that the structures of the heme proteins were intact in the ionic liquid composite films. UV-visible spectroscopy demonstrated that these proteins did not change their structures in the RTIL films. However, UV-vis analyses used transparent quartz, glass-slide, or Indium tin oxide (ITO) substrates, which may not have the strong affinity with the heme that graphite electrode surfaces have. So Groot et al. proposed that the strong affinity of the heme for

adsorbing onto the graphite electrode surfaces causes the heme to release out of myoglobin native structure [170].

### 2.5.2 Ionic Liquids as Electrolytes

However, direct electron transfer between electrode and protein in pure ionic liquids is more difficult than in conventional aqueous media, because the complete anhydrous environment provided by ionic liquids can change the protein structures. Such change of protein structures can be deleterious to enzyme activity [171]. To my best knowledge, only heme proteins and enzymes have been proven to achieve direct electron transfer with electrode. In 2003, Compton and co-workers reported that cytochrome *c* directly transfers electron to gold electrodes through mercaptoalkanoic acid/mercapto alcohol monolayer surface in $BMIMPF_6$. However, they reported that cytochrome *c* cannot retain its redox activity for long in ionic liquids[172].In 2005, a partially controversial study was reported. In the paper, the electrochemistry and electrocatalysis of some heme proteins entrapped in agarose hydrogel films in the RTIL 1-butyl-3-methylimidazolium hexafluorophosphate ([bmim][$PF_6$]) were investigated. UV-vis and FTIR spectroscopy show that the heme proteins retain their native structure in agarose film. The uniform distribution of hemoglobin in agarose-dimethylformamide film was demonstrated by atomic force microscopy. Cyclic voltammetry shows that direct electron transfer between the heme proteins and glassy carbon electrode is quasi-reversible in [bmim][$PF_6$]. The redox potentials for hemoglobin, myoglobin, horseradish peroxidase, cytochrome c, and catalase were found to be more negative than those in aqueous solution. The heme proteins catalyze the electroreduction of trichloroacetic acid and tert-butyl hydroperoxide in [bmim][PF6] [173]. A

controversial comment paper re-examined the electrochemical results presented in this work and proposed that the structures of the heme proteins changed in ionic liquids and that heme, which may be fully or partially removed from the protein, is responsible for the observed electrochemical reaction [174]. In 2010, Lojou and co-workers reported that catalytic oxidation of $H_2$ via *Desulfovibrio fructosovorans* [NiFe] hydrogenase(Df Hase) mediated by *Desulfovibrio vulgaris Hildenborough*cytochrome c3 (DvH cytc3) failed. By using hyperthermophilic [NiFe] membrane-bound hydrogenase from *Aquifex aeolicus* (Aa Hase), direct $H_2$ oxidation was not observed in pure RTIL, but an efficient direct catalytic oxidation process was obtained in mixed aqueous buffer/RTILs electrolytes. Chronoamperometric experiments showed that Aa Hase could afford 80% RTILs in aqueous buffer [175].In 2013, Bilirubin oxidase was reported to show zero catalytic activity in neat ILs. However, BOD-induced catalytic currents were observed when small quantities of water were added to hydrophobic ILs[176].

Successful direct electron transfer between proteins and electrodes in ionic liquids is important, because it opens the door to developing biofuel cells and biosensors using ionic liquids. Ionic liquids circumvent the problems brought by the traditional aqueous electrolytes in biofuel cells and biosensors, i.e. the high volatility of water, and limited temperature and pH range to guarantee protein stability.

However, no successful direct electron transfer between hydrogenases, bilirubin oxidases or carbon monoxide dehydrogenases in neat ionic liquids has been reported. In the next six chapters, readers will see how I have attempted to apply ionic liquids in biofuel cells and electrocatalytic reduction of $CO_2$ to CO.

# 3 Experimental Theory and Methods

## 3.1 Protein Film Electrochemistry

Protein film electrochemistry (PFE) is a technique investigating electrocatalytic properties of enzyme films adsorbed at electrodes. Between the electrode and enzyme, there was direct electron transfer (Figure 3.1). Figure 3.1 depicts a model of the electron transfer between the electrode and enzyme. In this model, the catalytic current flow has three separate stages, analogous to a series of resistors: $\Omega_{E,}$ $\Omega_{cat,}$ and $\Omega_{trans}$.

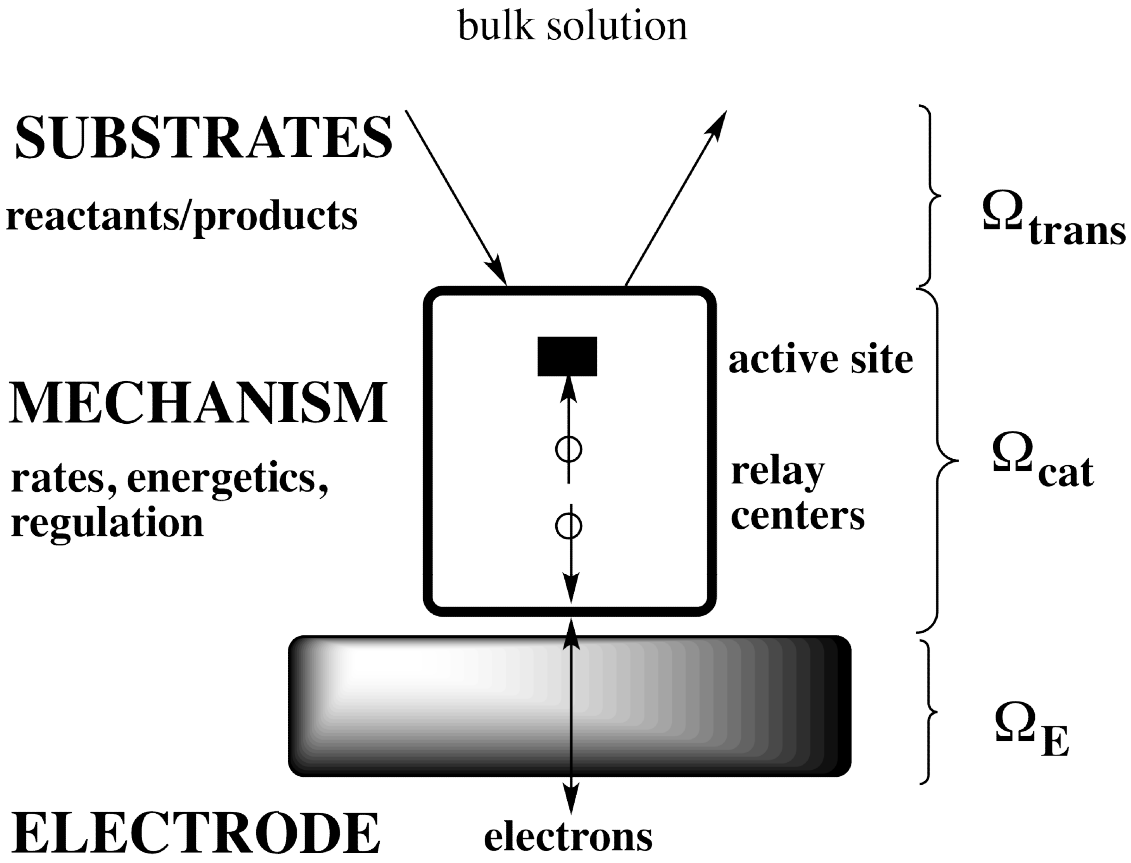



Figure 3.1 Model of protein film electrochemistry. Catalytic electron flow through an enzyme on an electrode in which the possible rate-determining stages are represented by resistors in series. The electron entry/exit site is the lower one of the relay centres indicated as circles. Adapted from ref [177].

The first factor determining the catalytic current is the interfacial electron transfer rate between the electrode and the electron entry/exit site of the enzyme ($1/\Omega_E$). $1/\Omega_E$ is related to the standard interfacial electron transfer rate $k_0$, which depends on the location of the electron entry/exit site of the enzyme and how effectively at least one of these centres (the electron entry/exit site) makes electronic contact with the electrode surface[64]. The actual interfacial electron transfer rate $k_E$, which relates to $k_0$, increases exponentially with overpotential ($E-E^{0'}$) in a reasonably small potential range, according to (eq 3.1 A for oxidation reaction and 3.1 B for reduction reaction),

$$k_E(\text{ox}) = k_0 \exp[\alpha n f(E-E^{0'})] \qquad (3.1\text{ A})$$

$$k_E(\text{red}) = k_0 \exp[-(1-\alpha) n f(E-E^{0'})] \qquad (3.1\text{ B})$$

where $f = F/RT$ and $\alpha$ is known as the transfer coefficient (a typical value is 0.5). The current i in either direction is proportional to the rate of electron flow by the equation (3.2),

$$i = nFk\Gamma A \qquad (3.2)$$

where $\Gamma$ is the electroactive coverage of the enzyme molecules and $A$ is the electrode surface area. Combining eq. 3.1 and 3.2 gives the equation for net current for any potential value $E$, also known as Butler-Volmer equation:

$$i_E = i_0(\exp(\alpha n f(E-E^{0'})) - \exp(-(1-\alpha) n f(E-E^{0'})) \qquad (3.3)$$

When $i_0$ is sufficiently large that fast interfacial electron transfer is achieved with little or no overpotential, the reaction is “reversible”. In this case, both cathodic ($i_c$) and anodic ($i_a$) contribute to the net current significantly. On the contrary, if $i_0$is small, a high overpotential is required to induce current flow, and the reaction is “irreversible”.

If the oxidative process is driven, then the corresponding reductive component is vanishingly small. Equally, at overpotentials that drive reductive process, negligible oxidation currents flow. The Butler-Volmer equation simplifies to eq. 3.4A and B for anodic and cathodic reactions, respectively. Eq. 3.4A and B are also known as Tafel equation.

$$\ln i = \ln i_0 + \alpha f(E - E^{0'}) \qquad (3.4A)$$

$$\ln i = \ln i_0 - (1-\alpha) f(E - E^{0'}) \qquad (3.4B)$$

The second factor is the inherent activity of the enzyme ($1/\Omega_{cat}$). When the other two factors are not rate determining, the current in PFE reflects the enzyme catalysis only. The maximum catalytic current obtained in an experiment at saturating substrate concentration is directly related to the inherent activity $k_{cat}$, as shown in eq. 3.5.

$$k_{cat} = i_{lim}/nFA\Gamma \qquad (3.5)$$

where $k_{cat}$ is the turnover frequency of the enzyme, $i_{lim}$ is the maximum catalytic current, and other terms have been identified previously.

The third factor is the mass transport rate of substrates of the enzymes at electrode ($1/\Omega_{trans}$). This factor can be eliminated when the electrode is rotating at a sufficiently high rate according to the Koutecky−Levich equation (eq 3.6),

$$\frac{1}{i_{lim\,(\omega)}} = \frac{1}{i_{lim}} + \frac{1}{0.62nF \quad {}^{2/3}\nu^{-1/6}\omega^{1/2}C} \qquad (3.6)$$

where $D$ is the diffusion coefficient of the substrate, $\nu$ is the kinematic viscosity of the solvent, $\omega$ is the electrode rotation rate, $C$ is the concentration of the substrate, $i_{lim(\omega)}$ is the limiting (plateau) current at rotation rate $\omega$, $i_{lim}$ is the maximum limiting current achieved at infinite rotation rate, and other terms have already been defined[37].

The sum of the three factors $1/\Omega_{E,}$ $1/\Omega_{cat,}$ and $1/\Omega_{trans}$ indicates the capability of the series for fast electron.

Using PFE alongside molecular biology, crystallography, and spectroscopy enables better understanding of structures and reaction mechanism of enzymes. PFE typically requires minuscule sample quantity (less than a picomole), whereas spectroscopic measurements require large amounts of enzymes (e.g. a typical EPR sample may contain several milligrams (tens of nanomoles) of enzyme).

In this thesis, I did two types of PFE experiments: cyclic voltammetry and chronoamperometry. Chronoamperometry is a measure of current as a function of time. The potential is kept constant or varied in potential steps.

## 3.2 Cyclic Voltammetry

In cyclic voltammetry, the potential is linearly swept at a constant rate between two limits, in a cyclic fashion, and the current response is recorded. The current is then typically displayed as a function of potential. The current recorded in a cyclic voltammogram consists of two components, anon-Faradaic and a Faradaic component.

### 3.2.1 Non-Faradaic Current

Non-Faradaic current is formed by what is referred to as the ‘electrical double-layer’. The electrical double-layer arises as a result of a build up of charge at the electrode-solution interface. For a given potential, there will be either a deficiency or excess of electrons at the electrode surface. The interface as a whole must maintain electrical neutrality and so the charge on the electrode, $q^m$, must be matched by an equal but

opposite charge at the solution interface, $q^s$, (i.e. $q^m = q^s$). This is acheived by the redistribution of ions at the electrode-solution interface, leading to an excess of either anions or cations (depending upon the charge of the electrode) near the electrode surface. As the applied potential is varied, the electrode-solution interface behaves like a capacitor as the charges at the interface rearrange, resulting in current flow between the working and counter electrode (in the case of a three-electrode system).

The charge on a capacitor, q, can be described by the product of the potential across the capacitor, E, and the capacitance, C:[37]

$$q = EC \tag{3.7}$$

The current, $i$, produced as the potential is modulated is equal to the change in charge with time:

$$i = \frac{dq}{dt} = C\frac{dE}{dt} \tag{3.8}$$

In cyclic voltammetry the change in potential with time ($\frac{dE}{dt}$) is simply the scan rate ($\nu$) so that:

$$i = C\nu \tag{3.9}$$

### 3.2.2 Faradaic Current

The oxidation or reduction of an electroactive species at an electrode, which occurs alongside electron transfer between the electroactive species and the electrode surface, results in Faradaic current. In cyclic voltammetry, the Faradaic currents arising from

these redox processes will be superimposed upon the non-Faradaic `background' current discussed above.

Under equilibrium conditions there is no net flow of electrons and the ratio of the concentrations of oxidised and reduced species adsorbed on the electrode surface is given by the Nernst equation (derived in Appendix); [37]

$$E=E^{\ominus}-\frac{RT}{nF}\ln\frac{[\text{ox}]}{[\text{red}]} \qquad (3.10)$$

where $E$ is the equilibrium potential, $E^{\ominus}$is the standard reduction potential for the redox couple, $R$ is the gas constant, $T$ is the temperature in Kelvin, $n$ is the number of electrons involved in the process, $F$ is Faraday's constant and [Ox] and[Red] are the concentration of the electroactive species in the oxidised and reduced states respectively.

In dynamic electrochemistry experiments such as cyclic voltammetry or linear sweep voltammetry, a potential is applied which induces a current to flow. In a PFE experiment, this current provides a measure of the catalytic activity of the enzyme adsorbed onto the electrode surface. Importantly, in non-ideal situations different processes may contribute to the overall activity of the enzyme-modified electrode and so the observed current may not be a direct measure of the inherent activity of the catalytic centre of the enzyme. Experiments should be designed to minimise these processes as far as possible, ensuring that they are not rate limiting and that the observed current is a true reflection of the rates and potentials of catalytic processes. The various non-catalytic processes that may affect the Faradaic current recorded during a PFE experiment are the rates of interfacial electron transfer ($1/\Omega_E$) and mass transport ($1/\Omega_{trans}$), which have been introduced earlier in the chapter.

## 3.3 Chronoamperometry

Chronoamperometry is a measure of current as a function of time. The potential is kept constant or varied in potential steps[37]. Chronoamperometry has been used to measure the stability of catalytic currents in bioelectrochemistry. This technique is also useful when determining the rates of processes such as enzyme inactivation and reactivation because, unlike in cyclic voltammetry, the potential and time domains are deconvoluted.

Similar to cyclic voltammetry experiments, chronoamperometry measurements consist of both Faradaic and non-Faradaic components: upon a change in potential, the non-Faradaic response will be observed as a charging current superimposed upon the enzymatic Faradaic current. The non-Faradaic charging current decays exponentially with time and is significant for approximately the first 10 s following a potential step [178].

## 3.4 The Three-Electrode System

The electrochemical cell for PFE is a typical three-electrode system. A voltage, E, applied between a working electrode and a reference electrode, can be described by Equation 3.11(assuming that a finite current $i$ is flowing between the two electrodes):

$$E = (\Phi_w - \Phi_S^w) + iR_S + (\Phi_S^{REF} - \Phi_{REF}) \quad (3.11)$$

where $\Phi_w$ and $\Phi_{REF}$ are the electric potentials of the working and reference electrodes,and $\Phi_S^w$ and $\Phi_S^{REF}$ are the electric potential of the solution close to the working and reference electrode respectively. The term $iR_S$represents the voltage drop in solution of electrical resistance $R_S$ due to the passage of current $i$ between two electrodes.

In an ideal case, often seen in microelectrode experiments, $iR_S$is negligible and the potential drop at the reference electrode/solution interface ($\Phi_S^{REF} - \Phi_{REF}$) is fixed by the chemical composition of the reference electrode. In turn, changes in the applied potential are simply reflected as changes in ($\Phi_w - \Phi_{REF}$). However, with large electrodes, $iR_S$ is no longer negligible and thepassage of large currents through the reference electrode may change its chemicalcomposition, altering ($\Phi_S^{REF} - \Phi_{REF}$).

So a three-electrode system using a counter electrode is used for accurate measurement of ($\Phi_S^{REF} - \Phi_{REF}$). In this system (Figure 3.2), current flows between the working and counter electrodes whilst the potential of the working electrode relative to the reference electrode is measured using a device with high resistance, ensuring that only a very small amount of current is drawn through the reference electrode and so its potential remains constant.

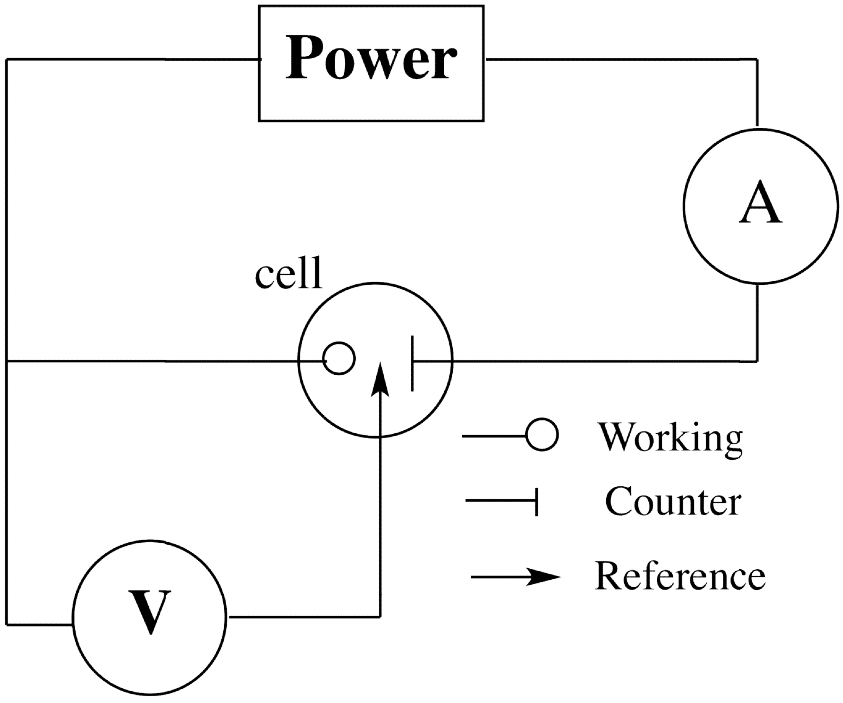



Figure 3.2 A schematic circuit diagram of the three-electrode system. Figure adapted from ref [37].

The all-glass electrochemical cells were constructed by Mrs Terri Adams in ICL Glass Workshop. The electrochemical cells for PFE in aqueous buffers (Figure 3.3 and 3.4) and ionic liquids (Figure 3.5 and 3.6) are different in reference electrode compartment and gas supply. The reference electrode compartment of electrochemical cell for aqueous experiments contains aqueous salt electrolyte (NaCl and $Na_2SO_4$ in this thesis) or standard calomel electrode (Figure 3.3 and 3.4). On the other hand, the reference electrode compartment of electrochemical cell for ionic liquid experiments contains ionic liquid of interest and a Pt wire as quasi-reference electrode (Figure 3.5 and 3.6).

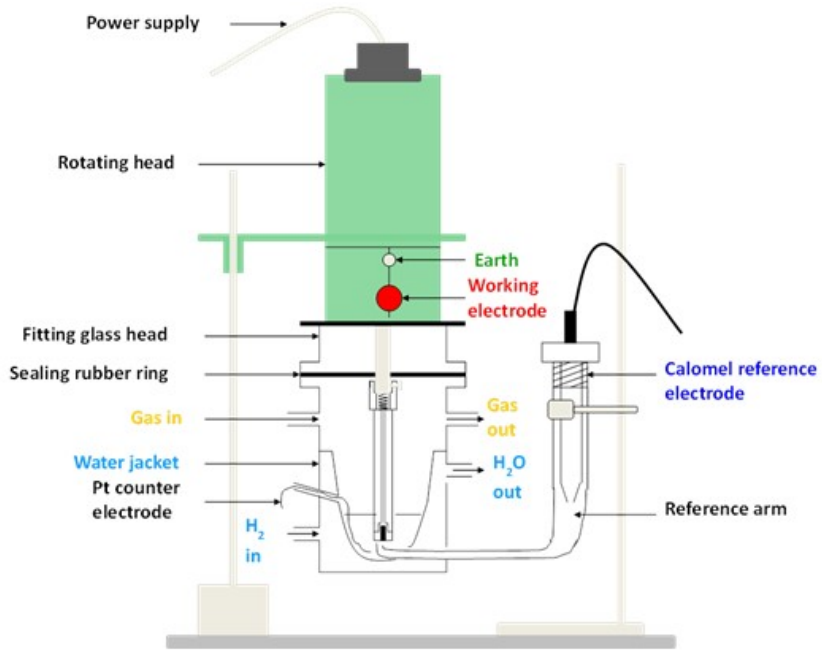



Figure 3.3 Schematic diagram of the glass electrochemical cell used for protein film electrochemistry in aqueous buffers. A Pt wire counter electrode enters the working electrode compartment of the cell through a rubber septum. The working electrode compartment holds aqueous buffer. Above the aqueous buffer, gases are introduced to the cell via a gas inlet. The reference electrode compartment holds 0.1 M NaCl

electrolyte. The sidearm of the reference electrode compartment was connected to the working electrode compartment via a Luggin capillary. The reference electrode is saturated calomel electrode. Adapted from ref [179].



Figure 3.4 Photo of the all-glass electrochemical cell used for protein film electrochemistry in aqueous buffers. Bar, 5 cm.

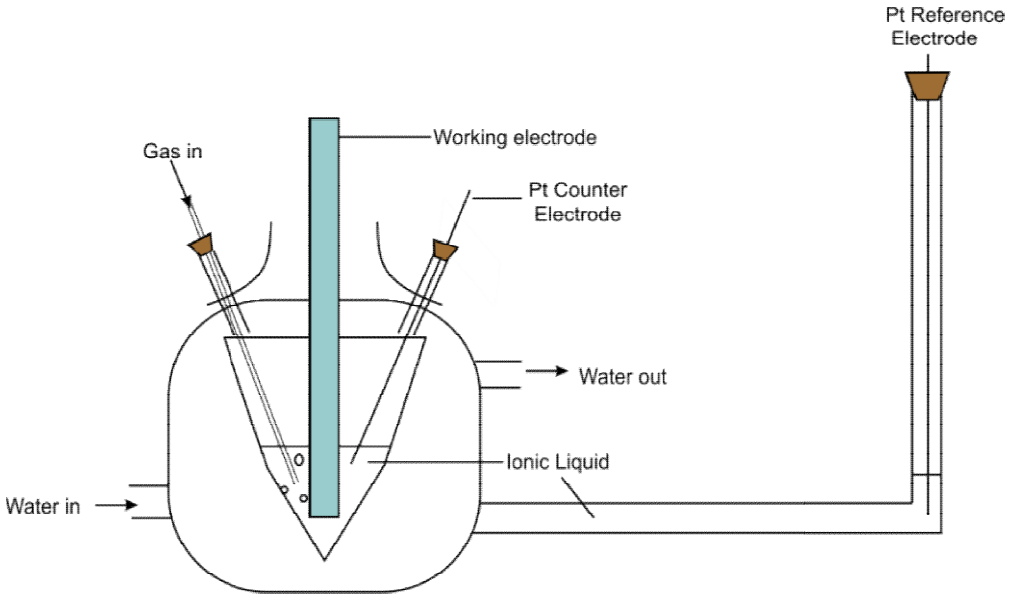



Figure 3.5 Schematic diagram of the glass electrochemical cell used for protein film electrochemistry in ionic liquids.Gases are introduced to the cell via a needle through a rubber septum. A Pt wire counter electrode enters the working electrode compartment of the cell through another septum. Both the working and reference electrode compartment hold the same IL. The sidearm of the reference electrode compartment was connected to the working electrode compartment via a Luggin capillary. The other Pt wire enters the sidearm to serve as a quasi-reference electrode.



Figure 3.6 Photo of the all-glass electrochemical cell used for protein film electrochemistry in ionic liquids. Bar, 5 cm.

All potentials measured in aqueous phases in this thesis have been corrected to give the potential value with respect to SHE using the relation[37]:

$$E_{SHE}(V) = E_{SCE}(V) + [0.2412 - 6.61 \times 10^{-4}(T-25) - 1.75 \times 10^{-6}(T-25)^2 - 9.0 \times 10^{-1}\ (T-25)^3$$

where T is the temperature of the reference electrode environment in degrees Celsius.

### 3.4.1 Experimental Procedures of Protein Film Electrochemistry in Aqueous Phases

Voltammograms of BOD in atmosphere were recorded with an Autolab PGSTAT 20controlled by GPES. Voltammograms of Hyd1 in anaerobic condition were recorded

with an Autolab PGSTAT 10controlled by NOVA software (version 1.10) in an anaerobic glove box (Tech Ltd., $O_2$< 4 ppm). The all-glass electrochemical cell and PGE working electrode were described earlier [5, 6]. The all-glass electrochemical cell consisted of a main compartment and a sidearm. The main compartment of the cell housed the working electrode, the platinum wire counter electrode and buffer (~ 2 mL). Gases were flushed through the sealed headspace of the main compartment.The main compartment was thermostated with a water jacket. The sidearm compartment was filled with 100 mM NaCl (for Hyd1) or $Na_2SO_4$ (for BOD, because dissolved BOD is inhibited by halides [24, 180]), housing a saturated calomel (SCE)as reference electrode. The sidearm compartment was connected to the main compartment via a Luggin capillary and kept close to 25 ˚C. Potentials were converted to the standard hydrogen electrode using the formula $E_{SHE}=E_{SCE}$ + 0.241 V at 25˚C.

The enzyme-modified electrode (see above) was introduced into the working electrode compartment of the electrochemical cell containing aqueous buffer. A mixed buffer (pH 6, 100 mM)[92] was used for Hyd1. A phosphate buffer (100 mM, pH 5 and 6.2) was used for BOD. All solutions in the electrochemical cell were free from enzymes. The total gas flow rate was 200 standard cubic centimetres $min^{-1}$, controlled precisely by flow meters (Sierra Instruments).

### 3.4.2 Experimental Procedures of Protein Film Electrochemistry in Ionic Liquids

Cyclic voltammograms of Hyd1 in anaerobic condition were recorded with an Autolab PGSTAT 10 controlled by NOVA software (version 1.10) in an anaerobic

glove box (Tech Ltd., $O_2$< 4 ppm). Cyclic voltammograms of BOD or Hyd1 in atmosphere were recorded with an Autolab PGSTAT 20 controlled by NOVA software (version 1.10). The all-glass electrochemical cell consisting of a main compartment and a sidearm and PGE working electrode was described earlier [30, 79]. The main compartment was thermostated with a water jacket. The setup for electrochemical experiments in ILs (Figure 3.5 and 3.6) was different from that in aqueous buffers (Figure 3.3 and 3.4). The main compartment of the cell housed the working electrode, the platinum wire counter electrode, IL (~ 1 mL) and a needle to pass gases into IL. The sidearm compartment was filled with the same IL, housing a Pt wire as a quasi-reference electrode. The sidearm compartment was connected to the main compartment via a Luggin capillary. The electrochemical cell was thoroughly dry. All electrodes were also completely dry except the area modified by enzyme films.

In a typical experiment, the PGE electrode was sanded with P400 sandpaper, rinsed and sonicated in purified water (18.2 MΩ cm at 25 ˚C) for 30 min. Then the PGE electrodes were covered by 5 μL of MWNT dispersion (2.5 mg $mL^{-1}$ in DMF). The MWNT dispersion was left to dry for 1 h. The enzyme-coating procedures for BOD and Hyd1 were slightly different. 1 or 2 μL of BOD was pipetted to the MWNT covered area of MWNT/PGE electrode on bench. The BOD film was left to stabilize on the electrode for 1 min, before the electrode was immersed in IL for voltammetry. Unlike BOD, Hyd1 was first activated by flowing $H_2$ above the enzyme solution for 0.5 h in an anaerobic glove box filled with $N_2$. Then 1 or 2 μL of the activated Hyd1 was pipetted to the MWNT/PGE electrode for cyclic voltammetry on bench or in an anaerobic glove box filled with $N_2$. The Hyd1 film was left to stabilize on the electrode for 1 min, before the electrode was immersed in IL for voltammetry. Enzyme films were prevented from

being completely dry on electrodes; otherwise negligible electrocatalytic activity was detected in ILs.

Because Pt quasi-reference electrode was used in the voltammetry, we calibrated all cyclic voltammograms against the reversible formal potential, $E_f^\circ$ ($E_f^\circ = E_{1/2} = (E_p^{red} + E_p^{ox})/2$, where $E_p^{red}$ and $E_p^{ox}$ are reduction and oxidation peak potentials, respectively) of $DmFc^{+/0}$, which is widely recognized as a reliable internal reference in a variety of nonaqueous solvents [144, 181]. This method neglects the possible difference on D coefficients between the neutral and charged species ($E_{1/2} = E^\circ + RT/(2F)$ ln $(D_r/D_0)$). To determine the $E_f^\circ$ of DmFc vs Pt wire, I performed cyclic voltammetry at a bare PGE electrode in ILs dissolved with 2 mM of DmFc after each set of Hyd1 film voltammetry. In initial experiments, DmFc was added after the completion of enzyme film electrochemistry in ILs to avoid complication of determining catalytic currents by Hyd1 electrocatalysis in cyclic voltammetry. 2 mM DmFc was dissolved in IL (~1mL) that was withdrawn from the working compartment after a series of voltammetry,by heating at 100 ˚C and stirring under vacuum for 1 h. Meanwhile, IL in the Luggin capillary and sidearm was remained intact. Then the IL dissolved with 2 mM DmFc was returned to the working electrode compartment mentioned above. The reversible formal potential, $E_f^\circ$ of $DmFc^{+/0}$ was measured by cyclic voltammetry of a bare PGE electrode in ILs in atmosphere. All cyclic voltammograms were referenced against $E_f^\circ$ of $DmFc^{+/0}$ vs Pt wire in ILs at 30 ˚C, 10 mV/s. The $E_f^\circ$ of $DmFc^{+/0}$ vs Pt wire was determined no later than three days after corresponding voltammetry of enzymesto ensure the accuracy of potential values. To confirm the validity of this method for calibrating the potentials of enzyme film voltammetry in ionic liquids, I carried out cyclic voltammetry in

EMIMTFSI dissolved with 2 mM DmFc and saturated with substrate gases. The results show that the potentials vs. $DmFc^{+/0}$obtained using both procedures are equal.

## 3.5 Materials

Multi-walled carbon nanotubes (MWNT, carbon > 95 %, produced by catalytic chemical vapour deposition, in powder form, outer diameter 6-9 nm, inner diameter 5.5 nm (mode), 6.6 nm (median), length 5 μm) were obtained from Sigma-Aldrich and used as received. Dithiothreitol was obtained from Melford. Bradford reagent was obtained from Sigma-Aldrich. Hydrazine hydrate was obtained from Alfa Aesar. Natural graphite flakes (325 mesh) were obtained from Alfa Aesar. Polytetrafluoroethy (PTFE) was obtained from Alfa Aesar. Conductive silver paint was obtained from Argar Company. Adhesive copper tape (0.04 mm thick, 9.52 mm wide, as received: resistance 0.005 Ω through adhesive) and P400 sandpaper were obtained from RS Components. All water used for electrochemical measurements was purified by reverse osmosis and ion exchange to a resistivity of 18.2 MΩ cm at 25 ˚C in a Milli-Q water purification system. The pH of all solutions used for electrochemical studies was determined at the temperature used for measurements. Pyrolytic graphite 'edge' (PGE) disk electrodes (geometric area of graphite: 0.03 $cm^2$) were made from pyrolytic graphite blocks (Momentive Performance Materials Ltd.), and used for all the voltammetric experiments.$H_2$ and $O_2$ were of technical grade and were supplied by compressed gas cylinders from British Oxygen Company. Gas flows were controlled precisely by mass-flow controllers (Sierra Instruments). All other chemicals and solvents were of analytical grade.

1-Ethyl-3-methylimidazolium bis(trifluoromethylsulfonyl)imide (EMIMTFSI, > 99%), 1-methyl-1-propyl pyrrolidinium bis(trifluoromethylsulfonyl)imide (PMPyrTFSI, > 99%), ethylammonium nitrate (> 99%) and diethylmethylammonium trifluoromethanesulfonate (> 99%) were obtained from Iolitec. Tris(2-hydroxyethyl)methylammonium methylsulfate (TEMAMS) was obtained from Sigma-Aldrich. All ionic liquids were heated at 100 ˚C under vacuum for 24 h before use. Decamethylferrocene (DmFc) was obtained from Sigma-Aldrich. A dispersion of MWNT (2.5 mg $mL^{-1}$) in dimethyl formamide (DMF) was achieved by ultrasonication for 2 h at room temperature.

## 3.6 Enzymes

### *3.6.1* Hydrogenase1 from *E.coli*(Hyd1)

Hyd1was isolated as described previously [77] with the kind help of Ms. Elena Nomerotskaia from Prof. Armstrong's group. Purified Hyd1 solution (1.01 mg $mL^{-1}$ in buffer C (Tris buffer containing 0.35 M NaCl, 1mM dithiothreitol, 0.02% Triton X-100, pH 7.2 at 5 ˚C)) was used throughout this thesis.

### 3.6.2 Bilirubin Oxidase

BOD (obtained from Amano Company, Japan) was isolated as described in the following steps using ÄKTA protein purification system [79].

1. Sample preparation: Weigh 50 mg BOD into falcon tube. Dissolve BOD into 20 mL of buffer A (Sodium phosphate 50 mM, Ammonium sulphate 1.7 M, pH 7.0 (at 5 °C).

2. Load Column: Hi Trap Phenyl HP 5 ml to ÄKTA protein purification system.

3. Pump wash A and B lines with water.

4. Set up wavelength 280 nm and 610 nm, autozero UV spectrometer.

5. Wash column with water (5 mL/min, 50 mL).

6. Pump wash A and B lines with buffers A and B (Sodium phosphate 50 mM, pH 7.0 at 5 °C).

7. Wash column with buffer A (5 mL/min, 50 mL).

8. Load BOD solution prepared in Step 1 onto the column (2 mL/min).

9. Wash the cylinder with 20 mL of buffer A (3 mL/min).

10. Wash the cylinder with 20 mL of buffer A (3 mL/min)

11. Put line A into buffer A, wash the column (5 mL/min, 50 mL).

12. Elute BOD using linear gradient (100% B in 20 minutes, 3 mL/min, 1.5mL fractions, outlet valve F2, autozero UV, wavelength 280 nm and 610 nm, 60 mL).

13. Collect fractions (about 8 fractions for the peak of the UV spectra, 6 for the tails of the UV spectra).

14. Concentrate using 50K concentrator on bench top centrifuge (3700 rpm, 4°C) to 0.5 mL.

15. Distribute concentrated BOD solution amongst Eppendorf tubes (10µL aliquots), freeze flash the BOD samples in liquid nitrogen.

16. Keep 10 µL in Eppendorf tube for determining the concentration via Bradford assay.

17. Put Eppendorf tubes into −80 °C freezer.

18. Pump-wash the ÄKTA protein purification system with DI water.

19. Wash the column with DI water (4 mL/min, 25 mL).

20. Pump-wash lines A and B with 20% ethanol.

21. Wash fractions collector line with 20% ethanol (4mL/min, outlet valve F2, 1.5 mL fractions, 10mL)

22. Clean the column with 20% ethanol (4 mL/min, 200 mL).

A solution of purified BOD (12.09 mg $mL^{-1}$ in 50 mM phosphate buffer, pH 7.0 at 5 ˚C) was obtained and stored at −80 ˚C, which was used throughout the whole thesis.

### 3.6.3 Concentration of Protein

The concentration of protein in enzyme samples were determined by Bradford method [182]. This method is based on the principle that the binding of the dye Coomassie Brilliant Blue G-250 to protein causes a shift in absorption maximum of the dye from 465 to 595 nm.

In a typical experiment, 500µL of 100 µg/mL bovine serum albumin solutions (BSA) stock solution (e.g. 25 µL of 2 mg/mL stored solution in 475 µL $H_2O$) is made. Then the following BSA-standard aliquots in Eppendorf tubes were made (Table 3.1).

Table 3.1 Calibration with BSA protein standard.

| **BSA concentration** | **Volume of 100 µg/mL BSA stock solution** | **Volume of $H_2O$** | **Recorded $A_{595}$** |
|---|---|---|---|
| 20 µg/mL | 100 µL | 400 µL | |
| 15 µg/mL | 75 µL | 425 µL | |
| 12 µg/mL | 60 µL | 440 µL | |
| 10 µg/mL | 50 µL | 450 µL | |
| 8 µg/mL | 40 µL | 460 µL | |
| 6 µg/mL | 30 µL | 470 µL | |
| 4 µg/mL | 20 µL | 480 µL | |
| 2 µg/mL | 10 µL | 490 µL | |
| 0 µg/mL | 0 µL | 500 µL | *Blank* |
| 0 µg/mL | 0 µL | 500 µL | *Blank* |

Then enzyme samples were prepared and calibrated against BSA standards in the following steps:

1. Add 693 of water 7µL of enzyme sample, giving 700 µL of a sample diluted by 100 times.

2. Similarly, prepare 500 µL of samples diluted by 500, 1000,2000and, if needed, 200 times, using the sample diluted by 100 times from step 1.

3. Add 800 µL of Bradford reagent to each aliquot of BSA standards and diluted enzyme samples. Incubate the mixtures for 15mins.

4. Set UV-Vis spectrometer to measure absorption at 595 nm ($A_{595}$).

5. Transfer aliquots into disposable UV cuvettes (to save pipette tips move from low to high concentrations). Use blanks (0µg/mL BSA) to zero spectrometer.

6. Measure BSA standard aliquots and enzyme samples in quick succession.

7. Plot recorded $A_{595}$ against BSA concentration to obtain the linear calibration curve (Figure 3.7).

8. Use linear equation to calculate enzyme concentrations from measured $A_{595}$.

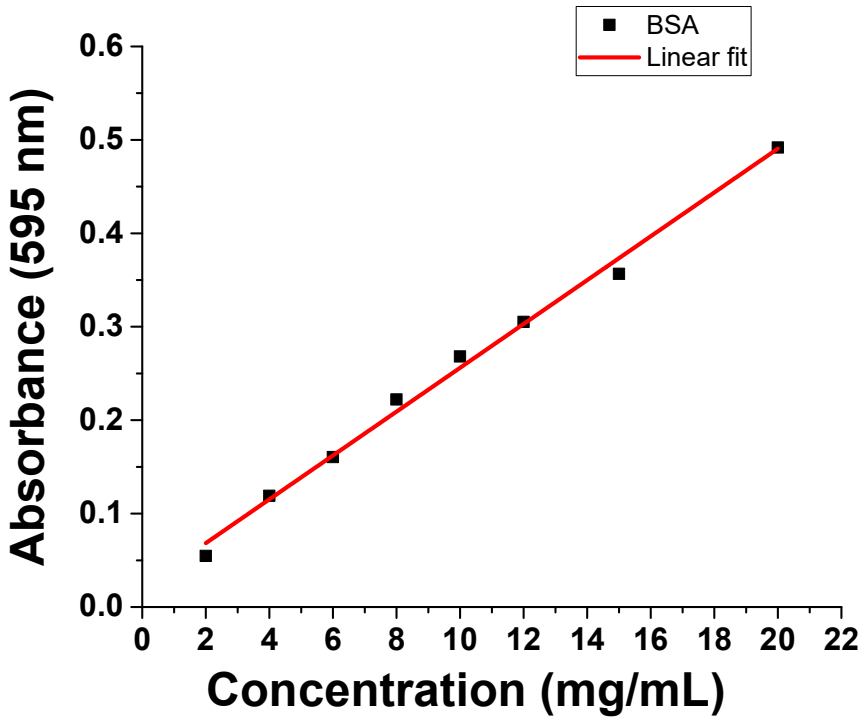



Figure 3.7 A typical calibration line in a Bradford assay. The black dot represents the absorbance of Bradford reagent in bovine serum albumin (BSA) solution.

## 3.7 Buffers

### 3.7.1 Mixed Hydrogenase Buffer

This buffer was used for the electrochemical experiments in Chapter 4, 5 and 7. Mixed hydrogenase buffer was prepared by mixing sodium chloride (100 mM), MES (15 mM), HEPES (15 mM), TAPS (15 mM), CHES(15 mM), sodium acetate (15 mM). In the end, sodium hydroxide or hydrochloric acid was added into the solution to achieve pH 6.0 at 30 ˚C.

### 3.7.2 Phosphate Buffer

Phosphate buffer was used for the electrochemical experiments in Chapter 4, 6 and 7. Phosphate buffer (pH 5.0, 100 mM) was prepared by mixing monosodium phosphate (Fisher) and disodium phosphate (Fisher) at appropriate ratios at 10, 25, 30, 40 ˚C. Phosphate buffer (pH 6.2, 100 mM) was prepared by mixing monosodium phosphate (Fisher) and disodium phosphate (Fisher) at appropriate ratios at 30 ˚C.

### 3.7.3 Borate Buffer

Borate buffer was used for the electrochemical experiments in Chapter 6. Borate buffer (pH 9.0 and 11.0, 100 mM) was prepared by mixing sodium hydroxide (Fisher) and sodium tetraborate (Fisher) at appropriate ratios at 30 ˚C.

# 4 Electrodes of Carbon Nanomaterials

## 4.1 Abstract

Enzymatic fuel cells use isolated enzymes as electrocatalysts to convert the chemical energy of fuels into electrical energy. Efficient enzyme wiring at electrodes of enzymatic fuel cells is important for the performance, i.e. power density (per electrode surface area) and stability, of enzymatic fuel cells. Here I use carbon nanomaterials including graphene and carbon nanotubes to support hydrogenase and bilirubin oxidase. I found that graphene and carbon nanotubes can increase the electrocatalytic activity of Hydrogenase 1 and bilirubin oxidase compared to conventional PGE electrodes. Therefore, graphene and carbon nanotubes are promising candidates for electrode materials of enzymatic fuel cells.

## 4.2 Introduction

The recent emergence of nanomaterials and nanotechnology has opened new horizons in designing electrodes for modification of electrode surfaces with biological entities (mainly enzymes, but also antibodies, whole cells, tissues, etc.). The nanoscale design of electrode surfaces is indeed likely to provide novel and sometimes unique properties due to the ability of the intrinsic properties of the nanomaterials used, the ability to control the architecture of the electrode interface at the nanoscale, or both. Examples in the field of integrated bioelectrochemical systems include: (1) nanostructured deposits prepared by layer-by-layer assembly or electrophoretic deposition, (2) nanosystems based on electrodes modified with various nano-objects, e.g., nanoparticles, nanowires, nanosheets or nanotubes, (3) nanoengineered and/or ordered porous materials, either dispersed in bulk composite electrodes or deposited as thin films onto a solid electrode surface,(4) functionalized and/or conductive polymeric materials, most often used as electrode coatings, alone or encapsulating nanoparticles,or (5) organic–inorganic hybrid nanoarchitectures[183].

The main motivations of application of nanomaterials to enzymatic fuel cells are: (1) to overcome the low volume density of electrocatalytic active sites of enzymes, because nanomaterials such as graphene and carbon nanotubes have large surface-to-volume ratios [183-187], which increase the enzyme density at electrodes, (2) the elaboration of new immobilization matrices ensuring long-term operational stability for enzymes as electrocatalysts of fuel cells, (3) the enhancement of the electronic conductivity, (4) appropriate wiring of the redox active sites of enzymes to electrode surface which might be difficult, as it has been proposed that the carbon nanomaterials have aspect

ratio that approach the molecular scale, thus effectively decrease the electron tunnelling distance and improve the direct electron transfer between enzymes and electrodes.

Graphene is a flat monolayer of carbon atoms tightly packed into a two-dimensional (2D) honeycomb lattice, and is a basic building block for graphitic materials of all other carbon allotropes including graphite, charcoals, carbon nanotubes, Buckminsterfullerene and other buck balls, etc [185]. Today graphene is attracting increasing attention as a novel material with many exceptional properties, i.e. unparalleled thermal conductivity (5000 W $m^{-1}K^{-1}$), excellent electrical conductivity (1738 S $m^{-1}$), electron mobility of $2.5 \times 10^5$ $cm^2 V^{-1} s^{-1}$at room-temperature [188] (theoretical limit ~$2 \times 10^5$ $cm^2 V^{-1} s^{-1}$[189]), high surface-to-volume ratio(2630 $m^2 g^{-1}$), remarkable mechanical strength (about1100 GPa), ability to sustain extremely high densities of electric current, which is a million times higher than copper [190], and biocompatibility [183]. Graphene's superior properties indicate their potentials as electrode materials for enzymatic fuel cells and biosensors. A recent work achieved direct electron transfer between glucose oxidase and chitosan/graphene thin film [191].

Graphene has been prepared by four different methods [192]. The first is chemical vapour deposition and epitaxial growth, which has already been commercialized. The second is mechanical exfoliation of graphite, also known as the 'Scotch tape' or peel-off method [193]. This method can only yield small samples of graphene that are useful for fundamental study. The third method is epitaxial growth on electrically insulating surfaces such as SiC [194]. The fourth method is chemical synthesis of colloidal suspension of graphene [195]. This method was used in this study.

Carbon nanotubes are nanowires constituted by one (called single-walled carbon nanotubes, SWNTs) or more (called multi-walled carbon nanotubes, MWNTs)

seamlessly enrolled graphene layers with different diameters, length and chirality [196]. MWNTs comprise of several concentric cylinders of grapheme sheets, with about 3.4 Å spacing between the layers. Carbon nanotubes having diameters between 1 nm (SWNTs) and 10 nm (MWNTs) are capable of approaching the active sites of enzymes and decreasing the electron tunnelling distance. In addition, carbon nanotubes have high surface areas [183], which increases the enzyme density on electrodes; large aspect ratio, remarkable mechanical strength, excellent chemical stability [183],rich electronic properties (able to sustain extremely high densities of electric current, which is 1000 times higher than copper [183]); and are benign to enzymes and other biomolecules [196]. All these desirable properties make carbon nanotubes extremely attractive candidates for electrode materials of enzymatic fuel cells and biosensors.

Various biomolecules (proteins, nucleic acids, carbohydrates, etc.) have been conjugated to CNTs for use in bioelectronic devices. These biomolecules were often attached to the sidewall of the CNTs via either noncovalent or covalent bonding. CNTs can thus be readily functionalized with various biomolecules through a variety of linkage chemistries. Acid treatment of CNTs commonly introduces oxide groups, primarily carboxylic acids, to the tube ends and defect sites. Further functionalization with additional groups can be carried out by established bioconjugation procedures at these oxide groups (e.g., using N-ethyl-N'-(3-dimethyl-aminopropyl) carbodiimidehydrochloride (EDC) for cross-linking proteins)[30]. Such changes in the surface of CNTs usually affect their solubility. CNTs can also be functionalized with various biomolecules without their covalent coupling. CNTs bear graphene sidewalls that are chemically inert and highly hydrophobic, with a dense p –p stacking. A simple nonspecific binding scheme can be used to form non covalent protein–CNT conjugates. Noncovalent couplings are commonly based on hydrophobic interactions between a

CNT and a biomolecule. For example, various proteins can adsorb spontaneously on the sidewalls of acid oxidized CNTs. Because CNTs have remarkable mechanical strength, it is practical to compress a mixture of CNTs and enzymes to prepare freestanding 3D pellets [183].

The first application of carbon nanotubes in enzymatic fuel cell was reported by Yan *et al* [197]. In their study, the SWNTs were used as electrode materials supporting and facilitating direct electron transfer of laccase. Later, MWNT grown on carbon paper via chemical vapour deposition were applied to immobilize glucose oxidase in a glucose fuel cell [198]. MWNT pellets, which ensure an efficient wiring of the active sites of enzymes and higher enzyme density per projected electrode surface area than MWNT films, were found to pushing the limit of power density (per electrode area) of enzymatic fuel cells using glucose oxidase and laccase as anodic and cathodic electrocatalysts, respectively [61].

Hydrogenase 1 from *Escherichia coli* (Hyd1) has been under extensive investigation for application as anodic electrocatalyst in $H_2$-$O_2$ enzymatic fuel cells since 2010 [27, 30, 79], and is considered as an interesting inspirational electrocatalyst for fuel cells. BOD is an interesting candidate for catalysing reduction of $O_2$ at cathodes of enzymatic fuel cells [5].

The question remains whether Hyd1 and BOD can achieve direct electron transfer at electrodes using graphene and MWNT pellet and how do the electrodes using graphene and MWNT pellet/film compare to PGE electrodes. To evaluate graphene and MWNT as electrode materials supporting Hyd1 and BOD in enzymatic fuel cells, I performed protein film electrochemistry of Hyd1 and BOD at electrodes using electrodes using graphene and MWNT pellet/film. I found that graphene and MWNT increase the

electrocatalytic activity of Hyd1 and BOD compared to conventional PGE electrodes, because both the carbon nanomaterials have superb properties mentioned above. Therefore, graphene and MWNT are promising candidates for electrode materials of enzymatic fuel cells.

## 4.3 Experimental

Please refer to Chapter 3 for detailed information of materials, buffers, enzymes and procedures of protein film electrochemistry.

### 4.3.1 Preparation of Graphene Film Electrodes

Graphene was synthesized using the method described previously [195]. Graphene oxide dissolved in waterwas first synthesized by Hummers' method [199]. Then graphene oxide was reduced by hydrazine hydrate to produce graphene. The graphene was suspended in purified water (18.2 MΩ cm at 25 ˚C) at a concentration of 1, 5, or 10 mg/mL for comparison by sonication for 1 h. The graphene suspension (20 μL) was then pipetted to a clean PGE electrode that had been sanded with P400 sandpaper, rinsed and sonicated in purified water (18.2 MΩ cm at 25 ˚C) for 30 min. The PGE electrode was left to dry overnight under ambient conditions. Right before protein film electrochemistry, 2 μL of Hyd1 or BOD was pipetted onto the dry graphene film.

### 4.3.2 Preparation of MWNT Film Electrodes

A dispersion of MWNT (2.5 mg $mL^{-1}$) in dimethyl formamide (DMF) was achieved by ultrasonication for 2 h under ambient conditions. Then 5 μL of the MWNT dispersion in DMF was pipetted to the graphite area of a clean PGE electrode, which had been sanded with P400 sandpaper, rinsed and sonicated in purified water (18.2 MΩ cm at 25 ˚C) for 30 min. The electrode covered with MWNT dispersion was left to dry for 2 h under ambient conditions. Right before protein film electrochemistry, 2 μL of Hyd1 or BOD was pipetted onto the dry MWNT film.

### 4.3.3 Preparation of MWNT Pellet Electrodes

MWNT pellet was prepared by pressing a mixture of MWNT and Polytetrafluoroethylene (PTFE) by hydraulic press. For Hyd1, the MWNT pellet was made with 0.050 g MWNT and 0.015g PTFE under a pressure of 3 tonnes. For BOD, the MWNT pellet was made with 0.060 g MWNT and 0.015 g PTFE under a pressure of 5 tonnes. The MWNT pellets were then cut to a cylinder whose cross section is a circle (radius= 0.85 cm) and stick to a clean PGE electrode base by conductive silver paint. After the silver paint was dry, 20 μL of Hyd1 or BOD was pipetted to the MWNT electrodes. The MWNT electrodes modified with enzymes were incubated in the cold room (4 °C) for 2 h to allow sufficient permeation of enzymes into the electrodes before electrochemical characterization.

### 4.3.4 IR Spectroscopy

The IR spectroscopy was measured with the kind help of Dr. Minwen Chung from Dr. Kylie Vincent's group. Attenuated total reflection (ATR)-IR measurements used a Varian 680-IR spectrometer was placed on a table secured to the rear of the dry glove box, with the IR beam diverted into the glove box *via* a short purged enclosure and a 5 mm thick KBr window. Inside the glove box the IR beam was directed onto an off-axis parabolic focusing mirror and into an ATR accessory (GladiATR, PIKE Technologies). The ATR accessory has been custom-modified to give five reflections at an incidence angle of 39° through a Si trapezoidal ATR prism (Crystal GmbH) measuring 8.39 × 5 × 1 $mm^3$. After exiting the ATR accessory the IR beam was detected by a narrow-band Mercury Cadnium Telluride (MCT) detector cooled with liquid $N_2$. Spectra were recorded at 2 $cm^{-1}$ resolution.

## 4.4 Results and Discussion

### 4.4.1 Graphene Film Electrode

Hyd1 and BOD both show high electrocatalytic activity at PGE electrodes in aqueous buffers [47, 64, 77]. To determine the effect of graphene film on the electrocatalytic activity of Hyd1 and BOD adsorbed at electrodes, I performed cyclic voltammetry of enzymes adsorbed at PGE electrodes with and without graphene film, all rotating at 1000 RPM, at 30 °C, under 100 % substrate gases, at a scan rate of 10 mV/s. I found that the limiting electrocatalytic current densities of Hyd1 and BOD at graphene film electrode were ca. 4 and 8 times higher than at PGE electrodes, respectively (Figure 4.1 and 4.2). For Hyd1, the catalytic current densities of $H_2$

oxidation were 6.54±0.12 and 1.33±0.03 mA $cm^{-2}$ (both values were based on three parallel experiments) at +200 mV at graphene film electrode and PGE electrode, respectively (Figure 4.1). For BOD, the catalytic current densities of $O_2$ reduction were 1.14±0.17 and 0.13±0.02 mA $cm^{-2}$ at +350 mV (both values were based on three parallel experiments) at graphene film electrode and PGE electrode, respectively (Figure 4.2). This indicates that graphene film can increase the electrocatalytic activity of Hyd1 and BOD.

In Figure 4.1, the onset potential for $H_2$ oxidation was −300 mV at both graphene film electrode and PGE electrode, only 60mV higher than the thermodynamic oxidation potential for the $H_2/2H^+$ couple at the same pH of 6 at 30 °C (–360 mV vs SHE).In Figure 4.2, the onset potential for $O_2$ reduction was +800 mV at both graphene film electrode and PGE electrode, only 59 mV lower than the thermodynamic reduction potential for the $O_2/2H_2O$ couple at the same pH of 6.2 (+859 mV vs SHE). This indicates that the onset potential of voltammetry of enzymes reflects the potential of the electron entry site of the enzyme, which is not influenced by electrode materials.

In addition, Figure 4.1 and 4.2 show that the cyclic voltammetry of enzymes at graphene film electrodes and PGE electrodes are both sigmoidal, indicating that the wave shape of cyclic voltammetry is irrelevant to electrode materials, but represents enzyme's inherent electrocatalytic properties.

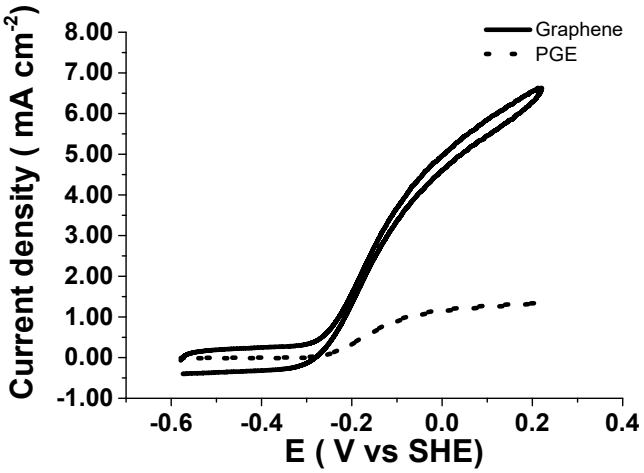



Figure 4.1 Cyclic voltammetry of Hyd1 (2 μL) at graphene film (10 mg/mL) electrode (solid line) and bare PGE (dotted line) electrodes. In pH 6 mixed hydrogenase buffer (100 mM), under 100 % $H_2$.Temperature 30 °C, electrode rotation rate 1000 RPM, scan rate 10 mV/s, electrode projected surface area 0.03 $cm^2$.

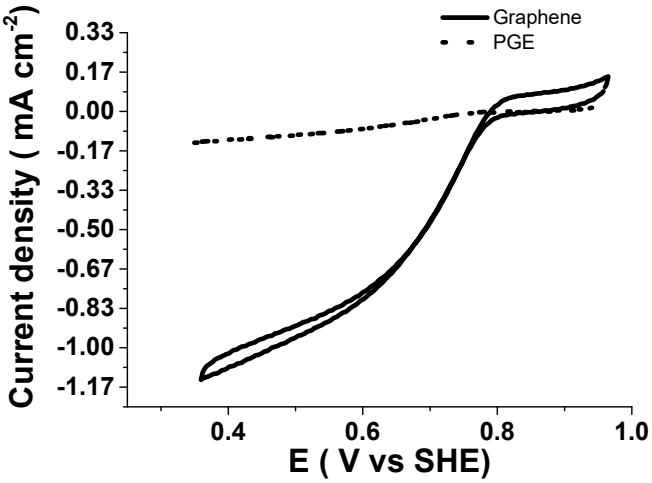



Figure 4.2 Cyclic voltammetry of BOD (2 μL) at graphene film (10 mg/mL) electrode (solid line) and bare PGE (dotted line) electrodes. In pH 6.2 phosphate buffer (100 mM), under 100 % $O_2$. Temperature 30 °C, electrode rotation rate 1000 RPM, scan rate 10 mV/s, electrode projected surface area 0.03 $cm^2$.

Figure 4.3 shows that of graphene film of higher concentration possess greater ability to increases the catalytic current density of $H_2$ oxidation electrocatalysed by Hyd1.The maximum current densities were 6.54± 0.12, 4.60± 0.10, 1.70± 0.06, 0.20± 0.05 mA $cm^{-2}$ (based on three parallel experiments). This indicates that the more concentrated the graphene films have larger conductive surface area, which increases the enzyme density at the electrodes.

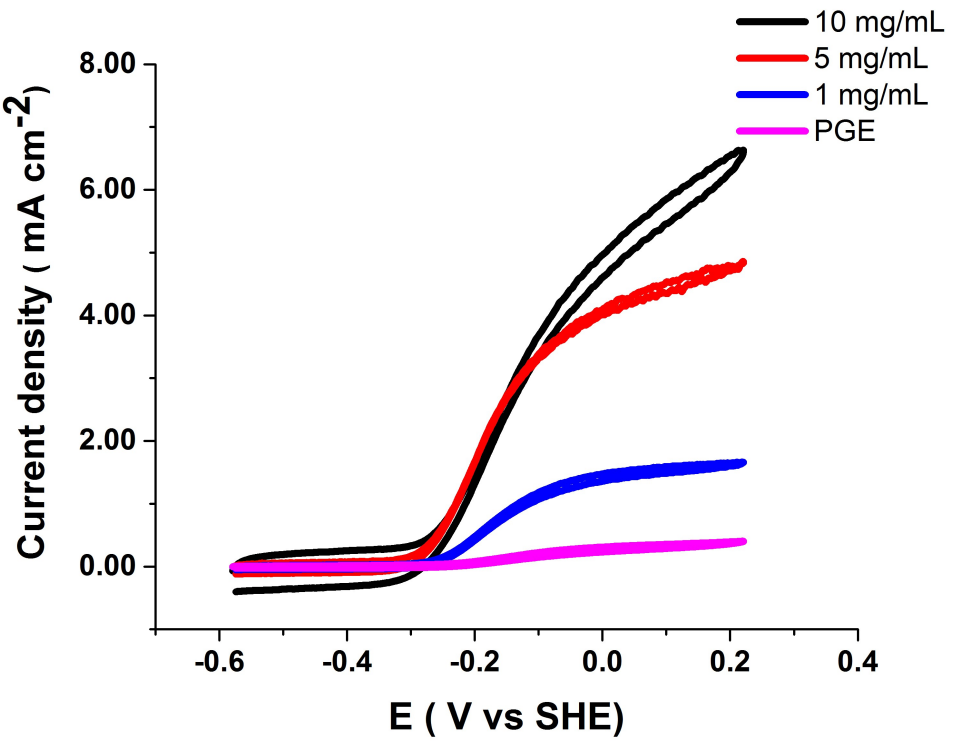



Figure 4.3 Cyclic voltammograms (current density) of Hyd1 (2 µL) at PGE electrodes modified with graphene suspensions (20 µL) of different concentrations: 10mg/ml (black) 5mg/ml (red) 1mg/ml (blue) and PGE electrode (magenta), in mixed buffer (100 mM pH 6.0), 30 °C, scan rate 10 mV/s, 100 % $H_2$, 1 bar, electrode rotation rate: 1000 RPM.

Graphene films increase the electrocatalytic activity of fuel cell enzymes, because of its excellent properties to function as electrode materials supporting enzymes: 1) high surface-to-volume ratio of 2630 $m^2$ $g^{-1}$ [183], which increases the enzyme density on electrodes;2) high electrical conductivity (room-temperature electron mobility of $2.5 \times 10^5$ $cm^2$ $V^{-1}$ $s^{-1}$ [188], ability to sustain extremely high densities of electric current, which is a million times higher than copper [190]); 3) decent biocompatibility [183].

Another reason graphene film increased the electrocatalytic activity of enzymes is that graphene as prepared can have some oxygenated groups at its surface, which can increase its biocompatibility with enzymes. To prove this proposition, I did an Infrared Spectroscopy of the graphene suspension (10 mg/mL). The results show that the graphene sample I synthesized contains C – O ($\nu_{C\text{-}O}$ at 1060 $cm^{-1}$), O – H ($\nu_{C\text{-}O}$ at 3354 $cm^{-1}$), C=C ($\nu_{C\text{-}O}$ at 3354 $cm^{-1}$), consistent with my proposition (Figure 4.4).

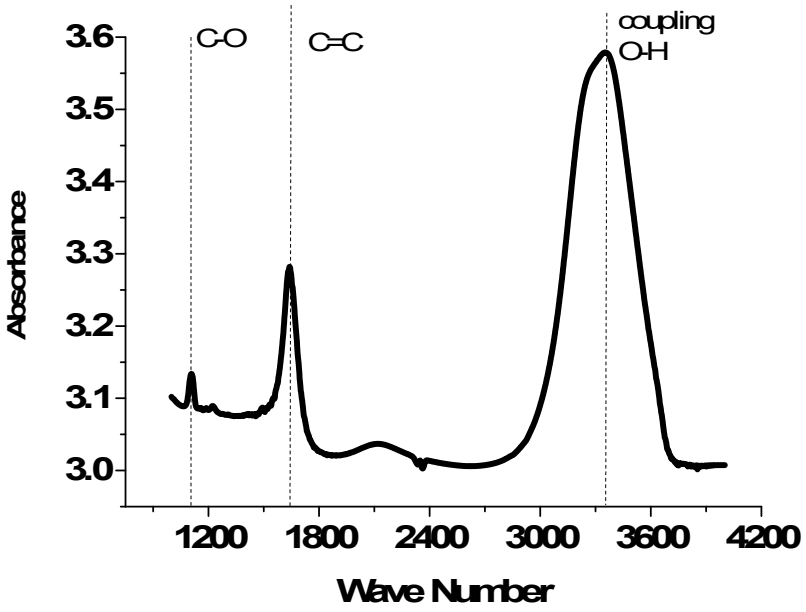



Figure 4.4 Infrared Spectroscopy of graphene suspensions.

### 4.4.2 MWNT Film Electrode

To establish if MWNT film electrodes can increase the electrocatalytic activity of Hyd1 and BOD, I performed cyclic voltammetry of enzymes at PGE electrodes with and without MWNT film, all rotating at 1000 RPM, at 30 °C, under 100 % substrate gases, at a scan rate of 10 mV/s. I found that the limiting electrocatalytic current densities of Hyd1 and BOD at MWNT film electrode were ca. 7 and 46 times higher than at PGE electrodes without MWNT film, respectively (Figure 4.5 and 4.6). For Hyd1, the catalytic current densities of $H_2$ oxidation were 10.92±0.43and 1.33±0.03 mA $cm^{-2}$ (both values were based on three parallel experiments) at +200 mV at MWNT film electrode and PGE electrode, respectively (Figure 4.5). For BOD, the catalytic current densities of $O_2$ reduction were 6.15±0.31 and 0.13±0.02 mA $cm^{-2}$ (both values were based on three parallel experiments) at +350 mV at MWNT film electrode and PGE electrode, respectively (Figure 4.6). This indicates that MWNT films increase the electrocatalytic activity of Hyd1 and BOD, because of MWNT's excellent properties to function as electrode materials supporting enzymes discussed above.

In Figure 4.5, the onset potential for $H_2$ oxidation was –300 mV at both at both MWNT film electrode and PGE electrode, only 60mV higher than the thermodynamic oxidation potential for the $H_2/2H^+$ couple at the same pH of 6 at 30 °C (–360 mV vs SHE). In Figure 4.6, the onset potential for $O_2$ reduction was +800 mV at both MWNT film electrode and PGE electrode, only 59mV lower than the thermodynamic reduction potential for the $O_2/2H_2O$ couple at the same pH of 6.2 (+859 mV vs SHE). This indicates that the onset potential of voltammetry of enzymes reflects the potential of the electron entry site of the enzyme, which is not influenced by electrode materials.

In addition, Figure 4.5 and 4.6 show that the cyclic voltammetry of enzymes at MWNT film electrodes and PGE electrodes are both sigmoidal. Such similarity indicates that the wave shape of cyclic voltammetry is controlled by enzyme's inherent electrocatalytic properties, rather than electrode materials.

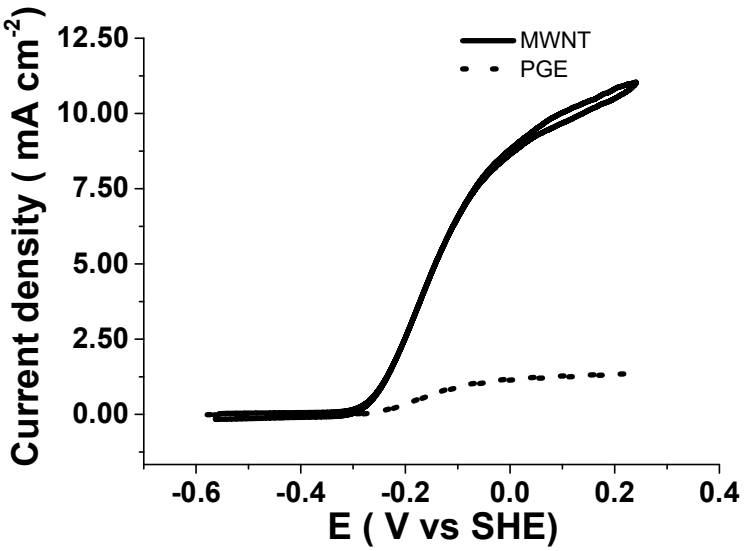



Figure 4.5 Cyclic voltammetry of Hyd1 (2 μL) at MWNT film electrode (solid line) and bare PGE (dotted line) electrodes. In pH 6.0 mixed hydrogenase buffer (100 mM), under 100 % $H_2$. 30 °C, electrode rotation rate 1000 RPM, scan rate 10 mV/s, electrode projected surface area 0.03 $cm^2$.

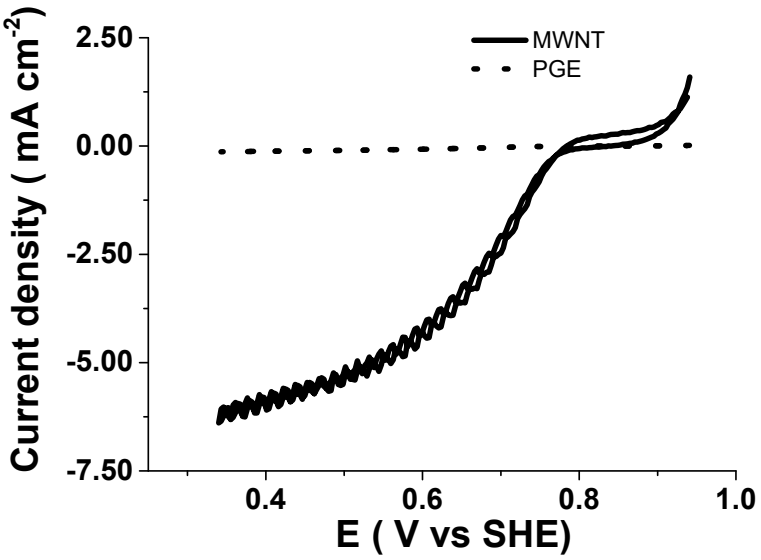



Figure 4.6 Cyclic voltammetry of BOD (2 µL) at MWNT film electrode (solid line) and bare PGE (dotted line) electrodes. In pH 6.2 phosphate buffer (100 mM), under 100 % $O_2$. 30 °C, electrode rotation rate 1000 RPM, scan rate 10 mV/s, electrode projected surface area 0.03 $cm^2$.

### 4.4.3 MWNT Pellet Electrode

To investigate how MWNT pellet electrodes increase the electrocatalytic activity of Hyd1, I performed cyclic voltammetry of 20 µL of the enzyme absorbed in the MWNT pellet attached to PGE electrodes by silver paint, at a scan rate of 4 mV/s. The MWNT pellet electrode was immersed in a mixed buffer of pH 6 at 30 °C, rotating at 1000 RPM, under 100 % $H_2$. I observed a sigmoidal electrocatalytic wave of $H_2$ oxidation by Hyd1, starting at the onset potential of −300 mV (Figure 4.7), which is equal to that at PGE electrodes. This indicates that the onset potential of the catalytic wave is determined by the potential of the electron entry site, i.e. the distal [4Fe–4S] cluster of Hyd1[202],

rather than electrode materials. However, the potential of the distal [4Fe–4S] cluster cannot be determined by titrations because [4Fe–4S] is EPR silent [203].

In Figure 4.7, the anodic current density reached 6.08 mA $cm^{-2}$ at +200 mV. The anodic current density reflects both the catalytic current and capacitive current. This MWNT pellet was cracked partially after loaded with Hyd1, resulting in its poor catalytic performance. So this measurement was performed only once. The capacitive current was large (4.05 mA $cm^{-2}$ at +200 mV, Figure 4.7, dotted line), due to the high surface area of MWNT pellets. The impact of high surface area of MWNT was exacerbated by large amount of MWNT powder present in the pellet.

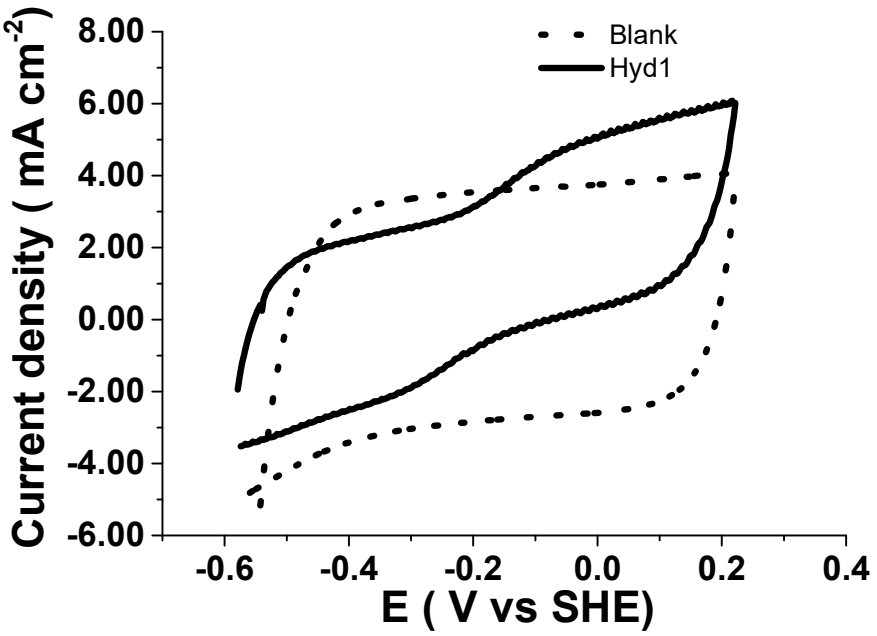



Figure 4.7 Cyclic voltammograms (current density) of Hyd1 (20 µL) at MWNT pellet electrode (solid line) and blank MWNT pellet electrode (dotted line). In mixed buffer (100 mM, pH 6.0), 25 °C, scan rate 4 mV/s, 100 % $H_2$, electrode rotation rate 1000 RPM, electrode projected surface area 0.56 $cm^2$. Experiment was performed once.

To eliminate the effect of high capacitive current caused by MWNT in cyclic voltammetry, I performed chronoamperometry of Hyd1 at a stationary MWNT pellet electrode in pH 5.0 phosphate buffer (100 mM) at 25 °C, at a potential of +23 mV, over 130 h. I found that the current density fluctuated in the range of 0.05 to 0.15 mA $cm^{-2}$ (Figure 4.8). This indicates that Hyd1 was stable at the MWNT pellet electrode for 130 h. The fluctuation can be due to: 1) that the enzyme was not evenly dispersed in the three dimensional MWNT pellet, 2) the pellet partially cracked during the measurement, which has been observed, and the catalytic current was diffusion-limited.

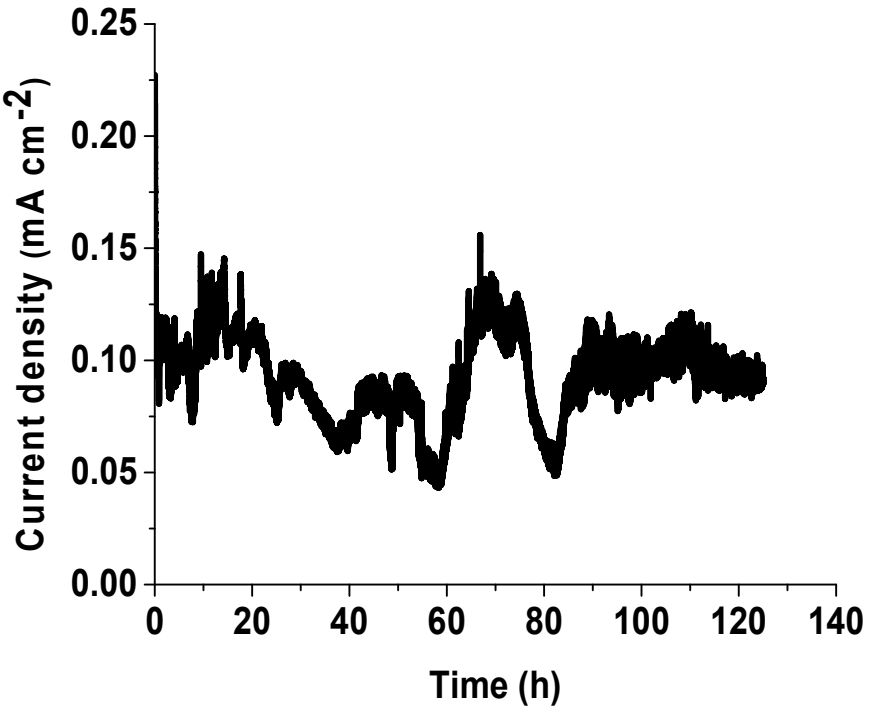



Figure 4.8 Chronoamperometry of Hyd-1 (20 μL) at the MWNT pellet electrode over 130 h. Experimental conditions: potential +23 mV vs SHE, rotation rate 0 RPM, 100mM pH 5.0 phosphate buffer, 25°C, 100% $H_2$, electrode projected surface area: 0.56 $cm^2$. This experiment was performed once.

To establish if MWNT pellet electrodes can increase the electrocatalytic activity of BOD, I performed cyclic voltammetry of 20 μL of the enzyme absorbed in MWNT pellet attached to PGE electrodes by silver paint, at a scan rate of 0.2 mV/s. The MWNT pellet electrode was immersed in a mixed buffer of pH 6.2 at 30 °C, rotating at 1000 RPM, under 100 % $O_2$. I observed a sigmoidal electrocatalytic wave of $O_2$ reduction by BOD, starting at the onset potential of 800 mV (Figure 4.9), equal to that at PGE electrodes. This indicates that the onset potential of the catalytic wave is determined by the potential of the electron entry site, i.e. the Type 1 Cu site (670 mV at pH 7 [55]), rather than electrode materials.

In Figure 4.9, the catalytic current density reached 0.06±0.02 mA $cm^{-2}$ (based on three parallel experiments) at +350 mV. The current density summed the catalytic current and capacitive current. The capacitive current was 0.0028 mA $cm^{-2}$ at +350 mV (Figure 4.9, dotted line). The effect of capacitive current brought by MWNT was diminished, because I used an extremely low scan rate of 0.2 mV/s. The insulating PTFE binder in the MWNT pellet that slows the electron transfer rate between the enzyme and electrode surface may cause the relatively small catalytic current density.

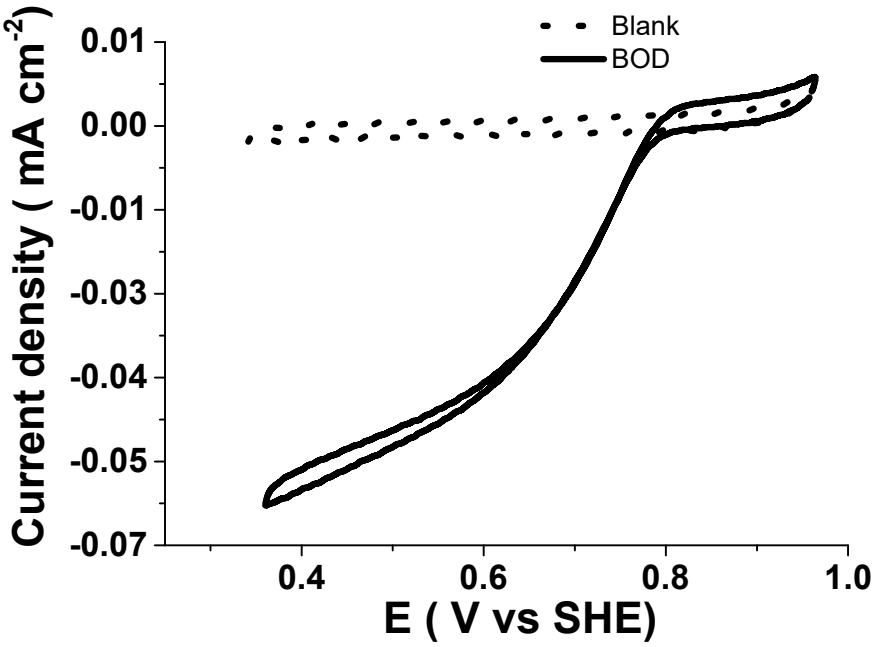



Figure 4.9 Cyclic voltammograms (current density) of BOD (20 μL) at MWNT pellet electrode (solid line) and blank MWNT pellet electrode (dotted line). In phosphate buffer (100 mM, pH 6.2), 25 °C, scan rate 0.2 mV/s, 100 % $O_2$, electrode rotation rate: 1000 RPM, electrode projected surface area: 0.56 $cm^2$.

To test the stability catalytic current of BOD at MWNT pellet electrode, I performed chronoamperometry of BOD at a stationary MWNT pellet electrode in pH 5 phosphate buffer (100 mM) at 21 °C, at a potential of +341 mV, over 100 h. I found that in the first 22 h, the current density fluctuated in the range from 0.14 to 0.17 mA $cm^{-2}$. After 50 h, the current density started to decrease by 71% over 50 h, from 0.14 to 0.04 mA $cm^{-2}$ (Figure 4.10). This indicates that BOD was stable at the MWNT pellet electrode for 50 h at most. The loss of catalytic current over an extended period of time may be due to either the denaturation of BOD *in vitro* or the desorption of BOD from the electrode or both.

The catalytic current densities of $O_2$ reduction electrocatalysed by BOD in Figure 4.9 and 4.10 are different, because of the variation of enzyme films between experiments performed in identical manner.

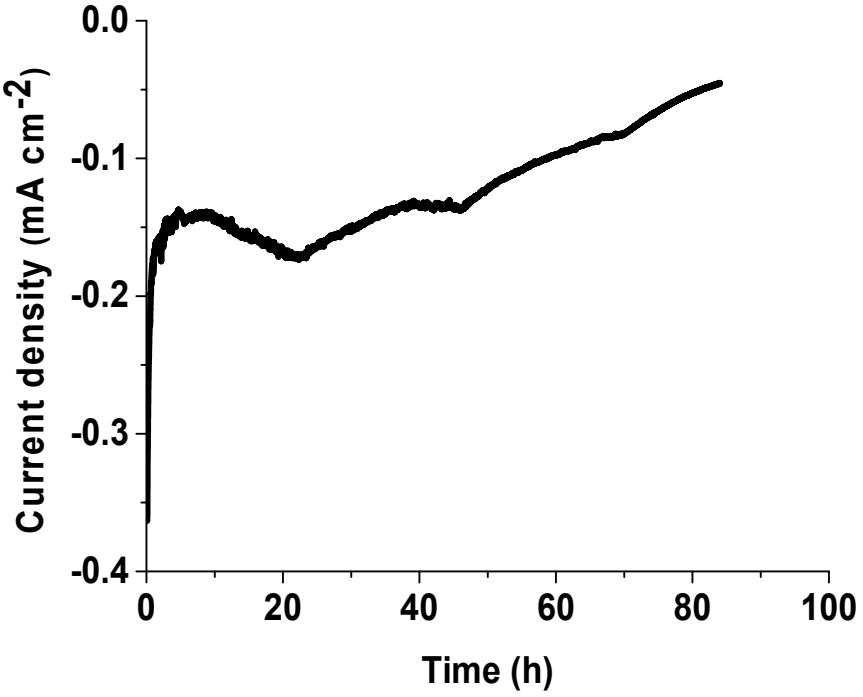



Figure 4.10 BOD (20 μL) protein film stability on MWNT pellet electrode over 100 h.Experimental conditions: potential +341mV vs SHE, rotation rate 0 RPM, pH 5.0 phosphate buffer (100 mM), 21 °C, 100% $O_2$, electrode projected surface area 0.56 $cm^2$. This experiment was performed once.

To determine the dependence of the catalytic current density of $H_2$ oxidation electrocatalysed by Hyd1 on the rotation rate of the MWNT pellet electrode, I performed chronoamperometry at 23 mV while changing the rotation rate of the MWNT pellet electrode, under 100% $H_2$, in pH 5.0 phosphate buffer (50 mM), at 25 °C.

I found that the relationship between the current density and rotation ratecan be fitted intoKoutecky-Levich equation, whose intercept indicated a limiting current density of 2.0 mA $cm^{-2}$ at +23 mV (Figure 4.11).

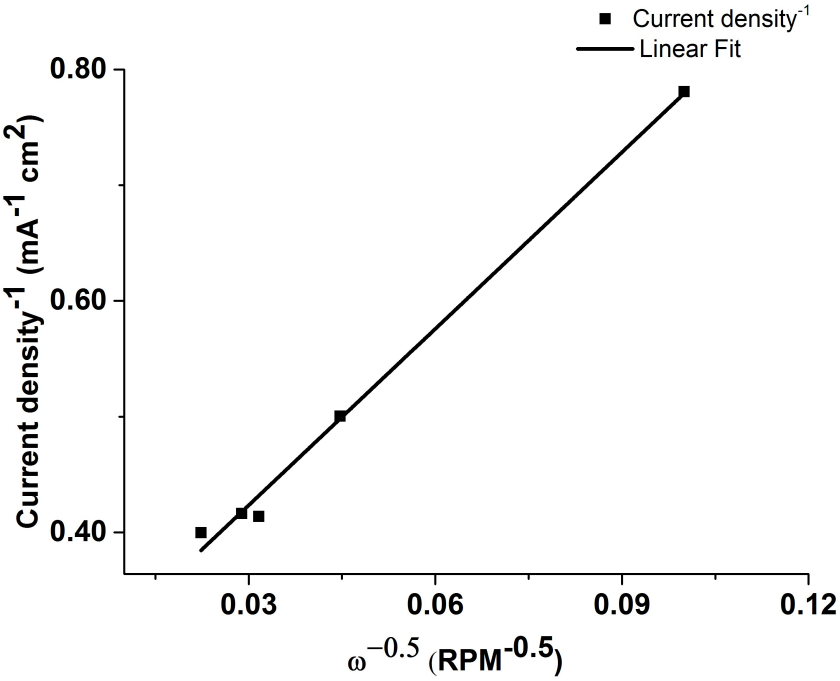



Figure 4.11 Rotation rate dependence of the current density of $H_2$ oxidation electrocatalysed by Hyd1 (20 μL) at MWNT pellet electrode. Experimental conditions: 100 % $H_2$, 25 °C, 50 mM pH 5.0 phosphate buffer, at potential +23 mV vs SHE.

To determine the dependence of the catalytic current density of $O_2$ reduction electrocatalyzed by BOD on the rotation rate of the MWNT pellet electrode, I performed chronoamperometry at +341 mV while changing the rotation rate of the MWNT pellet electrode, under 100% $O_2$, in pH 5.0 phosphate buffer (100 mM), at 22 °C. I found that the relationship between the current density and rotation rate can be

fitted into Koutecky-Levich equation, whose intercept indicated a limiting current density of 0.32 mA $cm^{-2}$ at +341 mV (Figure 4.12).

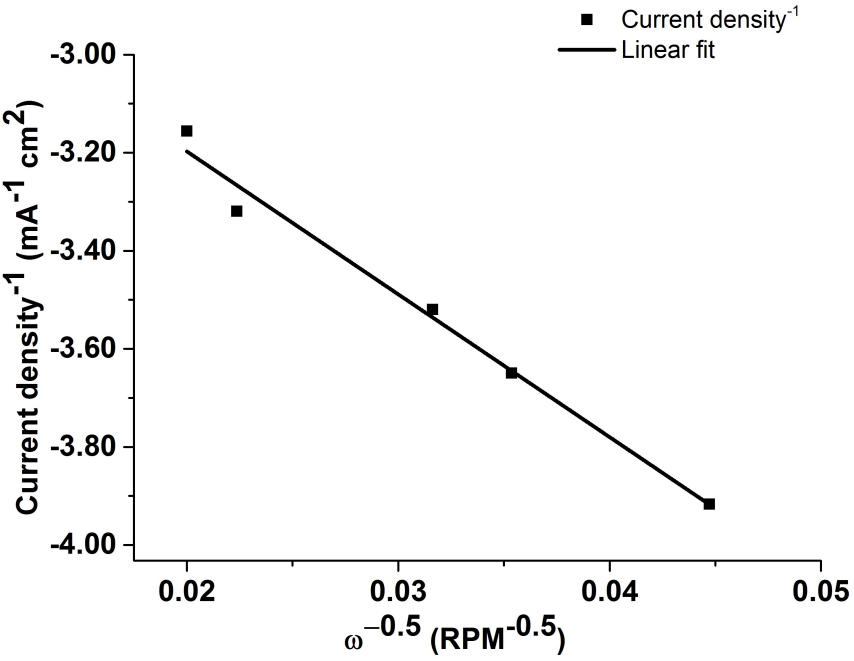



Figure 4.12 Rotation rate dependence of the current density of $O_2$ reduction electrocatalysed by BOD (20 μL) at MWNT pellet electrode. Experimental conditions: 100% $O_2$, 22 °C, 50 mM pH 5.0 phosphate buffer, at potential +341 mVvs SHE.

Table 4.1 Comparison of current density of the hydrogenase anode in this chapter with few other representative reported studies[30].

| Electrode | Current density (mA $cm^{-2}$) | Ref. |
|---|---|---|
| Au/MWNT-$NH_2$/covalent linked *Desulfovibrio gigas* [NiFe] $H_2$ase | ~2.5 (40 °C, pH 7, 2500 RPM) | [29] |
| PGE/SWNT/adsorbed*Desulfovibriofructosovorans* [NiFe] $H_2$ase | 0.11 (25 °C, pH 7.6) | [204, 205] |
| (a) PG/SWNT/ or (b) PG/SWNT-COOH/ adsorbed with *Aquifexaeolicus* [NiFe]-$H_2$ase | (a) 1.0 (60 °C, pH 7.2) (b) ~0.31 (60 °C, pH 7.2) | [206] |
| PGE/MWNT/pyrenyl covalent linked Hyd1 | 2.6 (25 °C, pH 6.0) | [30] |

| | | |
|---|---|---|
| Graphene/PGE | 6.54±0.12[b] (30 °C, pH 6.0, 1000 RPM) | This study |
| MWNT/PGE | 10.92±0.43[b] (30 °C, pH 6.0, 1000 RPM) | This study |
| MWNT Pellet | 2.08[c] (25 °C, pH 6.0, 1000 RPM) | This study |

Table 4.2 Comparison of current density of the BOD anode in this chapter with few other representative reported studies[a][30]

| Electrode | Current density (mA $cm^{-2}$) | Ref. |
|---|---|---|
| CNT fiber coated with Osmium polymer + BOD | 1.57 (quiescent air, 37 °C, pH 7.2) | [207] |
| PGE/MWNT/pyrenyl covalent linked BOD | 3.2 (saturated $O_2$), 1.2 (saturated air), 25°C | [30] |
| GCE/BOD linked to carboxylated MWNT | 0.06 (quiescent air, 25 °C, pH 5) | [208] |
| Au/BOD linked to thiolated MWNTvia maleimido carboxylic acid | 0.5 (quiescent air, 25 °C, pH 7) | [209] |
| PGE/MWNT-PQQ/linked BOD | 0.5 (quiescent air, 25 °C, pH 7) | [210] |
| ITO/SWNT- pyrenyl coated with BOD | ~1.0 (saturated $O_2$, 900 rpm, 25 °C, pH4.8); 0.02 (quiescent air, 25 °C, pH 4.8) | [211] |
| Graphene/PGE | 1.14±0.17[b](30 °C, pH 6.2, 1000 RPM) | This study |
| MWNT/PGE | 6.15±0.31[b] (30 °C, pH 6.2, 1000 RPM) | This study |
| MWNT Pellet | 0.06±0.02[b] (25 °C, pH 6.2, 1000 RPM) | This study |

[a]Where CNT - carbon nanotube; GCE - glassy carbon electrode; ITO - indium tin oxide; PQQ - pyrroloquinoline quinone; SWNT – single-walled nanotube. [b] Based on three parallel experiments. [c] Based on one experiment.

From Table 4.1 and 4.2 that compare the catalytic current densities of Hyd1 and BOD at the new carbon nanomaterials electrodes studied in this chapter with those reported in literature, I can see that the limiting catalytic current densities produced by the graphene and MWNT film in this study are higher than the literature values. Particularly, the MWNT film electrode has the greatest performance in PFE experiments in traditional aqueous buffers. The maximum catalytic current density for Hyd1 and BOD adsorbed at MWNT film electrodes are 10.92±0.43 mA $cm^{-2}$ (30 °C, pH 6.0, 1000 RPM, based on three parallel experiments) and 6.15±0.31 mA $cm^{-2}$ (30 °C, pH 6.2, 1000 RPM, based on three parallel experiments), respectively. So I chose to apply MWNT film electrode for further investigation in ionic liquids in the next four chapters.

## 4.5 Conclusions and Perspectives

In summary, I established that graphene and MWNT can increase the electrocatalytic activity of Hyd1 and BOD compared to conventional PGE electrodes, because both the carbon nanomaterials have superb properties such as high surface area [183], relatively high electric conductivity [192, 196]and decent biocompatibility [183], which increase the enzyme density at electrodes, and enhance the electronic conductivity and appropriate wiring of the redox active sites of enzymes to electrode surface.After comparison with literature values, I found that the graphene and MWNT film electrodes exhibit higher capability to increase the catalytic current density of enzymes. In particular, MWNT film shows the best ability to increase catalytic current densities of enzymes, so MWNT film electrodes have been chosen to study the catalytic activity of

Hyd1, BOD and Ni-CODH and enzymatic fuel cell performance in the experiments discussed from Chapter 5 to 8.

# 5 Oxidation of $H_2$ Electrocatalysed by Hydrogenase Confined in Ionic Liquids

## 5.1 Abstract

Hydrogenase 1 from *Escherichia coli* (Hyd1) catalyses $H_2$ oxidation at a turnover frequency above 100 $s^{-1}$, and requires a minimal driving force (the over potential is 60 mV at pH 6, 30 °C, according to data in Chapter 4). Such superb catalytic capability leads the enzyme to be an attractive working and inspirational anodic electrocatalyst in enzymatic fuel cells. To determine whether Hyd1 can function in enzymatic fuel cells using ionic liquids, I performed enzyme film electrochemistry of Hyd1 adsorbed on pyrolytic graphite edge electrodes modified by multiwalled carbon nanotubes confined by two pure water-immiscible ionic liquids: 1-ethyl-3-methylimidazolium bis(trifluoromethylsulfonyl)imide (EMIMTFSI) and 1-methyl-1-propyl pyrrolidinium bis(trifluoromethylsulfonyl)imide (PMPyrTFSI). I found that in aqueous microenvironment confined by both ionic liquids, Hyd1 was highly electrocatalytically active towards $H_2$ oxidation. The $H_2$ oxidation electrocatalysed by Hyd1 in aqueous microenvironment confined by either ionic liquid gave similar waveshapes and parameters of cyclic voltammetry (i.e. catalytic currents and onset potentials for $H_2$ oxidation). Specifically, in the ionic liquids, the catalytic current for $H_2$ oxidation electrocatalysed by Hyd1 decreased while the onset potential increased through continuous cyclic voltammetric scans. Based on these results, I proposed that the Hyd1 adsorbed on electrodes was enclosed in an aqueous pocket surrounded by water-immiscible ionic liquids. Water-immiscible ionic liquids are applicable to enzymatic fuel cells using Hyd1 as anodic electrocatalyst.

## 5.2 Introduction

Hydrogenase 1 from *Escherichia coli* (Hyd1) catalyses $H_2$ oxidation at a turnover frequency above 100 $s^{-1}$, whichis an excellent inspirational and working electrocatalyst for fuel cells, because it is easily produced in good yield and is very amenable to engineering by site-directed mutagenesis [78]. Hence Hyd1 has been under extensive investigation for application as anodic electrocatalyst in $H_2$-$O_2$ enzymatic fuel cells since 2010 [27, 30, 79].

Ionic liquids (ILs) are nonvolatile, highly ionic conductive, thermally and electrochemically stable, hence competent to serve as electrolyte for fuel cells [109]. However, to our best knowledge, no positive results of $H_2$ oxidation electrocatalysed by Hyd1 have been reported in neat ILs. Furthermore, the mechanism of electrocatalysis by Hyd1 in ILs is still unclear. Lojou and co-workers reported the failure of the catalytic oxidation of $H_2$ via *Desulfovibrio fructosovorans* [NiFe] hydrogenase (Df Hase) mediated by *Desulfovibrio vulgaris Hildenborough*cytochrome c3 (DvH cytc3). By using hyperthermophilic [NiFe] membrane-bound hydrogenase from*Aquifex aeolicus* (Aa Hase), direct $H_2$ oxidation was not observed in pure RTIL, but an efficient direct catalytic oxidation process was obtained in mixed aqueous buffer/RTILs electrolytes. Chronoamperometric experiments showed that Aa Hase could afford 80% RTILs in aqueous buffer [175].

To determine whether Hyd1 can function in enzymatic fuel cells using ionic liquids, I performed enzyme film electrochemistry of Hyd1 adsorbed on pyrolytic graphite edge electrodes modified by multiwalled carbon nanotubes in two neat water-immiscible ILs: EMIMTFSI and PMPyrTFSI. I found that in both ILs, Hyd1 was electrocatalytically active towards $H_2$ oxidation. The $H_2$ oxidation electrocatalysed by Hyd1 in both ILs

gave similar waveshapes and parameters (i.e. catalytic currents and onset potentials for $H_2$ oxidation) of cyclic voltammetry. Specifically, in both ILs, the catalytic current for $H_2$ oxidation electrocatalysed by Hyd1 decreased while the onset potential increased through continuous cyclic voltammetric scans. Therefore, water-immiscible ILs can serve as electrolyte in enzymatic fuel cells using Hyd1 as anodic electrocatalyst. Based on these results, I proposed that the Hyd1 adsorbed on electrodes was enclosed in an aqueous pocket surrounded by water-immiscible ILs.

## 5.3 Experimental

Please refer to Chapter 3 for detailed information of materials, buffers, enzymes and procedures of protein film electrochemistry.

## 5.4 Results and Discussion

### 5.4.1 Potential Calibration with DmFc as Internal Reference in Ionic Liquids

Because Pt quasi-reference electrode was used in the voltammetry, I calibrated all cyclic voltammograms against the reversible formal potential, $E_f^\circ$ of $DmFc^{+/0}$, which is widely recognized as a reliable internal reference in a variety of nonaqueous solvents [144, 181]. Iniially, to determine the $E_f^\circ$ of $DmFc^{+/0}$ vs Pt wire, I performed cyclic voltammetry at a bare PGE electrode in ILs dissolved with 2 mM of DmFc after each set of PFE, to prevent interference with the catalytic voltammetry. The time interval between each set of PFE and corresponding voltammetry of DmFc was less than three

daysto ensure the accuracy of potential values. I observed cyclic voltammograms indicating a well-defined reversible process of $DmFc^{+/0}$ at PGE electrodes in EMIMTFSI and PMPyrTFSI represented by Figure 5.1 and 5.3. Corresponding data (average of three parallel experiments) are summarized in Table 5.1. In this chapter, all the potentials of voltammograms of enzyme film electrochemistry were first reported against Pt wire and then subtracted by the value of $E_f^\circ$ of $DmFc^{+/0}$vs Pt wire at a PGE electrode in ILs at 10 mV/s, 30 ˚C.

#### 5.4.1.1 EMIMTFSI

Figure 5.1 shows a typical cyclic voltammetry of the process of eq. 5.1 in EMIMTFSI at a stationary PGE electrode at 30 ˚C.

$$DmFc - e^- \rightleftharpoons DmFc^+ \quad (5.1)$$

The voltammogram was reported against a platinum wire quasi-reference electrode that is housed in a sidearm connected to the working electrode compartment via a Luggin capillary. DmFc was oxidized by one electron to $DmFc^+$ at the peak potential of 124 mV vs Pt wire (10 mV/s) and reduced back to DmFc at the peak potential of 44 mV vs Pt wire (10 mV/s). $E_f^\circ$ of $DmFc^{+/0}$ did not vary with scan rates (Table 5.1), indicating the reversibility of the $DmFc^{+/0}$ process. The values of $E_f^\circ$ of $DmFc^{+/0}$ were from 84 to 89 mV vs Pt wire in EMIMTFSI respectively at scan rates from 10 to 200 mV/s. The peak-to-peak potential separation value, $\Delta E_p$ (80 mV at 10 mV/s) was larger than the theoretic value of 60 mV for reversible processes at 30 ˚C. This is due to the effect of uncompensated resistance of solution. Moreover, the $DmFc^{+/0}$ process may have not achieved steady state at the scan rate above and equal to 10 mV/s.

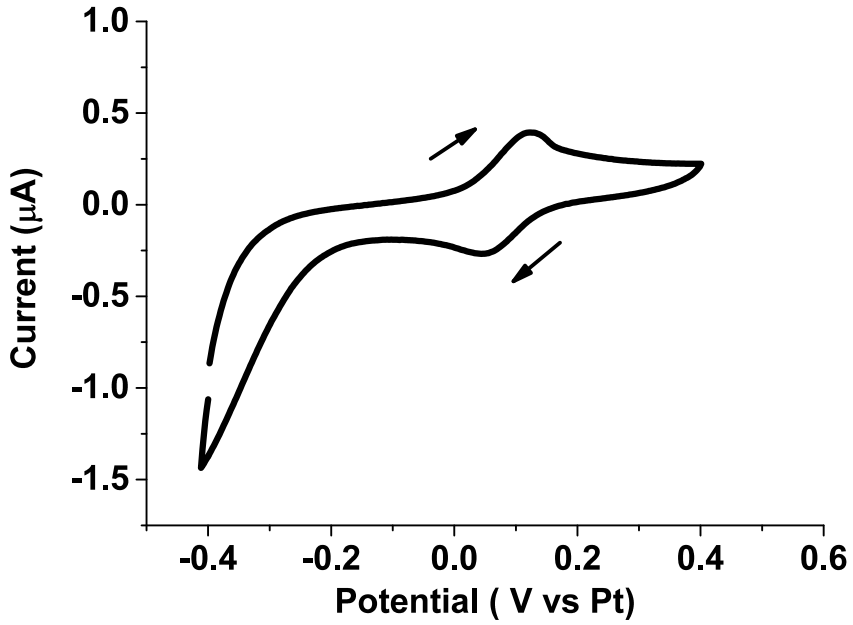



Figure 5.1 Cyclic voltammetry of DmFc (2 mM) at a bare PGE electrode (surface area 0.03 $cm^2$) in EMIMTFSI at 10 mV/s. Pt wire as quasi-reference electrode, working electrode rotation rate 0 RPM, temperature 30 ˚C, projected electrode surface area 0.03 $cm^2$. In fume hood.

Error of the value of peak currents may come from the uncertainty of double layer capacitance[37]. For the cyclic voltammetry in both EMIMTFSI and PMPyrTFSI, the forward scan is anodic, and the reversal scan is cathodic (as indicated by arrows in Figure 5.1). Because of the uncertainty for determining the base line for the reversal peak current, the value of $I_p^{red}$ is even more imprecise than $I_p^{ox}$, thus of less value for quantitative analysis [37]. Therefore in this study, I focused on analyzing $I_p^{ox}$. I found that the oxidation peak current ($I_p^{ox}$) was proportional to the square root of scan rate (Figure 5.2), which indicates that the $DmFc^{+/0}$ process in both EMIMTFSI was under diffusion control. The plot of peak current vs square root of scan rate did not pass the

origin, consistent with the characteristics of macro electrodes [212]. The slope of the linear fit of Figure 5.2 was equal to 0.132. Given this value, diffusion coefficient of DmFc in EMIMTFSI can be calculated from Randles-Sevcik equation (eq.5.2)

$$I_p = 0.4463nF(nF/RT)^{1/2}AD^{1/2}v^{1/2}C \quad (5.2)$$

where $I_p$ is the peak current (A), n is the number of electrons, $A$ is the electrode area ($cm^2$), $D$ is the diffusion coefficient, $C$ is the concentration (mol $cm^{-3}$), ν is the scan rate (V $s^{-1}$), and other symbols have their usual meaning. In my experimental conditions, $n$=1, $A$=0.03 $cm^2$, $C$=2 mol $cm^{-3}$. As a result, diffusion coefficient of DmFc in EMIMTFSI, $D = 2.72\times 10^{-8}$ $cm^2$ $s^{-1}$ at 30 ˚C.

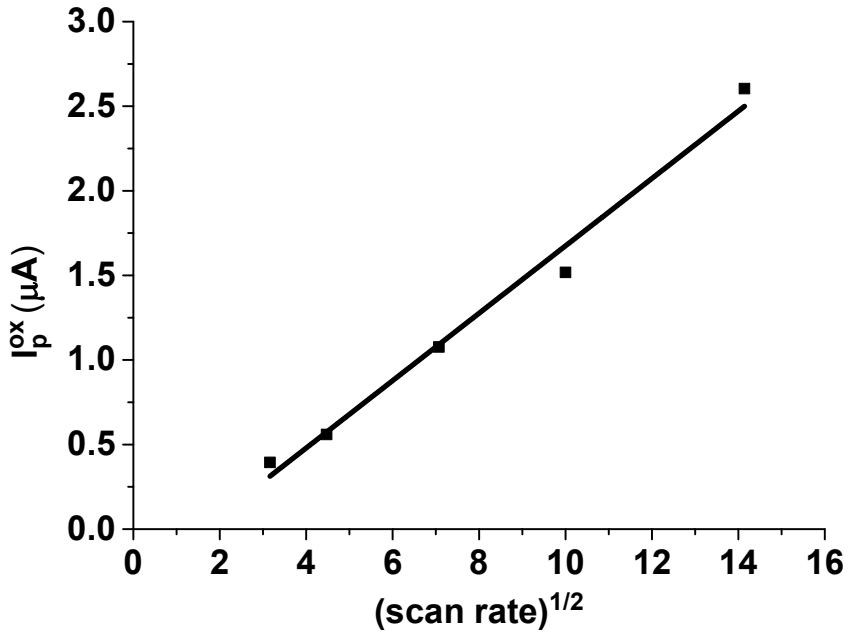



Figure 5.2 Dependence of oxidative peak current ($I_p^{ox}$)for the process of $DmFc^{+/0}$ on the square root of the scan rate in EMIMTFSI. Pt wire as quasi-reference electrode, working electrode rotation rate 0 RPM, temperature 30 ˚C, projected electrode surface area 0.03 $cm^2$. In fumehood.

Table 5.1 Cyclic Voltammetric Data (average of three parallel scans at the same electrode) for $DmFc^{+/0}$ at a PGE (0.03 $cm^2$) Electrode in EMIMTFSI and PMPyrTFSI, 30 ˚C. I didn't add any error bars in this table, because the CVs in parallel scans are completely the same.

| | EMIMTFSI | | | | | PMPyrTFSI | | | | |
|---|---|---|---|---|---|---|---|---|---|---|
| $v$[a] (mV/s) | $E_p^{ox}$ (mV) | $E_p^{Red}$ (mV) | $E_f^{\circ}$[b] (mV) | $\Delta E_p$[c] (mV) | $I_p^{ox}$[d] (μA) | $E_p^{ox}$ (mV) | $E_p^{Red}$ (mV) | $E_f^{\circ}$[b] (mV) | $\Delta E_p$[c] (mV) | $I_p^{ox}$[d] (μA) |
| 10 | 124 | 44 | 84 | 80 | 0.39 | 415 | 481 | 453 | 66 | 0.52 |
| 30 | 130 | 46 | 88 | 84 | 0.56 | 422 | 475 | 449 | 53 | 0.66 |
| 50 | 134 | 43 | 89 | 91 | 1.08 | 417 | 477 | 447 | 60 | 1.14 |
| 100 | 156 | 21 | 89 | 135 | 1.52 | 422 | 482 | 452 | 60 | 1.30 |
| 200 | 156 | 21 | 89 | 135 | 2.60 | 419 | 539 | 479 | 120 | 1.63 |

[a] Scan rate. [b] Reversible formal potential, $E_f^{\circ}=(E_p^{red}+E_p^{ox})/2$ where $E_p^{red}$ and $E_p^{ox}$ are reduction and oxidation peak potentials, respectively. [c] Peak-to-peak potential separation value, $\Delta E_p=E_p^{red}-E_p^{ox}$. [d] Oxidation peak current.

### 5.4.1.2 PMPyrTFSI

Figure 5.3 shows a typical cyclic voltammetry of the process of eq. 5.1 in PMPyrTFSI at a stationary PGE electrode at 30 ˚C. The voltammogram was reported against a platinum wire quasi-reference electrode that is housed in a sidearm connected to the working electrode compartment via a Luggin capillary. DmFc was oxidized by one electron to $DmFc^+$ at the peak potential of –414 mV vs Pt wire (10 mV/s) and reduced back to DmFc at the peak potential of –470 mV vs Pt wire (10 mV/s). $E_f^{\circ}$ of $DmFc^{+/0}$ at PGE electrode in PMPyrTFSI did not vary with scan rates (Table 5.1). The

values of $E_f^{\circ}$ of $DmFc^{+/0}$ were in the range from –417 to –422 mV vs Pt wire in PMPyrTFSI at scan rates from 10 to 200 mV/s. The peak-to-peak potential separation value, $\Delta E_p$ (60 mV at 50 and 100 mV/s) was equal to the theoretic value of 60 mV for reversible processes at 30 ˚C.

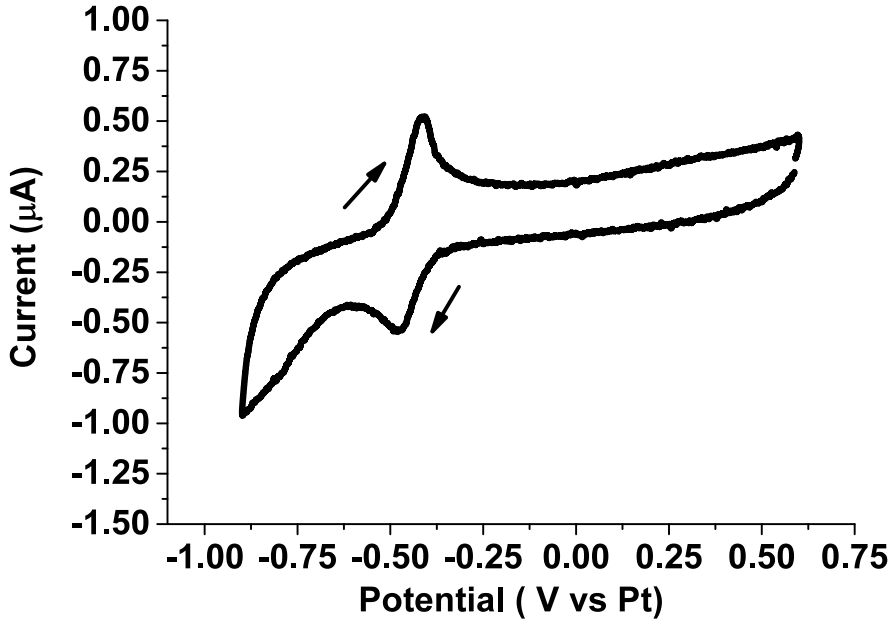



Figure 5.3 Cyclic voltammetry of DmFc (2 mM) at a bare PGE electrode (surface area 0.03 $cm^2$) in PMPyrTFSI at 10 mV/s.Pt wire as quasi-reference electrode, working electrode rotation rate 0 RPM, temperature 30 ˚C, projected electrode surface area 0.03 $cm^2$. In fume hood.

I found that the oxidation peak current was proportional to the square root of scan rate (Figure 5.4), which indicates that the $DmFc^{+/0}$ process in PMPyrTFSI was under diffusion control. The plot of peak current vs square root of scan rate did not pass the origin, consistent with the characteristics of macro electrodes [212]. The slope of the

linear fit of Figure 5.4 is equal to 0.101. From eq (5.2), the diffusion coefficient of DmFc in PMPyrTFSI, $D$=2.08× $10^{-8}$ $cm^2$ $s^{-1}$ at 30 ˚C, which is close to the $D$ value in EMIMTFSI (2.72× $10^{-8}$ $cm^2$ $s^{-1}$) in the same experimental conditions.

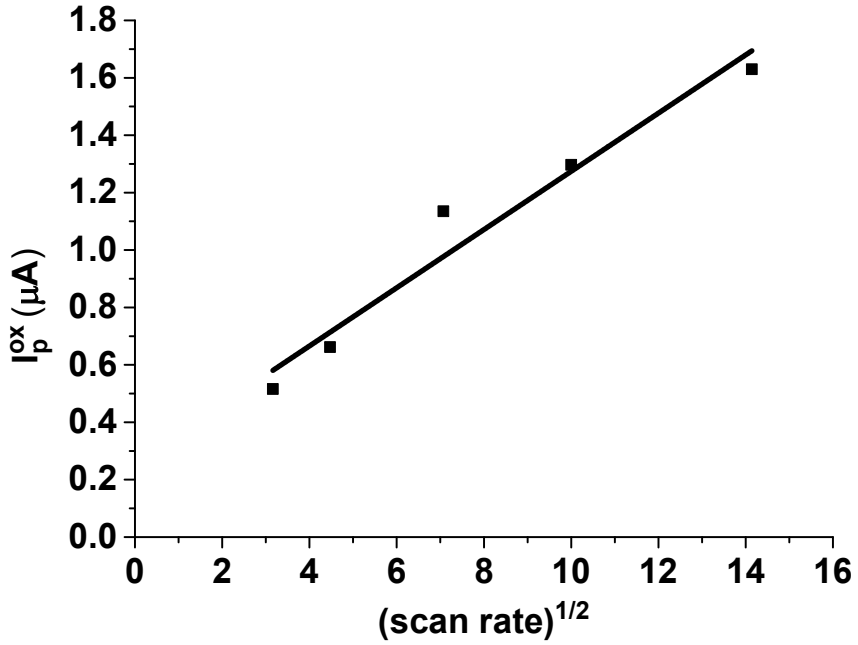



Figure 5.4 Dependence of oxidative peak current ($I_p^{ox}$) for the process of $DmFc^{+/0}$ on the square root of the scan rate in PMPyrTFSI. Pt wire as quasi-reference electrode, working electrode rotation rate 0 RPM, temperature 30 ˚C, projected electrode surface area 0.03 $cm^2$. In fume hood.

At room temperature, 2 mM of DmFc did not dissolve in EMIMTFSI or PMPyrTFSI (~ 1 mL for both ILs) under continuous stirring overnight. At 100 ˚C, under vacuum and continuous stirring, 2 mM of DmFc was dissolved in EMIMTFSI and PMPyrTFSI, giving light yellow liquids.

### 5.4.2 Enzyme Film Electrochemistry of Hyd1 Confined in EMIMTFSI and PMPyrTFSI

Hyd1 is a very attractive electrocatalyst for $H_2$ oxidation in aqueous buffers from pH 5 to 9 [77, 78, 83, 202, 213]. Voltammetry of $H_2$ oxidation by electrocatalysis of Hyd1 in pure ionic liquids has never been reported. The purpose of the voltammetry of the Hyd1 in ILs is to determine the electrocatalytic activity of Hyd1 confined in ILs and understand how the bioelectrocatalysis goes on in ILs.

Cyclic voltammetry was performed at a stationary MWNT/PGE electrodes adsorbing 2 μL of Hyd1 confined by ILs bubbling with 100 % $H_2$ at a scan rate of 10 mV/s. When the Hyd1 film on the electrode was completely dry, no catalytic current was observed. The electrodes were stationary rather than rotating to prevent draining water from enzyme films. Because of the low gas permeability of ILs, substrate gases had to pass through rather than flow above ILs to guarantee that enough substrate gases approach enzymes. When gases were flowing above ILs, tiny electrocatalytic current was observed. All potentials were referenced against $E_f^\circ$ of $DmFc^{+/0}$ at 30˚C.

My results indicate that there was direct bioelectrocatalysis of $H_2$ oxidation by Hyd1 confined by EMIMTFSI (Figure 5.5). Confined by EMIMTFSI, Hyd1 was highly electrocatalytically active in the first scan of voltammetry, but such activity decreased after each scan of voltammetry. Meanwhile, the onset potential of $H_2$ oxidation increased after each scan. The cyclic voltammogram of the blank MWNT/PGE electrode in EMIMTFSI bubbling with 100 % $H_2$ at 30 ˚C showed no catalytic current in the potential range from +300 to −600 mV (Figure 5.5, dotted line). In contrast, the

cyclic voltammograms of the Hyd1 on a stationary MWNT/PGE electrode in the same conditions showed a peak-shaped catalytic wave, indicating a $H_2$ oxidation electrocatalysed by Hyd1 (Figure 5.5, solid lines). After each scan of voltammetry, the peak potential ($E_p$), onset potential and magnitude of the catalytic current decreased monotonically. In the first scan (black solid line, Figure 5.5), the oxidation current started to increase drastically from −350 mV, indicating the onset of $H_2$ oxidation.

As the potential swept from −350 to −110 mV, the oxidation current continued to increase, reaching the peak current density of 0.81 mA $cm^{-2}$ at −110 mV. Then the oxidation current density decreased monotonically from 0.81 to 0.43 mA $cm^{-2}$, when the potential swept from −110 to +280 mV. This indicates a depletion of $H_2$ at the stationary electrode. The wave shapes of electrocatalysis by enzymes in EMIMTFSI are similar to those in quiescent aqueous buffers [64, 92, 214].

As more scans of cyclic voltammetry went on, I detected continuously decreasing oxidation current and increasing onset potential of $H_2$ oxidation electrocatalysed by Hyd1. Specifically, the peak current density decreased from 0.81 to 0.15 mA $cm^{-2}$ by 81 % after 4 scans. Meanwhile, the onset potential for electrocatalytic $H_2$ oxidation increased from −350 ($1^{st}$ scan) to −170 ($4^{th}$ scan) mV. Such trend of increasing onset potential indicates a decrease of pH by 3.0, if the system obeys Nernst equation.

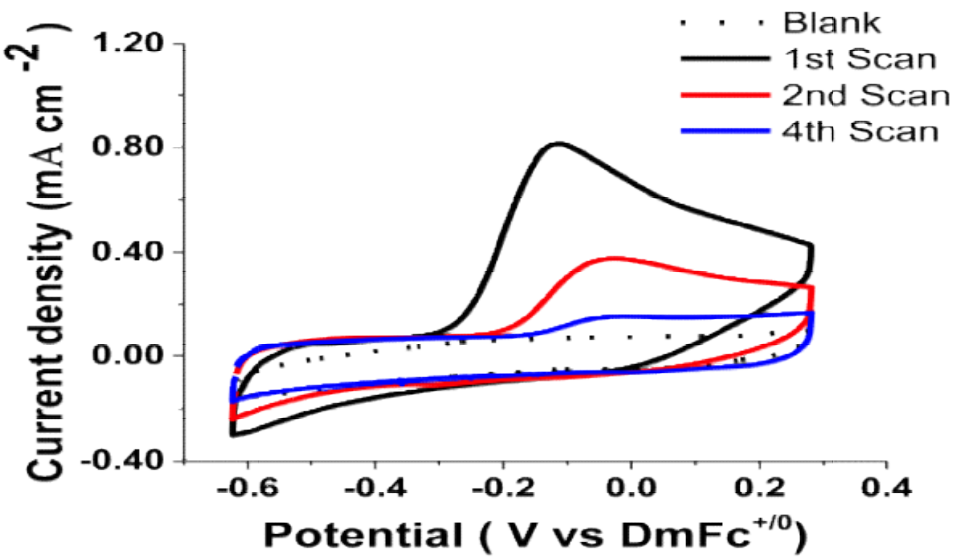



Figure 5.5 Cyclic voltammetric scans (current density) of Hyd1 (2 µL) at MWNT/PGE electrode surrounded by EMIMTFSI bubbling with 100 % $H_2$. Black solid line: 1st scan; red solid line: 2nd scan; blue solid line: 4th scan. Electrode rotation rate 0 RPM. Temperature 30 ˚C, scan rate 10 mV/s, projected electrode surface area 0.03 $cm^2$.

After the electrocatalytic activity vanished after continuous scans of cyclic voltammetry in EMIMTFSI, I moved the electrode into mixed hydrogenase buffer (pH 6, 100 mM). The cyclic voltammetry (Figure 5.6) shows a well-shaped sigmoidal voltammogram, indicating that the electrocatalytic activity of Hyd1 recovered. This observation indicates that the loss of electrocatalytic activity of Hyd1 by continuous cyclic voltammetry in EMIMTFSI is reversible. So the active of Hyd1 was preserved after the electrocatalytic activity was exhausted by continuous cyclic voltammetry.

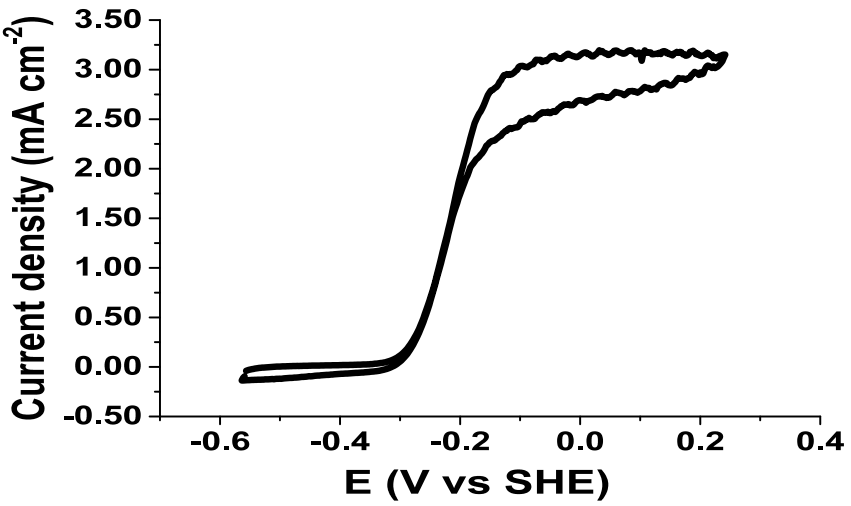



Figure 5.6 Cyclic voltammetry (current density) of Hyd1 at the same electrode as Figure 5.5transferred into mixed hydrogenase buffer (pH 6.0, 100 mM) right after the electrocatalytic activity vanished through continuous voltammetric scans in EMIMTFSI. Electrode rotation rate 1000 RPM. 100 % $H_2$. Temperature 30 ˚C, scan rate 10 mV/s, projected electrode surface area 0.03 $cm^2$.

My results indicate that there was direct bioelectrocatalysis of $H_2$ oxidation by Hyd1 confined by PMPyrTFSI (Figure 5.7). Confined by PMPyrTFSI, Hyd1 was very electrocatalytically active in the first scan of voltammetry, but such activity decreased after each scan of voltammetry. Meanwhile, the onset potential of $H_2$ reduction increased after each scan. The cyclic voltammogram of the blank MWNT/PGE electrode in PMPyrTFSI bubbling with 100 % $H_2$ at 30 ˚C showed no catalytic current in the potential range from +300 to −600 mV (Figure 5.7, dotted line). In contrast, the cyclic voltammograms of the Hyd1 on a stationary MWNT/PGE electrode in the same conditions showed a peak-shaped catalytic wave, indicating a $H_2$ oxidation electrocatalysed by Hyd1 (Figure 5.7, solid lines). After each scan of voltammetry, the

peak potential ($E_p$), onset potential and magnitude of the catalytic current decreased monotonically. In the first scan (black solid line, Figure 5.7), the oxidation current started to increase drastically from −380 mV, indicating the onset of $H_2$ oxidation reaction. As the potential swept from −380 to −160 mV, the oxidation current continued to increase, reaching the peak current density of 0.45 mA $cm^{-2}$ at −160 mV. As the potential increased further from −160 to +310 mV, the oxidation current density decreased monotonically from 0.45 to 0.41 mA $cm^{-2}$. This indicates a depletion of $H_2$ at the stationary electrode. The wave shapes for electrocatalysis by enzymes in PMPyrTFSI are similar to those in quiescent aqueous buffers and EMIMTFSI [64, 92, 215].

As more scans of cyclic voltammetry went on, I detected continuously decreasing oxidation current and increasing onset potential of $H_2$ oxidation electrocatalysed by Hyd1. Specifically, the peak current density decreased from 0.45 to 0.09 mA $cm^{-2}$ by 80 % after 10 scans. Meanwhile, the onset potential for electrocatalytic $H_2$ oxidation increased from −380 to −120 mV. Such trend of increasing onset potential indicates a decrease of pH by 4.3, if the system obeys Nernst equation.

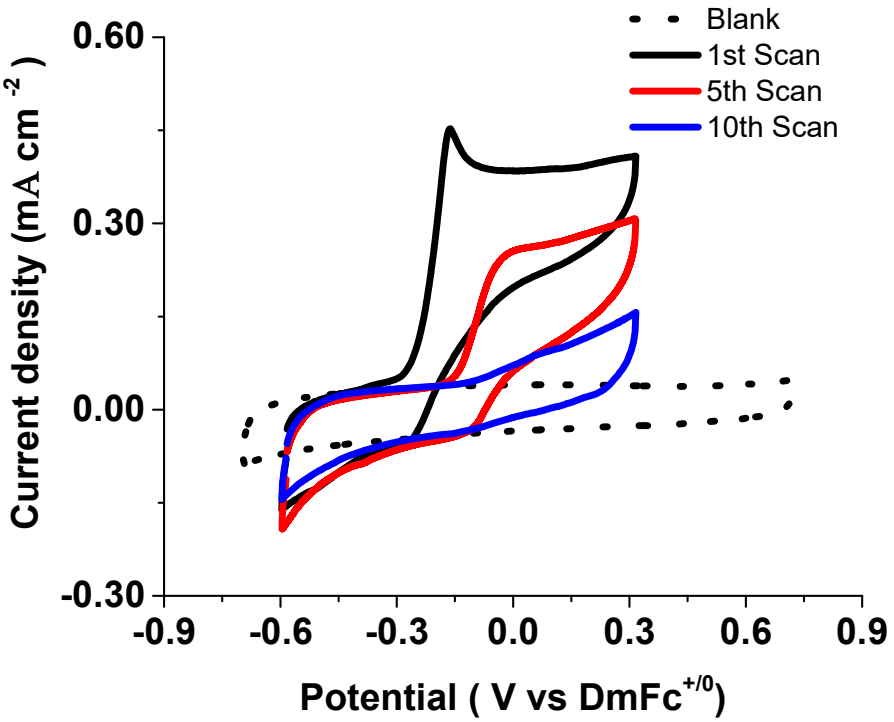



Figure 5.7 Cyclic voltammetric scans (current density) of Hyd1 (2 µL) at MWNT/PGE electrode surrounded by PMPyrTFSI bubbling with 100 % $H_2$.Black solid line: 1st scan; red solid line: 5th scan; blue solid line: 10th scan. Electrode rotation rate 0 RPM. Temperature 30 ˚C, scan rate 10 mV/s, projected electrode surface area 0.03 $cm^2$.

After the electrocatalytic activity vanished after continuous scans of cyclic voltammetry in PMPyrTFSI, I moved the electrode into mixed hydrogenase buffer (pH 6, 100 mM). The cyclic voltammetry (Figure 5.8) shows a well-shaped sigmoidal voltammogram, indicating that the electrocatalytic activity of Hyd1 recovered. This observation indicates that the loss of electrocatalytic activity of Hyd1 by continuous cyclic voltammetry in PMPyrTFSI is reversible. So the active site of Hyd1 was not damaged after the electrocatalytic activity was exhausted by continuous cyclic voltammetry.

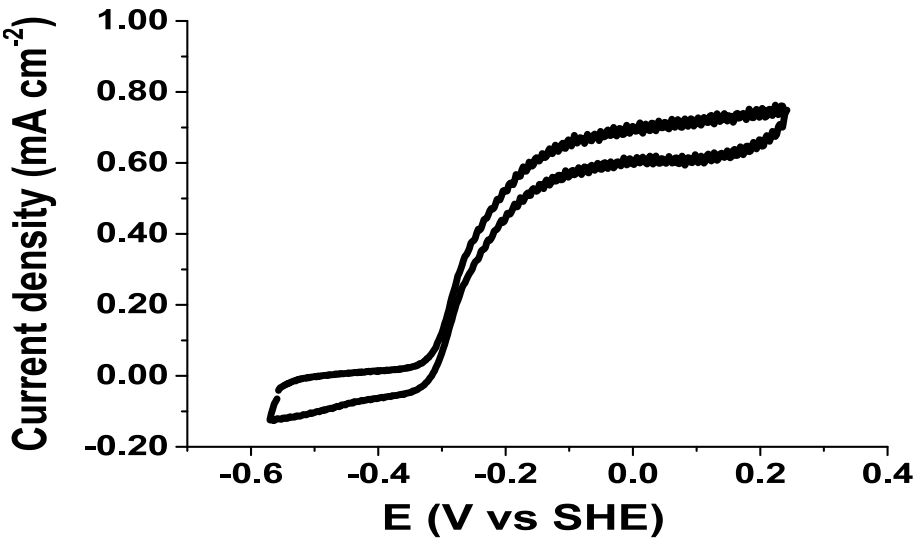



Figure 5.8 Cyclic voltammetry (current density) of Hyd1 at the same electrode as Figure 5.7transferred into mixed hydrogenase buffer (pH 6.0, 100 mM)right after the electrocatalytic activity vanished through continuous voltammetric scans in PMPyrTFSI. Electrode rotation rate: 1000 RPM. 100 % $H_2$. Temperature 30 ˚C, scan rate 10 mV/s, projected electrode surface area 0.03 $cm^2$.

To confirm the validity of the method for calibrating the potentials of enzyme film voltammetry in ionic liquids, I carried out cyclic voltammetry in EMIMTFSI dissolved with 2 mM DmFc and saturated with 100 % $H_2$ in quiescent condition. When EMIMTFSI was bubbling with $H_2$, $H_2$ oxidation via Hyd1 mediated by DmFc occurred. So EMIMTFSI was not bubbling with $H_2$ during the cyclic voltammetry, but had been saturated with substrate gases before cyclic voltammetry. The results confirm that the method used to estimate the potential of enzyme film voltammetry in the previous experiments is valid, because the potential values of enzyme film voltammetry of Hyd1 confined by ILs without DmFc are close to those of enzyme film voltammetry of Hyd1

confined by EMIMTFSI dissolved with 2 mM DmFc. Figure 5.9 shows cyclic voltammograms obtained for $H_2$ oxidation by Hyd1 adsorbed on a MWNT/PGE electrode and encapsulated in 1 μL of 100 mM phosphate buffer, initially pH 6.2 at 30 ˚C. The aqueous phase had been saturated with $H_2$ and surrounded by EMIMTFSI dissolved with 2 mM DmFc and saturated with 100 % $H_2$. The cyclic voltammogram of the blank MWNT/PGE electrode showed no catalytic current from −700 to +200 mV (Figure 5.9, dotted line). In contrast, the cyclic voltammograms of Hyd1 adsorbed on an MWNT/PGE electrode in contact with 1 μL of 100 mM phosphate buffer (initially pH 6.2 at 30 ˚C) on a stationary MWNT/PGE electrode in the same conditions show a peak-shaped catalytic wave, indicating diffusion-controlled $H_2$ oxidation. The $H_2$ oxidation wave decreased in amplitude upon successive cycles and shifted to more positive potential. The potential shift in EMIMTFSI dissolved with DmFc (+40 mV over first 10 scans, Figure 5.9) is smaller than in EMIMTFSI without DmFc (+180 mV over first 4 scans, Figure 5.5), because DmFc in EMIMTFSI phase may transfer $H^+$ from the aqueous phase to EMIMTFSI phase [216].

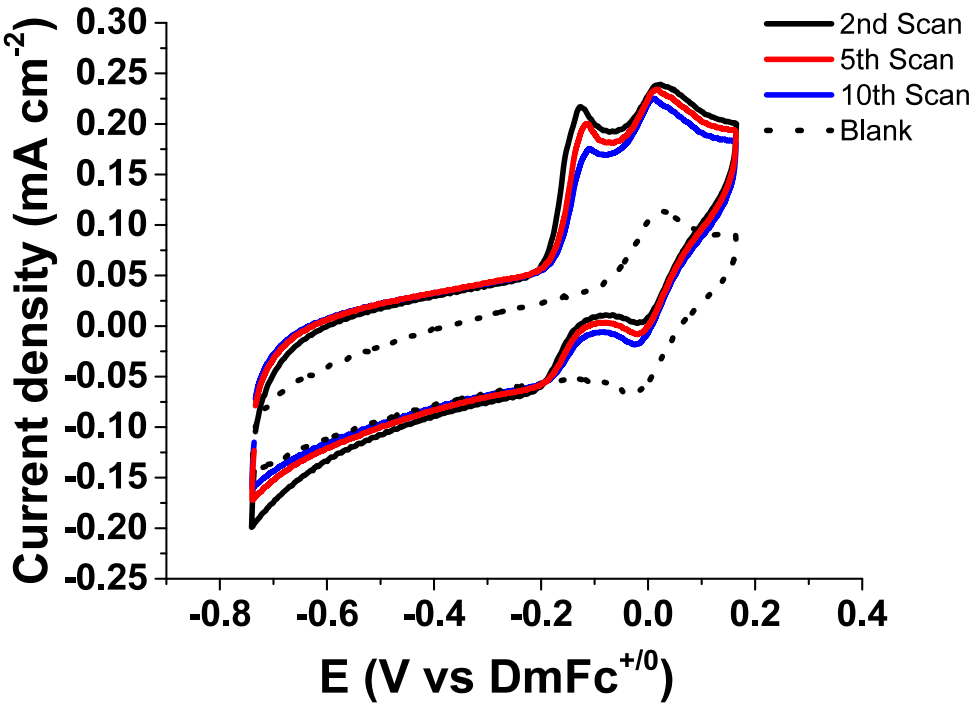



Figure 5.9 Continuous cyclic voltammetric scans (current density) of 1 µL of Hyd1 suspended in 100 mM phosphate buffer (pH 6.2), adsorbed at an MWNT/PGE electrode surrounded by EMIMTFSI (~1 mL) dissolved with 2 mM DmFc and saturated with $H_2$. Black, red and blue solid lines represent 2nd, 5th and 10th scan respectively. Electrode rotation rate 0 RPM. Temperature 30 ˚C, scan rate 10 mV/s, projected electrode surface area 0.03 $cm^2$.

The catalytic current densities of $H_2$ oxidation electrocatalysed by Hyd1 vary between experiments performed in identical manner, due to enzyme film variation in those experiments. So the difference of catalytic activity of Hyd1 in Figure 5.5 and 5.7 is not caused by the difference of ionic liquids between the two experiments.

Experiments discussed above were conducted in EMIMTFSI and PMPyrTFSI, which are water-immiscible. I have also experimented with water-miscible ionic liquids

including ethylammonium nitrate (EAN), diethylmethylammonium trifluoromethanesulfonate (DEMATFO), and tris(2-hydroxyethyl)methylammonium methylsulfate (TEMAMS). In none of these ionic liquids I detected oxidation of $H_2$ at MWNT/PGE electrode adsorbing Hyd1.

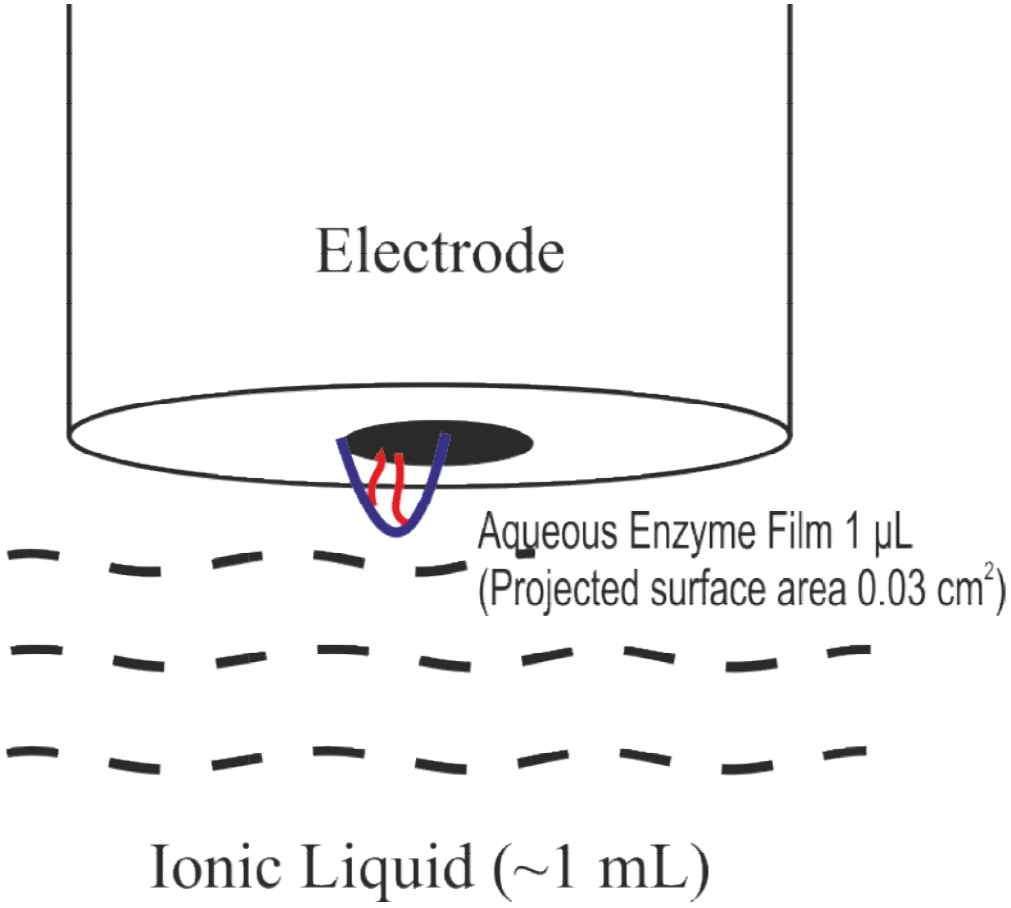



Figure 5.10 A schematic representation of a MWNT/PGE electrode modified with enzyme film and immersed in water-immiscible ionic liquid.The aqueous enzyme film is enclosed in a small pocket surrounded by water-immiscible ionic liquid.

From the electrochemical data using neat EMIMTFSI and PMPyrTFSI as electrolyte, I hypothesize that Hyd1 film is enclosed in a small pocket surrounded by

water-immiscible ionic liquid (Figure 5.10). During electrocatalytic reaction, $H_2$ diffuses from water-immiscible ionic liquid to reach the Hyd1 film at electrodes where the electrocatalysis of $H_2$ oxidation took place. As the $H_2$ oxidation proceeded by continuous cyclic voltammetry, more protons were produced in the small aqueous pocket, hence decreasing the pH of the small aqueous pocket surrounded by ionic liquids. Lower pH led to lower Hyd1 activity, according to thermodynamic laws. This is consistent with the decreasing $H_2$ oxidation currents that I have observed in continuous cyclic voltammetry in EIMITFSI and PMPyrTFSI (Figure 5.5 and 5.7).

On the contrary, in conventional mixed hydrogenase buffer (pH 6, 100 mM), the cyclic voltammetry of $H_2$ oxidation catalysed by Hyd1 showed constant onset potential of the $H_2$ oxidation in 14 cycles, indicating a constant pH of the electrocatalytic environment provided by the mixed hydrogenase buffer (Figure 5.11). The continuous cyclic voltammetry of Hyd1 in conventional buffer also shows increasing catalytic currents due to reductive Hyd1 activation under 100 % $H_2$ in the first 14 cycles [77]. Confined in EMIMTFSI and PMPyrTFSI that are water-immiscible, 2 µL of Hyd1 exhibited maximum catalytic current densities of 0.81±0.05 and 0.45±0.05 mA $cm^{-2}$ (based on five parallel experiments), respectively. These values are more than one order of magnitude lower than those observed in 100 mM pH 6.0 mix hydrogenase buffers at the same temperature (10.92±0.43 mA $cm^{-2}$, Table 4.2 and Figure 5.11). This indicates that although Hyd1 is electrocatalytically active towards $H_2$ oxidation confined in the hydrophobic RTILs, the catalytic current is partially lost. Reasons may be that: 1) the diffusion coefficients of $H_2$ are lower in RTILs, which are more viscous than aqueous buffers, 2) the Hyd1 is less active confined in RTILs than the native proteins in aqueous media.

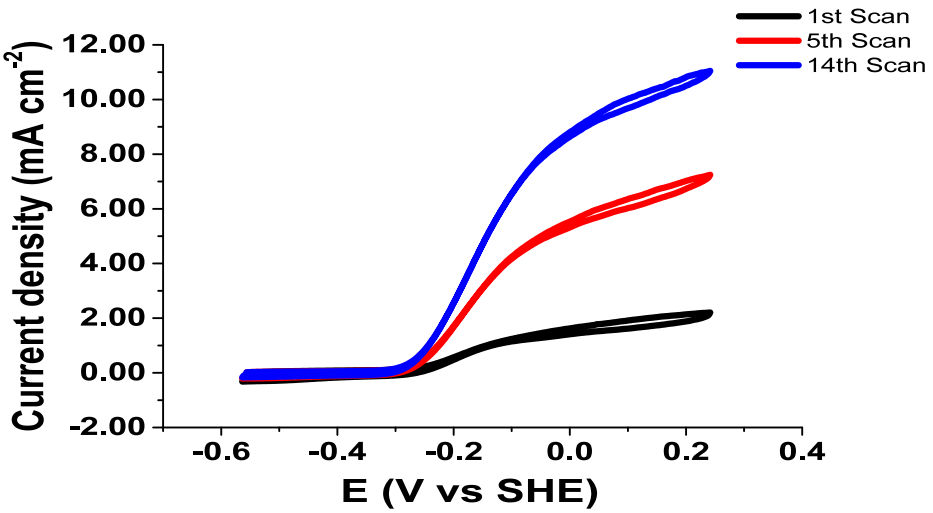



Figure 5.11 Cyclic voltammetric scans (current density) of Hyd1 (2 µL) modified MWNT/PGE electrode in pH 6mixed buffer (100 mM) under 100 % $H_2$. Black: 1$^{st}$ Scan, red: 5th Scan, blue: 14$^{th}$ Scan. Electrode rotation rate 1000 RPM. Temperature 30 ˚C, scan rate 10 mV/s, projected electrode surface area 0.03 cm$^2$.

### 5.4.3 Cyclic Voltammetry of Ferricyanide (aq.) at PGE in EMIMTFSI

To establish if some water molecules of the aqueous films at PGE electrodes are dissolved in EMIMTFSI, I performed cyclic voltammetry of 2 µL of ferricyanide (5 mM, aq.) at PGE electrode immersed in EMIMTFSI, at a scan rate of 10 mV/s (Figure 5.12).I found that the cyclic voltammetry shows a well-defined reversible one-electron process. The voltammogram was reported against a platinum wire quasi-reference electrode that is housed in a sidearm connected to the working electrode compartment via a Luggin capillary. During the scans from –800 to +900 mV, the electrode reaction was $Fe(CN)_6^{3-} + e^- \rightarrow Fe(CN)_6^{4-}$. The reversal scan led to the one-electron oxidation: $Fe(CN)_6^{4-} - e^- \rightarrow Fe(CN)_6^{3-}$.The peak current increased after each scan, indicating an

increasing concentration of $Fe(CN)_6^{3-}$ and $Fe(CN)_6^{4-}$ in the aqueous film at PGE electrode confined by EMIMTFSI, i.e. some water molecules were dissolved in EMIMTFSI.

The peak-to-peak potential separation value, $\Delta E_p$ (76 mV at 10 mV/s) was larger than the theoretic value of 60 mV for reversible processes at 30 ˚C. One reason is the effect of uncompensated resistance of solution. The other reason is that the $Fe(CN)_6^{4-/3-}$ process may have not achieved steady state at the scan rate above and equal to 10 mV/s.

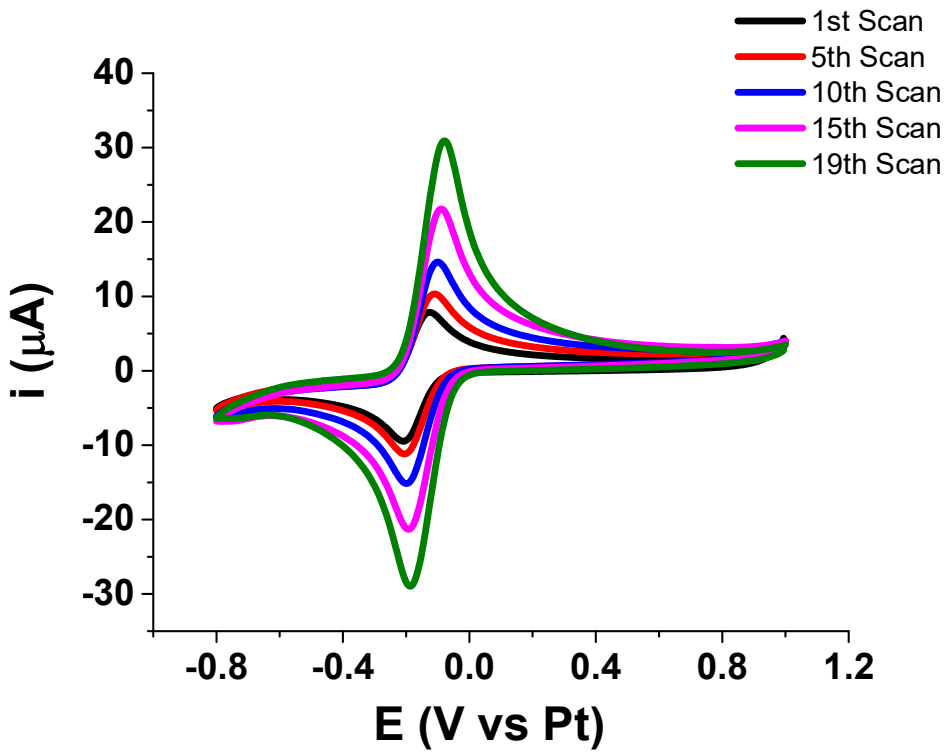



Figure 5.12 Cyclic voltammetry of 2 μL of ferricyanide (5 mM, aq.) at PGE electrode surrounded by EMIMTFSI. Scan rate 10 mV/s, temperature 30 ˚C, projected electrode surface area 0.03 $cm^2$.

## 5.5 Conclusions and Perspectives

In conclusion, I have determined the cyclic voltammograms of Hyd1 in aqueous microenvironment confined by two pure water-immiscible ILs: EMIMTFSI and PMPyrTFSI. All the voltammograms were referenced against $DmFc^{+/0}$. I found that confined in theILs, Hyd1 was electrocatalytically active towards $H_2$ oxidation. The $H_2$ oxidation electrocatalysed by Hyd1 confined inthe two different ionic liquids gave similar waveshapes and parameters (i.e. catalytic currents and onset potentials for $H_2$ oxidation) of cyclic voltammetry. Specifically, confined by either ionic liquid, the catalytic current for $H_2$ oxidation electrocatalysed by Hyd1 decreased while the onset potential increased through continuous cyclic voltammetric scans. On the contrary, I detected zero electrocatalytic activity of Hyd1 confined by three water-miscible ionic liquids. Based on these results, I proposed that the Hyd1 adsorbed on electrodes was enclosed in an aqueous pocket surrounded by water-immiscible ionic liquids. Water-immiscible ionic liquids provide a suitable matrix for Hyd1 to retain its catalytic activity toward $H_2$ oxidation.

Currently, there is very limited literature on the diffusivity and solubility of $H_2$ in ionic liquids. For example, no data on the diffusivity and solubility of $H_2$ in EMIMTFSI or PMPyrTFSI are currently available. Most study in this field focus on the solubility and diffusivity of $CO_2$ in RTILs, because $CO_2$ is usually much more soluble in RTILs than in water and $CO_2$ can be captured more efficiently by RTILs. For instance, the solubility of $CO_2$ is 0.0315 in EMIMTFSI at 298 K [217], more than 50 times higher than that in water ($6.15 \times 10^{-4}$ at 298 K [218]). Solubilities of diatomic gases (e.g., $H_2$, $O_2$, CO, $N_2$) measured in the same IL but by different authors show large discrepancies. For example, the Henry's constant for $O_2$ in $BMIMPF_6$ at 283 K was reported by

Anthony et al. to be 650 ± 425 MPa, while Kumelan et al. reported a value of 51.5 ± 0.6 MPa at 283 K. Nevertheless, the solubility trends of several gases observed in ILs are more or less similar. Simple gases often interact weakly with the IL ions, hence the polarizability of the gases is reflected in the solubility behaviour, leading to the series $H_2$< CO < $N_2$< $O_2$< Ar < $CH_4$ < $C_2H_6$< $CO_2$. Molecules that possess an electric quadrupole moment (e.g., $CO_2$ and $C_2H_4$) show higher solubilities. Accordingly, polar gases like $SO_2$, $H_2S$, and water vapour show very high solubilities. Fundamental research on gas diffusivity and solubility in RTILs is progressing these years to promote the technological application of ionic liquids [219, 220].

As this thesis focuses on the electrochemical properties of enzymes confined in RTILs, the properties of interface between the aqueous Hyd1 “pocket” and ionic liquids need further investigation by microscopy and spectroscopy linked to electrochemical measurements.

# 6 Reduction of $O_2$ Electrocatalysed by Bilirubin Oxidase Confined inIonic Liquids

## 6.1 Abstract

Bilirubin oxidase (BOD) catalyses $O_2$ reduction at a turnover frequency of ~100 $s^{-1}$, and requires a lower overpotential than Pt does. So this enzyme has often been considered asan attractive cathodic electrocatalyst for enzymatic fuel cells. To determine whether ionic liquids can function in enzymatic fuel cells, I performed enzyme film electrochemistry of BOD adsorbed on pyrolytic graphite edge electrodes modified by multiwalled carbon nanotubes in two pure water-immiscible ionic liquids: 1-ethyl-3-methylimidazolium bis(trifluoromethylsulfonyl)imide (EMIMTFSI) and 1-methyl-1-propyl pyrrolidinium bis(trifluoromethylsulfonyl)imide (PMPyrTFSI). I found that confined in either ionic liquid, BOD was highly electrocatalytically active towards $O_2$ reduction. The $O_2$ reduction electrocatalysed by BOD confined by either neat ionic liquid gave similar waveshapes and parameters of cyclic voltammetry (i.e. catalytic currents and onset potentials for $O_2$ reduction). Specifically, confined in both ionic liquids, the catalytic current and the onset potential for $O_2$ reduction electrocatalysed by BOD decreased through continuous cyclic voltammetric scans; the onset potential for $O_2$ reduction electrocatalysed by BOD in aqueous microenvironment confined by the ionic liquids decreased with pH of the small aqueous pocket. Based on these results, I proposed that the BOD adsorbed on electrodes was enclosed in an aqueous pocket surrounded by water-immiscible ionic liquids. Water-immiscible ionic liquidscan be suitable electrolyte for enzymatic fuel cellsusing BOD as cathodic electrocatalyst.

## 6.2 Introduction

The enzyme film electrochemistry of BOD in aqueous buffers has been widely reported. The early studies focused on $O_2$ reduction electrocatalysed by BOD embedded in the mediator of Os complexes at electrodes [26, 221-223]. Such mediated electrocatalytic $O_2$ reduction have three drawbacks. First, the amount of BOD was high at electrodes. Specifically, in one study, surfaceenzymecoverage was 12 nmol $cm^{-2}$, ca. $10^3$times higher than saturated monolayer coverage [223]. Second, ratios of Os complexes to enzyme were high. For example, the ratio achieved 43 Os atoms perenzyme [223]. Third, Os complexes are toxic and limit the onset potential of $O_2$ reduction. So electrocatalysis via direct electron transfer between BOD and electrodes, which requires less amount of enzyme and eliminates Os complexes, is preferred for application in fuel cells and biosensors and under extensive investigation nowadays [47, 53, 56, 224-228].

Ionic liquids (ILs) are gaining more attention to function as electrolyte for bioelectrochemistry and electrochemical devices such as fuel cells, capacitors and batteries [109]. However, ILs have been considered to be deleterious for proteins to perform direct electron transfer to electrodes. To my best knowledge, no positive results of $O_2$ reduction electrocatalysed by BOD have been reported in pure ILs. In 2013, Ohno and co-workers reported that they observed no catalytic current induced by BOD at a gold nanoparticle(AuNP) electrode when neat ILs were used as an electrolyte solution. However, BOD-induced catalyticcurrents were observed when small quantities of water were added to hydrophobic ILs. In their paper, they examined a direct electron transfer

reaction of BOD at an AuNP electrode in the mixtures of hydrophobic ionic liquid (IL) and water. The BOD-modified AuNP electrode provided a current density as high as 218 μA $cm^{-2}$ in 1-(2-hydroxyethyl)-3-methylimidazolium bis(trifluoromethane-sulfonyl)imide ([$C_2$OHmim][$Tf_2$N]) containing 7.4 wt% $H_2O$[176].

To evaluate the electrocatalytic performance of BOD in ILs, I performed enzyme film electrochemistry of BOD adsorbed on pyrolytic graphite edge electrodes (PGE) modified by multiwalled carbon nanotubes in two pure water-immiscible ionic liquids: EMIMTFSI and PMPyrTFSI. I found that confined in both pure ILs, BOD was electrocatalytically active towards $O_2$ reduction. The $O_2$ reduction electrocatalysed by BOD confined by both ILs gave similar waveshapes and parameters (i.e. catalytic currents and onset potentials for $O_2$ reduction) of cyclic voltammetry. Specifically, confined by the ILs, the catalytic current and the onset potential for $O_2$ reduction electrocatalysed by BOD decreased through continuous cyclic voltammetric scans; the onset potential for $O_2$ reduction electrocatalysed by BOD confined inthe ionic liquids decreased with pH of the small aqueous phase. Based on these results, I proposed that the BOD adsorbed on electrodes was enclosed in an aqueous pocket surrounded by water-immiscible ILs. Water-immiscible ionic liquids are interesting candidates as electrolyte for enzymatic fuel cellsusing BOD as cathodic electrocatalyst.

## 6.3 Experimental

Please refer to Chapter 3 for detailed information of materials, buffers, enzymes and procedures of protein film electrochemistry.

## 6.4 Results and discussion

### 6.4.1 Potential Calibration with DmFc as Internal Reference in Ionic Liquids

Please refer to Chapter 5 for the data.

### 6.4.2 Enzyme Film Electrochemistry of BOD Confined in EMIMTFSI and PMPyrTFSI

BOD catalyses $O_2$ reduction at a turnover frequency of ~100 $s^{-1}$, and requires a lower overpotential than Pt does from pH 5 to 8 [38, 44, 46, 54, 229, 230]. For example, the overpotential is only ca. 59 mV at pH 6, 30 °C, according to the data in Chapter 4. Voltammetry of $O_2$reduction by electrocatalysis of BOD in pure ionic liquids has never been reported. The purpose of carrying out PFE of the BODconfined in ILs is to determine the electrocatalytic activity of BOD confined in ILs and understand how the bioelectrocatalysis goes on in the aqueous shell confined by ILs.

Cyclic voltammetry was performed at a stationary MWNT/PGE electrodes adsorbing 2 μL of BOD (suspended in phosphate buffers) in ILs bubbling with 100 % $O_2$ at a scan rate of 10 mV/s. When the BOD film on the electrode was completely dry, tiny catalytic current was observed. The electrodes were stationary rather than rotating to prevent draining water from enzyme films. Because of the relatively low gas permeability of ILs, substrate gases had to pass through rather than flow above ILs to guarantee that enough substrate gases approach enzymes. When gases were flowing above ILs, tiny

electrocatalytic current was observed. All potentials were referenced against $E_f^\circ$ of $DmFc^{+/0}$ at 30˚C.

My results indicate that there was direct bioelectrocatalysis of $O_2$ reduction by BOD confined by EMIMTFSI (Figure 6.1). Confined by EMIMTFSI, BOD was highly electrocatalytically active in the first scan of voltammetry, but such activity decreased after each scan of voltammetry. Meanwhile, the onset potential of $O_2$ reduction decreased after each scan. The cyclic voltammogram of the blank MWNT/PGE electrode in EMIMTFSI bubbling with 100 % $O_2$ at 30 ˚C showed no catalytic current from +650 to −150 mV (Figure 6.1, dotted line). In contrast, thecyclic voltammograms of the BOD on a stationary MWNT/PGE electrode in the same conditions showed a peak-shaped catalytic wave, indicating a diffusion-controlled $O_2$ reduction electrocatalysed by BOD (Figure 6.1, solid lines). After each scan of voltammetry, the peak potential ($E_p$), onset potential and magnitude of the catalytic current decreased monotonically. In the first scan, the reduction current increased steeply from +560 mV, indicating the onset of $O_2$ reduction reaction.

As the potential decreased from +560 to +459 mV, the reduction current continued to increase, reaching the peak current density of 0.88 mA $cm^{-2}$ at +459 mV. As the potential decreased further from +459 to −150 mV, the reduction current density decreased monotonically from 0.88 to 0.67 mA $cm^{-2}$. This indicates a depletion of $O_2$ at the stationary electrode. The waveshapes of electrocatalysis by enzymes in EMIMTFSI is similar to those in quiescent aqueous buffers [53, 56, 64, 92, 215, 224, 227, 228, 231].

As more scans of cyclic voltammetry went on, I detected continuously decreasing oxidation current and decreasing onset potential of $O_2$ reduction electrocatalysed by BOD. Specifically, in the first 7 continuous scans of cyclic voltammetry, the peak current density lost by 71 % from 0.51 to 0.15 mA $cm^{-2}$. Meanwhile, the onset potential for electrocatalytic $O_2$ reduction decreased from +860 (1st scan) to +710 (7th scan) mV. Such trend of decreasing potential indicates an increase of pH by 2.5 in the aqueous enzyme film of 1 μL confined by EMIMTFSI, if the system obeys Nernst equation. This is consistent with the feature of $O_2$ reduction reaction, which produces hydroxides and makes the microenvironment more alkaline. When the microenvironment of BOD was too alkaline for the enzyme to function, the reduction current will eventually decreased to zero.

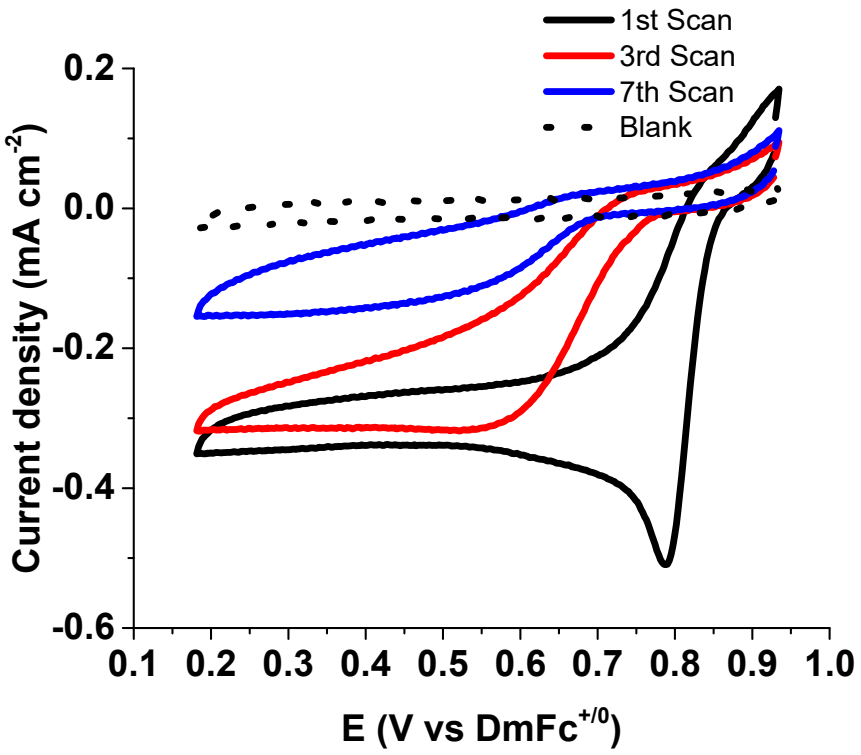



Figure 6.1 Cyclic voltammetric scans (current density) in 1 μL of BOD (suspended in pH 6.2 phosphate buffer, 100 mM) at MWNT/PGE electrode surrounded byEMIMTFSI bubbling with 100 % $O_2$.Black, red and blue solid lines represent the 1$^{st}$, 5$^{th}$ and 10$^{th}$scan of BOD respectively. Dotted lines: blank MWNT/PGE electrode. Electrode rotation rate: 0 RPM. Temperature 30 ˚C, scan rate 10 mV/s, projected electrode surface area 0.03 cm$^2$.

After the electrocatalytic activity vanished after continuous scans of cyclic voltammetry in EMIMTFSI, I moved the electrode into phosphate buffer (pH 6.2, 100 mM). The cyclic voltammetry (Figure 6.2) shows a well-shaped sigmoidal voltammogram, indicating that the electrocatalytic activity of BODgradually recovered.

This observation indicates that the loss of electrocatalytic activity of BOD by continuous cyclic voltammetry in EMIMTFSI is reversible. So the protein structure of BOD was not completely damaged after the electrocatalytic activity was exhausted by continuous cyclic voltammetry.

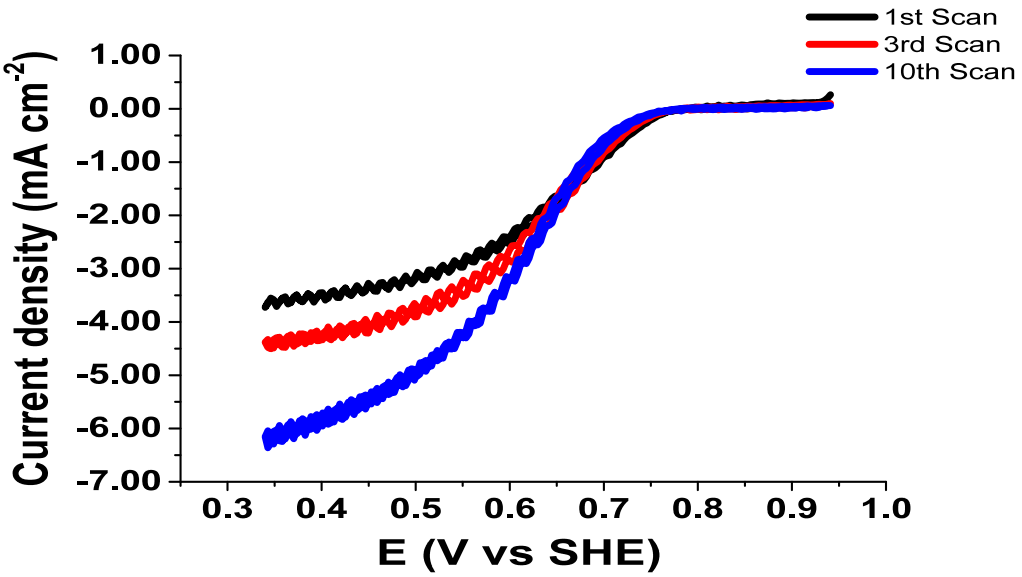



Figure 6.2 Cyclic voltammetric scans (current density) of BOD in phosphate buffer (pH 6.2, 100 mM) after the electrocatalytic activity vanished through continuous voltammetric scans in EMIMTFSI at the same electrode.Electrode rotation rate: 1000 RPM. 100 % $O_2$. Temperature: 30 ˚C, scan rate 10 mV/s, projected electrode surface area 0.03 $cm^2$.

For the purpose of understanding the effect of pH on the voltammetry of BOD in EMIMTFSI, I performed cyclic voltammetry of 1 µL of BOD suspended in phosphate

buffers of different pH at MWNT/PGE electrode in EMIMTFSI bubbling with 100 % $O_2$. I detected direct electrocatalytic reduction of $O_2$ by BOD at pH from 5.0 to 11.0 confined by EMIMTFSI (Figure 6.3 and 6.4). Corresponding data based on three parallel experiments are summarized in Table 6.1. The cyclic voltammograms of 1 μL of BOD suspended in phosphate buffers of different pH at stationary MWNT/PGE electrode in the same conditions showed a peak-shaped catalytic wave, indicating a diffusion-controlled $O_2$ reduction electrocatalysed by BOD. After each scan of voltammetry, the peak potential, onset potential and magnitude of the catalytic current all decreased monotonically. These features were observed in all cyclic voltammetry of aqueous BOD films confined by ILs.

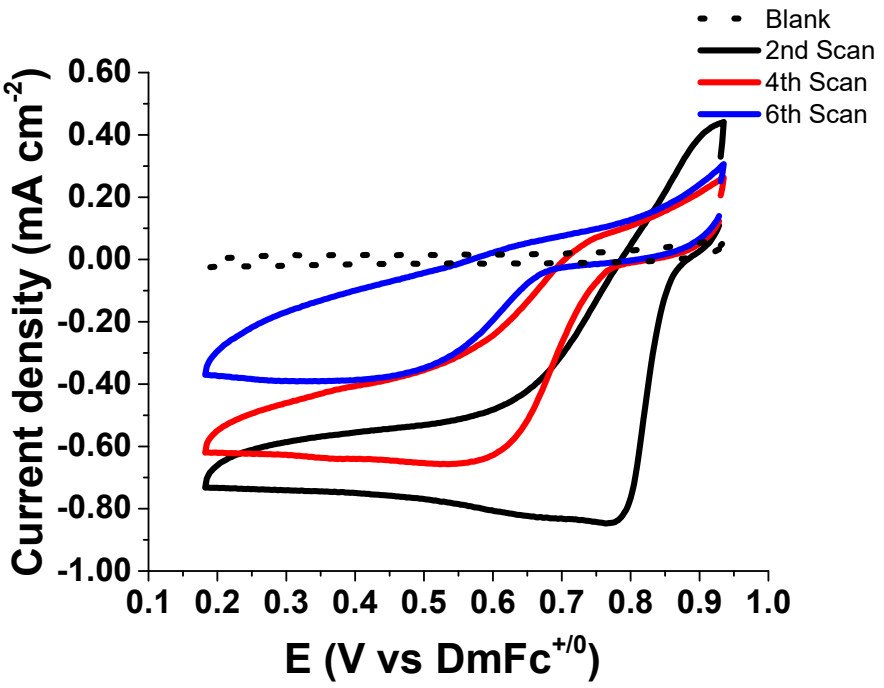



Figure 6.3 Cyclic voltammetric scans (current density) of 1 µL of BOD (suspended in pH 5.0 phosphate buffer, 100 mM) at MWNT/PGE electrode surrounded byEMIMTFSI bubbling with 100 % $O_2$. Black, red and blue solid lines represent the 1$^{st}$, 3$^{th}$ and 5$^{th}$ scan of BOD respectively. Dotted lines: blank MWNT/PGE electrode. Electrode rotation rate: 0 RPM. Temperature 30 ˚C, scan rate 10 mV/s, projected electrode surface area 0.03 cm$^2$.

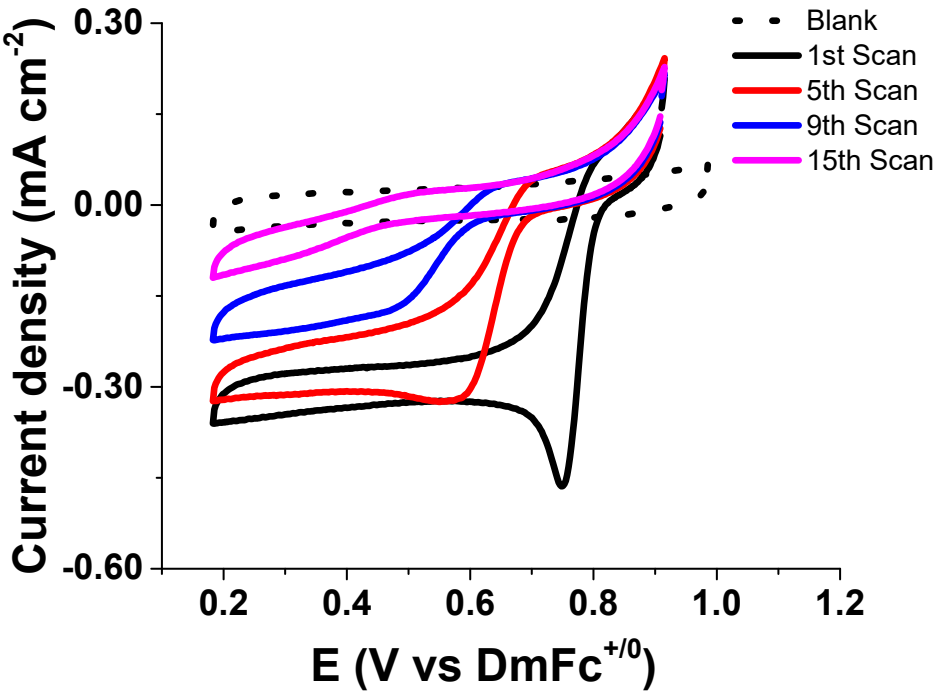



Figure 6.4 Cyclic voltammetric scans (current density) of 1 µL of BOD (suspended in pH 7.0 phosphate buffer, 50 mM) at MWNT/PGE electrode surrounded by EMIMTFSI bubbling with 100 % $O_2$. Black, red, blue and magenta solid lines represent the 1$^{st}$, 5$^{th}$, 9$^{th}$ and 15$^{th}$ scan of BOD respectively. Dotted lines: blank MWNT/PGE electrode. Electrode rotation rate: 0 RPM. Temperature 30 ˚C, scan rate 10 mV/s, projected electrode surface area 0.03 cm$^2$.

Table 6.1 Cyclic voltammetric data for $O_2$ reduction (1st Scan) catalysed by BOD (in 100 mM phosphate buffer) at MWNT/PGE electrode in EIMIMTFSI bubbling with 100% $O_2$ at 30 ˚C, scan rate 10 mV/s, projected electrode surface area 0.03 $cm^2$. All data are based on three parallel experiments.

| pH | Onset potential (mV vs $DmFc^{+/0}$) | Maximum current density (mA $cm^{-2}$) |
|---|---|---|
| 5.0 | 880 | 0.85±0.08 |
| 6.2 | 850 | 0.88±0.08 |
| 7.0 | 800 | 0.46±0.06 |

The potential at which catalysis occurs is also known as the onset potential. It reflects the identity of the electrochemical "control centre". The control centre is the redox site up to which there is fast and reversible electron exchange with the electrode [64]. I took the potential at which the slope of the reduction curve started to increase as the onset potential. I did not compare half wave potential (the potential corresponding to half of the maximum current density) of electrocatalytic $O_2$ reduction at different pH, because the half wave potential cannot display the inherent electrocatalytic activity of BOD, in my experimental conditions where the catalytic current was limited by mass transport.

As the pH increased from 5.0 to 7.0, the onset potential for $O_2$ reduction electrocatalysed by BOD decreased from +880 to +800 mV, i.e. the onset potential decreased by 40 mV/ pH on average, which deviatesthe thermodynamic potential for the $O_2/H_2O$ couple decreases by 61.5 mV/ pH as the pH increased at 30 ˚C (Table 6.1). One reason is that there is a requirement of overpotential. The other reason is that

different pH changes the formal potential of Type 1 copper site. Type 1 copper site has been proposed to be the first electron acceptor in direct electron transfer from carbon electrodes and determine the onset potential of the electrocatalysis of BOD [47, 52, 56, 232]. Similar pH dependence of onset or half wave potential for the electrocatalytic reduction of $O_2$ by BOD has been observed in bulk aqueous buffers [47, 224]. In one study, the half wave potential for the electrocatalytic reduction of $O_2$ by unpurified BOD decreased by about 30 mV/pH as the pH increased from 4.5 to 9 [224]. In another study, the onset potential decreased by 17 mV/pH as the pH increased from 5 to 8. A later study showed that the formal potential of the Type 1 copper site of BOD decreased by 35 mV/pH as the pH increased from 3.0 to 8.5 [233], indicating that the pH dependence of onset or half wave potential for the electrocatalytic reduction of $O_2$ by BOD is originated from the shifting of formal potential of Type 1 copper site with pH. Last but not least, the liquid junction potential between the aqueous BOD film and EMIMTFSI, which depends on the compositions of aqueous buffer film covering BOD at the electrode, can change as the concentration of hydroxide ions in the BOD film increased through continuous cyclic voltammetric scans.

The limiting catalytic current density for $O_2$ reduction fluctuated in the range from 0.46 to 0.98 mA $cm^{-2}$at pH from 5.0 to 7.0 (Table 6.1). This observation is different from the trend observed in aqueous buffer at an electrode rotating at sufficiently high rate to eliminate mass transport limit [47]. In the situation where mass transport is not limiting, the pH-profile of limiting catalytic current density for $O_2$ reduction shows a bell-shape at pH from 5.0 to 8.0, the optimum being 5.5. However, the mass transport limited the catalytic currents of $O_2$ reduction, although EMIMTFSI was bubbling with

$O_2$, according to the cyclic voltammograms that indicate the diffusion-limited catalysis of $O_2$ reduction. So I cannot compare the current density in my experiment with that obtained under the circumstances where the limit of mass transport was deconvoluted from the current signals by rotating electrodes.

For the purpose of determining the effect of buffer concentration of the BOD film at electrode on cyclic voltammetry, I performed cyclic voltammetry of 1 μL of BOD suspended in 1 mM phosphate buffer (pH 6.2 at 30˚C) at MWNT/PGE in EMIMTFSI bubbling with 100 % $O_2$ at 30˚C (Figure 6.5). Specifically, in the first 6 continuous scans of cyclic voltammetry, the peak current density lost by 69 % from 0.55 to 0.17 mA $cm^{-2}$, which is equal to 13.8% per scan. Meanwhile, the onset potential for electrocatalytic $O_2$ reduction decreased from +860 ($1^{st}$scan) to +650 ($6^{th}$ scan) mV, which is equal to 42 mV per scan. Such trend of decreasing potential indicates an increase of pH by 3.3 in the aqueous enzyme film of 1 μL confined by EMIMTFSI, if the system obeys Nernst equation. For 1 μL of BOD suspended in 100 mM phosphate buffer (pH 6.2 at 30˚C) at MWNT/PGE in EMIMTFSI bubbling with 100 % $O_2$ at 30˚C (Figure 6.1), the peak catalytic current density decreased by 11.8 % per scan, and the onset potential decreased by 25 mV per scan. Taken together, when the buffer concentration of the BOD film decreased from 100 mM to 1 mM, both the electrocatalytic current and onset potential of $O_2$ reduction decreased faster through continuous cyclic voltammetry. This is consistent with my hypothesis that the $O_2$ reduction takes place in the small aqueous pocket surrounded by ILs. When the buffer concentration decreased, the pH of the aqueous pocket increased faster through

continuous cyclic voltammetry, leading to faster decrease of electrocatalytic current and onset potential of $O_2$ reduction.

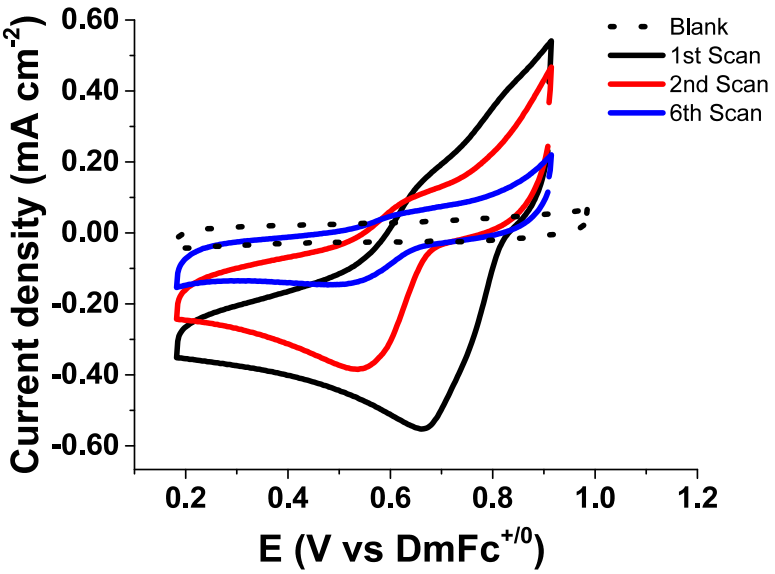



Figure 6.5 Cyclic voltammetric scans (current density) of 1 µL of BOD (suspended in pH 6.2 phosphate buffer, 1 mM) at MWNT/PGE electrode surrounded by EMIMTFSI (~1 mL) bubbling with 100 % $O_2$. Black, red and blue solid lines represent the 1$^{st}$, 2$^{nd}$ and 5$^{th}$ scan of BOD respectively. Dotted lines: blank MWNT/PGE electrode. Electrode rotation rate: 0 RPM. Temperature 30 ˚C, scan rate 10 mV/s, projected electrode surface area 0.03 cm$^2$.

My results indicate that there was direct bioelectrocatalysis of $O_2$ reduction by BOD confined byPMPyrTFSI (Figure 6.6). In PMPyrTFSI, BOD was

electrocatalytically active in the first scan of voltammetry, but such activity decreased after each scan of voltammetry. Meanwhile, the onset potential of $O_2$ reduction decreased after each scan. The cyclic voltammogram of the blank MWNT/PGE electrode in PMPyrTFSI bubbling with 100 % $O_2$ at 30 ˚C showed no catalytic current in the potential range from +15 to +1000 mV (Figure 6.6, dotted line). In contrast, the cyclic voltammograms of the BOD on a stationary MWNT/PGE electrode in the same conditions showed a peak-shaped catalytic wave, indicating a diffusion-controlled $O_2$ reduction electrocatalysed by BOD (Figure 6.6, solid lines). After each scan of voltammetry, the onset potential and magnitude of the catalytic current decreased monotonically. In the first scan (black solid line,Figure 6.6), the reduction current increased steeply from +810 mV, indicating the onset of $O_2$ reduction. As the potential decreased from +810 to+620 mV,the reduction current continued to increase, reaching the peak current density of 1.10 mA $cm^{-2}$ at +620 mV. As the potential decreased further from +620 to +30 mV,the reduction current density decreased monotonically from 1.10 to 0.87 mA $cm^{-2}$. This indicates a depletion of $O_2$ at the stationary electrode. The waveshapes of electrocatalysis by enzymes in EMIMTFSI is similar to those in quiescent aqueous buffers [53, 56, 64, 92, 215, 224, 227, 228, 231].

As more scans of cyclic voltammetry went on, I detected continuously decreasing oxidation current and decreasing onset potential of $O_2$ reduction electrocatalysed by BOD. Specifically, in the first continuous 15 scansof cyclic voltammetry, the maximum current density lost by 79% from 1.10 to 0.46 mA $cm^{-2}$. Meanwhile, the onset potential for electrocatalytic $O_2$ reduction decreased from +810 to +560 mV.Such trend of

decreasing potential indicates an increase of the concentration the hydroxide ion, according to Nernst equation.

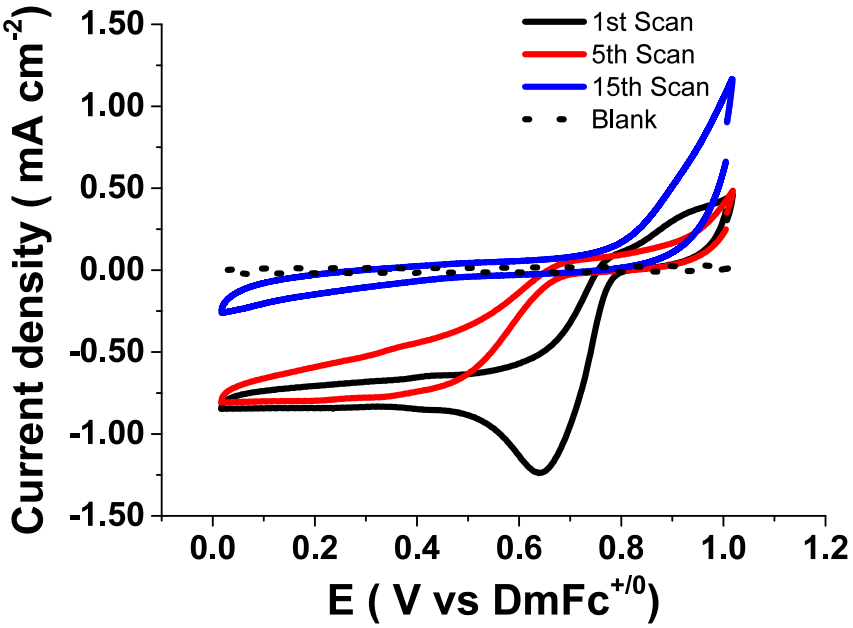



Figure 6.6 Cyclic voltammetric scans (current density) of 2 μL of BOD (suspended in pH 7 phosphate buffer, 50 mM) at MWNT/PGE electrode surrounded by PMPyrTFSI bubbling with 100 % $O_2$.Black, red and blue solid lines represent the 1$^{st}$, 5$^{th}$ and 15$^{th}$ scan of BOD respectively. Dotted lines: blank MWNT/PGE electrode. Electrode rotation rate: 0 RPM. Temperature 30 ˚C, scan rate 10 mV/s, projected electrode surface area 0.03 cm$^2$.

After the electrocatalytic activity vanished after continuous scans of cyclic voltammetry in PMPyrTFSI, I moved the electrode into phosphate buffer (pH 6.2, 100 mM). The cyclic voltammetry (Figure 6.7) showed a well-shaped sigmoidal

voltammogram, indicating that the electrocatalytic activity of BOD gradually recovered. This observation indicates that the loss of electrocatalytic activity of BOD by continuous cyclic voltammetry in PMPyrTFSI is reversible. So the structure of BOD was not completely damaged after the electrocatalytic activity was exhausted by continuous cyclic voltammetry.

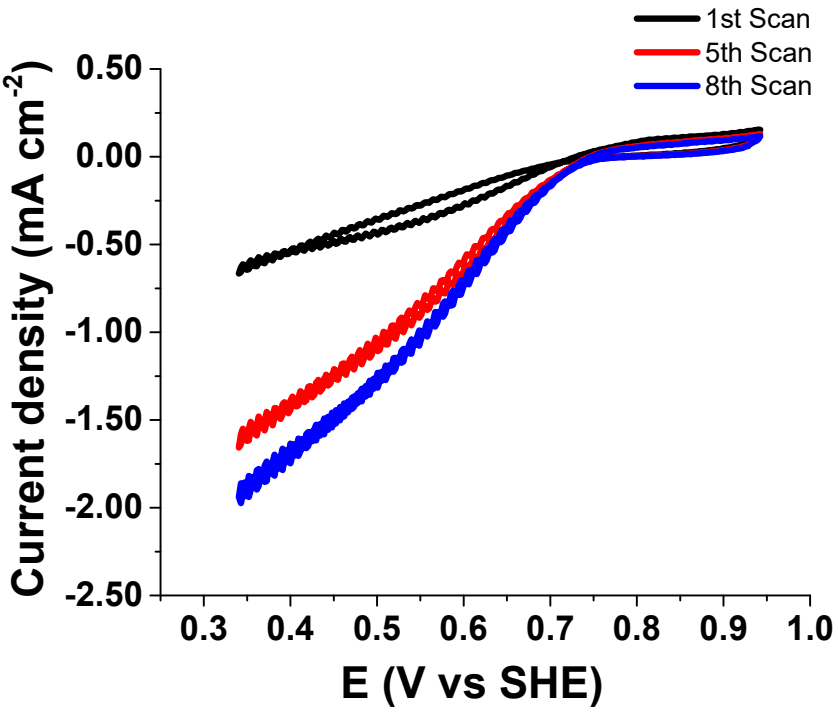



Figure 6.7 Cyclic voltammetric scans (current density) of BOD in phosphate buffer (pH 6.2, 100 mM) after the electrocatalytic activity vanished through continuous voltammetric scans in PMPyrTFSI at the same electrode. Electrode rotation rate: 1000 RPM. 100 % $O_2$.Temperature: 30 ˚C, scan rate 10 mV/s, projected electrode surface area 0.03 $cm^2$.

Both EMIMTFSI and PMPyrTFSI are water-immiscible. I have also experimented with water-miscible ionic liquids including ethylammonium nitrate (EAN), diethylmethylammonium trifluoromethanesulfonate (DEMATFO), and tris(2-hydroxyethyl)methylammonium methylsulfate (TEMAMS). In none of these water-miscible ionic liquids I detected reduction of $O_2$ at MWNT/PGE electrode covered by BOD.

From these electrochemical data I hypothesize that BOD film is enclosed in a small pocket surrounded by water-immiscible ionic liquid (Figure 5.10). During electrocatalytic reaction, $O_2$ diffuses from water-immiscible ionic liquid to reach the BOD film at electrodes where the electrocatalysis of $O_2$ reduction took place. As the $O_2$reduction proceeded by continuous cyclic voltammetry, more hydroxide ions were producedin the small aqueous pocket, hence increasing the pH of the small aqueous pocket surrounded by ionic liquids. Hence the onset potential of $O_2$ reduction decreased, according to thermodynamic laws. The pH of the small aqueous pocket is not only influencing the onset potential of $O_2$ reduction, but also affecting the catalytic currents. As the pH increased from the optimal pH of BOD (~ 5.5 [47]), I observed decreasing $O_2$ oxidation currents in continuous cyclic voltammetry EIMITFSI and PMPyrTFSI (Figure 6.1 and 6.6). This current-pH dependency reflects the impact of $pK_a$ of the group(s) that the proton transfer depends on [51]. The proton transfer was proposed to depend on a conserved aspartate (D105 in Figure 1.2) with a $pK_a$ of 5.4 and is 0.5 nm from the Type 2/Type 3 trinuclear cluster [234]. When the pH increased from ~5.4, the carboxylate was deprotonated, thus unable to bind and supply protons for $O_2$reduction. Consequently, the $O_2$reduction currents decreased.

On the contrary,in conventional phosphate buffer (pH 6.2, 100 mM), the continuous cyclic voltammetry of $O_2$ reduction catalysed by BOD showed constant onset potential of the $O_2$reduction in 20 cycles, indicating a constant pH of the electrocatalytic environment provided by the phosphate buffer (Figure 6.8). The continuous cyclic voltammetry of BOD in conventional buffer shows a gradually decreasing electrocatalytic current, as a result of film loss of BOD at the working electrode [235]. The film loss of enzyme adsorbed at electrode surfaces is caused by the desorption of enzymes from the electrode or denaturation of enzymes *in vitro*or both.

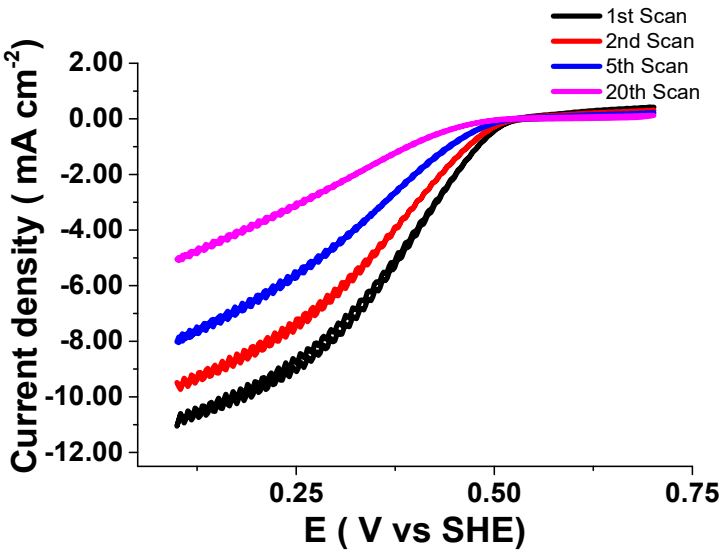



Figure 6.8 Cyclic voltammetry (current density) of BOD modified MWNT/PGE electrode in pH 6.2 phosphate buffer (100 mM) under 100 % $O_2$.Black: 1st Scan, red: 2nd Scan, blue: 5th Scan, magenta: 20th Scan.Electrode rotation rate: 1000 RPM. 100 % $O_2$.Temperature: 30 ˚C, scan rate 10 mV/s, projected electrode surface area 0.03 $cm^2$.

To confirm the validity of the method for calibrating the potentials of enzyme film voltammetry in ionic liquids, I carried out cyclic voltammetry in EMIMTFSI dissolved with 2 mM DmFc and saturated with 100 % $O_2$. When the RTIL was bubbling with $O_2$, $O_2$ reduction via BOD mediated by DmFc was detected in cyclic voltammetry. The results confirm that the method used to estimate the potential of enzyme film voltammetry in the previous experiments in this chapters is valid, because the potential values of enzyme film voltammetry of BOD in the aqueous shell surrounded by ILs without DmFc are close to those of enzyme film voltammetry of BOD in the aqueous shell surrounded by EMIMTFSI dissolved with 2 mM DmFc. Figure 6.9 shows similar experiments conducted to investigate electrocatalytic $O_2$ reduction by BOD. The cyclic voltammogram of the blank MWNT/PGE electrode showed no catalytic current from +970 to −130 mV in EMIMTFSI dissolved with 2 mM DmFc and saturated with 100 % $O_2$ at 30 ˚C (Figure 6.9, purple solid line). The redox peaks around 0 V were from the reversible one-electron process of $DmFc^{+/0}$. In contrast, the cyclic voltammograms of BOD adsorbed on an MWNT/PGE electrode in contact with 1 μL of 100 mM phosphate buffer (initially pH 6.2 at 30 ˚C) on a stationary MWNT/PGE electrode in the same conditions show a peak-shaped catalytic wave, indicating diffusion-controlled $O_2$ reduction. The $O_2$ reductioncatalytic wave decreased in amplitude upon successive cycles and shifted to more negative potential. Specifically, in the first 3 continuous scans of cyclic voltammetry, the onset potential for electrocatalytic $O_2$ reduction decreased from +890 ($1^{st}$ scan) to +780 ($3^{rd}$ scan) mV.

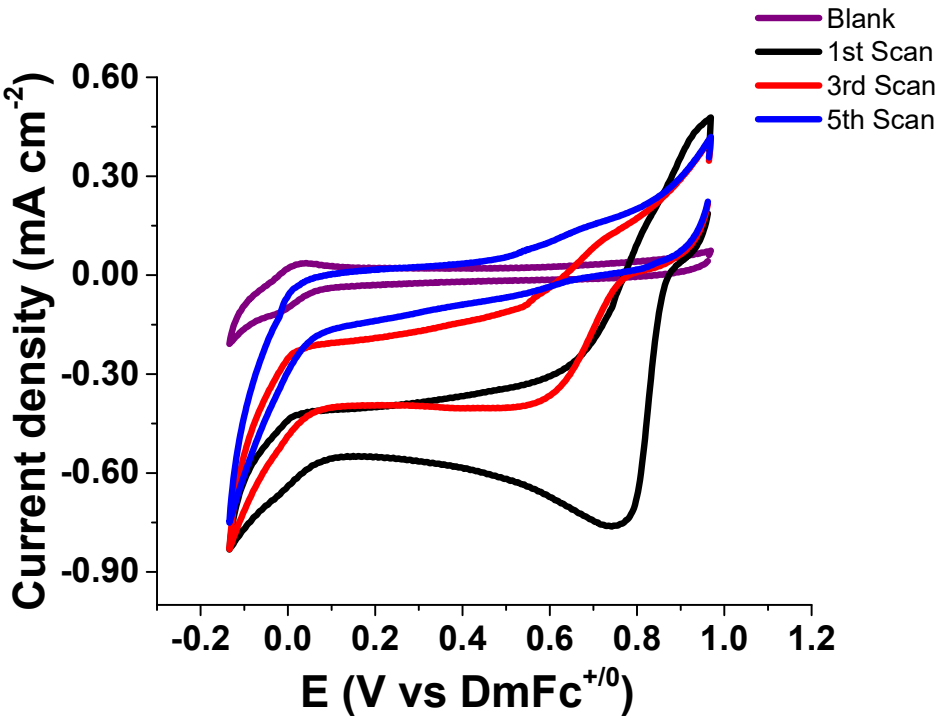



Figure 6.9 Cyclic voltammetric scans (current density) of 1 µL of BOD suspended in 100 mM phosphate buffer (pH 6.2), at an MWNT/PGE electrode in EMIMTFSI (~1 mL) dissolved with 2 mM DmFc and saturated with $O_2$. Black, red and blue lines represent the 1st, 3rd and 5th scan of BOD respectively. Purple line: blank MWNT/PGE electrode. Electrode rotation rate: 0 RPM. Temperature 30 ˚C, scan rate 10 mV/s, projected electrode surface area 0.03 $cm^2$.

## 6.5 Conclusions and Perspectives

In summary, I determined the voltammograms of $O_2$ reduction electrocatalysed by BOD at MWNT/PGE confined by two purewater-immiscible ionic liquids: EMIMTFSI and PMPyrTFSI referenced against $DmFc^{+/0}$. I found that confined by both pure ionic

liquids, BOD was electrocatalytically active towards $O_2$ reduction. The $O_2$ reduction electrocatalysed by BOD confined by eitherionic liquid gave similar waveshapes and parameters (i.e. catalytic currents and onset potentials for $O_2$ reduction) of cyclic voltammetry. Specifically, confined in theionic liquids, the catalytic current and the onset potential for $O_2$ reduction electrocatalysed by BOD decreased through continuous cyclic voltammetric scans; the onset potential for $O_2$ reduction electrocatalysed by BOD confined by both ionic liquids decreased with pH of the tiny aqueous phase. On the contrary, I detected zero electrocatalytic activity of BOD confined by two water-miscible ionic liquids. Therefore, water-immiscible ionic liquids are promising candidates as electrolyte in enzymatic fuel cells.Based on these results, I proposed that the BOD adsorbed on electrodes was enclosed in an aqueous pocket surrounded by water-immiscible ionic liquids.

Due to the lack of literature on $O_2$ solubility and diffusivity in RTILs (there has only been one publication reporting the$O_2$ solubility in EMIMTFSI), quantitative analysis of the bioelectrocatalytic activity of BOD towards $O_2$ reduction is not feasible at the moment.

In addition to the electrochemical properties of BOD confined in hydrophobic ionic liquids, the properties of interface between the aqueous BOD phase and ionic liquids need to be investigated by spectroscopic and microscopic techniques alongside electrochemical techniques.

# 7 Synaptic Enzymatic $H_2$-$O_2$ Fuel Cell Using an Ionic Liquid

## 7.1 Abstract

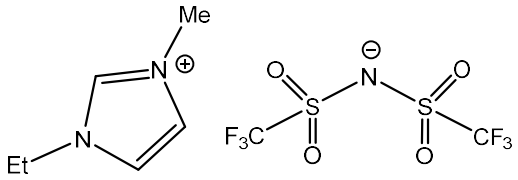
A tiny fuel cell using $O_2$-tolerant hydrogenase and bilirubin oxidase as anode and cathode electrocatalyst respectively was designed. This is the first enzymatic fuel cell using ionic liquid as electrolyte to date. The cathode and anode were two identical 8×8 mm carbon papers that are modified by multiwalled carbon nanotubes. They were separated by a gap of 0.5 mm, like a synapse. The gap was connected by 2 μL of 1-ethyl-3-methylimidazolium bis(trifluoromethylsulfonyl)imide (EMIMTFSI), which is a water-immiscible ionic liquid. The wet enzymes films (1 μL) on both anode and cathode were also covered with 2 μL of EMIMTFSI. Theopen circuit voltage (OCV) of the synaptic fuel cell (SFC) was 0.90 ± 0.1 V (based on three parallel experiments), which is close to 1.23 V: the reversible OCV of a $H_2$-$O_2$ fuel cell at 25˚C. It reached a maximum power density of 7.3± 0.3 μW $cm^{-2}$ (per total electrode area, based on three parallel experiments)with 96 % $H_2$–4 % $O_2$, 26 ± 2 ˚C. On the other hand, a synaptic fuel cell that uses conventional aqueous buffer in lieu of EMIMTFSI reached a maximum power density of 175 ± 5 μW $cm^{-2}$ (per total electrode area, based on three parallel experiments) in the same conditions. The synaptic fuel cell using EMIMTFSI showed slower gas transport than that uses aqueous buffer as electrolyte. Increasing the pressure of $H_2$-$O_2$ gas mixture, optimizing the enzyme-electrode interface, or designing new ionic liquids that are more gas permeable and enzyme-friendly can further improve the power density of the synaptic fuel cell.

## 7.2 Introduction

Enzymes are inspirational alternatives for precious metal catalysts in specialized fuel cells because they have the merits of high turnover rate per active site, high substrate-selectivity, availability from abundant raw materials and ability to operate under ambient conditions at low overpotentials. The insight that enzymes provide with regard to understanding electrocatalytic mechanism can more than compensate for the practical limitations due to size and stability. Unlike conventional catalysts that lack strong specificity, enzymes allow fuel cells to be miniaturized, operating on a mixed fuel-oxidant feed without a membrane separating the fuel and oxidant [5]. One such enzyme, hydrogenase-1 from *E. coli* (Hyd-1), catalyses $H_2$ oxidation with a high turnover frequency at moderate driving potentials in the presence of $O_2$ [236]. Hydrogenase-1 is easily isolated from a common organism, making it very suitable for developing an enzyme-based hydrogen fuel cell [64, 77, 78]. Another enzyme, bilirubin oxidase (BOD), is commercially available, highly active and catalyses the four-electron $O_2$ reduction reaction under mild pH conditions at a smaller overpotential than platinum [47]. Consequently, Hyd-1 and BOD are being exploited as anode and cathode catalysts respectively, in studies of enzymatic $H_2$-$O_2$ fuel cells [27, 30, 79].

Room temperature ionic liquids (RTILs) are non-volatile, conductive, thermally stable and have wide electrochemical windows, allowing them to be competent electrolytes in fuel cells [111]. Recently an experiment was described in which BOD was shown to be electrochemically active when enclosed with a small amount of water in such a RTIL shell [176]. Experiments with a hydrogenase and RTIL confirmed further that water was essential for activity with these enzymes [175]. In the quest to establish if a $H_2/O_2$ fuel cell could be miniaturized along similar lines to that achieved with other enzyme fuel cells [39, 223, 237], a logical step forward is to incorporate

RTILs into new designs. The concepts illustrated in Figure 7.1 represent development of synaptic membraneless fuel cells that use RTILs to entrap and protect an aqueous microvolume that contains dissolved $H_2$ and $O_2$. In the experiments I now describe, I have used the water-immiscible, hydrophobic RTIL: 1-ethyl-3-methyl-imidazolium-bis(trifluoromethylsulfonyl)imide (EMIMTFSI) (**1**) to protect a thin layer of water around Hyd-1 and BOD, each immobilized on an electrode. The viscosity of EMIMTFSI (26.28 cp at 30 ˚C) is about 30 times greater than water (0.798 cp at 30 ˚C), thus providing a good level of mechanical stability.




**1**

## 7.3 Experimental

### 7.3.1 Characterisation of anode and cathode in EMIMTFSI

Please refer to Chapter 3 for detailed information of materials, buffers, enzymes and procedures of protein film electrochemistry.

### 7.3.2 The Synaptic Fuel Cell (SFC)

Synaptic fuel cells were constructed in which an anode modified with Hyd-1 and a cathode modified with BOD were brought close together and electrically connected in one of two ways, within a thin gap (hence, a ‘synapse’) as depicted in Figure 7.1. The

electrodes were identical pieces of Toray carbon paper modified with MWNTs. They were prepared by pipetting 10 μL of MWNT dispersion (2.5 mg $mL^{-2}$ in DMF) onto the middle of one side of each piece of carbon paper measuring 8.0 × 8.0 mm. In each case, the MWNT dispersion was left to dry for 1 h to form a circular MWNT film (diameter ≈ 2.0 mm). Half of the other side of each piece of carbon paper was then attached to a piece of adhesive copper tape (4.0 × 8.0 mm) and thus to copper wire. The two electrodes were then placed on a microscope slide using double-sided tape so that there was a gap of 0.5 mm between the carbon surfaces on each side. The microscope slide was attached to the bottom of a plastic 'sandwich box' (2 L, 14 ×14 ×5.5 cm). Two needles were inserted into the centre of the lid to enable gas mixture to enter and exit, and wires from each electrode exited the box through two very small holes (Figure 7.2). After the synaptic enzyme fuel cell had been assembled, enzymes were applied to the electrodes under the anaerobic glove box atmosphere by pipetting 2 μL aliquots of activated Hyd-1 and BOD stock solution, respectively, onto the MWNT-modified carbon surfaces of anode and cathode. The enzyme deposits on both electrodes, (diameter approximately 1 mm in each case, based on the average of three independent films at the electrode) were left to dry for 15 minutes in the anaerobic glove box. This drying step is crucial to prevent Hyd-1 and BOD films from crossing the synapse and mixing with each other.

The enzyme-loaded fuel cell was moved to the bench to complete the construction. Before application to fuel cells, both water and EMIMTFSI were saturated with 96 % $H_2$–4 % $O_2$ by passing the gas mixture through 1 mL of the liquids via a needle for 0.5 h. In one case the dry Hyd-1 and BOD films on the two electrodes were hydrated by pipetting 1 μL of water, respectively. Then another 1 μL of water was pipetted across the synaptic gap and spread across the two enzyme films. Each of the two aqueous

enzyme films was then coated with 1 µL of EMIMTFSI. Finally, the synaptic gap that was already connected by 1 µL of water was coated with another 1 µL of EMIMTFSI. In the second case, the Hyd-1 and BOD films on the electrodes were rehydrated with two separate 1 µL aliquots of water then each droplet was coated with 2 µL of EMIMTFSI, and finally, a further 2 µL of the same EMIMTFSI was applied to fill the 0.5 mm synaptic gap between the two electrodes.

A. B.

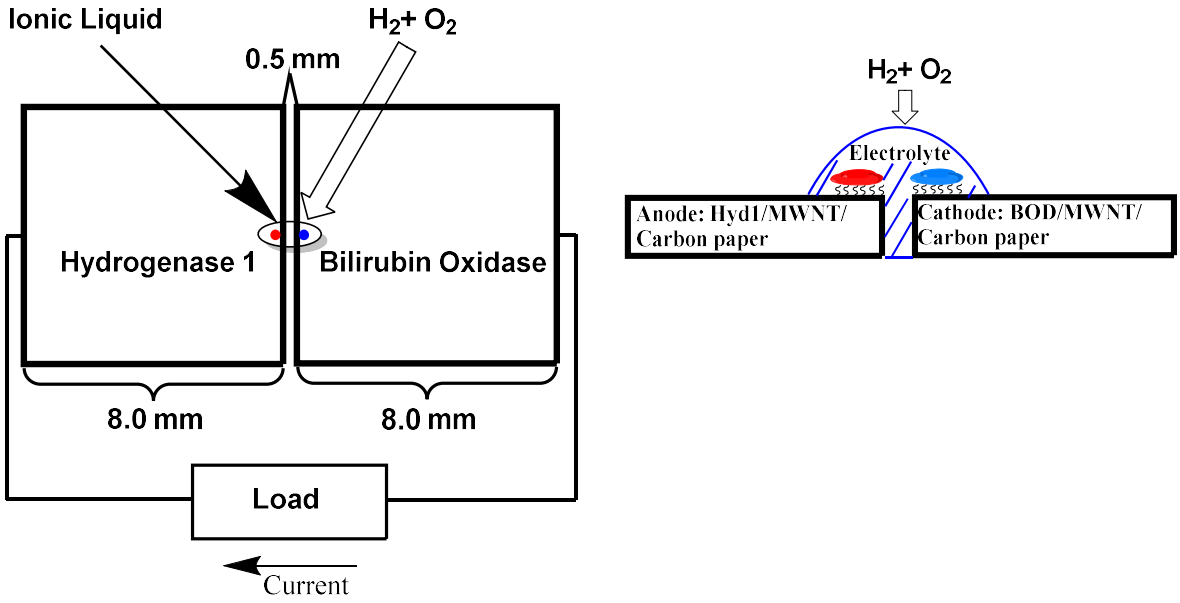



Figure 7.1 (Panel A) Vertical view diagram of the synaptic fuel cell. (Panel B) Side view diagram of the synaptic fuel cell.Two carbon papers modified with MWNT are separated with a gap of 0.5 mm. Each carbon paper sticks to electric wire with copper tape.

A. B.

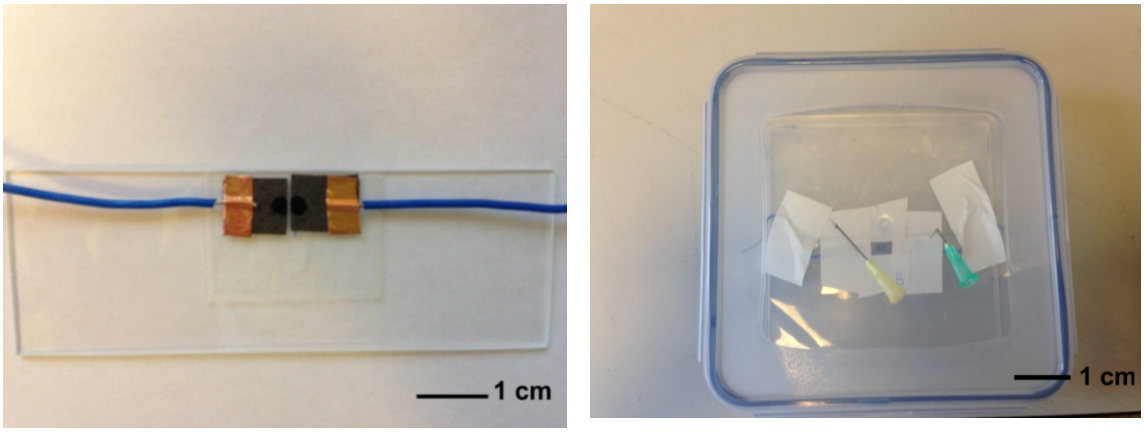



Figure 7.2 (PanelA) Photo of the synaptic fuel cell. (PanelB) Photo of the whole setup of SFC in a sandwich box.Two needles transport gas mixtures to the SFC. The electric wires connected to the carbon papers reach out of the sandwich box via two holes on the opposite walls of the box. Scotch tape stabilizes the SFC onto the bottom of the sandwich box.

In a comparative experiment, an SFC running with only aqueous buffer (buffer-SFC) was constructed and tested. First, the enzymes were loaded in the same procedure as described above. Next, 96 % $H_2$–4 % $O_2$was run through 2 mL of phosphate buffer (100 mM, pH 5.0) for 30 min to saturate the buffer solution before it was applied to the enzyme-loaded SFC. Last, on bench, 2 µL ofthe buffer solution was pipetted onto each dry enzyme films at electrode. Another 2 µL of the buffer solution was pipetted to connect the 0.5 mm gap between the two electrodes.

Within 1 min after the SFC was constructed, the complete SFC was connected to the Autolab PGSTAT 20 to measure the performance when gas mixtures of $H_2$ and $O_2$ were supplied into the sandwich box via the needle on top of its lid. The buffer-SFC

was supplied with gas mixtures humidified with a bottle of water (purified bya Milli-Q water purification system to 18.2 MΩ cm) before entering the sandwich box. Both EMIMTFSI and buffer-SFCwere analyzed by identical experiments at 26 ± 2 ˚C. At the start of each experiment, a chronopotentiometry at zero current was applied to the SFC with 96 % $H_2$–4 % $O_2$ until the voltage leveled off at its maximum. The voltage obtained here when there was no current between anode and cathode was the open circuit voltage (OCV) of the fuel cell. In order to operate the SFCs at a certain voltage, chronoamperometry at a certain voltage was applied to the fuel cell. The power curve which illustrates the relationship between power density and cell voltage was obtained by linear scan voltammetry of the whole SFC starting from its OCV to 0 V at 1 mV/s with 96 % $H_2$–4 % $O_2$. From the linear scan voltammetry, a current value (I) was obtained at each voltage (*E*), and the correspondent fuel cell power (P) was calculate from the equation $P = E \times I$. *P* was divided by the cathode area of SFC (0.00785 $cm^2$), giving the power density. The power density was plotted against E to achieve a power curve.

The experimental procedures for creating a working enzymatic fuel cell are determined after numerous experiments that had failed. MWNT pellets were used as electrodes, but they cracked and lead to short-circuit of the fuel cell. Wax (Icosane, $C_{20}H_{42}$, from Sigma-Aldrich) was used to protect the thin layer of aqueous phase from drying, however, the wax did not seal the aqueous phase as perfectly as RTILs, and led the fuel cell to dry out in 30 min.

## 7.4 Results

### 7.4.1 Characterisation of Cathode and Anode in EMIMTFSI

Voltammetry of aqueous Hyd1 or BOD film at electrode confined by pure ionic liquid was reported in Chapter 5 and 6. The purpose of the voltammetry of the two enzymes in EMIMTFSI is to determine the electrocatalytic activity of cathode and anode electrocatalysts of the EMIMTFSI-SFC. In addition, the OCV of the EMIMTFSI-SFC can be estimated from the difference between the onset potentials of the anode and cathode electrocatalytic reactions in the voltammograms.

I determined voltammograms of 1 μL of Hyd1 or BOD suspended in phosphate buffer (100 mM, pH 6.2) at MWNT/PGE electrode in EMIMTFSI saturated with 96 % $H_2$–4 % $O_2$ (v/v) at 30 ˚C, which is similar to the fuel cell operating conditions. If the enzyme film on the electrode was completely dry, no catalytic current was observed. The electrodes were stationary rather than rotating to prevent draining water from enzyme films. In such quiescent condition, the voltammetry was limited by mass transport, unlike those recorded with rotating disk electrodes that rotate at sufficiently high rates to eliminate the restriction by mass transport of substrate gases. EMIMTFSI was saturated with 96 % $H_2$–4 % $O_2$ by passing gases through it. All potentials were referenced against $E_f^{\circ}$ of $DmFc^{+/0}$. My results indicate that direct electron transfer was achieved between the electrodes and enzymes in EMIMTFSI. Both enzymes were highly electrocatalytically active confined by EMIMTFSI (Figure 7.3), proving the feasibility of a synaptic fuel cell running with EMIMTFSI as electrolyte shows catalytic voltammograms of Hyd-1 and BOD, each contained within a 1 μL aqueous droplet (0.10 M phosphate, pH 6.2) on a MWNT/PGE electrode and immersed in EMIMTFSI saturated with 96 % $H_2$–4 % $O_2$ (v/v) at 30 ˚C. The blank MWNT/PGE electrode

showsonly direct, non-enzymatic reduction of $O_2$ at a potential below –0.19± 0.1 V vs $DmFc^{+/0}$ (based on three parallel experiments). For Hyd-1, this non-enzymatic $O_2$ reduction commences close to that for the enzyme-catalysed $H_2$ oxidation, and the actual onset potential for $H_2$ oxidation is obscured. For electrocatalytic $O_2$ reduction by BOD, a sharp peak is observed at +0.89 V vs $DmFc^{+/0}$ and the onset potential is close to + 1 V. The onset potentialsmeasured under these$H_2$-$O_2$ fuel cell conditions indicate that an open-circuit voltage of 1.1 V is achievable.

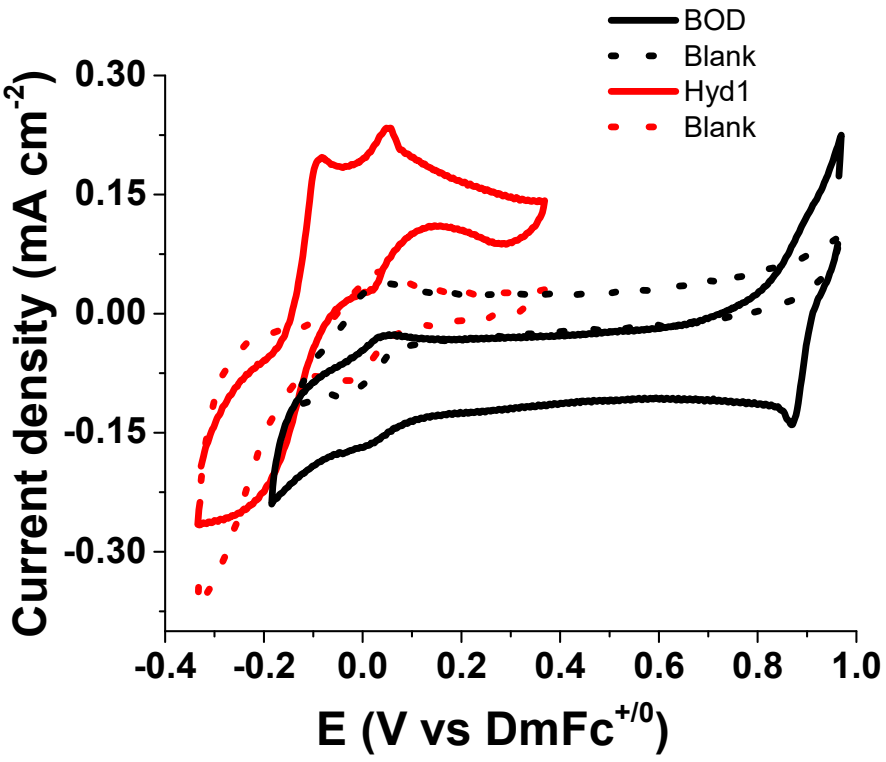



Figure 7.3 Cyclic voltammograms (current density, first scans) of Hyd1 (black solid line) and BOD (red solid line) modified MWNT/PGE electrodes and blank MWNT/PGE electrodes (dotted lines) in $H_2$-$O_2$ fuel cell conditions. Scan rate 10 mV/s, electrode rotation rate 0 RPM, the projected electrode surface area 0.03 $cm^2$.

The lifetime of enzymes through continuous cyclic voltammetry depends on the experimental conditions: the scan rate, temperature, and buffer capacity of the aqueous enzyme film. The electrocatalytic activities of both Hyd-1 and BOD diminished upon continuous cyclic voltammetry scans of ~ 2 h in the experimental conditions described above. However, even when the activities had become negligible, catalytic activity was still observed when the electrode was transferred to aqueous buffer saturated with either $H_2$ or $O_2$, respectively (Chapter 5 and 6). EMIMTFSI was stable after prolonged exposure to $H_2$ oxidation and $O_2$ reduction for at least 4 weeks.

### 7.4.2 Synaptic Fuel Cell Performance

The OCV of a fuel cell is the voltage between anode and cathode when no current flows. OCVs of enzymatic hydrogen fuel cells are influenced by factors such as enzyme film, electrode material, temperature, and gas compositions. For fuel cells operating with the same enzymes in buffers with 96 % $H_2$–4 % $O_2$ at 25 ˚C, the OCVs were reported to be about 1 V [30, 79]. The OCVs of both buffer-SFC and EMIMTFSI-SFC were 0.9 ± 0.1 V (based on three independent measurements), consistent with previous results.The experimental OCV the SFCs was close to the theoretical value of 1.1 V calculated from the difference between onset potentials of anode and cathode electrocatalytic reactions in EMIMTFSI with saturated with 96 % $H_2$–4 % $O_2$ at 30˚C (Figure 7.3).

Power curves illustrate the dependence of fuel cell power density on its voltage. We detected power curves of SFCs by linear scan voltammetry at 1 mV/s from its OCV to 0 V with 96 % $H_2$–4 % $O_2$ (Figure 7.4 and 7.5). Both the power curves of buffer-SFC and EMIMTFSI-SFC were bell-shaped.For buffer-SFC operating with humidified gases

(Figure 7.4), the maximum power density reached 175 μW $cm^{-2}$at 0.44 V. After 9 h's operation at 0.9 V with 96 % $H_2$–4 % $O_2$, the overall SFC's power density decreased. The maximum power density decreased by 13 % to 152 μW $cm^{-2}$ at 0.41 V. For EMIMTFSI-SFC with separate aqueous film electrodes linked only by ionic liquid under 96 % $H_2$–4 % $O_2$ (Figure 7.5), the maximum power density was initially 7.3 μW $cm^{-2}$at 0.62 V, lower than that of buffer-SFC. After 9 h's operation at 0.75 V with 96 % $H_2$–4 % $O_2$, the EMIMTFSI-SFC's power density maintained. The maximum power density was 7.2 μW $cm^{-2}$ (at 0.72 V). Based on three independent measurements, the maximum initial power densities of Buffer-SCF and EMIMTFSI-SFC are 175 ± 5 and 7.3± 0.3 μW $cm^{-2}$ (per total electrode area), respectively.

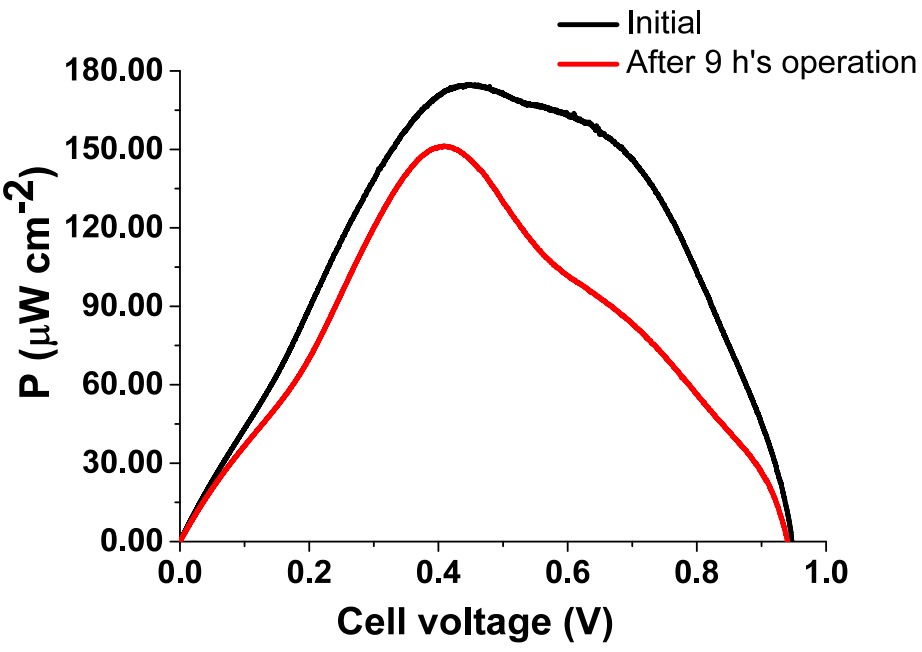



Figure 7.4 Dependence of power density (P, per total electrode area) on fuel cell voltage for the buffer-SFC before (black) and after (red) 9 h's operation at 0.75 V with a humidified gas mixture of 96 % $H_2$–4 % $O_2$. Temperature: 24 ˚C.

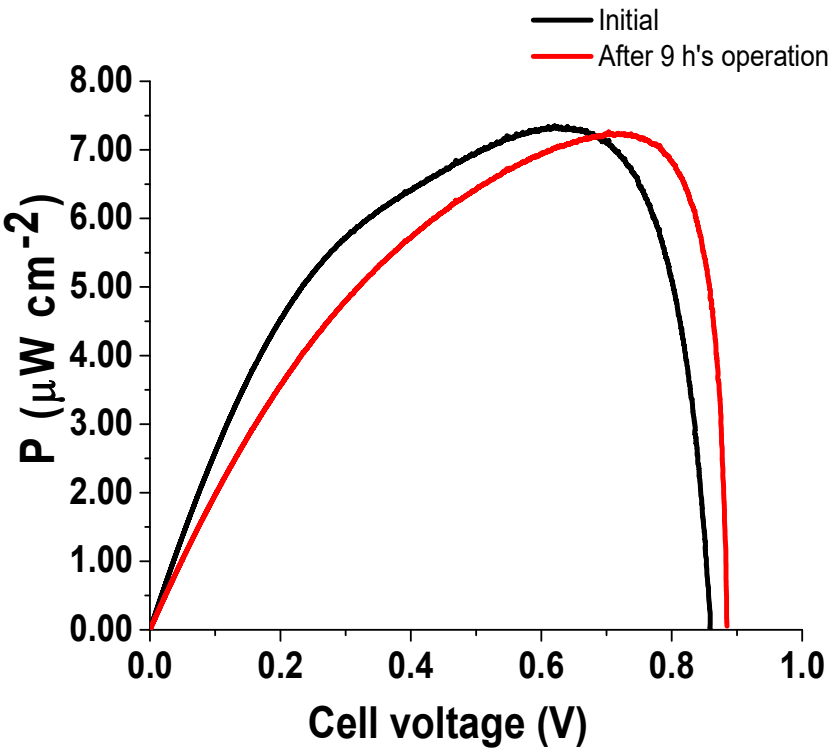



Figure 7.5 Dependence of power density (P,per total electrode area) on fuel cell voltage for the buffer-SFC before (black) and after (red) 9 h's operation at 0.75 V with a gas mixture of 96 % $H_2$–4 % $O_2$. Temperature: 25 ˚C.The fuel cell is with separate aqueous film electrodes linked only by ionic liquid under 96 % $H_2$–4 % $O_2$.

Figure 7.6 A shows synaptic fuel cells constructed in which an anode modified with Hyd-1 and a cathode modified with BOD were brought close together and electrically connected by either aqueous phase or ionic liquid. Because the fuel cells run under small flow rates of gases (96 standard cubic centimeters $min^{-1}$ of $H_2$ and 4 standard cubic centimeters $min^{-1}$ of $O_2$) in this study, the gas flow does not affect the shape/formation of this liquid connection between two electrodes.

Figure 7.6B shows the polarisation and power curves of the fuel cell with two electrodes linked by the aqueous synapse as well as the RTIL coating. This fuel cell

provided an OCV of 0.85 V, with a maximum power density (4.5 μW $cm^{-2}$) close to 0.7 V. Figure 7.6 C shows the polarisation and power curves of the fuel cell with separate aqueous film electrodes linked only by ionic liquid under 96 % $H_2$–4 % $O_2$. This fuel cell provided an OCV of 0.86 V, with a maximum power density (7.3 μW $cm^{-2}$) close to 0.6 V. In both cases the fuel cell OCV and maximum power density were essentially unchanged (the maximum power voltage actually increased slightly) after 9 h operation, in contrast to the cyclic voltammetry experiments. The longer lifetime of the fuel cells can be caused by the increasing amount of water produced by the $H_2$-$O_2$ fuel cell operation, which effectively retards the pH change at either electrode and improves the proton transfer of the fuel cell. As the $H_2$-$O_2$ fuel cells operated, the amount of water in the fuel cells increased, which can slightly increase the OCV of the fuel cell after 9 h's operation. Unlike other larger fuel cells reported previously [27, 30], the individual electrode potential of the synaptic fuel cell is immeasurable experimentally, because the tiny amount of electrolyte of the fuel cell (~ 6 L) cannot hold conventional reference and counter electrodes. The robust similarity regardless of whether the two aqueous zones are merged into one across the synapse suggests that water molecules in the aqueous enzyme shells can easily move into the EMIMTFSI to serve as the proton carrier, although H(2) at $EMIM^+$ cation is weakly acidic [128, 129] and EMIMTFSI may be directly active in proton transport [238].

Because the power density of EMIMTFSI-SFC with two electrodes linked by IL (7.3± 0.3 μW $cm^{-2}$, based on three parallel experiments) is higher than that of the EMIMTFSI-SFC with electrodes linked by aqueous buffer (4.5 ± 0.2 μW $cm^{-2}$, based on three parallel experiments), I used the data obtained with the EMIMTFSI-SFC with two electrodes linked by IL in the following discussion.

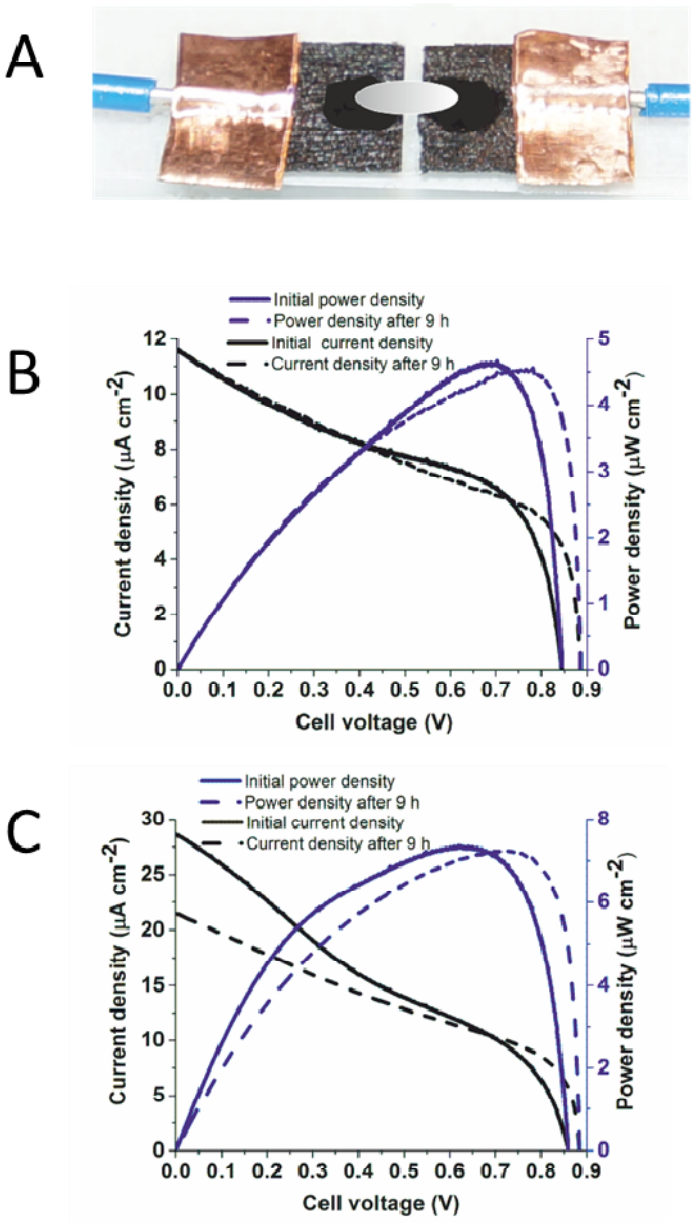



Figure 7.6 (A) The synaptic fuel cell assembly. Black areas correspond to aqueous zones where enzymes have been spotted on the electrodes and the pale grey area indicates the protective coverage of EMIMTFSI over the two electrodes. (B and C) Performances of the fuel cells, 26 ± 2 ˚C, box atmosphere 96 % $H_2$–4 % $O_2$. Solid lines show initial polarisation curve (black) and power curve (blue). Dashed lines show polarisation curve (black) and power curve (blue) of the fuel cells after 9 h's operation under at 0.75 V. Panel B shows results for two electrodes linked by synaptic aqueous

phase and RTIL coating. Panel C shows results for two electrodes linked by ionic liquid alone.

To assess the gas transport in SFCs, I monitored the OCV while changing gas compositions between 96 % $H_2$–4 % $O_2$ and 100 % $H_2$. I did not experiment with 100 % $O_2$ because Hyd1 will be irreversibly inactivated in this way. The OCV of buffer-SFC dropped fast from its maximum of 0.87 (± 0.03) V to 0.10 V when $O_2$ was eliminated and climbed back to the maximum as soon as $O_2$ restored (Figure 7.7). In contrast, when SFCs started with EMIMTFSI that had not been saturated with 96 % $H_2$–4 % $O_2$, the OCVs of the SFCs remained below 0.15 V after flowing 96 % $H_2$–4 % $O_2$ for 30 min. So EMIMTFSI had to be saturated with 96 % $H_2$–4 % $O_2$ before application to the SFC. In this way, when the OCV of EMIMTFSI-SFC reached its maximum of 0.96 V, it stayed above 0.6 V even after 30 min's flowing of 100 % $H_2$ into the sandwich box (Figure 7.8). This observation indicates that $O_2$ was still trapped in the 6 μL of EMIMTFSI in SFC even though 100 % $H_2$ had flown above EMIMTFSI for 30 min. The gas exchange was slower at EMIMTFSI than aqueous buffer.

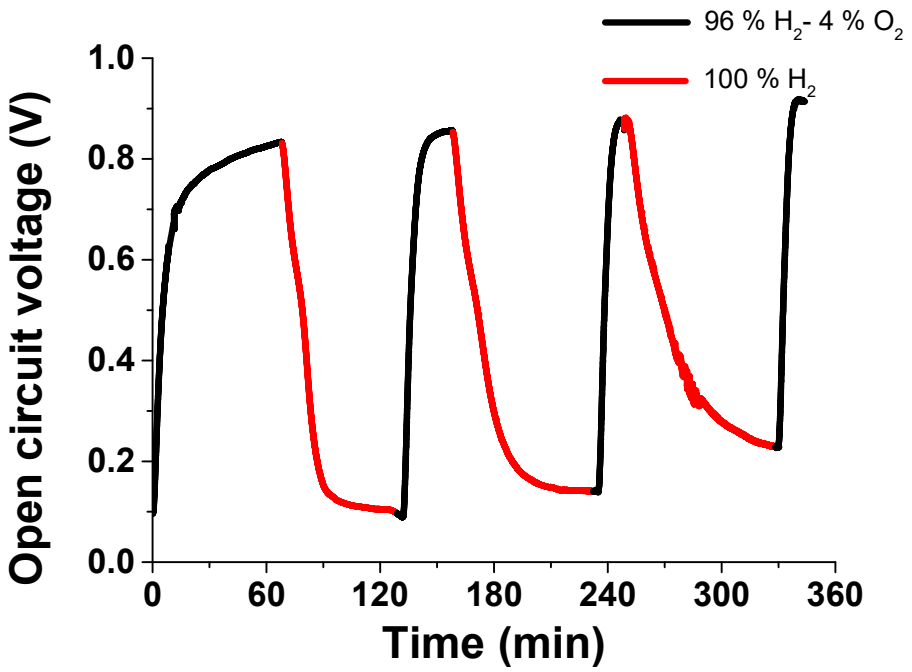



Figure 7.7 Open circuit voltage of the tiny enzymatic fuel cell using phosphate buffer (100 mM, pH 5) as electrolyte under 96 % $H_2$–4 % $O_2$ (black line) and100 % $H_2$ (red line).Temperature: 26˚C. Gas mixtures were humidified.

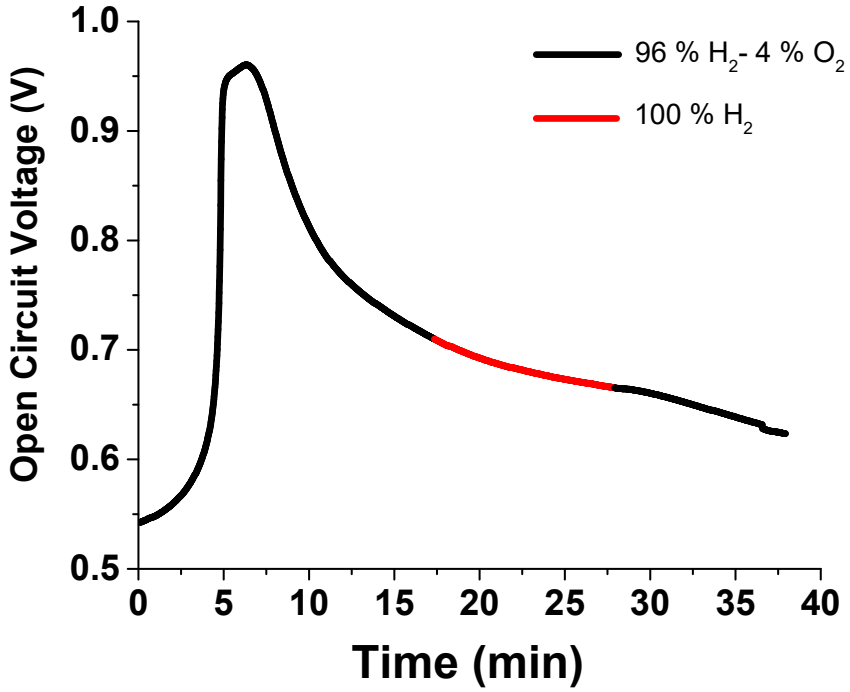



Figure 7.8 Open circuit voltage of the tiny enzymatic $H_2$-$O_2$ fuel cell using EMIMTFSI as electrolyte under 96 % $H_2$–4 % $O_2$ (black line) and100 % $H_2$ (red line). Temperature: 28 ˚C.

The previous result shows that once $O_2$ dissolved in EMIMTFSI, $O_2$ cannot be removed by flowing $H_2$ only. Can $O_2$ permeate into EMIMTFSI successfully when I run 96% $H_2$ and 4 % $O_2$above EMIMTFSI? The answer is yes. Because I found that when the EMIMTFSI-SFC began with 6μL of EMIMTFSI that has not been treated with any gases, the OCV increased from zero to 0.15 V with 96% $H_2$–4 % $O_2$ flowing in the sandwich box. Although the OCV cannot increase further as I flew 96% $H_2$–4 % $O_2$ for more than 30 min, the increase of OCV from 0 to 0.15 V proves that $H_2$ and $O_2$ were permeating into EIMITFSI in SFC when flowing above it, but the concentration of gases in EMIMTFSI obtained by flowing gases above the liquid surface was lower than

obtained by passing gases through the liquid. To validate my answer further, I carried out another experiment in three steps (Figure 7.9). First, both the SFCs started with electrolytes saturated with 96% $H_2$–4 % $O_2$. Chronopotentiometry at zero current was applied to both SFCs. OCVs of buffer-SFC (Figure 7.9A) and EMIMTFSI-SFC (Figure 7.9B) reached 1.00 V in the first step.

Second, chronoamperometry at 0.10 V was applied to the SFCs. Meanwhile, $O_2$ flow was paused, leaving the SFCs to run with 100 % $H_2$ until the current dropped to zero to eat up all the $O_2$ already dissolved in the electrolyte of SFCs. The time $t$ (min) dependence of current density $i$ (mA $cm^{-2}$, per cathode area 0.00785 $cm^2$) can be fitted into eq 7.1 for buffer-SFC (Figure 7.9C) and eq 7.2 for EMIMTFSI-SFC (Figure 7.9D).

$$i = \begin{cases} 0 & (0 \leqslant t < 14.4) \\ -4.03 \times 10^{-9} t + 1.02 \times 10^{-6} & (14.4 \leqslant t < 18.8) \\ -5.48 \times 10^{-9} + 8.62 \times 10^{-4} \times 0.70^{t} & (18.8 \leqslant t < 26.3) \\ 0 & (26.3 \leqslant t \leq 57.8) \end{cases} \quad (7.1)$$

$$i = \begin{cases} 0 & (0 \leqslant t < 18.52) \\ 1.41 \times 10^{-8}(1 - e^{-0.0694t})^{-4.56} & (18.52 \leqslant t < 34.28) \\ 0 & (34.28 \leqslant t < 178.0) \end{cases} \quad (7.2)$$

For buffer-SFC, some $O_2$ dissolved in the water in the humidifier. So $O_2$ that remained in the humidifier still went into the buffer-SFCshortly after I switched off $O_2$. Therefore in C the current density was almost constant, with a tiny slope of $-4.03 \times 10^{-9}$ (mA $cm^{-2}min^{-2}$) for the first 4.4 min ($14.4 \leq t < 18.8$) of the second step ($14.4 \leqslant t < 26.3$).

On the other hand, the current density of EMIMTFSI-SFC dropped exponentially from the start of the second step because no humidifier was connected in the gas line.

Third, I resupplied 96 % $H_2$–4 % $O_2$ to the SFCs while a chronopotentiometry at zero current was applied. The OCV of buffer-SFC recovered from 0.10 to 0.90 V in 10 min. On the other hand, the OCV of EMIMTFSI-SFC climbed up slower, from 0.05 to 0.34 V in 130 min. This difference tells that $O_2$ permeated into EMIMTFSI slower than into aqueous buffers when $O_2$ is flowing above the liquid surface. When compare the final and initial OCVs, I found that the OCV of buffer-SFC decreased from 1.00 to 0.90 V while the OCV of EMIMTFSI-SFC decreased from 1.00 to 0.34 V. Based on the assumption that both enzymes were of the same activity throughout the experiment, the small drop of OCV of buffer-SFC by 0.1 V suggests that by flowing humidified $O_2$above the 6 μL of aqueous buffer surface in SFC, the concentration of $O_2$ can arrive at the similar value when $O_2$ was passed through the aqueous buffer. However, the loss of OCV of EMIMTFSI-SFC by 0.66 V indicates that the concentration of $O_2$ in EMIMTFSI obtained by flowing $O_2$ above the liquid surface was lower than by passing $O_2$ through the liquid.

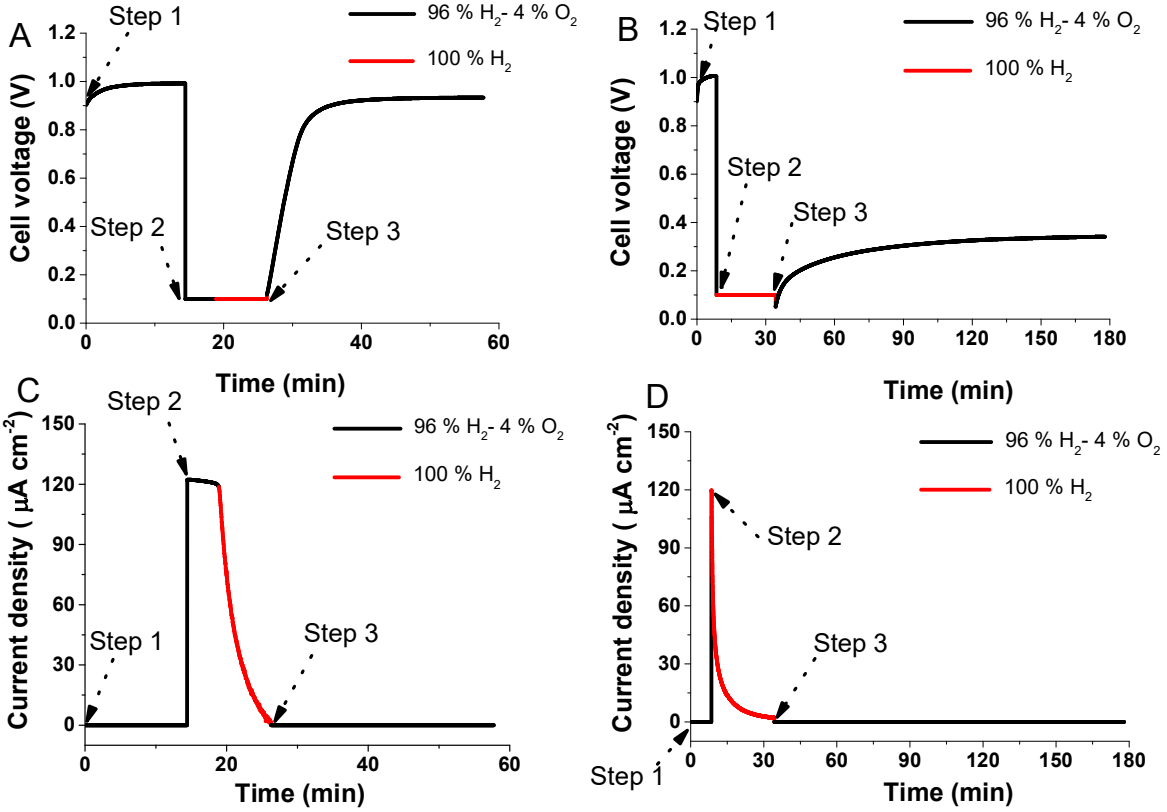



Figure 7.9 Time dependence of cell voltage of buffer-SFC (Panel A), EMIMTFSI-SFC (Panel B) and that of current density (cathode area 0.00785 $cm^2$) of buffer-SFC (Panel C), EMIMTFSI-SFC (Panel D) over the course of 3 steps: 1, operated the SFC at zero current with 96 % $H_2$–4 % $O_2$; 2, switched off $O_2$ to flow 100 % $H_2$, meanwhile, applied a chronoamperometry at 0.1 V to the SFC until the current drop to zero to consume all $O_2$ dissolved in the electrolyte; 3, put $O_2$ back and operated the buffer-SFC at zero current with 96 % $H_2$–4 % $O_2$. Black line represents that the SFC was operating again with 96 % $H_2$–4 % $O_2$. Red line represents that the SFC was operating with 100 % $H_2$, i.e. anaerobically. Gas mixtures for buffer-SFC were humidified. Gas mixtures for EMIMTFSI-SFC were dry.

## 7.5 Discussion

My findings suggest that an almost dry enzymatic fuel cell with ionic liquid as electrolyte can work successfully when both enzyme films were wet. I have shown that wet films of both Hyd1 and BOD adsorbed onto MWNT/PGE electrodes were electrocatalytically active when confined by EMIMTFSI. The EMIMTFSI-SFC can achieve an OCV as high as 0.9 ± 0.1 V and a maximum power density of 7.3 ± 0.3 μW $cm^{-2}$(per total electrode area, based on three parallel experiments) under 96 % $H_2$–4 % $O_2$, 26 ± 2 ˚C.

Enzyme film voltammetry of Hyd1 and BOD in aqueous microenvironment confined by EMIMTFSI in the previous chapters leads to the conclusion that electrocatalysis can take place in a small pocket of aqueous enzyme solution surrounded by EMIMTFSI that is water-immiscible. Water-immiscibility is vital for enzyme solutions adsorbed onto electrodes to keep electrocatalytically active in the ionic liquids.Enzyme film voltammetry of Hyd1 and BOD in water-miscible ionic liquids including ethylammonium nitrate (EAN), diethylmethylammonium trifluoromethanesulfonate (DEMATFO), and tris(2-hydroxyethyl)methylammonium methylsulfate (TEMAMS) showed no catalytic activity of enzymes. One reason is that water-miscible ionic liquids can penetrate into enzyme films and deactivate them; on the contrary, water-immiscible ionic liquids can cover and protect aqueous enzymes without penetrating or deactivating them. In a synaptic enzymatic fuel cell, the water-immiscible ionic liquid is shielding and transporting substrate gases to the wet aqueous enzyme films on electrodes.

In addition, I found that after continuous scans on the same electrode with enzyme coating, the onset potential $H_2$ oxidation electrocatalysed by Hyd1 shifted positively while the onset potential $O_2$ reduction electrocatalysed by BOD shifted negatively

(Chapter 5 and 6). This can be attributed to change of the pH values in the small pocket of aqueous enzyme solution enclosed by EMIMTFSI when reactions continued. Reaction of $H_2$ oxidation produced protons, thus the pH value in the small pocket along with the onset potential increased as continuous scans proceeded. Reaction of $O_2$ reduction consumed protons, so the pH value in the small pocket together with the onset potential decreased as continuous scans proceeded. For both$O_2$ reduction and $H_2$ oxidation reactions, electrocatalytic currents decreased, indicating the enzyme activity was gradually decreasing as the pH values of the microenvironment became harsher. These observations support our "small pocket theory", i.e. the electrocatalysis took place in the small pocket of aqueous enzyme solution surrounded by EMIMTFSI.

Power curves of buffer-SFC and EMIMTFSI-SFC were similar in shapes under 96 % $H_2$–4 % $O_2$. This gas composition was chosen because it leads to the optimal performance of the fuel cell, according to previous studies using Hyd1 and BOD as electrocatalysts in enzymatic fuel cells [5, 13, 27, 30, 79]. The power density and stability of buffer-SFC operating on humidified gases were superior to those of EMIMTFSI-SFC. One reason is that EMIMTFSI transports gases slower than aqueous buffer does, which limits the SFC's performance. Such difference in gas exchange rates originatefrom their difference in viscosity: at 30 ˚C, 1 bar, the dynamic viscosity of EMIMTFSI (38.6 mPa s [239]) is 32 times higher than that of water (0.7972 mPa s [240]). According to Walden's rule, gas diffusion coefficient $D$ is inversely proportional to dynamic viscosity of the ionic liquid (eq 7.3):

$$D\eta = \text{const.} \tag{7.3}$$

Another reason for inferior power density of EMIMTFSI-SFC is that enzymes are less active in tiny aqueous phases confined by EMIMTFSI than in aqueous buffer, which is supported by the smaller and continuously decreasing catalytic current density

of enzymes confined in EMIMTFSI than in aqueous buffer. The maximum current density of Hyd1 adsorbed at MWNT/PGE electrode in buffer was10.92±0.43 mA $cm^{-2}$(at 1000 RPM, Chapter 4), which is one order of magnitude larger than that in EMIMTFSI (0.81±0.05 mA $cm^{-2}$, with $H_2$ bubbling, Chapter 5) at 30 °C, pH 6.0. The maximum current density of BOD modified MWNT/PGE electrode in buffer was 6.15±0.31 mA $cm^{-2}$(at 1000 RPM, Chapter 4), which was larger than that in EMIMTFSI (0.88 mA $cm^{-2}$, with $O_2$ bubbling Chapter 6) at 30 °C, pH 6.2.

I found that once $O_2$ dissolved in EMIMTFSI, it remained trapped in the 6 μL of EMIMTFSI even after EMIMTFSI was exposed to 100 % $H_2$ for 30 min (Figure 7.9 B). To deplete gases dissolved in ionic liquid, a conventional way was to apply vacuum [241]. Vacuum is necessary to remove gases dissolved in ionic liquids according to some models speculating that the structures of ionic liquids may change after gases dissolved in them, one gas cannot escape from the ionic liquid when another gas is running above the liquid surface [219].

My data confirm that $O_2$ permeated into EMIMTFSI slower than aqueous buffer (Figure 7.9). I integrated the red curve in Figure 7.9C and D. The area I obtained is equal to the amount of charge burned by electric load in buffer-SFC and EMIMTFSI-SFC when operating at 0.1V anaerobically: $1.32 \times 10^{-4}$and $1.51\times 10^{-4}$C respectively. For buffer-SFC, some $O_2$ dissolved in the water in the humidifier. So $O_2$ that remained in the humidifier still went into the buffer-SFCshortly after I switched off $O_2$. Therefore in Figure 7.9C, the current first almost stayed constant (with a negligible slope of $-4.03 \times 10^{-9}$ (mA $cm^{-2}min^{-1}$) for the first 5 min in the second step with the presence of $O_2$ from the humidifier. I count only the latter part of the curve decreasing exponentially as anaerobic. The amount of charge calculated from the integration should be equal to the amount of charge carried by $O_2$ dissolved in the electrolyte

before currents flew. I used the eq 7.4 to calculate the theoretical amount of charge carried by $O_2$ dissolved in electrolyte.

$$n(e^-) = 4 \times 4\% \times F \times c \times V \quad (7.4)$$

Here F is Faraday constant: 96486 C $mol^{-1}$. c is the solubility of $O_2$ in water: 1.27mM [242] or EMIMTFSI 3.9 mM [241] at one bar, 25˚C. V is the volume of buffer or EMIMTFSI: 6 μL, in the SFCs. As a result, the values of charge contained in the electrolyte of SFCs were $1.17 \times 10^{-4}$ and $3.61 \times 10^{-4}$ C for buffer-SFC and EMIMTFSI-SFC respectively. For buffer-SFC, the amount of charge by integration of red curve in Figure 7.9 C was $1.32\times 10^{-4}$ C, agreeing well with the value of $1.17 \times 10^{-4}$ C resulting from eq. 7.4. For EMIMTFSI-SFC, the amount of charge by integration of red curve in Figure 7.9 C was $1.51\times 10^{-4}$ C, 58 % lower than the value of $3.61 \times 10^{-4}$ C calculated from eq. 7.4. Such discrepancy may be caused by two factors: first, the validity of solubility of $O_2$ in EMIMTFSI has not been fully confirmed yet; second, $H_2$ coexisting can change the $O_2$ solubility in EMIMTFSI.

My study shows the power density of the synaptic buffer-SFC was 0.175 ± 0.005 mW $cm^{-2}$(per total electrode area), higher than the reported value of 0.1 mW $cm^{-2}$of an enzymatic hydrogen fuel cell operated in phosphate buffer with 80 % $H_2$-20 % air at 25˚C[30]. The successful improvement of power density of buffer-SFC demonstrates that the synaptic design is feasible for miniaturized enzymatic fuel cells. But the power density of EMIMTFSI-SFC (7.3± 0.3 μW $cm^{-2}$,per total electrode area) was lower than the literature value, owing to the inferior mass transport property of EMIMTFSI that is highly viscous. The synaptic enzymatic $H_2$-$O_2$ fuel cell using EMIMTFSI reported here uses much smaller volume of electrolyte (~ 6 μL) than previous enzymatic $H_2$-$O_2$ fuel cells did (> 1 mL) [30, 79, 243]. The OCV of the fuel cell using EMIMTFSI is over 0.8

V, which is comparable to literature values (Table 7.1) and close to the thermodynamic reversible value of 1.23 V at 25 ˚C.

Table 7.1 Comparison of open circuit voltage (OCV) and power density of the Hydrogenase-BOD fuel cell in this chapter with few other representative reported studies

| Electrode | Electrolyte | Fuel/ Oxidant | OCV (V) | Max power density ($\mu W\ cm^{-2}$) | Ref. |
|---|---|---|---|---|---|
| PGE adsorbing Hyd1, BOD | 0.1 M pH 5.0 phosphate buffer, 25 °C, quiescent | 96% $H_2$/ 4% $O_2$ | 0.95 | 12.9 | [79] |
| PGE/MWNT/Pyrenyl covalent linked to Hyd1, BOD | 0.1 M pH 5.0 phosphate buffer, 25 °C, quiescent | 80% $H_2$/ 20% Air | 1.0 | 100 | [30] |
| Carbon cloth /MWNT/BOD, GCE[a] drop-coated with *Dv*MF[b] [NiFe] hydrogenase/viologen based redox polymer | 100 mM phosphate buffer (pH 7), 40 °C, stirring | 95% $H_2$/ 5% $O_2$ | 0.947 ± 0.003 | 178 ± 19 | [244] |
| MWNT pellet adsorbing Hyd2[c], BOD | 0.1 M sodium phosphate buffer, pH 6.0. | 89%$H_2$/ 11% air | 1.114 | 90 | [245] |
| PGE/MWNT/Hyd1, BOD | 100 mM phosphate buffer (pH 5), 26±2 °C, quiescent | 96% $H_2$/ 4% $O_2$ | 0.9 ± 0.1 | 175 ± 5 | This study |
| PGE/MWNT/Hyd1, BOD | EMIMTFSI, 26±2 °C, quiescent | 96% $H_2$/ 4% $O_2$ | 0.9 ± 0.1 | 7.3± 0.3 | This study |

[a]glassy carbon electrode. [b]*Desulfovibrio vulgaris* Miyazaki F.[c]Hydrogenase-2 from *E. coli*

## 7.6 Conclusions

In summary, I have demonstrated the scope for enzymatic fuel cells that can be miniaturized by coating with an ionic liquid to trap the enzymes within aqueous microenvironments. Both fuel cell enzymes: Hyd-1 and BOD are highly active in an almost dry condition contained within a shell of water-immiscible EMIMTFSI. The results help highlight the possibilities for enzymes operating under limited aqueous conditions with the aid of ionic liquids as conductive media.

# 8 Reduction of $CO_2$ Electrocatalysed by Carbon Monoxide Dehydrogenase Confined in an Ionic Liquid

## 8.1 Abstract

Carbon monoxide dehydrogenases from *Carboxydothermus hydrogenoformans* I CODH $I_{Ch}$ is electrocatalytically active in tiny aqueous shell confined by a hydrophobic ionic liquid saturated with $CO_2$. $CO_2$ is exceptionally soluble in ionic liquids, which are practical for $CO_2$ uptake, capture and storage. $CO_2$ reduction and CO oxidation electrocatalysed by CODH $I_{Ch}$ occurred at the same time in the tiny aqueous shell, according to cyclic voltammetry. Finally, a steady state is achieved. This work allows us to understand the reversible $CO_2$/CO electrochemistry in a tiny aqueous environment confined by hydrophobic ionic liquids.

## 8.2 Introduction

Global warming is a result of increasing level of $CO_2$ produced by consumption of fossil fuels. To curb the $CO_2$ increase, room temperature ionic liquids (RTILs) are being investigated urgently for $CO_2$uptake, capture and storage, because of the desirable properties of RTILs: exceptionally high $CO_2$ solubility, negligible vapour pressures, thermal stability, a large liquid range [246]. Particularly, imidazolium based RTILs have unusually high solubility of carbon dioxide in those media, which likely arises from complexation between the solute gas and the constituent ion(s) of the RTILs as reported for 3-methylimidazolium acetate: $CO_2$+ A ↔$CO_2$·A where A is a component of the ionic liquid. The solubility of carbon dioxide in these RTILs can be around the Molar level with the number of solute molecules approaching that of the RTIL solvent itself [247].

Carbon monoxide dehydrogenases (CODHs) catalyse the rapid and direct redox interconversion of CO and $CO_2$ (8.1).

$$CO + H_2O \longleftrightarrow CO_2 + 2H^+ + 2e^- \quad (8.1)$$

Ni-containing CODH found in anaerobic organisms are referred to as Ni-CODHs. Five Ni-CODHs are expressed by the thermophilic bacterium *Carboxydothermus hydrogenoformans* (Ch), which can grow chemolithoautotrophically on CO as sole carbon and energy source. Two of these enzymes, CODH $I_{Ch}$ and CODH $II_{Ch}$ only catalyse the CO/$CO_2$ interconversion and have similar spectroscopic properties [8]. Both enzymes show turnover frequencies as high as 30 000 $s^{-1}$ at pH 8, 70 °C, according to conventional kinetic assays [99]. Because CODH $I_{Ch}$ shows lower CO product inhibition than CODH $II_{Ch}$ in $CO_2$ reduction, CODH $I_{Ch}$ is a more interesting candidate in reducing $CO_2$ to CO as fuel.

Here, for the first time, I report the application of a RTIL to allow CODH $I_{Ch}$ to operate in an almost dry state. I demonstrate that CODH $I_{Ch}$ is highly active when trapped in an aqueous microenvironment enclosed by a viscous, water-immiscible RTIL: 1-ethyl-3-methylimidazolium bis(trifluoromethylsulfonyl)imide (EMIMTFSI). The concept is illustrated in Figure 8.1. The solubility of $CO_2$ in EMIMTFSI is about 0.03 (mole fraction) under ambient conditions (Table 8.1), highest among commercially available hydrophobic RTILs [219]. So I used EMIMTFSI in this study.

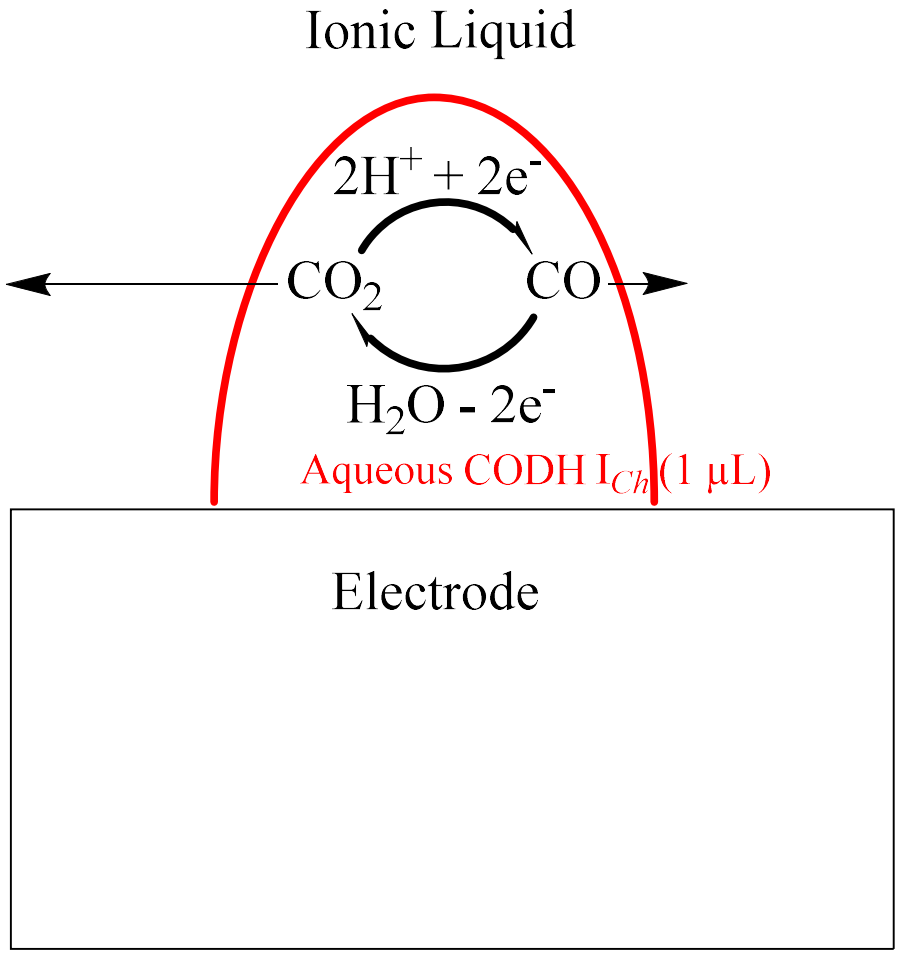



Figure 8.1 Scheme showing an electrode modified with CODH $I_{Ch}$ film (hydrated with approx. 1 µL of buffer) and immersed in water-immiscible ionic liquid.

Table 8.1 Solubility (mole fraction) of CO and $CO_2$ in water and EMIMTFSI at 1 bar.

| | Solubility of CO at 1 bar | Solubility of $CO_2$ at 1 bar |
|---|---|---|
| EMIMTFSI | $6.02 \times 10^{-4}$ at 298 K [248] | 0.0315 at 295 K [217] |
| $H_2O$ | $1.66 \times 10^{-5}$ at 303 K,<br>$1.77 \times 10^{-5}$ at 303 K[218] | $5.41 \times 10^{-4}$ at 303 K,<br>$6.15 \times 10^{-4}$ at 298 K[218] |

## 8.3 Experimental

$CO_2$ was of technical grade and were supplied by compressed gas cylinders from British Oxygen Company. The flow of $CO_2$ was controlled precisely by mass-flow controllers (Sierra Instruments). All other chemicals and solvents were of analytical grade.

Isolation and purification of CODH $I_{Ch}$ from *Carboxydothermus hydrogenoformans* were carried out as previously described [249]. The enzyme was stored in the buffer containing Tris/HCl, 50 mM, pH 7.5 at 30 ˚C**,** 1 mM Dithiothreitol and 1 mM sodium dithionite. The protein concentration was 5.25 mg/ml.

Protein film electrochemistry was recorded with Autolab PGSTAT 20 workstations controlled by NOVA software (version 1.10). All experiments were carried out anaerobically in a glove box filled with $N_2$ ($O_2$< 4 ppm). The PGE electrode was then modified by 5 µL of MWNT dispersion (2.5 mg $mL^{-1}$ in DMF). The coating was left to dry for 1 hour before depositing a 1 µL aliquot of the stock CODH $I_{Ch}$ solution, applied so that only approximately 25% of the MWNT film was covered, the remaining area being dry. 1 µL of the enzyme solution was pipetted onto the MWNT/PGE electrode in an anaerobic glove box filled with $N_2$. The enzyme film was left to stabilize on the electrode for 1 min, before transferring to the electrochemical cell containing 2 mM DmFc in EMIMTFSI.

For other experimental details, please refer to Experimental Procedures of Protein Film Electrochemistry in Ionic Liquids in Chapter 3.

## 8.4 Results and Discussion

Figure 8.2shows the first four successive cyclic voltammograms obtained for $CO_2$ reduction by CODH $I_{Ch}$ adsorbed on a MWNT/PGE electrode and entrapped within 1 µL of the buffer containing 50 mM Tris/HCl, 1 mM Dithiothreitol and 1 mM sodium dithionite, initially pH 7.5 at 30 ˚C. The enzyme was applied to a small area of the electrode for 1 minute before placing carefully into the cell containing EMIMTFSI dissolved with 2 mM DmFc and previously saturated with 1 bar $CO_2$. Cyclic voltammograms were then recorded, as shown in Figure 8.2and translated onto the DmFc reference scale using the reversible redox signal due to DmFc in the EMIMTFSI phase. The voltammograms show a sharp peak due to enzymatic $CO_2$ reduction occurring in the aqueous phase. Upon successive cycles, the signal diminishes in size and the onset of $CO_2$ reduction shifts to more negative potential, consistent with the aqueous phase becoming more basic and the substrate inhibition by CO. Specifically, the onset potential for $CO_2$ reduction decreased from −320 mV ($2^{nd}$ scan) to −360 mV ($4^{th}$ scan). The small peak in the $4^{th}$ scan at +280 mV indicates the oxidation of CO in the aqueous phase produced by the first three scans. At this stage, the concentration of CO produced by $CO_2$ reduction in the aqueous phase is still low, because there is no CO present initially.

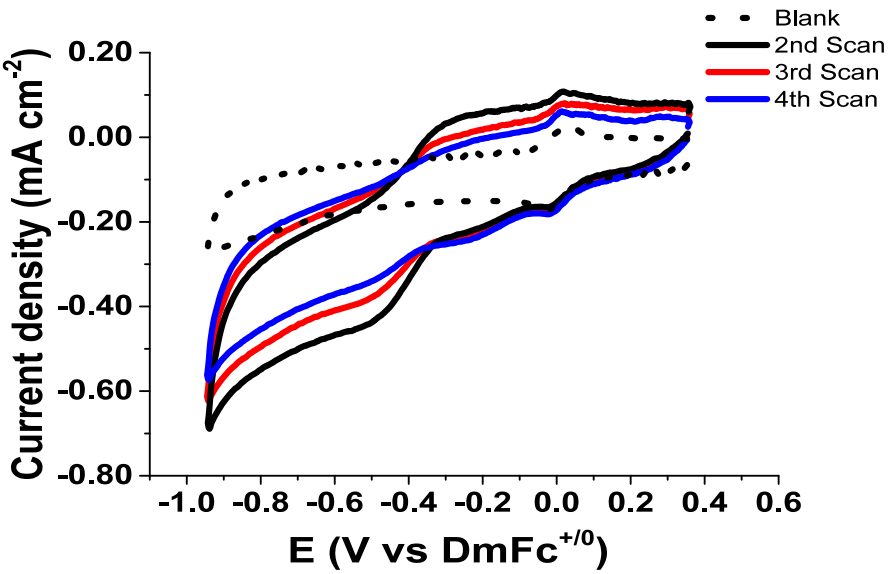



Figure 8.2 Continuous cyclic voltammetric scans (current density) of 1 µL of CODH $I_{Ch}$ (suspended in the buffer containing 50 mM Tris/HCl, initially pH 7.5 at 30 ˚C, 1 mM Dithiothreitol and 1 mM sodium dithionite) adsorbed at an MWNT/PGE electrode surrounded by EMIMTFSI (~1 mL) dissolved with 2 mM DmFc and saturated with 1 bar $CO_2$. Black, red and blue solid lines represent 2nd, 3rd and 4th scan respectively. Electrode rotation rate 0 RPM. Temperature 30 ˚C, scan rate 10 mV/s, projected electrode surface area 0.03 $cm^2$.

Figure 8.3 shows further cyclic voltammetric scans of the same CODH $I_{Ch}$ film adsorbed on the same MWNT/PGE electrode asFigure 8.2. The peaks of CO oxidation shift negatively, from +240 mV (6th scan) to −180 mV (12th scan), indicating an increase of thermodynamic driving force of CO oxidation, which is caused by increase of CO concentration in the aqueous phase. At the same time, $CO_2$ reduction also took place in the aqueous phase, showing a reduction wave starting around −100 mV. The

onset potential is more positive than those in the first four scans, indicating a decrease of pH of the aqueous shell from the initial state.

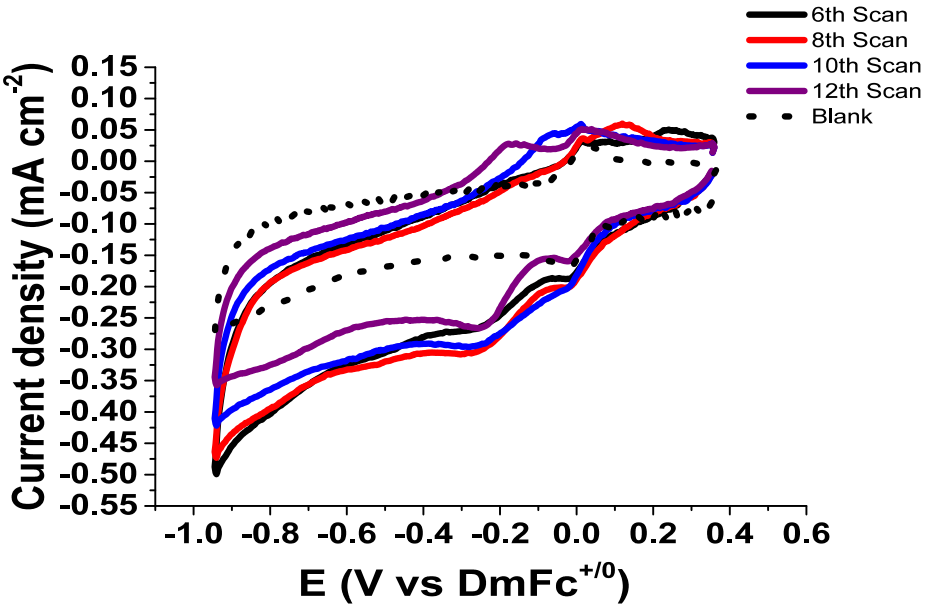



Figure 8.3 Cyclic voltammetric scans (current density) of 1 µL of CODH $I_{Ch}$ (suspended in the buffer containing 50 mM Tris/HCl, initially pH 7.5 at 30 ˚C, 1 mM Dithiothreitol and 1 mM sodium dithionite) adsorbed at an MWNT/PGE electrode surrounded by EMIMTFSI (~1 mL) dissolved with 2 mM DmFc and saturated with 1 bar $CO_2$. Black, red, blue and purple solid lines represent 6$^{th}$, 8$^{th}$, 10$^{th}$ and 12$^{th}$ scan respectively. Electrode rotation rate 0 RPM. Temperature 30 ˚C, scan rate 10 mV/s, projected electrode surface area 0.03 cm$^2$.

Figure 8.4 shows final cyclic voltammetric scans (the 16$^{th}$ – 20$^{th}$ scan) of the same CODH $I_{Ch}$ film adsorbed on the same MWNT/PGE electrode as Figure 8.2 and 8.3. The CO oxidation peak at −140 mV and $CO_2$ reduction wave starting at −130 mV are stable

at this stage, indicating that the reaction rate of CO oxidation and $CO_2$ reduction are equal in the aqueous phase, i.e. the system achieved a steady state. All CO produced during CVs are unlikely to be fully reoxidised in the oxidative scan, because in each of Fig.8.2 and 8.3, the oxidative current is always lower than the reductive current in the same scan.

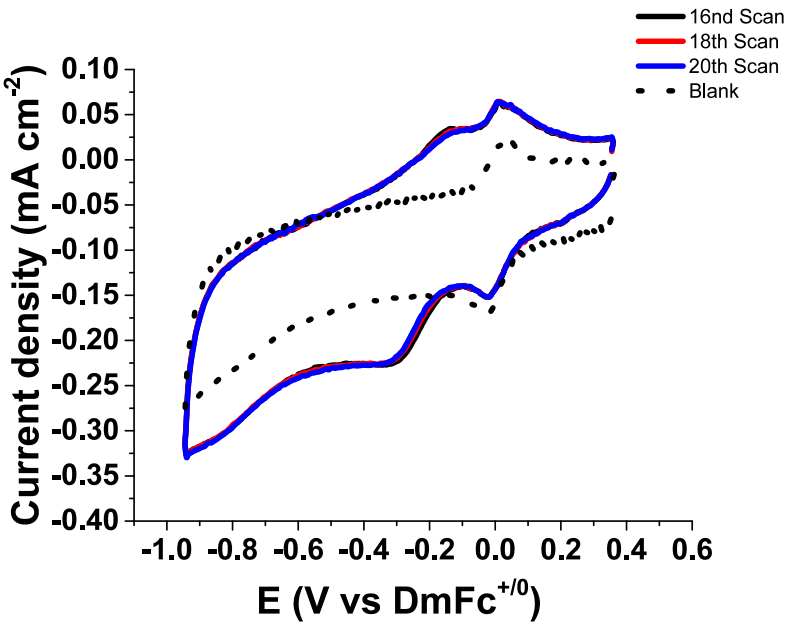



Figure 8.4 Cyclic voltammetric scans (current density) of 1 µL of CODH $I_{Ch}$ (suspended in the buffer containing 50 mM Tris/HCl, initially pH 7.5 at 30 ˚C, 1 mM Dithiothreitol and 1 mM sodium dithionite) adsorbed at an MWNT/PGE electrode surrounded by EMIMTFSI (~1 mL) dissolved with 2 mM DmFc and saturated with 1 bar $CO_2$. Black, red, blue and purple solid lines represent $16^{th}$, $18^{th}$ and $20^{th}$ scan respectively. Electrode rotation rate 0 RPM. Temperature 30 ˚C, scan rate 10 mV/s, projected electrode surface area 0.03 $cm^2$.

Figure 8.5A shows the chronoamperometry at −0.45 V vs $DmFc^{+/0}$ of CODH $I_{Ch}$ adsorbed on a MWNT/PGE electrode and entrapped within 1 μL of the buffer containing 50 mM Tris/HCI, initially pH 7.5 at 30 ˚C, 1 mM Dithiothreitol and 1 mM sodium dithionite. The enzyme was applied to a small area of the electrode for 1 minute before placing carefully into the cell containing EMIMTFSI previously saturated with 1 bar $CO_2$. The first 10 seconds of chronoamperometry is not taken into consideration, because of high double layer charging current. The reduction current first reached its maximum of −9.5 μA at 11 s, and then decreased monotonically to −2.2 μA, at which the reduction current levelled off. The final steady current value is close to background current (−2.9 μA) estimated by chronoamperometry of a blank MWNT/PGE electrode in the same experimental conditions (Figure 8.5B). Hence the final current value is close to zero after subtracted by the background current. This indicates that the net current produced by $CO_2$ reduction and CO oxidation is nearly zero at steady state. Integration of Figure 8.5A gives the net amount of charge produced by $CO_2$ reduction and CO oxidation catalysed by 1 μL of CODH $I_{Ch}$ confined by EMIMTFSI saturated with 1 bar $CO_2$, which is equal to 0.0097 C (average of three experiments, data shown in Table 8.2).

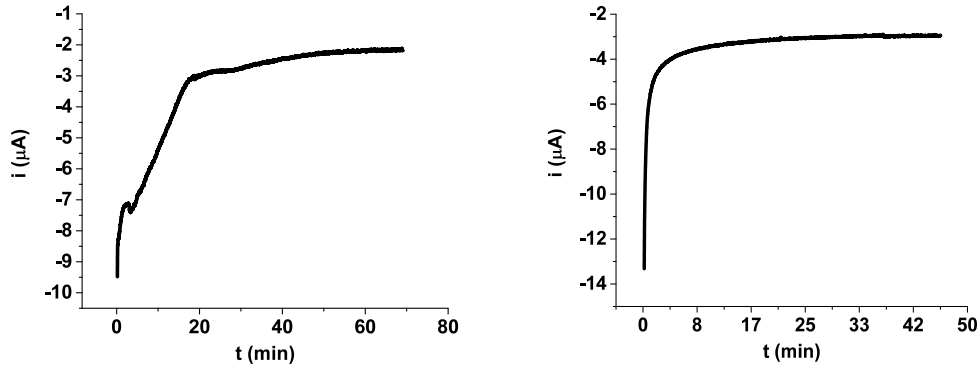



Figure 8.5 Chronoamperometry of (A) 1 μL of CODH $I_{Ch}$ (suspended in the buffer containing 50 mM Tris/HCl, initially pH 7.5 at 30 ˚C, 1 mM Dithiothreitol and 1 mM sodium dithionite) adsorbed at an MWNT/PGE electrode; (B) a blank MWNT/PGE electrode surrounded by EMIMTFSI (~1 mL) dissolved with 2 mM DmFc and saturated with 1 bar $CO_2$. Electrode rotation rate 0 RPM. Temperature 30 ˚C, potential=–0.45 V vs $DmFc^{+/0}$, projected electrode surface area 0.03 $cm^2$. First 10 s are removed.

Figure 8.6A shows the chronoamperometry at –0.65 V vs $DmFc^{+/0}$of CODH $I_{Ch}$ adsorbed on a MWNT/PGE electrode and entrapped within 1 μL of the buffer containing 50 mM Tris/HCI, initially pH 7.5 at 30 ˚C**,** 1 mM Dithiothreitol and 1 mM sodium dithionite. The enzyme was applied to a small area of the electrode for 1 minute before placing carefully into the cell containing EMIMTFSI previously saturated with 1 bar $CO_2$. The first ten seconds of chronoamperometry is not taken into consideration, because of high double layer charging current. The reduction current first reached its maximum of –23 μA at 11 s, and then decreased monotonically to –3.2 μA, at which the reduction current levelled off. The final steady current value is close to background current (–2.9 μA) estimated by chronoamperometry of a blank MWNT/PGE electrode in the same experimental conditions (Figure 8.6B). Hence the final current value is

close to zero after subtracted by the background current. This indicates that the net current produced by $CO_2$ reduction is nearly zero at steady state. Integration of Figure 8.6A gives the net amount of charge produced by $CO_2$ reduction and CO oxidation catalysed by 1 μL of CODH $I_{Ch}$ confined by EMIMTFSI saturated with 1 bar $CO_2$, which is equal to 0.0048 C (average of three experiments, data shown in Table 8.2).

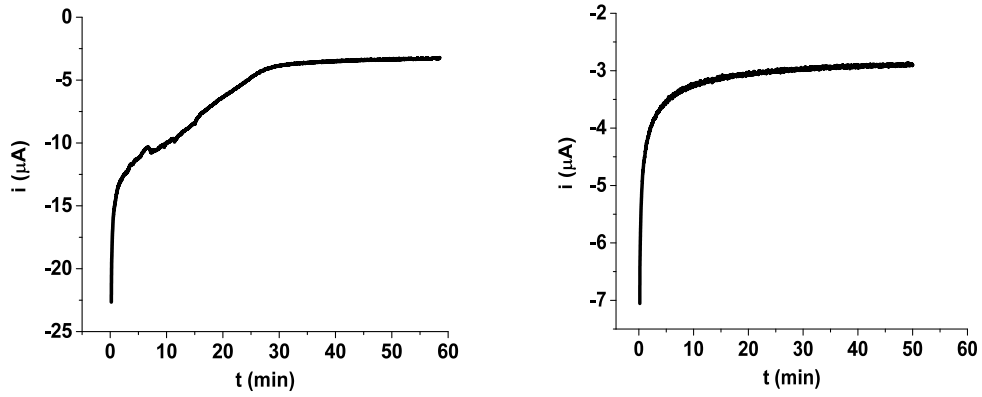



Figure 8.6 Chronoamperometry of (A) 1 μL of CODH $I_{Ch}$ (suspended in the buffer containing 50 mM Tris/HCl, initially pH 7.5 at 30 ˚C, 1 mM Dithiothreitol and 1 mM sodium dithionite) adsorbed at an MWNT/PGE electrode; (B) a blank MWNT/PGE electrode surrounded by EMIMTFSI (~1 mL) dissolved with 2 mM DmFc and saturated with 1 bar $CO_2$. Electrode rotation rate 0 RPM. Temperature 30 ˚C, potential=–0.65 V vs $DmFc^{+/0}$, projected electrode surface area 0.03 $cm^2$. First 10 s are removed.

Table 8.2 Summary of data obtained by chronoamperometry at –0.45 and –0.65 V vs $DmFc^{+/0}$.

| Chronoamperometry Potential | Integration obtained by Experiment 1 | Integration obtained by Experiment 2 | Integration obtained by Experiment 3 | Average |
|---|---|---|---|---|
| –0.45 V | 0.00967 | 0.00994 | 0.00939 | 0.009667 |
| –0.65 V | 0.0043 | 0.0048 | 0.0054 | 0.0048 |

The decrease of reduction current produced by 1 μL of CODH $I_{Ch}$ confined by EMIMTFSI saturated with 1 bar $CO_2$ before steady state in chronoamperometry at –0.45 and –0.65 V vs $DmFc^{+/0}$ is a result of three factors: product inhibition by CO and proton, increase of CO oxidation current in the aqueous phase, and film loss of CODH $I_{Ch}$. At -0.45 and –0.65 V vs $DmFc^{+/0}$, the net amount of CO produced by $CO_2$ reduction is equal to $2.49\times 10^{-8}$ and $5.00\times 10^{-8}$ mol, respectively.

Hydrophobicity and high $CO_2$ solubility of ILs are both important for the aqueous enzyme film of CODH $I_{Ch}$ to be electrocatalytically active in an almost dry condition. The hydrophobicity of ILs ensures that the small aqueous enzyme film is confined by IL. The solubility of $CO_2$ in EMIMTFSI is 0.0315, which is ~ 6 times higher than that in water ($5.41 \times 10^{-4}$). Consequently, the aqueous shell of CODH $I_{Ch}$ (1 μL) at the electrode is saturated with $CO_2$ throughout the reversible electrocatalysis between CO and $CO_2$, when surrounded by EMIMTFSI (~ 1 mL) that is saturated with $CO_2$.

## 8.5 Conclusions

In summary, I demonstrate that CODH $I_{Ch}$ is highly electrocatalytically active when confined by the hydrophobic ionic liquid of EMIMTFSI saturated with $CO_2$. This is the first report of electrocatalytic activity of CODH $I_{Ch}$ in an almost dry condition confined by an ionic liquid. In the initial stage, the main reaction in the tiny aqueous phase (1 μL) is $CO_2$ reduction. Consequently, the concentration of product of protons and CO increase in the aqueous phase, leading to more negative onset potential and lower reduction current of $CO_2$ reduction. In the second stage, the rate of CO oxidation increases because of the increase of CO concentration. Meanwhile, the rate of $CO_2$ reduction decreases as a result of product inhibition by CO and proton. Finally, the rate of $CO_2$ reduction is equal to that of CO oxidation, i.e. a steady state is achieved. This work allows us to understand the reversible $CO_2$/CO electrochemistry in a tiny aqueous environment confined by hydrophobic ionic liquids.

# 9 Conclusions and Perspectives

In brief, this thesis demonstrates that three metalloenzymes:hydrogenase-1 from *Escherichia coli* (Hyd-1),bilirubin oxidase (BOD), and carbon monoxide dehydrogenases from *Carboxydothermus hydrogenoformans*I (CODH $I_{Ch}$) shows considerable electrocatalytic activity in aqueous microenvironment confined by hydrophobic ionic liquids.This thesis is the first to report the protein film electrochemistry of Hyd-1,BOD, and CODH $I_{Ch}$confined in neationic liquids, which helps us to understand theelectrocatalytic performance of the three "clean energy enzymes" in an almost dry condition in ionic liquids.

Cyclic voltammetry of the Hyd1 and BOD shows dramatic changes of pH over a few potential cycles in an aqueous microenvironment confined by ionic liquids: 1-ethyl-3-methylimidazolium bis(trifluoromethylsulfonyl)imide (EMIMTFSI) and 1-methyl-1-propyl pyrrolidinium bis(trifluoromethylsulfonyl)imide. For Hyd1 adsorbed on a carbon electrode surrounded by ionic liquids saturated with $H_2$, the pH decreases as a result of proton produced in the aqueous shell over a few cycles. For BODadsorbed on a carbon electrode surrounded by ionic liquids saturated with $O_2$, the pH increases as a result of hydroxide produced in the aqueous shell over a few cycles.

The synaptic enzymatic$H_2$-$O_2$ fuel cell using EMIMTFSI generates an OCV of 0.90 ± 0.10 V,which is close to 1.23 V: the reversible OCV of a $H_2$-$O_2$ fuel cell at 26 ± 2 ˚C. The synaptic fuel cell using EMIMTFSI reached a maximum power density of 7.3 ± 0.3 μW $cm^{-2}$(per cathode area) with 96 % $H_2$–4 % $O_2$, 26 ± 2 ˚C. This is the first time a miniature enzymatic fuel cell using ionic liquid as electrolyte was reported.As control, a synaptic fuel cell using conventional aqueous buffer in lieu of EMIMTFSI reached a maximum power density of 175± 5 μW $cm^{-2}$ at 0.44 V in the same conditions. The synaptic fuel cell using EMIMTFSI showed slower gas transport than that uses aqueous

buffer as electrolyte. The synaptic enzymatic $H_2$-$O_2$ fuel cell using EMIMTFSI reported here uses much smaller volume of electrolyte (~ 6 μL) than previous enzymatic $H_2$-$O_2$ fuel cells did (> 1 mL) [30, 79, 243]. The OCV of the fuel cell using EMIMTFSI is over 0.8 V, which is comparable to literature values and close to the thermodynamic reversible value of 1.23 V at 25 ˚C. The power density of the synaptic fuel cell can be engineered to a greater value by: 1) increasing operational pressure to increase gas diffusion to ionic liquids,2) incorporating strategies for faster electron transfer between enzymes and electrodes, 3) improving the catalytic activity of enzymes, 4) improving the ability to load high quantities of enzymes on electrode surfaces, by using high surface area electrode materials or engineering enzymes to smaller volumes or both, 5) designing new ionic liquids that are more gas permeable and at the same time enzyme-friendly.To achieve these goals, fundamental study of physicochemical properties of ionic liquids and interface between proteins and ionic liquids is necessary.

CODH $I_{Ch}$ is highly electrocatalytically active in a tiny aqueous shell confined by a hydrophobic ionic liquid saturated with $CO_2$. $CO_2$ reduction and CO oxidation electrocatalysed by CODH $I_{Ch}$ occurred at the same time in the tiny aqueous shell, according to cyclic voltammetry. Finally, a steady state was achieved. These results allow us to understand the reversible $CO_2$/CO electrochemistry in a tiny aqueous environment confined by hydrophobic ionic liquids.

As this thesis focuses on the electrochemical properties of enzymes confined in RTILs, the properties of interface between the aqueous enzyme “pocket” and ionic liquids need further investigation by microscopy and spectroscopy linked to electrochemical measurements.

The electrode materials were films of multiwalled carbon nanotubes, which showed more capacity to increase enzymatic catalytic current densities according to PFE carried out at graphene film, MWNT film and MWNT pellet in Chapter 4. To increase the enzymatic catalytic current densities obtained in Chapter 5 – 8 further, other electrode surface modification techniques can be applied. For example, covalent binding of enzymes to electrode surfaces has been reported to improve the stability of enzymes at electrodes. Crosslinking enzymes into the polymer hydrogel and entrapping it has been found to increase the enzyme loading and allow facile transport of fuel and product through the membrane, and the entrapment provided some additional stability versus a solution of the enzymes. However, cross-linking or covalent binding of enzymes in anyway can decrease the degrees of freedom of the enzyme and therefore decrease the activity. I have tried using covalent binding of enzymes to MWNT films, but the catalytic activity of the enzyme was lower than that of the enzyme physically adsorbed to MWNT films, which is consistent with some literature. A final recent approach to enzyme stabilization is to use enzymes from thermophilic microorganisms, because enzymes that are stable at high temperatures usually have higher stability at room temperature than the non-thermophilic versions [250].

All in all, this thesis demonstrates that there is a considerable scope for the application of ionic liquids for selective enzymatic fuel cells and electrocatalysed $CO_2$ reduction. More data on the gas diffusivity and solubility in RTILs are necessary for quantitativeanalyses of the electrochemical behaviour of enzymes as well as other catalysts functioning in RTIL. No solubility data on $H_2$ in EMIMTFSI or PMPyrTFSI have been reported, and only one paper was found reporting the solubility of $O_2$ in EMIMTFSI [241]. The fundamental study of gas solubility and diffusivity is taking off, which is necessary for the effective exploitingof the superb electrochemical properties

of RTILs to various technologies including fuel cells, batteries, supercapacitors, carbon dioxide capture, biosensors, organic synthesis, etc.

# 10 Appendices

## 10.1 The Nernst Equation

The following scheme represents a general reaction:

$$\nu_A A + \nu_B B \rightleftharpoons \nu_C C + \nu_D D$$

If the extent of reaction, $\xi$, increases by $d\xi$ , then the amounts of reactants and products change according to $dn_J = \nu_J d\xi$:

$$dn_A = \nu_A d\xi,\ dn_B = \nu_B d\xi,\ dn_C = \nu_C d\xi \text{ and } dn_D = \nu_D d\xi$$

where the stoichiometric number of species J, $\nu_J$, is negative for the reactants and positive for the products.

The corresponding infinitesimal change in the Gibbs energy, d$G$, at constant pressure and temperature is given by:

$$dG = \left(\sum_J \nu_J \mu_J\right) d\xi$$

where $\mu_J$ is the chemical potential of species J. The reaction Gibbs energy, $\Delta_r G$, is therefore given by:

$$\Delta_r G = \left(\frac{\partial G}{\partial \xi}\right)_{p,T} = \nu_A \mu_A + \nu_B \mu_B + \nu_C \mu_C + \nu_D \mu_D$$

Then, since $\mu_J = \mu_J^{\ominus} + RT \ln a_J$ (where $a_J$ is the activity of species J and $R$ is the gas constant) and $\Delta G^{\ominus} = \nu_A \mu_A^{\ominus} + \nu_B \mu_B^{\ominus} + \nu_C \mu_C^{\ominus} + \nu_D \mu_D^{\ominus}$:

$$\Delta_r G = \Delta G^{\ominus} - RT \ln Q$$

where $Q$ is the reaction quotient, given by $\prod_J a_J^{\nu_J}$.

The maximum non-expansion work that can be performed as the reaction advances by $d\xi$ at constant temperature and pressure is given by $dw_e = \Delta_r G\, d\xi$. The total charge that must be transported from the anode to cathode in order for the reaction to proceed by this amount is given by $q = -nFd\xi$, where $n$ is the number of electrons involved in the process and $F$ is Faraday's constant. Therefore, the work done upon transport of this infinitesimal charge is given by the equation $dw_e = -nFE\, d\xi$, where $E$ is the potential difference. Since $dw_e = \Delta_r G\, d\xi$, then $\Delta_r G = -nFE$ and $\Delta G^{\ominus} = -nFE^{\ominus}$. Therefore:

$$E = E^{\ominus} - \frac{RT}{nF} \ln Q$$

This is the Nernst equation.

An alternative derivation of this equation can be obtained by equating the electrochemical potentials of the reactants and products, where the electrochemical potential of species J, $\bar{u}_J$, is related to the chemical potential by $\bar{u}_J = \mu_J + zFE$ (where $z$ is the charge on J).[251]

## 10.2 The Arrhenius Equation

The Arrhenius equation[242] describes the empirical observation that, for most reactions, the rate constant, *k*, increases as the temperature is raised:

$$k=A\exp\left(\frac{-E_a}{RT}\right)$$

The terms R and T correspond respectively to the gas constant and temperature in Kelvin. The activation energy, $E_a$, is the minimum kinetic energy required by reactants in order for a collision to lead to product formation. The exponential factor arises from a Boltzmann distribution of the fraction of collisions with sufficient energy to lead to reaction. The pre-exponential factor, *A*, corresponds to the rate of collisions, but does not take into consideration the energy of the reactants. Therefore, the product of *A*and the exponential factor represents the rate of successful collisions (i.e. the rate of reaction).

A natural logarithmic transform of the Arrhenius equation generates the following:

$$lnk=lnA-\frac{E_a}{RT}$$

Therefore, the activation energy, $E_a$, can be determined from the gradient of a plot of lnk against *1/T*.

# Bibliography


1. *Global Warming: News, Facts, Causes & Effects*. [cited 2015 05/06]; Available from:http://www.livescience.com/topics/global-warming/.
2. Pollack, H.N., *A World without Ice*. 2009, New York: Avery/Penguin Group.
3. Cammack, R., M. Frey, and R. Robson, *Hydrogen As a Fuel: Learning from Nature*. 2001, London and New York: Taylor and Francis.
4. Larminie, J., Dicks, A., *Fuel Cell Systems Explained*. 2003.
5. Cracknell, J.A., Vincent, K. A., Armstrong, F. A., *Enzymes as working or inspirational electrocatalysts for fuel cells and electrolysis.* Chemical Reviews, 2008. **108**(7): p. 2439-2461.
6. Barton, S.C., J. Gallaway, and P. Atanassov, *Enzymatic biofuel cells for Implantable and microscale devices.* Chemical Reviews, 2004. **104**(10): p. 4867-4886.
7. *Toyota FCV Mirai launches in LA; initial TFCS specs; $57,500 or $499 lease; leaning on Prius analogy*. 2014 18 November 2014; Available from: http://www.greencarcongress.com/2014/11/20141118-mirai.html.
8. Wang, V.C.C., Can, M., Pierce, E., Ragsdae, S. W., Armstrong, F. A., *A Unified Electrocatalytic Description of the Action of Inhibitors of Nickel Carbon Monoxide Dehydrogenase.* Journal of the American Chemical Society, 2013. **135**(6): p. 2198-2206.
9. Sakai, H., Nakagawa, T., Tokita, Y., Hatazawa, T., Ikeda, T., Tsujimura, S., Kano, K., *A high-power glucose/oxygen biofuel cell operating under quiescent conditions.* Energy & Environmental Science, 2009. **2**(1): p. 133-138.
10. Woolerton, T.W., Sheard, S., Chaudhary, Y. S., Armstrong, F.A., *Enzymes and bio-inspired electrocatalysts in solar fuel devices.* Energy & Environmental Science, 2012. **5**(6): p. 7470-7490.
11. Kim, J., Jia, H., Wang, P., *Challenges in biocatalysis for enzyme-based biofuel cells.* Biotechnol Adv, 2006. **24**(3): p. 296-308.
12. Watson, V.J. and B.E. Logan, *Analysis of polarization methods for elimination of power overshoot in microbial fuel cells.* Electrochemistry Communications, 2011. **13**(1): p. 54-56.
13. Vincent, K.A., Cracknell, J. A., Clark, J. R., Ludwig, M., Lenz, O., Friedrich, B., Armstrong, F. A., *Electricity from low-level $H_2$ in still air - an ultimate test for an oxygen tolerant hydrogenase.* Chemical Communications, 2006(48): p. 5033-5035.
14. Yahiro, A.T., Lee, S. M., Kimble, D. O., *Bioelectrochemistry .I. Enzyme Utilizing Bio-Fuel Cell Studies.* Biochimica Et Biophysica Acta, 1964. **88**(2): p. 375-&.
15. Plotkin, E.V., Higgins, I. J., Hill, H. A. O., *Methanol Dehydrogenase Bioelectrochemical Cell and Alcohol Detector.* Biotechnology Letters, 1981. **3**(4): p. 187-192.
16. Cass, A.E.G., Davis, G., Francis, G. D., Hill, H. A. O., Aston, W. J., Higgins, I. J., Plotkin, E. V., Scott, L. D. L., Turner, A. P. F., *Ferrocene-Mediated Enzyme*

*Electrode for Amperometric Determination of Glucose.* Analytical Chemistry, 1984. **56**(4): p. 667-671.

17. Katz, E., Willner, I., Kotlyar, A. B., *A non-compartmentalized glucose vertical bar $O_2$ biofuel cell by bioengineered electrode surfaces.* Journal of Electroanalytical Chemistry, 1999. **479**(1): p. 64-68.
18. Katz, E., Filanovsky, B., Willner, I., *A biofuel cell based on two immiscible solvents and glucose oxidase and microperoxidase-11 monolayer-functionalized electrodes.* New Journal of Chemistry, 1999. **23**(5): p. 481-487.
19. Mano, N., Mao, F., Heller, A., *Characteristics of a miniature compartment-less glucose-O-2 biofuel cell and its operation in a living plant.* Journal of the American Chemical Society, 2003. **125**(21): p. 6588-6594.
20. Zayats, M., Katz, E., Baron, R., Willner, I., *Reconstitution of apo-glucose dehydrogenase on pyrroloquinoline quinone-functionalized Au nanoparticles yields an electrically contacted biocatalyst.* Journal of the American Chemical Society, 2005. **127**(35): p. 12400-12406.
21. Blanford, C.F., Heath, R. S., Armstrong, F. A., *A stable electrode for high-potential, electrocatalytic $O_2$ reduction based on rational attachment of a blue copper oxidase to a graphite surface.* Chemical Communications, 2007(17): p. 1710-1712.
22. Minson, M., Meredith, M. T., Shrier, A., Giroud, F., Hickey, D., Glatzhofer, D. T., Minteer, S. D., *High Performance Glucose/$O_2$ Biofuel Cell: Effect of Utilizing Purified Laccase with Anthracene-Modified Multi-Walled Carbon Nanotubes.* Journal of the Electrochemical Society, 2012. **159**(12): p. G166-G170.
23. Kamitaka, Y., Tsujimura, S., Setoyama, N., Kajino, T., Kano, K., *Fructose/dioxygen biofuel cell based on direct electron transfer-type bioelectrocatalysis.* Physical Chemistry Chemical Physics, 2007. **9**(15): p. 1793-1801.
24. Tsujimura, S., .Fujita, M.,Tatsumi, H., Kano, K., Ikeda, T., *Bioelectrocatalysis-based dihydrogen/dioxygen fuel cell operating at physiological pH.* Physical Chemistry Chemical Physics, 2001. **3**(7): p. 1331-1335.
25. Mano, N., Kim, H. H., Heller, A., *On the relationship between the characteristics of bilirubin oxidases and $O_2$ cathodes based on their "wiring".* Journal of Physical Chemistry B, 2002. **106**(34): p. 8842-8848.
26. Barton, S.C., Kim, H..H., Binyamin, G., Zhang, Y., Heller, A., *The "Wired" Laccase Cathode: High Current Density Electroreduction of $O_2$ to Water at +0.7 V (NHE) at pH 5.* Journal of the American Chemical Society, 2001. **123**(24): p. 5802-5803.
27. Xu, L., Armstrong, F. A., *Optimizing the power of enzyme-based membrane-less hydrogen fuel cells for hydrogen-rich $H_2$–air mixtures.* Energy & Environmental Science, 2013. **6**(7): p. 2166.
28. Barton, S.C., Sun, Y. H., Chandra, B., White, S., Hone, J., *Mediated enzyme electrodes with combined micro- and nanoscale supports.* Electrochemical and Solid State Letters, 2007. **10**(5): p. B96-B100.
29. Alonso-Lomillo, M.A., Rudiger, O., Maroto-Valiente, A., Velez, M., Rodriguez-Ramos, I., Munoz, F. J., Fernandez, V. M., De Lacey, A. L., *Hydrogenase-coated carbon nanotubes for efficient $H_2$ oxidation.* Nano Letters, 2007. **7**(6): p. 1603-1608.

30. Krishnan, S., Armstrong, F. A., *Order-of-magnitude enhancement of an enzymatic hydrogen-air fuel cell based on pyrenyl carbon nanostructures.* Chemical Science, 2012. **3**(4): p. 1015-1023.
31. Liu, C., Alwarappan, S., Chen, Z., Kong, X., Li, C. Z., *Membraneless enzymatic biofuel cells based on graphene nanosheets.* Biosensors and Bioelectronics, 2010. **25**(7): p. 1829-1833.
32. Mani, V., Devasenathipathy, R., Chen, S. M., Gu, J. A., Huang, S. T., *Synthesis and characterization of graphene-cobalt phthalocyanines and graphene-iron phthalocyanine composites and their enzymatic fuel cell application.* Renewable Energy, 2015. **74**: p. 867-874.
33. Palanisamy, S., Cheemalapati, S., Chen, S. M., *An Enzymatic Biofuel cell Based On Electrochemically Reduced Graphene Oxide and Multiwalled Carbon nanotubes/Zinc oxide Modified Electrode.* International Journal of Electrochemical Science, 2012. **7**(11): p. 11477-11487.
34. Decréau, R.A., Collman, J.P., Yang, Y., Yan, Y., Devaraj, N. K., *Syntheses of Hemoprotein Models that can be Covalently Attached onto Electrode Surfaces by Click Chemistry.* The Journal of Organic Chemistry, 2007. **72**(8): p. 2794-2802.
35. Collman, J.P., Devaraj, N. K., Decreau, R. A., Yang, Y., Yan, Y. L., Ebina, W., Eberspacher, T. A., Chidsey, C. E. D., *A cytochrome c oxidase model catalyzes oxygen to water reduction under rate-limiting electron flux.* Science, 2007. **315**(5818): p. 1565-1568.
36. Dutta, A., DuBois, D. L., Roberts, J. A. S., Shaw, W. J., *Amino acid modified Ni catalyst exhibits reversible $H_2$ oxidation/production over a broad pH range at elevated temperatures.* Proceedings of the National Academy of Sciences of the United States of America, 2014. **111**(46): p. 16286-16291.
37. Bard, J., Faulkner, L., *Electrochemical Methods Fundamentals and Applications*. 2001.
38. Solomon, E.I., Sundaram, U. M., Machonkin, T. E., *Multicopper oxidases and oxygenases.* Chemical Reviews, 1996. **96**(7): p. 2563-2605.
39. Chen, T., Barton, S. C., Binyamin, G., Gao, Z. Q., Zhang, Y. C., Kim, H. H., Heller, A., *A miniature biofuel cell.* Journal of the American Chemical Society, 2001. **123**(35): p. 8630-8631.
40. Mano, N., Fernandez, J. L., Kim, Y., Shin, W., Bard, A. J., Heller, A., *Oxygen Is Electroreduced to Water on a "Wired" Enzyme Electrode at a Lesser Overpotential than on Platinum.* Journal of the American Chemical Society, 2003. **125**(50): p. 15290-15291.
41. Murao, S. and N. Tanaka, *A New Enzyme "Bilirubin Oxidase" Produced by Myrothecium verrucaria MT-1.* Agricultural and Biological Chemistry, 1981. **45**(10): p. 2383-2384.
42. Goldfinch, M.E., Maguire, G. A., *Investigation of the use of bilirubin oxidase to measure the apparent unbound bilirubin concentration in human plasma.* Annals of Clinical Biochemistry, 1988. **25**(1): p. 73-77.
43. Tsujimura, S., Tatsumi, B., Ogawa, J., Shimizu, S., Kano, K., Ikeda, T., *Bioelectrocatalytic reduction of dioxygen to water at neutral pH using bilirubin oxidase as an enzyme and 2,2 '-azinobis (3-ethylbenzothiazolin-6-sulfonate) as an electron transfer mediator.* Journal of Electroanalytical Chemistry, 2001. **496**(1-2): p. 69-75.

44. Mano, N., *Features and applications of bilirubin oxidases.* Applied Microbiology and Biotechnology, 2012. **96**(2): p. 301-307.
45. Osman, M.H., Shah, A. A., Walsh, F. C., *Recent progress and continuing challenges in bio-fuel cells. Part I: Enzymatic cells.* Biosensors & Bioelectronics, 2011. **26**(7): p. 3087-3102.
46. Cracknell, J.A., McNamara, T. P., Lowe, E. D., Blanford, C. F., *Bilirubin oxidase from Myrothecium verrucaria: X-ray determination of the complete crystal structure and a rational surface modification for enhanced electrocatalytic $O_2$ reduction.* Dalton Transactions, 2011. **40**(25): p. 6668-6675.
47. dos Santos, L., Climent, V., Blanford, C. F., Armstrong, F. A., *Mechanistic studies of the 'blue' Cu enzyme, bilirubin oxidase, as a highly efficient electrocatalyst for the oxygen reduction reaction.* Physical Chemistry Chemical Physics, 2010. **12**(42): p. 13962-13974.
48. Quintanar, L., Stoj, C., Taylor, A. B., Hart, P. J., Kosman, D. J., Solomon, E. I., *Shall We Dance? How A Multicopper Oxidase Chooses Its Electron Transfer Partner.* Accounts of Chemical Research, 2007. **40**(6): p. 445-452.
49. Durão, P., Bento, I., Fernandes, A., Melo, E. P., Lindley, P. F., Martins, L.O., *Perturbations of the T1 copper site in the CotA laccase from Bacillus subtilis: structural, biochemical, enzymatic and stability studies.* JBIC Journal of Biological Inorganic Chemistry, 2006. **11**(4): p. 514-526.
50. DeLano, W., L., *PyMol*. DeLano Scientific: San Carlos, CA.
51. Shimizu, A., Kwon, J. H., Sasaki, T., Satoh, T., Sakurai, N., Sakurai, T., Yamaguchi, S., Samejima, T., *Myrothecium verrucaria Bilirubin Oxidase and Its Mutants for Potential Copper Ligands.* Biochemistry, 1999. **38**(10): p. 3034-3042.
52. Shimizu, A., Sasaki, T., Kwon, J. H., Odaka, A., Satoh, T., Sakurai, N., Sakurai, T., Yamaguchi, S., Samejima, T., *Site-directed mutagenesis of a possible type 1 copper ligand of bilirubin oxidase; a Met467Gln mutant shows stellacyanin-like properties.* Journal of Biochemistry, 1999. **125**(4): p. 662-668.
53. Ramírez, P., Mano, N., Andreu, R., Ruzgas, T., Heller, A., Gorton, L., Shleev, S., *Direct electron transfer from graphite and functionalized gold electrodes to T1 and T2/T3 copper centers of bilirubin oxidase.* Biochimica et Biophysica Acta (BBA) - Bioenergetics, 2008. **1777**(10): p. 1364-1369.
54. Solomon, E.I., Augustine, A. J., Yoon, J., *$O_2$ Reduction to $H_2O$ by the multicopper oxidases.* Dalton Transactions, 2008(30): p. 3921-3932.
55. Christenson, A., Shleev, S., Mano, N., Heller, A., Gorton, L., *Redox potentials of the blue copper sites of bilirubin oxidases.* Biochimica et biophysica acta, 2006. **1757**(12): p. 1634-41.
56. Kamitaka, Y., Tsujimura, S., Kataoka, K., Sakurai, T., Ikeda, T., Kano, K., *Effects of axial ligand mutation of the type I copper site in bilirubin oxidase on direct electron transfer-type bioelectrocatalytic reduction of dioxygen.* Journal of Electroanalytical Chemistry, 2007. **601**(1–2): p. 119-124.
57. Pizzariello, A., Stred'ansky, M., Miertus, S., *A glucose/hydrogen peroxide biofuel cell that uses oxidase and peroxidase as catalysts by composite bulk-modified bioelectrodes based on a solid binding matrix.* Bioelectrochemistry, 2002. **56**(1-2): p. 99-105.
58. Mondal, M.S., Goodin, D. B., Armstrong, F. A., *Simultaneous voltammetric comparisons of reduction potentials, reactivities, and stabilities of the high-potential catalytic states of wild-type and distal-pocket mutant (W51F) yeast*

*cytochrome c peroxidase.* Journal of the American Chemical Society, 1998. **120**(25): p. 6270-6276.
59. Heller, A., *Electrical Connection of Enzyme Redox Centers to Electrodes.* Journal of Physical Chemistry, 1992. **96**(9): p. 3579-3587.
60. Reuillard, B., Le Goff, A., Agnes, C., Holzinger, M., Zebda, A., Gondran, C., Elouarzaki, K., Cosnier, S., *High power enzymatic biofuel cell based on naphthoquinone-mediated oxidation of glucose by glucose oxidase in a carbon nanotube 3D matrix.* Physical Chemistry Chemical Physics, 2013. **15**(14): p. 4892-4896.
61. Zebda, A., Gondran, C., Le Goff, A., Holzinger, M., Cinquin, P., Cosnier, S., *Mediatorless high-power glucose biofuel cells based on compressed carbon nanotube-enzyme electrodes.* Nature Communications, 2011. **2**.
62. Arechederra, R.L., Minteer, S. D., *Complete Oxidation of Glycerol in an Enzymatic Biofuel Cell.* Fuel Cells, 2009. **9**(1): p. 63-69.
63. Arechederra, R.L., Treu, B. L., Minteer, S. D., *Development of glycerol/$O_2$ biofuel cell.* Journal of Power Sources, 2007. **173**(1): p. 156-161.
64. Vincent, K.A., Parkin, A., Armstrong, F. A., *Investigating and exploiting the electrocatalytic properties of hydrogenases.* Chemical Reviews, 2007. **107**(10): p. 4366-4413.
65. Parkin, A., Cavazza, C., Fontecilla-Camps, J. C., Armstrong, F. A., *Electrochemical investigations of the interconversions between catalytic and inhibited states of the [FeFe]-hydrogenase from Desulfovibrio desulfuricans.* Journal of the American Chemical Society, 2006. **128**(51): p. 16808-16815.
66. Goldet, G., Brandmayr, C., Stripp, S. T., Happe, T., Cavazza, C., Fontecilla-Camps, J. C., Armstrong, F. A., *Electrochemical Kinetic Investigations of the Reactions of [FeFe]-Hydrogenases with Carbon Monoxide and Oxygen: Comparing the Importance of Gas Tunnels and Active-Site Electronic/Redox Effects.* Journal of the American Chemical Society, 2009. **131**(41): p. 14979-14989.
67. Korbas, M., Vogt, S., Meyer-Klaucke, W., Bill, E., Lyon, E. J., Thauer, R. K., Shima, S., *The iron-sulfur cluster-free hydrogenase (Hmd) is a metalloenzyme with a novel iron binding motif.* Journal of Biological Chemistry, 2006. **281**(41): p. 30804-30813.
68. Page, C.C., Moser, C. C., Chen, X. X., Dutton, P. L., *Natural engineering principles of electron tunnelling in biological oxidation-reduction.* Nature, 1999. **402**(6757): p. 47-52.
69. Garcin, E., Vernede, X., Hatchikian, E. C., Volbeda, A., Frey, M., Fontecilla-Camps, J. C., *The crystal structure of a reduced [NiFeSe] hydrogenase provides an image of the activated catalytic center.* Structure, 1999. **7**(5): p. 557-566.
70. Dementin, S., Belle, V., Bertrand, P., Guigliarelli, B., Adryanczyk-Perrier, G., De Lacey, A. L., Fernandez, V. M., Rousset, M., Leger, C., *Changing the ligation of the distal [4Fe4S] cluster in NiFe hydrogenase impairs inter- and intramolecular electron transfers.* Journal of the American Chemical Society, 2006. **128**(15): p. 5209-5218.
71. Montet, Y., Amara, P., Volbeda, A., Vernede, X., Hatchikian, E. C., Field, M. J., Frey, M., FontecillaCamps, J. C., *Gas access to the active site of Ni-Fe hydrogenases probed by X-ray crystallography and molecular dynamics.* Nature Structural Biology, 1997. **4**(7): p. 523-526.

72. Nicolet, Y., Piras, C., Legrand, P., Hatchikian, C. E., Fontecilla-Camps, J. C., *Desulfovibrio desulfuricans iron hydrogenase: the structure shows unusual coordination to an active site Fe binuclear center.* Structure, 1999. **7**(1): p. 13-23.
73. Cohen, J., Kim, K., Posewitz, M., Ghirardi, M. L., Schulten, K., Seibert, M., King, P., *Molecular dynamics and experimental investigation of $H_2$ and $O_2$ diffusion in [Fe]-hydrogenase.* Biochemical Society Transactions, 2005. **33**: p. 80-82.
74. Teixeira, V.H., Baptista, A. M., Soares, C. M., *Pathways of $H_2$ toward the Active Site of [NiFe]-Hydrogenase.* Biophysical Journal, 2006. **91**(6): p. 2035-2045.
75. Buhrke, T., Lenz, O., Krauss, N., Friedrich, B., *Oxygen tolerance of the $H_2$-sensing [NiFe] hydrogenase from Ralstonia eutropha H16 is based on limited access of oxygen to the active site.* Journal of Biological Chemistry, 2005. **280**(25): p. 23791-23796.
76. Duche, O., Elsen, S., Cournac, L., Colbeau, A., *Enlarging the gas access channel to the active site renders the regulatory hydrogenase HupUV of Rhodobacter capsulatus O-2 sensitive without affecting its transductory activity.* Febs Journal, 2005. **272**(15): p. 3899-3908.
77. Lukey, M.J., Parkin, A., Roessler, M. M., Murphy, B. J., Harmer, J., Palmer, T., Sargent, F., Armstrong, F. A., *How Escherichia coli Is Equipped to Oxidize Hydrogen under Different Redox Conditions.* Journal of Biological Chemistry, 2010. **285**(6): p. 3928-3938.
78. Lukey, M.J., Roessler, M. M., Parkin, A., Evans, R. M., Davies, R. A., Lenz, O., Friedrich, B., Sargent, F., Armstrong, F. A., *Oxygen-Tolerant [NiFe]-Hydrogenases: The Individual and Collective Importance of Supernumerary Cysteines at the Proximal Fe-S Cluster.* Journal of the American Chemical Society, 2011. **133**(42): p. 16881-16892.
79. Wait, A.F., Parkin, A., Morley, G. M., dos Santos, L., Armstrong, F. A., *Characteristics of Enzyme-Based Hydrogen Fuel Cells Using an Oxygen-Tolerant Hydrogenase as the Anodic Catalyst.* The Journal of Physical Chemitry C, 2010. **114**(27): p. 12003-12009.
80. Volbeda, A., Amara, P., Darnault, C., Mouesca, J. M., Parkin, A., Roessler, M. M., Armstrong, F. A., Fontecilla-Camps, J. C., *X-ray crystallographic and computational studies of the O-2-tolerant [NiFe]-hydrogenase 1 from Escherichia coli.* Proceedings of the National Academy of Sciences of the United States of America, 2012. **109**(14): p. 5305-5310.
81. Shomura, Y., Yoon, K. S., Nishihara, H., Higuchi, Y., *Structural basis for a [4Fe-3S] cluster in the oxygen-tolerant membrane-bound [NiFe]-hydrogenase.* Nature, 2011. **479**(7372): p. 253-U143.
82. Wulff, P., Thomas, C., Sargent, F., Armstrong, F. A., *How the oxygen tolerance of a NiFe -hydrogenase depends on quaternary structure.* Journal of Biological Inorganic Chemistry, 2016. **21**(1): p. 121-134.
83. Murphy, B.J., Sargent, F., Armstrong, F. A., *Transforming an oxygen-tolerant [NiFe] uptake hydrogenase into a proficient, reversible hydrogen producer.* Energy & Environmental Science, 2014. **7**(4): p. 1426-1433.
84. Evans, R.M., Brooke, E. J., Wehlin, S. A. M., Nomerotskaia, E., Sargent, F., Carr, S. B., Phillips, S. E. V., Armstrong, F. A., *Mechanism of hydrogen activation by [NiFe] hydrogenases.* Nature Chemical Biology, 2016. **12**(1): p. 46.
85. Brecht, M., van Gastel, M., Buhrke, T., Friedrich, B., Lubitz, W., *Direct detection of a hydrogen ligand in the [NiFe] center of the regulatory H-2-*

*sensing hydrogenase from Ralstonia eutropha in its reduced state by HYSCORE and ENDOR spectroscopy.* Journal of the American Chemical Society, 2003. **125**(43): p. 13075-13083.
86. Siegbahn, P.E.M., Tye, J. W., Hall, M. B., *Computational studies of [NiFe] and [FeFe] hydrogenases.* Chemical Reviews, 2007. **107**(10): p. 4414-4435.
87. Keith, J.M., Hall, M. B., *Potential Hydrogen Bottleneck in Nickel-Iron Hydrogenase.* Inorganic Chemistry, 2010. **49**(14): p. 6378-6380.
88. Ogata, H., Lubitz, W., Higuchi, Y., *[NiFe] hydrogenases: structural and spectroscopic studies of the reaction mechanism.* Dalton Transactions, 2009(37): p. 7577-7587.
89. Ogata, H., Mizoguchi, Y., Mizuno, N., Miki, K., Adachi, S., Yasuoka, N., Yagi, T., Yamauchi, O., Hirota, S., Higuchi, Y., *Structural studies of the carbon monoxide complex of [NiFe]hydrogenase from Desulfovibrio vulgaris Miyazaki F: Suggestion for the initial activation site for dihydrogen.* Journal of the American Chemical Society, 2002. **124**(39): p. 11628-11635.
90. Hamnett, A.C., P. A., *Techniques and Mechanisms in Electrochemistry*. 1994, London: Blackie Academic and Professional.
91. Sørensen, B., *Hydrogen and Fuel Cells*. 3rd ed ed. 2004: Elsevier Academic Press: Burlington, MA.
92. Jones, A.K., Sillery, E., Albracht, S. P. J., Armstrong, F. A., *Direct comparison of the electrocatalytic oxidation of hydrogen by an enzyme and a platinum catalyst.* Chemical Communications, 2002(8): p. 866-867.
93. Karyakin, A.A., Morozov, S. V., Karyakina, E. E., Zorin, N. A., Perelygin, V. V., Cosnier, S., *Hydrogenase electrodes for fuel cells.* Biochemical Society Transactions, 2005. **33**: p. 73-75.
94. Petrii, O.A., Tsirlina, G. A., *Electrocatalytic activity prediction for hydrogen electrode reaction: intuition, art, science.* Electrochimica Acta, 1994. **39**(11): p. 1739-1747.
95. Conway, B.E., Jerkiewicz, G., *Relation of energies and coverages of underpotential and overpotential deposited H at Pt and other metals to the 'volcano curve' for cathodic $H_2$ evolution kinetics.* Electrochimica Acta, 2000. **45**(25–26): p. 4075-4083.
96. Fauque, G.D., Berlier, Y. M., Czechowski, M.H., Dimon, B., Lespinat, P.A., LeGall, J., *A proton-deuterium exchange study of three types of Desulfovibrio hydrogenases.* Journal of Industrial Microbiology, 1987. **2**(1): p. 15-23.
97. [cited 2016; Available from: http://www.esrl.noaa.gov/gmd/ccgg/trends/weekly.html.
98. Ragsdale, S.W., *Life with carbon monoxide.* Critical Reviews in Biochemistry and Molecular Biology, 2004. **39**(3): p. 165-195.
99. Svetlitchnyi, V., Peschel, C., Acker, G., Meyer, O., *Two membrane-associated NiFeS-carbon monoxide dehydrogenases from the anaerobic carbon-monoxide-utilizing eubacterium Carboxydothermus hydrogenoformans.* Journal of Bacteriology, 2001. **183**(17): p. 5134-5144.
100. Dobbek, H., Svetlitchnyi, V., Gremer, L., Huber, R., Meyer, O., *Crystal structure of a carbon monoxide dehydrogenase reveals a [Ni-4Fe-5S] cluster.* Science, 2001. **293**(5533): p. 1281-1285.
101. Drennan, C.L., Heo, J. Y., Sintchak, M. D., Schreiter, E., Ludden, P. W., *Life on carbon monoxide: X-ray structure of Rhodospirillum rubrum Ni-Fe-S carbon*

*monoxide dehydrogenase.* Proceedings of the National Academy of Sciences of the United States of America, 2001. **98**(21): p. 11973-11978.
102. Parkin, A., et al., *Rapid and Efficient Electrocatalytic $CO_2$/CO Interconversions by Carboxydothermus hydrogenoformans CO Dehydrogenase I on an Electrode.* Journal of the American Chemical Society, 2007. **129**(34): p. 10328-10329.
103. Jeoung, J.H., Dobbek, H., *Carbon dioxide activation at the Ni,Fe-cluster of anaerobic carbon monoxide dehydrogenase.* Science, 2007. **318**(5855): p. 1461-1464.
104. Jeffrey, G.A., *An introduction to hydrogen bonding*. Oxford University Press.
105. Dobbek, H., et al., *Carbon monoxide induced decomposition of the active site [Ni-4Fe-5S] cluster of CO dehydrogenase.* Journal of the American Chemical Society, 2004. **126**(17): p. 5382-5387.
106. Armand, M., Endres, F., MacFarlane, D. R., Ohno, H., Scrosati, B., *Ionic-liquid materials for the electrochemical challenges of the future.* Nature Materials, 2009. **8**(8): p. 621-629.
107. Walden, P., Bull. Acad. Imp. Sci. St Petersbourg, 1914(8): p. 405.
108. Chum, H.L., Koch, V. R., Miller, L. L., Osteryoung, R. A., *Electrochemical scrutiny of organometallic iron complexes and hexamethylbenzene in a room temperature molten salt.* Journal of the American Chemical Society, 1975. **97**(11): p. 3264-3265.
109. Hapiot, P., Lagrost, C., *Electrochemical reactivity in room-temperature ionic liquids.* Chemical Reviews, 2008. **108**(7): p. 2238-2264.
110. Hallett, J.P., Welton, T., *Room-Temperature Ionic Liquids: Solvents for Synthesis and Catalysis. 2.* Chemical Reviews, 2011. **111**(5): p. 3508-3576.
111. Welton, T., *Room-temperature ionic liquids. Solvents for synthesis and catalysis.* Chemical Reviews, 1999. **99**(8): p. 2071-2083.
112. Barrosse-Antle, L.E., Bond, A. M., Compton, R. G., O'Mahony, A. M., Rogers, E. I., Silvester, D. S., *Voltammetry in Room Temperature Ionic Liquids: Comparisons and Contrasts with Conventional Electrochemical Solvents.* Chemistry-an Asian Journal, 2010. **5**(2): p. 202-230.
113. Shamsipur, M., Beigi, A. A. M., Teymouri, M., Pourmortazavi, S. M., Irandoust, M., *Physical and electrochemical properties of ionic liquids 1-ethyl-3-methylimidazolium tetrafluoroborate, 1-butyl-3-methylimidazolium trifluoromethanesulfonate and 1-butyl-1-methylpyrrolidinium bis(trifluoromethylsulfonyl)imide.* Journal of Molecular Liquids, 2010. **157**(1): p. 43-50.
114. Tokuda, H., Tsuzuki, S., Susan, M. A. B. H., Hayamizu, K., Watanabe, M., *How ionic are room-temperature ionic liquids? An indicator of the physicochemical properties.* Journal of Physical Chemistry B, 2006. **110**(39): p. 19593-19600.
115. González, B., González, E. J., *Physical properties of the pure 1-methyl-1-propylpyrrolidinium bis(trifluoromethylsulfonyl)imide ionic liquid and its binary mixtures with alcohols.* The Journal of Chemical Thermodynamics, 2014. **68**: p. 109-116.
116. MacFarlane, D.R., Meakin, P., Sun, J., Amini, N., Forsyth, M., *Pyrrolidinium imides: a new family of molten salts and conductive plastic crystal phases.* The Journal of Physical Chemistry B, 1999. **103**(20): p. 4164-4170.
117. Allen, M., Evans, D. F., Lumry, R., *Thermodynamic properties of the ethylammonium nitrate+ water system: Partial molar volumes, heat*

*capacities, and expansivities.* Journal of Solution Chemistry, 1985. **14**(8): p. 549-560.
118. Greaves, T.L., Weerawardena, A., Fong, C., Krodkiewska, I., Drummond, C. J., *Protic ionic liquids: solvents with tunable phase behavior and physicochemical properties.* The Journal of Physical Chemistry B, 2006. **110**(45): p. 22479-22487.
119. Yasuda, T., Kinoshita, H., Miran, M. S., Tsuzuki, S., Watanabe, M., *Comparative study on physicochemical properties of protic ionic liquids based on allylammonium and propylammonium cations.* Journal of Chemical & Engineering Data, 2013. **58**(10): p. 2724-2732.
120. Aparicio, S., Atilhan, M., Khraisheh, M., Alcalde, R., *Study on Hydroxylammonium-Based Ionic Liquids. I. Characterization.* Journal of Physical Chemistry B, 2011. **115**(43): p. 12473-12486.
121. Moniruzzaman, M., Nakashima, K., Kamiya, N., Goto, M., *Recent advances of enzymatic reactions in ionic liquids.* Biochemical Engineering Journal, 2010. **48**(3): p. 295-314.
122. Hunt, P.A., *Why Does a Reduction in Hydrogen Bonding Lead to an Increase in Viscosity for the 1-Butyl-2,3-dimethyl-imidazolium-Based Ionic Liquids?* The Journal of Physical Chemistry B, 2007. **111**(18): p. 4844-4853.
123. Okoturo, O.O., VanderNoot, T. J., *Temperature dependence of viscosity for room temperature ionic liquids.* Journal of Electroanalytical Chemistry, 2004. **568**(1-2): p. 167-181.
124. Sun, J., Forsyth, M., MacFarlane, D. R., *Room-Temperature Molten Salts Based on the Quaternary Ammonium Ion.* Journal of Physical Chemistry B, 1998. **102**(44): p. 8858-8864.
125. Every, H.A., Bishop, A. G., MacFarlane, D. R., Oraedd, G., Forsyth, M., *Transport properties in a family of dialkylimidazolium ionic liquids.* Physical Chemistry Chemical Physics, 2004. **6**(8): p. 1758-1765.
126. Noda, A., Hayamizu, K. Watanabe, M., *Pulsed-Gradient Spin–Echo 1H and 19F NMR Ionic Diffusion Coefficient, Viscosity, and Ionic Conductivity of Non-Chloroaluminate Room-Temperature Ionic Liquids.* The Journal of Physical Chemistry B, 2001. **105**(20): p. 4603-4610.
127. Suarez, P.A.Z., Consorti, C. S., De Souza, R. F., Dupont, J. Goncalves, R. S., *Electrochemical behavior of vitreous glass carbon and platinum electrodes in the ionic liquid 1-n-butyl-3-methylimidazolium trifluoroacetate.* Journal of Brazilian Chemical Society, 2002. **13**(1): p. 106-109.
128. Bonhôte, P., Dias, A. P., Papageorgiou, N., Kalyanasundaram, K., Grätzel, M., *Hydrophobic, Highly Conductive Ambient-Temperature Molten Salts.* Inorganic Chemistry, 1996. **35**(5): p. 1168-1178.
129. Koddermann, T., Wertz, C., Heintz, A., Ludwig, R., *Ion-pair formation in the ionic liquid 1-ethyl-3-methylimidazolium bis(triflyl)imide as a function of temperature and concentration.* Chemphyschem, 2006. **7**(9): p. 1944-1949.
130. Suarez, P.A.Z., Consorti, C. S., de Souza, R. F., Dupont, J., Goncalves, R. S., *Electrochemical behavior of vitreous glass carbon and platinum electrodes in the ionic liquid 1-n-butyl-3-methylimidazolium trifluoroacetate.* Journal of the Brazilian Chemical Society, 2002. **13**(1): p. 106-109.
131. Xiao, L., Johnson, K. E., *Electrochemistry of 1-butyl-3-methyl-1H-imidazolium tetrafluoroborate ionic liquid.* Journal of the Electrochemical Society, 2003. **150**(6): p. E307-E311.

132. Howlett, P.C., Izgorodina, E. I., Forsyth, M., MacFarlane, D. R., *Electrochemistry at negative potentials in bis(trifluoromethanesulfonyl)amide ionic liquids.* Zeitschrift Fur Physikalische Chemie-International Journal of Research in Physical Chemistry & Chemical Physics, 2006. **220**(10-11): p. 1483-1498.
133. Widegren, J.A., Laesecke, A., Magee, J. W., *The effect of dissolved water on the viscosities of hydrophobic room-temperature ionic liquids.* Chemical Communications (Cambridge), 2005(12): p. 1610-1612.
134. Widegren, J.A., Saurer, E. M., Marsh, K. N., Magee, J. W., *Electrolytic conductivity of four imidazolium-based room-temperature ionic liquids and the effect of a water impurity.* Journal of Chemical Thermodynamics, 2005. **37**(6): p. 569-575.
135. Fitchett, B.D., Knepp, T. N., Conboy, J. C., *1-Alkyl-3-methylimidazolium bis(perfluoroalkylsulfonyl)imide water-immiscible ionic liquids. The effect of water on electrochemical and physical properties.* Journal of Electrochemical Society, 2004. **151**(7): p. E219-E225.
136. Schroder, U., et al., *Water-induced accelerated ion diffusion: voltammetric studies in 1-methyl-3-[2,6-(S)-dimethylocten-2-yl]imidazolium tetrafluoroborate, 1-butyl-3-methylimidazolium tetrafluoroborate and hexafluorophosphate ionic liquids.* New Journal of Chemistry, 2000. **24**(12): p. 1009-1015.
137. Seddon, K.R., Stark, A., Torres, M.J., *Influence of chloride, water, and organic solvents on the physical properties of ionic liquids.* Pure and Applied Chemistry, 2000. **72**(12): p. 2275-2287.
138. Saheb, A., Janata, J., Josowicz, M., *Reference electrode for ionic liquids.* Electroanalysis, 2006. **18**(4): p. 405-409.
139. Snook, G.A., Best, A. S., Pandolfo, A. G., Hollenkamp, A. F., *Evaluation of a Ag vertical bar Ag+ reference electrode for use in room temperature ionic liquids.* Electrochemistry Communications, 2006. **8**(9): p. 1405-1411.
140. Lewandowski, A., Waligora, L., Galinski, M., *Ferrocene as a Reference Redox Couple for Aprotic Ionic Liquids.* Electroanalysis, 2009. **21**(20): p. 2221-2227.
141. Sukardi, S.K., Zhang, J., Burgar, I., Horne, M. D., Hollenkamp, A. F., MacFarlane, D. R., Bond, A. M., *Prospects for a widely applicable reference potential scale in ionic liquids based on ideal reversible reduction of the cobaltocenium cation.* Electrochemistry Communications, 2008. **10**(2): p. 250-254.
142. Rogers, E.I., et al., *Voltammetric characterization of the ferrocene vertical bar ferrocenium and cobaltocenium vertical bar cobaltocene redox couples in RTILs.* Journal of Physical Chemistry C, 2008. **112**(7): p. 2729-2735.
143. Silvester, D.S., Ward, K. R., Aldous, L., Hardacre, C., Compton, R. G., *The electrochemical oxidation of hydrogen at activated platinum electrodes in room temperature ionic liquids as solvents.* Journal of Electroanalytical Chemistry, 2008. **618**(1-2): p. 53-60.
144. Torriero, A.A.J., Sunarso, J., Howlett, P. C., *Critical evaluation of reference systems for voltammetric measurements in ionic liquids.* Electrochimica Acta, 2012. **82**(0): p. 60-68.
145. Zhao, C., et al., *Electrochemistry of room temperature protic ionic liquids.* Journal of Physical Chemistry B, 2008. **112**(23): p. 6923-6936.

146. Fu, C., et al., *The Kinetics of Ferrocene Volatilisation from an Ionic Liquid.* A European Journal of Chemical Physics and Physical Chemistry, 2011. **12**(9): p. 1708-1713.
147. Fu, C., et al., *Volatilisation of ferrocene from ionic liquids: kinetics and mechanism.* Chemical Communications, 2011. **47**(25): p. 7083-7085.
148. Torriero, A.A.J., et al., *Physical and electrochemical properties of thioether-functionalized ionic liquids.* Journal of Physical Chemistry B, 2009. **113**(32): p. 11222-11231.
149. Kornyshev, A.A., *Double-Layer in Ionic Liquids: Paradigm Change?* The Journal of Physical Chemistry B, 2007. **111**(20): p. 5545-5557.
150. Garcia, B., Lavallée, S., Perron, G., Michot, C., Armand, M., *Room temperature molten salts as lithium battery electrolyte.* Electrochimica Acta, 2004. **49**(26): p. 4583-4588.
151. Howlett, P.C., MacFarlane, D. R., Hollenkamp, A. F., *High Lithium Metal Cycling Efficiency in a Room-Temperature Ionic Liquid.* Electrochemical and Solid-State Letters, 2004. **7**(5): p. A97-A101.
152. Seki, S., Kobayashi, Y., Miyashiro, H., Ohno, Y., Usami, A., Mita, Y., Kihira, N., Watanabe, M., Terada, N., *Lithium Secondary Batteries Using Modified-Imidazolium Room-Temperature Ionic Liquid.* The Journal of Physical Chemistry B, 2006. **110**(21): p. 10228-10230.
153. Shin, J.H., Henderson, W. A., Passerini, S., *PEO-Based Polymer Electrolytes with Ionic Liquids and Their Use in Lithium Metal-Polymer Electrolyte Batteries.* Journal of The Electrochemical Society, 2005. **152**(5): p. A978-A983.
154. Seki, S., Kobayashi, Y., Miyashiro, H., Ohno, Y., Mita, Y., Usami, A., Terada, N., Watanabe, M., *Reversibility of Lithium Secondary Batteries Using a Room-Temperature Ionic Liquid Mixture and Lithium Metal.* Electrochemical and Solid-State Letters, 2005. **8**(11): p. A577-A578.
155. Ogasawara, T., Débart, A., Holzapfel, M., Novák, P., Bruce, P. G., *Rechargeable Li2O2 Electrode for Lithium Batteries.* Journal of the American Chemical Society, 2006. **128**(4): p. 1390-1393.
156. Fuller, J., Breda, A. C., Carlin, R. T., *Ionic Liquid‐Polymer Gel Electrolytes.* Journal of The Electrochemical Society, 1997. **144**(4): p. L67-L70.
157. Navarra, M.A., Panero, S., Scrosati, B., *Novel, Ionic-Liquid-Based, Gel-Type Proton Membranes.* Electrochemical and Solid-State Letters, 2005. **8**(6): p. A324-A327.
158. Winther-Jensen, B., Winther-Jensen, O., Forsyth, M., MacFarlane, D. R., *High rates of oxygen reduction over a vapor phase-polymerized PEDOT electrode.* Science, 2008. **321**(5889): p. 671-674.
159. Susan, M.A.B.H., Kaneko, T., Noda, A., Watanabe, M., *Ion Gels Prepared by in Situ Radical Polymerization of Vinyl Monomers in an Ionic Liquid and Their Characterization as Polymer Electrolytes.* Journal of the American Chemical Society, 2005. **127**(13): p. 4976-4983.
160. Diaz, M., Ortiz, A., Ortiz, I., *Progress in the use of ionic liquids as electrolyte membranes in fuel cells.* Journal of Membrane Science, 2014. **469**: p. 379-396.
161. Yasuda, T., Watanabe, M., *Protic ionic liquids: Fuel cell applications.* Mrs Bulletin, 2013. **38**(7): p. 560-566.

162. Arbizzani, C., Biso, M., Cericola, D., Lazzari, M., Soavi, F., Mastragostino, M., *Safe, high-energy supercapacitors based on solvent-free ionic liquid electrolytes.* Journal of Power Sources, 2008. **185**(2): p. 1575-1579.
163. Sato, T., Masuda, G., Takagi, K., *Electrochemical properties of novel ionic liquids for electric double layer capacitor applications.* Electrochimica Acta, 2004. **49**(21): p. 3603-3611.
164. Turner, M.B., Spear, S. K., Holbrey, J. D., Daly, D. T., Rogers, R. D., *Ionic liquid-reconstituted cellulose composites as solid support matrices for biocatalyst immobilization.* Biomacromolecules, 2005. **6**(5): p. 2497-2502.
165. Turner, M.B., Spear, S. K., Holbrey, J. D., Rogers, R. D., *Production of bioactive cellulose films reconstituted from ionic liquids.* Biomacromolecules, 2004. **5**(4): p. 1379-1384.
166. Lozano, P., de Diego, T., Carrie, D., Vaultier, M., Iborra, J. L., *Continuous green biocatalytic processes using ionic liquids and supercritical carbon dioxide.* Chemical Communications, 2002(7): p. 692-693.
167. Yu, P., Lin, Y., Xiang, L., Su, L., Zhang, J., Mao, L., *Molecular Films of Water-Miscible Ionic Liquids Formed on Glassy Carbon Electrodes: Characterization and Electrochemical Applications.* Langmuir, 2005. **21**(20): p. 9000-9006.
168. Chen, H., Wang, Y., Liu, Y., Wang, Y., Qi, L., Dong, S., *Direct electrochemistry and electrocatalysis of horseradish peroxidase immobilized in Nafion-RTIL composite film.* Electrochemistry Communications, 2007. **9**(3): p. 469-474.
169. Sun, W., Gao, R., Jiao, K., *Electrochemistry and Electrocatalysis of Hemoglobin in Nafion/nano-CaCO3 Film on a New Ionic Liquid BPPF6 Modified Carbon Paste Electrode.* The Journal of Physical Chemistry B, 2007. **111**(17): p. 4560-4567.
170. de Groot, M.T., Merkx, M., Koper, M. T. M., *Additional evidence for heme release in myoglobin-DDAB films on pyrolitic graphite.* Electrochemistry Communications, 2006. **8**(6): p. 999-1004.
171. DiCarlo, C.M., Compton, D. L., Evans, K. O., Laszlo, J. A., *Bioelectrocatalysis in ionic liquids. Examining specific cation and anion effects on electrode-immobilized cytochrome c.* Bioelectrochemistry, 2006. **68**(2): p. 134-143.
172. Compton, D.L., Laszlo, J. A., *Loss of cytochrome c Fe(III)/Fe(II) redox couple in ionic liquids.* Journal of Electroanalytical Chemistry, 2003. **553**: p. 187-190.
173. Wang, S.F., Chen, T., Zhang, Z. L., Shen, X. C., Lu, Z. X., Pang, D. W., Wong, K. Y., *Direct electrochemistry and electrocatalysis of heme proteins entrapped in agarose hydrogel films in room-temperature ionic liquids.* Langmuir, 2005. **21**(20): p. 9260-9266.
174. Brusova, Z., Gorton, L., Magner, E., *Comment on "Direct electrochemistry and electrocatalysis of heme proteins entrapped in agarose hydrogel films in room-temperature ionic liquids".* Langmuir, 2006. **22**(26): p. 11453-11455.
175. Ciaccafava, A., Alberola, M., Hameury, S., Infossi, P., Giudici-Orticoni, M. T., Lojou, E., *Hydrogen bioelectrooxidation in ionic liquids: From cytochrome c3 redox behavior to hydrogenase activity.* Electrochimica Acta, 2011. **56**(9): p. 3359-3368.
176. Kuwahara, J., Ikari, R., Murata, K., Nakamura, N., Ohno, H., *Electrocatalytic reduction of oxygen by bilirubin oxidase in hydrophobic ionic liquids containing a small quantity of water.* Catalysis Today, 2013. **200**: p. 49-53.
177. Leger, C., Jones, A. K., Albracht, S. P. J., Armstrong, F. A., *Effect of a dispersion of interfacial electron transfer rates on steady state catalytic electron*

*transport in [NiFe]-hydrogenase and other enzymes.* Journal of Physical Chemistry B, 2002. **106**(50): p. 13058-13063.
178. Hirst, J., Armstrong, F. A., *Fast-scan cyclic voltammetry of protein films on pyrolytic graphite edge electrodes: Characteristics of electron exchange.* Analytical Chemistry, 1998. **70**(23): p. 5062-5071.
179. Roessler, M.M., *EPR Investigations of Iron-Sulfur Cluster Relays in Enzymes*. 2011, University of Oxford.
180. Xu, F., Shin, W. S., Brown, S. H., Wahleithner, J. A., Sundaram, U. M., Solomon, E. I., *A study of a series of recombinant fungal laccases and bilirubin oxidase that exhibit significant differences in redox potential, substrate specificity, and stability.* Biochimica Et Biophysica Acta-Protein Structure and Molecular Enzymology, 1996. **1292**(2): p. 303-311.
181. Noviandri, I., Brown, K. N., Fleming, D. S., Gulyas, P. T., Lay, P. A., Masters, A. F., Phillips, L., *The Decamethylferrocenium/Decamethylferrocene Redox Couple: A Superior Redox Standard to the Ferrocenium/Ferrocene Redox Couple for Studying Solvent Effects on the Thermodynamics of Electron Transfer.* The Journal of Physical Chemitry B, 1999. **103**(32): p. 6713-6722.
182. Bradford, M.M., *Rapid and Sensitive Method for Quantitation of Microgram Quantities of Protein Utilizing Principle of Protein-Dye Binding.* Analytical Biochemistry, 1976. **72**(1-2): p. 248-254.
183. Walcarius, A., Minteer, S. D., Wang, J., Lin, Y., Merkoçi, A., *Nanomaterials for bio-functionalized electrodes: recent trends.* Journal of Materials Chemistry B, 2013. **1**(38): p. 4878.
184. Minteer, S.D., Atanassov, P., Luckarift, H. R., Johnson, G. R., *New materials for biological fuel cells.* Materials Today, 2012. **15**(4): p. 166-173.
185. Geim, A.K., Novoselov, K. S., *The rise of graphene.* Nature Materials, 2007. **6**(3): p. 183-191.
186. Baughman, R.H., Zakhidov, A. A., de Heer, W. A., *Carbon nanotubes - the route toward applications.* Science, 2002. **297**(5582): p. 787-792.
187. Centi, G., Perathoner, S., *Problems and perspectives in nanostructured carbon-based electrodes for clean and sustainable energy.* Catalysis Today, 2010. **150**(1-2): p. 151-162.
188. Mayorov, A.S., Gorbachev, R. V., Morozov, S. V., Britnell, L., Jalil, R., Ponomarenko, L. A., Blake, P., Novoselov, K. S., Watanabe, K., Taniguchi, T., Geim, A. K., *Micrometer-Scale Ballistic Transport in Encapsulated Graphene at Room Temperature.* Nano Letters, 2011. **11**(6): p. 2396-2399.
189. Morozov, S.V., Novoselov, K. S., Katsnelson, M. I., Schedin, F., Elias, D. C., Jaszczak, J. A., Geim, A. K., *Giant intrinsic carrier mobilities in graphene and its bilayer.* Physical Review Letters, 2008. **100**(1).
190. Moser, J., Barreiro, A., Bachtold, A., *Current-induced cleaning of graphene.* Applied Physics Letters, 2007. **91**(16): p. 163513.
191. Wu, P., Shao, Q. A., Hu, Y. J., Jin, J. A., Yin, Y. J., Zhang, H., Cai, C. X., *Direct electrochemistry of glucose oxidase assembled on graphene and application to glucose detection.* Electrochimica Acta, 2010. **55**(28): p. 8606-8614.
192. Park, S., Ruoff, R. S., *Chemical methods for the production of graphenes.* Nature Nano, 2009. **4**(4): p. 217-224.
193. Novoselov, K.S., Geim, A. K., Morozov, S. V., Jiang, D., Zhang, Y., Dubonos, S. V., Grigorieva, I. V., Firsov, A. A., *Electric field effect in atomically thin carbon films.* Science, 2004. **306**(5696): p. 666-9.

194. Berger, C., Song, Z. M., Li, X. B., Wu, X. S., Brown, N., Naud, C., Mayou, D., Li, T. B., Hass, J., Marchenkov, A. N., Conrad, E. H., First, P. N., de Heer, W. A., *Electronic confinement and coherence in patterned epitaxial graphene.* Science, 2006. **312**(5777): p. 1191-1196.
195. Alwarappan, S., Erdem, A., Liu, C., Li, C. Z., *Probing the Electrochemical Properties of Graphene Nanosheets for Biosensing Applications.* Journal of Physical Chemistry C, 2009. **113**(20): p. 8853-8857.
196. Holzinger, M., Le Goff, A., Cosnier, S., *Carbon nanotube/enzyme biofuel cells.* Electrochimica Acta, 2012. **82**: p. 179-190.
197. Yan, Y.M., Zheng, W., Su, L., Mao, L. Q., *Carbon-nanotube-based glucose/$O_2$ biofuel cells.* Advanced Materials, 2006. **18**(19): p. 2639.
198. Ivnitski, D., Artyushkova, K., Rincon, R. A., Atanassov, P., Luckarift, H. R., Johnson, G. R., *Entrapment of enzymes and carbon nanotubes in biologically synthesized silica: Glucose oxidase-catalyzed direct electron transfer.* Small, 2008. **4**(3): p. 357-364.
199. Hummers, W.S., Offeman, R. E., *Preparation of Graphitic Oxide.* Journal of the American Chemical Society, 1958. **80**(6): p. 1339-1339.
200. Walcarius, A., et al., *Nanomaterials for bio-functionalized electrodes: recent trends.* Journal of Materials Chemistry B, 2013. **1**(38): p. 4878-4908.
201. Minteer, S.D., et al., *New materials for biological fuel cells.* Materials Today, 2012. **15**(4): p. 166-173.
202. Hexter, S.V., Esterle, T. F., Armstrong, F. A., *A unified model for surface electrocatalysis based on observations with enzymes.* Physical Chemistry Chemical Physics, 2014. **16**(24): p. 11822-11833.
203. Roessler, M.M., Evans, R. M., Davies, R. A., Harmer, J., Armstrong, F. A., *EPR Spectroscopic Studies of the Fe-S Clusters in the $O_2$-Tolerant [NiFe]-Hydrogenase Hyd-1 from Escherichia coli and Characterization of the Unique [4Fe-3S] Cluster by HYSCORE.* Journal of the American Chemical Society, 2012. **134**(37): p. 15581-15594.
204. Lojou, E., Luo, X., Brugna, M., Candoni, N., Dementin, S., Giudici-Orticoni, M. T., *Biocatalysts for fuel cells: efficient hydrogenase orientation for $H_2$ oxidation at electrodes modified with carbon nanotubes.* Journal of Biological Inorganic Chemistry, 2008. **13**(7): p. 1157-1167.
205. Lojou, E., *Hydrogenases as catalysts for fuel cells: Strategies for efficient immobilization at electrode interfaces.* Electrochimica Acta, 2011. **56**(28): p. 10385-10397.
206. Luo, X.J., Brugna, M., Tron-Infossi, P., Giudici-Orticoni, M. T., Lojou, E., *Immobilization of the hyperthermophilic hydrogenase from Aquifex aeolicus bacterium onto gold and carbon nanotube electrodes for efficient $H_2$ oxidation.* Journal of Biological Inorganic Chemistry, 2009. **14**(8): p. 1275-1288.
207. Gao, F., Viry, L., Maugey, M., Poulin, P., Mano, N., *Engineering hybrid nanotube wires for high-power biofuel cells.* Nature Communications, 2010. **1**.
208. Weigel, M.C., Tritscher, E., Lisdat, F., *Direct electrochemical conversion of bilirubin oxidase at carbon nanotube-modified glassy carbon electrodes.* Electrochemistry Communications, 2007. **9**(4): p. 689-693.

209. Schubert, K., Goebel, G., Lisdat, F., *Bilirubin oxidase bound to multi-walled carbon nanotube-modified gold.* Electrochimica Acta, 2009. **54**(11): p. 3033-3038.
210. Gobel, G., Lisdat, F., *Organic interlayers for oxygen reducing electrodes based on bilirubin oxidase and MWCNT modified gold.* Electrochemistry Communications, 2008. **10**(11): p. 1691-1694.
211. Jonsson-Niedziolka, M., Kaminska, A., Opallo, M., *Pyrene-functionalised single-walled carbon nanotubes for mediatorless dioxygen bioelectrocatalysis.* Electrochimica Acta, 2010. **55**(28): p. 8744-8750.
212. Compton, R.G., Banks, C. E., *Understanding Voltammetry, 2nd Edition.* Understanding Voltammetry, 2nd Edition, 2011: p. 1-429.
213. Hexter, S.V., Grey, F., Happe, T., Climent, V., Armstrong, F. A., *Electrocatalytic mechanism of reversible hydrogen cycling by enzymes and distinctions between the major classes of hydrogenases.* Proceedings of the National Academy of Sciences of the United States of America, 2012. **109**(29): p. 11516-11521.
214. Vincent, K.A., Parkin, A., Lenz, O., Albracht, S. P. J., Fontecilla-Camps, J. C., Cammack, R., Friedrich, B., Armstrong, F. A., *Electrochemical definitions of $O_2$ sensitivity and oxidative inactivation in hydrogenases.* Journal of the American Chemical Society, 2005. **127**(51): p. 18179-18189.
215. Vincent, K.A., et al., *Electrochemical definitions of $O_2$ sensitivity and oxidative inactivation in hydrogenases.* Journal of the American Chemical Society, 2005. **127**(51): p. 18179-18189.
216. Su, B., Hatay, I., Ge, P. Y., Mendez, M., Samec, Z., Ersoz, M., Girault, H. H., *Oxygen and proton reduction by decamethylferrocene in non-aqueous acidic media.* Chemical Communications, 2010. **46**(17): p. 2918-2919.
217. Yokozeki, A., Shiflett, M. B., Junk, C. P., Grieco, L. M., Foo, T., *Physical and Chemical Absorptions of Carbon Dioxide in Room-Temperature Ionic Liquids.* Journal of Physical Chemistry B, 2008. **112**(51): p. 16654-16663.
218. Lide, D.R., *CRC handbook of chemistry and physics*. 2004: CRC press.
219. Lei, Z.G., Dai, C. N., Chen, B. H., *Gas Solubility in Ionic Liquids.* Chemical Reviews, 2014. **114**(2): p. 1289-1326.
220. Morgan, D., L. Ferguson, and P. Scovazzo, *Diffusivities of gases in room-temperature ionic liquids: Data and correlations obtained using a lag-time technique.* Industrial & Engineering Chemistry Research, 2005. **44**(13): p. 4815-4823.
221. Soukharev, V., Mano, N., Heller, A., *A Four-Electron $O_2$-Electroreduction Biocatalyst Superior to Platinum and a Biofuel Cell Operating at 0.88 V.* Journal of the American Chemical Society, 2004. **126**(27): p. 8368-8369.
222. Kang, C., Shin, H., Heller, A., *On the stability of the "wired" bilirubin oxidase oxygen cathode in serum.* Bioelectrochemistry, 2006. **68**(1): p. 22-26.
223. Kim, H.H., Mano, N., Zhang, X. C., Heller, A., *A miniature membrane-less biofuel cell operating under physiological conditions at 0.5 V.* Journal of Electrochem Society, 2003. **150**(2): p. A209-A213.
224. Shleev, S., Elkasmi, A., Ruzgas, T., Gorton, L., *Direct heterogeneous electron transfer reactions of bilirubin oxidase at a spectrographic graphite electrode.* Electrochemistry Communications, 2004. **6**(9): p. 934-939.

225. Thuesen, M.H., Farver, O., Reinhammar, B., Ulstrup, J., *Cyclic voltammetry and electrocatalysis of the blue copper oxidase Polyporus versicolor laccase.* Acta Chemica Scandinavica, 1998. **52**(5): p. 555-562.
226. Tsujimura, S., Kamitaka, Y., Kano, K., *Diffusion-Controlled Oxygen Reduction on Multi-Copper Oxidase-Adsorbed Carbon Aerogel Electrodes without Mediator.* Fuel Cells, 2007. **7**(6): p. 463-469.
227. Zheng, W., Li, Q. F., Su, L., Yan, Y. M., Zhang, J., Mao, L. Q., *Direct electrochemistry of multi-copper oxidases at carbon nanotubes noncovalently functionalized with cellulose derivatives.* Electroanalysis, 2006. **18**(6): p. 587-594.
228. Tsujimura, S., Nakagawa, T., Kano, K., Ikeda, T., *Kinetic study of direct bioelectrocatalysis of dioxygen reduction with bilirubin oxidase at carbon electrodes.* Electrochemistry, 2004. **72**(6): p. 437-439.
229. Ivnitski, D.M., Khripin, C., Luckarift, H. R., Johnson, G. R., Atanassov, P., *Surface characterization and direct bioelectrocatalysis of multicopper oxidases.* Electrochimica Acta, 2010. **55**(24): p. 7385-7393.
230. Leech, D., Kavanagh, P., Schuhmann, W., *Enzymatic fuel cells: Recent progress.* Electrochimica Acta, 2012. **84**: p. 223-234.
231. Yaropolov, A.I., Kharybin, A. N., Emneus, J., MarkoVarga, G., Gorton, L., *Electrochemical properties of some copper-containing oxidases.* Bioelectrochemistry and Bioenergetics, 1996. **40**(1): p. 49-57.
232. Shleev, S., et al., *Direct heterogeneous electron transfer reactions of bilirubin oxidase at a spectrographic graphite electrode.* Electrochemistry Communications, 2004. **6**(9): p. 934-939.
233. Otsuka, K., Sugihara, T., Tsujino, Y., Osakai, T., Tamiya, E., *Electrochemical consideration on the optimum pH of bilirubin oxidase.* Analytical Biochemistry, 2007. **370**(1): p. 98-106.
234. Kataoka, K., Kitagawa, R., Inoue, M., Naruse, D., Sakurai, T., Huang, H. W., *Point Mutations at the Type I Cu Ligands, Cys457 and Met467, and at the Putative Proton Donor, Asp105, in Myrothecium verrucaria Bilirubin Oxidase and Reactions with Dioxygen†.* Biochemistry, 2005. **44**(18): p. 7004-7012.
235. Singh, K., McArdle, T., Sullivan, P. R., Blanford, C. F., *Sources of activity loss in the fuel cell enzyme bilirubin oxidase.* Energy & Environmental Science, 2013. **6**(8): p. 2460-2464.
236. Evans, R.M., Parkin, A., Roessler, M. M.,Murphy, B. J., Adamson, H., Lukey, M. J., Sargent, F.,Volbeda, A., Fontecilla-Camps, J. C., Armstrong, F. A., *Principles of Sustained Enzymatic Hydrogen Oxidation in the Presence of Oxygen – The Crucial Influence of High Potential Fe–S Clusters in the Electron Relay of [NiFe]-Hydrogenases.* Journal of the American Chemical Society, 2013. **135**(7): p. 2694-2707.
237. Mano, N., Mao, F., Heller, A., *A miniature biofuel cell operating in a physiological buffer.* Journal of the American Chemical Society, 2002. **124**(44): p. 12962-12963.
238. Kreuer, K.D., *Proton conductivity: Materials and applications.* Chemistry of Materials, 1996. **8**(3): p. 610-641.
239. Froba, A.P., Kremer, H., Leipertz, A., *Density, refractive index, interfacial tension, and viscosity of ionic liquids [EMIM][$EtSO_4$], [EMIM][$NTf_2$], [EMIM][$N(CN)_2$], and [OMA][$NTf_2$] in dependence on temperature at*

*atmospheric pressure.* Journal of Physical Chemistry B, 2008. **112**(39): p. 12420-12430.
240. Kestin, J., Sokolov, M., Wakeham, W. A., *Viscosity of Liquid Water in Range -8-Degrees-C to 150-Degrees-C.* Journal of Physical and Chemical Reference Data, 1978. **7**(3): p. 941-948.
241. Buzzeo, M.C., Klymenko, O. V., Wadhawan, J. D., Hardacre, C., Seddon, K. R., Compton, R. G., *Voltammetry of oxygen in the room-temperature ionic liquids 1-ethyl-3-methylimidazolium bis((trifluoromethyl)sulfonyl)imide and hexyltriethylammonium bis((trifluoromethyl)sulfonyl)imide: One-electron reduction to form superoxide. Steady-state and transient behavior in the same cyclic voltammogram resulting from widely different diffusion coefficients of oxygen and superoxide.* Journal of Physical Chemistry A, 2003. **107**(42): p. 8872-8878.
242. Atkins, P., *Physical Chemistry*. 2010, Oxford University Press.
243. Zhang, S., Sun, N., He, X., Lu, X., Zhang, X., *Physical Properties of Ionic Liquids: Database and Evaluation.* Journal of Physical and Chemical Reference Data, 2006. **35**(4): p. 1475.
244. Plumere, N., Rudiger, O., Oughli, A. A., Williams, R., Vivekananthan, J., Poller, S., Schuhmann, W., Lubitz, W., *A redox hydrogel protects hydrogenase from high-potential deactivation and oxygen damage.* Nature Chemistry, 2014. **6**(9): p. 822-827.
245. Xu, L., Armstrong, F. A., *Pushing the limits for enzyme-based membrane-less hydrogen fuel cells - achieving useful power and stability.* RSC Advances, 2015. **5**(5): p. 3649-3656.
246. Bara, J.E., Camper, D. E., Gin, D. L., Noble, R. D., *Room-Temperature Ionic Liquids and Composite Materials: Platform Technologies for $CO_2$ Capture.* Accounts of Chemical Research, 2010. **43**(1): p. 152-159.
247. Li, P.L., Henstridge, M. C., Xiong, L. H. J., Compton, R. G., *Rate and Extent of Carbon Dioxide Uptake In Room Temperature Ionic Liquids: A New Approach Using Microdisc Electrode Voltammetry.* Electroanalysis, 2013. **25**(10): p. 2268-2274.
248. Ohlin, C.A., Dyson, P. J., Laurenczy, G., *Carbon monoxide solubility in ionic liquids: determination, prediction and relevance to hydroformylation.* Chemical Communications, 2004(9): p. 1070-1071.
249. Ragsdale, S.W., Clark, J. E., Ljungdahl, L. G., Lundie, L. L., Drake, H L, *Properties of purified carbon monoxide dehydrogenase from Clostridium thermoaceticum, a nickel, iron-sulfur protein.* Journal of Biological Chemistry, 1983. **258**(4): p. 2364-9.
250. Rasmussen, M., S. Abdellaoui, and S.D. Minteer, *Enzymatic biofuel cells: 30 years of critical advancements.* Biosensors and Bioelectronics, 2016. **76**: p. 91-102.
251. Compton, R.G., Sanders, G. H. W., *Electrode Potentials*. Oxford Chemistry Primers, ed. R.G. Compton, et al. 1998, New York, USA: Oxford University Press.